INFORMATION TO USERS

This manuscript has been reproduced from the microfilm master. UMI films the text directly from the original or copy submitted. Thus, some thesis and dissertation copies are in typewriter face, while others may be from any type of computer printer.

The quality of this reproduction is dependent upon the quality of the copy submitted. Broken or indistinct print, colored or poor quality illustrations and photographs, print bleedthrough, substandard margins, and improper alignment can adversely affect reproduction.

In the unlikely event that the author did not send UMI a complete manuscript and there are missing pages, these will be noted. Also, if unauthorized copyright material had to be removed, a note will indicate the deletion.

Oversize materials (e.g., maps, drawings, charts) are reproduced by sectioning the original, beginning at the upper left-hand corner and continuing from left to right in equal sections with small overlaps.

Photographs included in the original manuscript have been reproduced xerographically in this copy. Higher quality 6" x 9" black and white photographic prints are available for any photographs or illustrations appearing in this copy for an additional charge. Contact UMI directly to order.

Bell & Howell Information and Learning
300 North Zeeb Road, Ann Arbor, MI 48106-1346 USA

UMI®
800-521-0600

NOTE TO USERS

This reproduction is the best copy available.
Page 261

UMI

INFLUENCE OF DYNAMIC BEHAVIOUR OF MATERIALS ON MACHINABILITY

By

HARON OGEGA GEKONDE

A Thesis

Submitted to the School of Graduate studies

in Partial Fulfilment of the Requirements

for the Degree

Doctor of Philosophy

McMaster University

© Copyright by Haron Ogega Gekonde. April 1998

INFLUENCE OF DYNAMIC BEHAVIOUR OF MATERIALS ON MACHINABILITY

DOCTOR OF PHILOSOPHY (1998) McMaster University

(Materials Engineering) Hamilton, Ontario

TITLE : Influence of Dynamic Behaviour of Materials on Machinability.

AUTHOR: Haron Ogega Gekonde, B.Sc., M.Sc., (University of Nairobi, Kenya)

SUPERVISOR: Professor S.V. Subramanian

NUMBER OF PAGES: xxxii, 313

ABSTRACT

The influence of dynamic behaviour of materials (i.e., the response of materials to large strain, high strain rate, deformation under large hydrostatic pressure occurring during metal cutting) on machinability (i.e., chip morphology, tool wear and surface finish) has been investigated in ferrous alloys with a wide range of matrix properties and volume fraction of second phase particles.

With the increase of cutting speed, there is change in the tribological phenomenon at the tool-chip interface from sliding to seizure. A physical model for seizure is proposed based on atomic contact at the tool-chip interface. The model predicts the critical cutting speed for onset of seizure from force measurements. Seizure is said to occur when the normal stress exceeds the yield strength of asperities such that the true area of contact approaches the apparent area of contact. The tribological phenomenon of seizure is shown to cause thermoplastic shear localisation. In consequence, the temperature at the tool-chip interface rises, leading to dissolution wear of the tool into the chip by a diffusion mechanism which causes chemical wear of the tool.

The technique of ICP-MS has been developed and used to separate the physical and chemical wear aspects of the tool by measurement of minute concentrations of tungsten present in the chips as WC as distinct from tungsten atomically dissolved in the chips. The results have confirmed that chemical crater wear dominates at high cutting speeds. The temperature distribution at the tool-chip interface has been predicted by finite element analysis and used to compute diffusion wear. A comparison of theoretical and experimental values of diffusion wear suggests that high diffusivity paths operate at the tool-chip interface to enhance the diffusivity by more than two orders of magnitude. The maximum depth of the measured crater depth profile has been found to coincide with

the phase transformation temperature of the workpiece material rather than the maximum predicted temperature at the tool-chip interface. The amount of dissolution wear, as measured by the amount of tungsten transferred into the chips is attributed to dislocation pipe diffusion. It is further suggested that dislocations generated by deformation concomitant with phase transformation provide high diffusivity paths that contribute to enhanced diffusion wear. The implication is that dissolution crater wear of the tool is phase transformation coupled. Dissolution crater wear can be suppressed if the tribological phenomenon of seizure can be prevented. This can be achieved by in-situ lubrication at the tool-chip interface through inclusion engineering of the workpiece. Alternatively, the diffusion wear can be minimised by coating the tool with a compound which has the least solubility in the workpiece.

The microstructural response to changes of metal cutting variables during the machining of a range of iron alloys with varying heat treatment condition and microstructural constituents of the matrix has been investigated to establish the inter-relationship among chip morphology, tool wear and surface finish. The microstructural changes in the chips have been analysed by optical microscopy, scanning electron microscopy, transmission electron microscopy and x-ray diffraction techniques. The results from the chips formed during machining of martensitic Fe-28.9%Ni-0.1%C alloy confirmed the presence of austenite, exhibiting grains as fine as 40-100 nm, in the white shear bands. This structure is attributed to a sequence of events: the reverse phase transformation of martensite to austenite, shear localisation, formation of the transformation shear bands, and probably dynamic recrystallisation. Thus it is demonstrated that thermal softening due to phase transformation causes shear localisation leading to chip segmentation in the primary shear zone.

Phenomenological observations are presented to confirm that shear localisation is caused by (i) geometrical softening due to second phase particles (graphite inclusions in cast iron, inclusions in free cutting steels), (ii) thermal softening of the matrix due to phase transformation or recrystallisation, and (iii) a combination of the above. Shear localisation causes steep temperature rise in a narrow band,

referred to as shear band. The interaction of the primary shear band with the cutting edge of the tool is found to cause dissolution wear of the cutting edge of the tool. The loss of the cutting edge in turn is shown to impair surface finish. The effect of metal cutting variables, i.e., speed, feed, depth of cut, external lubricants on shear localisation, chip morphology and tool wear is investigated. It is is shown that chip segmentation can be suppressed by decreasing the feed. This is analysed in terms of damage concepts underlying chip fracture behaviour.

To Mary, Joan, Maureen
and my parents
Gekonde and Nyabiage

ACKNOWLEDGEMENTS

I wish to thank most sincerely my supervisor, Dr. S.V. Subramanian for his constant guidance and encouragement throughout the course of this study. I wish to thank members of my supervisory committee, Drs. G.R. Purdy, J.D. Embury and M.A. Elbestawi for their guidance and helpful discussion. I am indebted to Dr. Z.S. Basinski for his intuition on the role of phase transformation in high strain rate deformation, which has formed the basis of interpretation of results reported in this thesis. I am grateful to Dr G.C. Weatherly for his generosity to provide me with TEM results, Dr. R. Sowerby for helpful discussion on ductile fracture behaviour of materials, Dr.J.Gao for helpful discussion with thesis draft.

I am grateful to the International Development Research Centre (IDRC), Canada, for providing me a scholarship and travel expenses. I wish to acknowledge with grateful thanks, research supports in the form of NSERC Strategic Grant, NSERC CRD Grant and MRCO (Manufacture Research Corporation of Ontario).

I wish to express special thanks to Mr. Jim McAndrew for help with Inductively Coupled Plasma Mass Spectrometry (ICP-MS), Ms Alice Pidruczny for help with Neutron Action Analysis (INAA), Dr. Dave Kingston, Surface Sciences, University of Western Ontario for help with Secondary Ion Mass Spectrometry and Mrs T. Castillo for help with SEM characterization of the chips, Mr. Chris Butcher and Mr. John Hudak for help with optical and SEM microscopy.

I wish to express my grateful thanks to Dofasco Inc. and in particular I.O'Reilly, M.Ichikawa and A.Cavicchioli of Dofasco Research for making available the Fe-Ni-C alloys used

in this research. I thank Dr G.A. Redfern for arranging the supply of steel from Elwood City Forge Corporation, Pa.,U.S.A., Mr.P.Khindri, Wellworth Manufacturing, Oakville for supply of ductile iron bars, Dr. J.Oakes, Telydyne Firth Sterling, TN, U.S.A. for Hafnium nitride coating of the tools.

TABLE OF CONTENTS

LIST OF FIGURES

Figure **Page**

Figure **Page**

LIST OF TABLES

Table **Page**

CHAPTER 1

INTRODUCTION

High speed machining may be defined as machining in the cutting speed range where the workpiece undergoes shear instabilities and localisation due to high strain rate deformation. It may also be regarded as the machining of a material in the range of cutting speeds where the chip makes intimate contact with the tool. Even though a large amount of literature has been reported on machining, the influence of dynamic behaviour of materials on metal cutting has not been given adequate attention. The tribological condition at the tool-chip interface and the morphology of the chip influence the mechanism of tool wear and the surface finish. The chip morphology is influenced by the tribological condition at the tool-chip interface and the shear instabilities (characteristic of the workpiece material). However, the tribological condition at the tool-chip interface at high cutting speeds is not well understood. Thus the source of the shear instabilities has been a subject of great controversy in the literature. The understanding of the tribological condition at the tool-chip interface and the role of the microstructural response to the strain, strain rate, temperature and pressure effects imposed by metal cutting variables is needed in order to clarify the controversy. These shear instabilities could be caused by geometrical softening or thermal softening of the workpiece material and hence lead to thermoplastic shear localisation which causes chip segmentation.

Thermoplastic shear localisation also known as adiabatic shear localisation is encountered in various fields notably; armour penetration and projectile fragmentation, and high speed machining and forming. The mechanism of thermoplastic shear localisation first proposed by Zener and

Hollomon [1] more than 50 years ago still holds namely; when an increment of stress due to strain hardening is overcome by a decrease in stress due to thermal softening plastic deformation will become unstable, and homogeneous deformation will give way to a localised band-like deformation mode to form adiabatic shear bands. Processes such as strain hardening and strain rate hardening which increase the flow stress contribute negatively while geometrical softening and thermal softening which lower the flow stress contribute positively to thermoplastic shear localisation. Recent developments by Meyers [2] suggest that thermoplastic shear localisation is caused by a sudden drop in flow stress accompanying a major microstructural event. Dynamic recrystallisation has been proposed to be the possible microstructural change responsible for shear localisation in a cold worked material. The role of phase transformation in shear localisation (i.e., whether phase transformation is the cause or effect of shear localisation) is not established in the literature. An important objective of the present study is to clarify the role of phase transformation in thermoplastic shear localisation and its consequence on chip segmentation, tool wear and surface finish in metal cutting.

Even though few attempts have been made in the literature to explain the mechanisms of chip formation and tool wear, adequate attention has not been given to inter-relationships among chip morphology, tool wear and surface finish. In recent studies of the micro-mechanisms of tool crater wear carried out by Ingle [3], experimental measurements of dissolution wear could not be accounted for by theoretical predictions of inter-diffusion at the tool-chip interface based on lattice diffusion. The enhanced diffusion was attributed to high diffusivity paths. An integrated approach has been adopted in the present work to use quantitative tool wear measurement and detailed optical and electron microscopy of the chips, coupled with temperature profile based on seizure model to clarify the inter-relationship among chip formation, tool wear and surface finish in high speed machining. The role of phase transformation in providing high diffusivity paths through dislocations has been elucidated.

The recent progress in nanotribology has underscored the importance of the chemical nature of atomic bonding at the interface in determining the frictional force rather than the normal force by itself. The interface strength is specific to the nature of the chemical bonds and is shown to vary by several orders of magnitude. Even though significant progress has been made in recent years on theoretical and experimental aspects of research in nanotribology, there is considerable difficulty in linking these findings on the atomic scale directly with the macro-engineering world. The approach in the present work is to link the macro-engineering observations (mm scale) to micro-mechanisms (on micrometer scale using microstructural characterisation and microanalytical tools) as an intermediate step in order to relate ultimately these findings to observations on nano- or atomic scale. In the present work on metal cutting with carbide tools, it is shown that a physical model based on atomic contact gives an adequate description of the conditions of seizure at the tool-chip interface wherein thermoplastic shear localised at the tool-chip interface raises the local temperature when thermally activated processes set in, causing inter-diffusion of solutes at the tool-chip interface.

Even though the technique of instrumental neutron activation analysis (INAA) is well developed to separate the physical and chemical wear by measuring minute concentrations of tungsten present as tungsten carbide in the chips as distinct from tungsten atomically dissolved in the chips, it is not adequately sensitive in analysing of elements with short half-life like titanium. Therefore the technique of inductively coupled plasma mass spectrometry (ICP-MS) has been developed in the current work and used to separate the physical and chemical wear in uncoated and TiN/TiC coated cemented carbide tools. ICP-MS combines the elegance of the ICP for atomizing and ionizing injected samples with the power of high sensitivity and selectivity of mass spectrometry. Using ICP-MS the limit of detection was 0.1 ppm with 4-7% relative standard deviation (RSD) at 95% confidence which is better than that of INAA (1 ppm with an accuracy of ±0.1 ppm). The results obtained by the two techniques on identical specimens have confirmed that ICP-MS is a quantitative tool, even more

powerful than INAA for the separation of physical and chemical wear during machining.

The microstructural response to changes in metal cutting variables and its influence on chip morphology, tool wear and surface finish has been investigated in the present work in a broad range of iron alloys with varying heat treatment condition and microstructural constituents of the matrix. The microstructural properties of the workpiece material influence shear localisation and hence the critical speed for chip segmentation. The ductile behaviour of the chip can be analysed using damage concepts. Thus the critical accumulated damage before fracture (CAD), which is a measure of ductile fracture behaviour of workpiece material, has been used to classify the workpiece materials according to their critical speed for chip segmentation. The classification is based on the microstructural parameters of the workpiece material, i.e., volume fraction of second phase particles and matrix plasticity. The presence of inclusions in the matrix lowers the (CAD) and the critical speed for chip segmentation by increasing the contribution of geometrical softening to shear localisation in the primary shear zone. Hardening of the matrix lowers the CAD and the critical speed for chip segmentation by increasing the material's susceptibility to thermoplastic shear localisation in the primary shear zone. In the absence of geometrical and thermal softening, strain rate hardening of the matrix increases the damage rate to promote chip segmentation at high cutting speeds.

Ferritic ductile iron with a large volume fraction of graphite nodules was chosen in the present study to elucidate the effect of geometrical softening on shear localisation and chip segmentation. A comparative study with AISI 1020 steel was carried out in an iron matrix identical to ferritic ductile iron but devoid of graphite nodules. The effect of changing the hardness and ductility, by increasing the volume fraction of pearlite content in the iron matrix on shear localisation and chip segmentation was investigated by comparing the machinability behaviour of AISI 1020 steel with AISI 1045 and AISI 1080 steel, i.e., by increasing the carbon content from 0.20, 0.45 to 0.80 wt%. In order to clarify the role of thermal softening, Fe-xNi-0.1wt%C alloy was chosen where x was varied from 1.5 wt%

to 30wt%. This series of alloys allowed the present work to clarify the role of thermal softening due to phase transformation as distinct from tempering of the hardened matrix. The Fe-Ni-C system is well characterised in the literature in terms of the phase transformation temperature as a function of nickel content and deformation and pressure effects on phase transformation temperature The study was conducted by use of optical microscopy, scanning electron microscopy, transmission electron microscopy and x-ray diffraction techniques to analyse the changes in microstructure in the chips.

The effect of metal cutting variables, i.e., speed, feed, depth of cut and external lubrication on microstructural response to machining was analysed in terms of strain, strain rate, temperature and pressure effects to rationalise experimental observations on chip segmentation and tool wear in iron-nickel-carbon alloys. The analysis of the results has been presented in light of the flow stress behaviour under conditions of large strain, high strain rate, high pressure and temperature plastic deformation which cause thermoplastic shear localisation triggered by microstructural changes. The results are presented in chapter 4 and are analysed and discussed in chapter 5. The technological implications of the study are presented in chapter 6 and a summary of the conclusions arising from the discussion is presented in chapter 7.

CHAPTER 2

LITERATURE REVIEW

There is a large volume of literature reporting various aspects of metal cutting. A comprehensive review of a number of subject areas is required in order to realise fully the complex situation created by the interaction between the tool and the workpiece when subjected to a range of cutting conditions. The literature review presented here focuses on some of the most important materials issues affecting machinability. The mechanics and mechanisms of chip formation and tool wear and surface finish are influenced by the tribological condition at the tool-chip interface. The deformation mechanism involved in high speed machining has a major influence on the chip formation and tool wear mechanisms hence the surface finish. Therefore the review begins with the knowledge in tribology and its application in defining the conditions at the tool-chip interface. This is followed with a review of the chip formation and tool wear mechanisms. The effect of material behaviour, while undergoing high strain-rate, large strain and high temperature deformation, on these aspects of machining is examined in this review.

2.1 The Tribology of Sliding Interfaces

The term tribology is used to describe the science and the technology of the interface between contacting surfaces in relative motion. The nature and the consequence of the interactions that take place at the interface control the friction and wear behaviour of the materials involved. The word friction is used to describe the gradual loss of kinetic energy in many situations where bodies or

substances move relative to one another. Friction is classified into several forms:

1. Solid friction (the friction between two solid bodies that move relative to one another)
2. Internal friction (the damping of vibrations in solids)
3. Viscous friction (the slowing down of the internal motion of liquids)
4. Skin friction (the resistance between a moving object and the surrounding air)

In metal cutting the type of friction occurring at the tool-chip interface is mainly solid friction. Solid friction can be defined as the resistance to movement of one solid body over another. In metal cutting the movement may involve sliding or seizure at the tool-chip interface. The main focus for this section is on understanding of the basic mechanisms and prediction of practical performance in the friction and wear process during metal cutting. Accordingly this section will begin with a brief survey of the basic understanding of solid friction and end with its application to metal cutting.

2.1.1 Basic Mechanism of Friction

From the literature it appears that a universal agreement at to what truly causes friction does not seem to exist. It is clear however, that friction is due to a number of mechanisms that probably act together but that may appear in different proportions under different circumstances. The microscopic mechanisms that are involved, to varying degrees, in generating friction include: (1) adhesion (2) mechanical interactions of surface asperities (3) plowing of one surface by asperities on the other (4) deformation and /or fracture of surface layers such as oxides, and (5) interference and local plastic deformation caused by third bodies, primarily agglomerated wear particles, trapped between the moving surfaces. The distinction of the most important of these factors in accounting for friction has for centuries been a subject of research efforts.

2.1.2. The Early Laws of Solid Friction and their Validity

The historic development in friction has been documented by Dawson [4]. The first comprehensive scientific investigation of friction behaviour is attributed to Amontons, who established modern phenomenological concepts of friction in the 17th century. These concepts constitute the classical laws of friction written as:

1. The frictional force that resists sliding at an interface is proportional to the normal load or the force that squeezes the surfaces together.
2. The amount of friction force does not depend on the apparent area of contact.

A third law added to these rules which is attributed to the 18th century physist Coulomb is:

3. The friction force is independent of sliding velocity once motion begins.

The conception of these laws was followed with the more basic question of what causes friction. This has received a long lasting attention and is hitherto not fully resolved. Coulomb's early studies of friction attempted to explain the frictional force in terms of surface roughness. This feature has now been ruled out as a significant source of friction [5]. The adhesion theory advanced by Bowden and Tabor [5] has dominated other theories for many decades [6-7] even though the experimental results often deviate from the theory.

For metals, the current view is that friction force is essentially the force required to shear intermetallic junctions at the regions of real contact, plus the force required to plough the surface of the softer material by the asperities of the harder material [8]. Nanometre scale studies of friction have contributed new experimental observation. Employing highly sensitive techniques such as (1) the scanning tunnelling microscope which allows imaging with atomic resolution, (2) the atom force microscope which can measure atom-atom friction, (3) the friction force microscope which can detect friction, adhesion and external loading forces as small as a piconewton and (4) the quartz balance that can weigh as light as a few nanograms, has enabled measurement of friction that exhibits no

dependence on normal load [9-10]. Based on experimental observations made in the nanometre scale the classical laws have been re-written as follows:

(1) The friction force is dependent on how easily two surfaces become stuck relative to becoming unstuck; it is proportional to the degree of irreversibility of the force that squeezes the two surfaces together, rather than the outright strength of the force.

(2) The friction force is proportional to the actual, rather than apparent, area of contact.

(3) The frictional force is directly proportional to the sliding speed of the interface at the true contact points, so long as the surfaces are not allowed to heat up and the sliding speed remains below the speed of sound.

The discrepancy between microscopic and macroscopic frictional phenomena greatly diminishes if one notes that the true area of contact between macroscopic objects is proportional to the squeezing force. So friction appears to be proportional to the normal load as Amontons stated. Experiments using Mica have ruled out the importance of surface roughness as measurable friction has been observed on an atomically smooth (cleaved) surface of mica [9-10].

2.1.3 The Adhesive Theory of Solid Friction

Clean metal surfaces if pressed together adhere very strongly. The strength of adhesion is the force to pull the surfaces apart. The adhesive theory of friction often attributed to Bowden and Tabor [5] includes the plastic deformation of surface asperities which shows that mechanical properties of the surface material are also important in influencing friction. They also found that friction, though independent of apparent macroscopic area, as Amontons had stated, is in fact proportional to the true contact area. That is microscopic irregularities of the surface touch and push into one another. The sum of these contact points constitutes the true contact area. The adhesion theory of Bowden and Tabor proposes that the surface asperities and the interface are made up of asperity contacts. The real

area of contact is much smaller than the apparent area of contact except in such applications as in metal cutting, where the real area of contact can approach the apparent area of contact. Bowden and Tabor proposed that contacting surfaces held together by a load would deform to the point of plastic flow and reach a contact pressure equal to the indentation hardness of the material. The real area of contact A_r is then determined from:

$$A_r = \frac{N}{H} \qquad (2.1)$$

where N is the normal load and H is the flow hardness of the material.

If it is assumed that friction is due to the shearing of bonds (i.e. a tangential force causes each pair of contacting asperities to weld together and shear to accommodate the relative motion imparted to the interface by the force), then to a first approximation the frictional force is given as:

$$F = A_r \tau \qquad (2.2)$$

where τ is the shear strength of the junction. Then the coefficient of friction, μ is given as:

$$\mu = \frac{F}{N} = \frac{A_r \tau}{A_r H} = \frac{\tau}{H} \qquad 2.3$$

This expression satisfies both Amonton's laws since the contact area is eliminated. Because $H \sim 3\sigma_y$, where σ_y is the flow stress and $\tau \sim 0.5$ to $0.6\sigma_y$ a value of 0.17 to 0.2 results as a universal value of the coefficient friction. However in vacuum much higher values of the coefficient of friction are found. In that case the weaker material would be subjected to wear.

The interfacial forces caused by adhesion dominate friction when surfaces are very clean.

Cold welding of the contacting asperities can take place at virtually no load. Recent work using molecular dynamics [11] and atomic force microscopy [12] has shown that when two surfaces are brought close together at a distance of a few atomic diameters, they attract each other to form interatomic bonds. Clean metal surfaces seize or cold weld to each other, when they are brought together in a vacuum. When they are separated, chunks of materials are usually transferred from one surface to the other, even for self-mated couples. When molecules that can adsorb to the surface such as oxygen or water vapour are admitted to the system, the friction drops because surface sites become covered with adsorbed atoms or even thin layers of oxide, and thus the surface area available for cold welding decreases. These observations made by Bowden and Tabor [5] are illustrated in Fig. 2.1.

Experimental observations found in the literature show a number of factors that influence adhesion. The work by Buckley [13] has demonstrated that the adhesion between two surfaces depends on the degree of matching of crystal planes. The highest adhesion and friction forces are observed for matched planes of the same material. Adhesion decreases when the materials are different and even further more when the materials are insoluble in each other, thus underscoring the importance of the chemistry of the surfaces in adhesion. Lowest values of coefficient of friction in vacuum are found in planes with highest atomic density. These planes also have the lowest surface energy. In general it appears that, as the coordination number decreases, the modulus of elasticity decreases, the surface energy increases, and the force of adhesion increases [13]. Another fundamental property affecting adhesion is the degree of d-valence bond character of transition metals. Buckley [13] has shown that the adhesion force falls very rapidly in similar metals as the amount of d-electrons increases. Fig. 2.2 illustrates this fact for various metals. As the degree of d-bond character increases, the friction coefficient decreases [13]. This has been interpreted in terms of reduced bond strength. Another important factor on which adhesion depend is the flow stress properties of the near-surface material, because this is where deformation to accommodate the sliding most often takes place. This

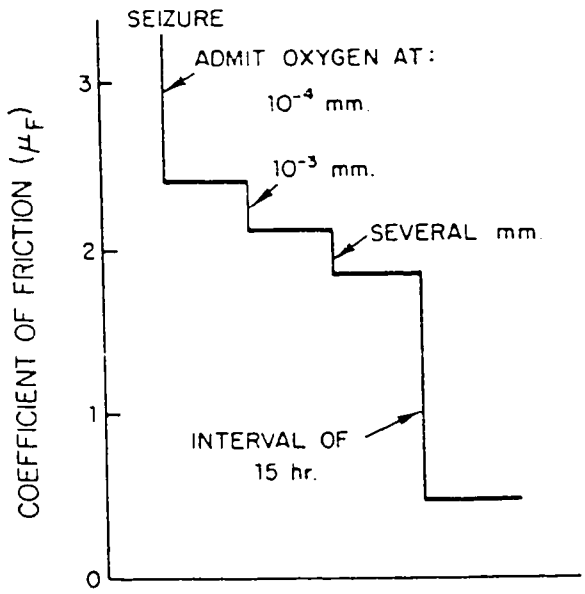

Fig. 2.1: Effect of oxygen on friction of out gassed iron. For the naked metals seizure occurs. A very small amount of oxygen reduces the friction to values of the order of μ=2 to μ=1. (After Tabor [5]).

has been confirmed by results of friction tests with changing temperature for metals and alloys that undergo phase transformations [13]. The friction coefficient has been reported to increase when due to phase changes, a phase with a high degree of strain hardening is formed [13], which underscores the importance of the flow stress behaviour in influencing adhesion. If as a result of friction, the temperature at the interface rises to the phase transformation temperature, the occurrence of phase transformation can affect the coefficient of friction. Buckley has demonstrated this fact by performing friction tests with changing temperature. Fig. 2.3 illustrates the results obtained from cobalt, which is hcp below 417°C and fcc above this temperature. As shown in Fig. 2.3, the coefficient of friction for cobalt below the transition temperature is 0.35. This is because the basal hexagonal planes develop a preferred orientation, slip takes place between them, and there is little strain hardening. In this range cobalt behaves like a solid lubricant. For the fcc structure above the transition temperature, the coefficient of friction rises rapidly, possibly because of the significant work hardening of the structure. It is plausible to conclude that low friction occurs only for those structures that deform

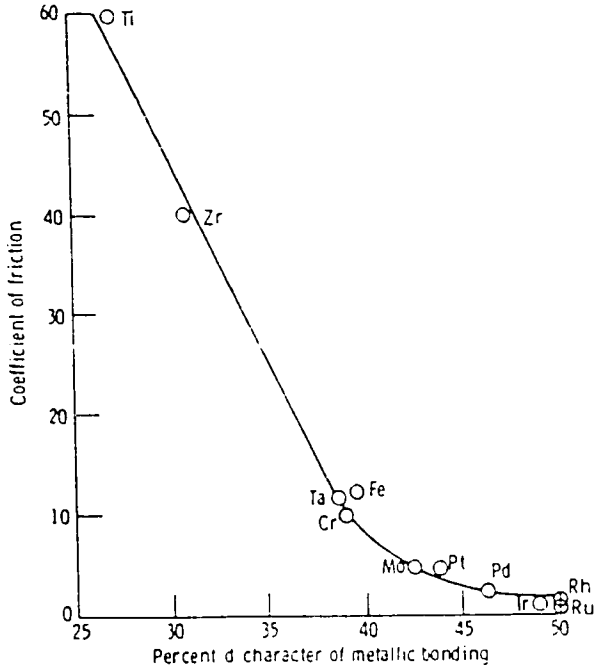

Fig. 2.2: Coefficient of friction as a function of percent of d bond character for various metals in contact with themselves in atomically clean state. Sliding velocity, 0.7 mm/min.; load, 1 gm; temperature, 23 ^{0}C; pressure, 10^{-8} N/m^{2}. (After Buckley [14]).

exclusively in the basal plane and that show low work hardening because the basal planes slide readily over one another.

Some of the events occurring at the surface to affect friction through the change in composition are segregation [14], change in crystal structure [14,15], chemisorption and physisorption [14], chemical compound formation [16] and mechanical compound formation [17]. Segregation of impurities and solutes causes a change in chemical composition at the surface. The segregation may occur as a result of the need to lower the strain energy created by the difference in atomic size. Surface enrichment by segregation has been shown [14] to increase adhesion in certain systems. Chemisorption and physisorption are caused by adsorbed species which may include water molecules from the atmospheric moisture and carbon and carbon compounds derived from the atmosphere or lubricants used during operation or manufacture. These substances substantially reduce adhesion

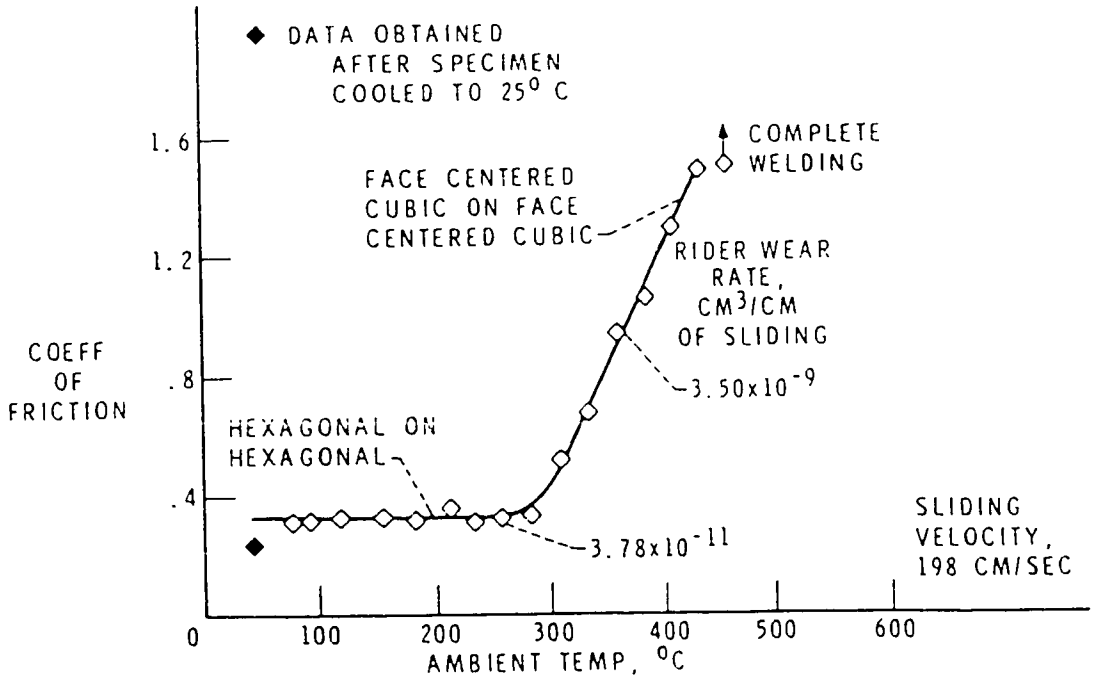

Fig. 2.3: Coefficient of friction at various ambient temperatures for cobalt sliding on cobalt in vacuum (10^{-9} to 10^{-7} torr). Sliding velocity, 97 cm/s; load 9.8 N. (After Buckley [14]).

between two surfaces thereby influencing friction. For example, when a monolayer of ethane is introduced on a clean iron surface, the adhesive force drops from 400 dynes to 280 dynes. If the monolayer is acetylene the force drops to 80 dynes. For a vinyl chloride monolayer, the force drops to 30 dynes [14]. Chemisorption also aids chemical compound formation. When two surfaces rub against each other, they may adhere at local spots that can reach elevated temperatures by frictional heating; interdiffusion may then take place, resulting in local compound formation in the surface layers. The friction between two metals that can form alloy solutions or alloy compounds with each other is greater than if the two are mutually insoluble [16]. Mechanical compound formation is caused by the mechanical alloying of metallic wear particles and surface debris to form solid layers known as transfer layers [17], that may keep the surfaces from coming into direct contact with each other. The dislocation and electronic configurations at the surface have also been reported to influence friction. These have been reviewed in detail by Rigney [17].

2.1.4 Asperity Deformation Theory of Friction

The close dependence of friction on the surface topography and on the properties of the surface and the near-surface layers has been reviewed by Suh [6]. The micro roughness is of primary concern in friction. This may extend down to the near-atomic scale and may be caused by internal imperfections in the material, non-uniform deformation of individual grains at the surface, or corrosion and oxidation processes on exposure to the environment. The peaks of surface roughness are called asperities. The distribution of the asperities play a major role in determining the interfacial conditions of a tribological system. If it is assumed that the asperity deformation is the only phenomenon that takes place under a given load, the coefficient of friction due to asperity deformation varies from 0.39 to 1 as the slope of asperities increases from 0 to 45^0 [6]. Greenwood and Williamson [18] used the height of asperities to derive an expression for the elastic contact stress which is commonly used to analyse contact mechanics of rough surfaces. The authors modelled the condition at which changeover from elastic to plastic contact takes place. They used a multi asperity model and assumed that the asperities had a Gaussian distribution and the same tip radius. It was assumed that the elastic deformation and stress could be calculated from equations based on Hertzian contact between spheres. The onset of plastic flow was taken to be the point where the maximum Hertzian pressures reaches about 0.6H, where H is the indentation hardness (in Nm^{-2}). A plasticity index ψ, which combines the mechanical properties (E_{12} and H) and topographical properties (σ and ξ) of the solids in contact, was introduced and expressed as:

$$\psi = \frac{E_{12}}{H}\sqrt{\frac{\sigma}{\xi}} \qquad (2.4a)$$

where H is the indentation hardness (in Nm^{-2}), σ is the standard deviation of the asperity height distribution, ξ is the radius of the asperity tips, and E_{12} is the effective elastic modulus from Hertzian

expressions given by:

$$E_{12} = \left(\frac{1-\nu_1^2}{E_1} + \frac{1-\nu_2^2}{E_2}\right)^{-1} \qquad (2.4b)$$

where E_1 and E_2 are the elastic moduli and ν_1 and ν_2 are the Poisson ratios of the two materials. When one material is considerably harder than the other:

$$E_{12} = \frac{E}{1-\nu^2} \qquad (2.4c)$$

which is called the "plane stress modulus". When the two materials are identical, E_{12} is half of this. Greenwood and Williamson [18] found that while ψ may vary from 0.1 to 100 for real surfaces, in practice it falls in a narrow range. Typically, if $\psi>1$, there is significant plastic flow; if $0.6<\psi<1$, there is some elastic and some plastic deformation; and if $\psi<0.6$, plastic flow is unlikely.

Since the load does not enter into the expression, it is clear that surface properties and surface topography, according to this model, play much greater roles in determining whether plastic deformation takes place. If surface topography is such that plastic flow occurs initially, surface interactions in repeated passes may sooth the surface during run-in, until the standard deviation of the asperity height distribution (σ) decreases and /or the radius of curvature of the asperities (ξ) increases such that the plasticity index falls into the elastic range of contact. In the Greenwood-Williamson model the real area of contact is almost proportional to the load, even when the contact is entirely elastic, thus satisfying Amontons' laws by elastic as well as plastic contact conditions. It is probable, however, that the nature of the asperity height and shape distribution will change significantly once the surfaces begin to move against each other. In this case the general validity of this model is not well established.

According to Bowden and Tabor [5], when asperities contact they undergo elastic and plastic deformation to accommodate the stresses. The authors divided the friction force into two components; a ploughing term and an adhesion term. The ploughing term is due to energy dissipated in plastic deformation when the asperities interact with one another. In normal engineering surfaces the presence of films of oxides, adsorbates, chemical and physical reaction products inhibit significant adhesion from occurring. But if sliding occurs then junction growth occurs by plastic deformation of asperities causing adhesion [5]. Adhesion is thought to be a component of plastic deformation of asperities, a component that strongly influences the amount and nature of deformation at the interface [19]. Several other theories have been proposed to account for friction [20-21]. For example deformation energy [20] and third body effects [21] have been proposed to account for friction but adhesion and deformation in ploughing are still components of the entire process mainly because of their roles in energy dissipation and in the formation of wear particles.

Summary

The basic mechanisms of friction are adhesion and mechanical deformation. Their relative roles are still the subject of much discussion. Friction energy appears to be lost primarily as energy dissipated through deformation of the surface layers by elastic, plastic, and visco-elastic deformation and/or by micro fracture of the surface material and possibly some shear fracture of adhesive interface bonds. Adhesion is a primary cause of friction in high-vacuum environments and in instances of seizure. In most cases, however, surface films and contamination limit adhesion to a few small spots (asperities), where it can strongly influence the amount and nature of the local friction-generated deformation. The link between friction and material properties is the key information needed to elucidate these basic mechanisms. For example, in most cases, friction depends on the flow stress of the subsurface material, because that is usually where deformation takes place to accommodate the sliding.

2.1.5 Friction in Metal Cutting

Traditionally, it has been assumed that coulombic friction controls the interface forces at low loads and that as the load grows to the point where the real area of contact is equal to the apparent area of contact, friction becomes independent of pressure and takes on the value of k, which is the shear flow stress of the weaker material [5]. In metal cutting k is not a simple value. It is modified by the hydrostatic pressure, high strain rates, large strains and high temperatures at high cutting speeds so that the final value is lower than the k determined from uniaxial tension tests [22]. A recent analysis of friction in metal working processes based on slip line field studies has been presented by Kopalinsky et al [23]. The frictional processes in metal cutting are complex because of the existence of very high normal loads. Friction under high normal loads has been discussed in detail by Thomsen [24]. An increase in the normal load across the contacting surfaces produces an increase in the real area of contact. Relative motion between the surfaces produces shearing of welded asperities and some subsurface plastic flow. The frictional force F is given by the equation $F = A_r S$, where s is the shear strength of the asperities of the softer material, but is not linearly related to the normal force N. These conditions are shown in Fig. 2.4 (Region II) where it is shown that at very high normal loads the real area of contact approaches the apparent area of contact A_a. With this condition A_r has reached its maximum value ($A_r/A_a = 1$); conditions of sticking friction are said to exist. Relative motion between the surfaces produces gross subsurface flow and the coefficient of friction reaches its limiting value of 0.577 if it is assumed that the Von Mises flow rule applies. Then the frictional force F is independent of the normal force N and the coefficient of friction decreases with a further increase in normal load. Friction in metal cutting occurs at the flank and the rake faces of the tool. There is ample evidence in the literature supporting the existence of sticking friction at the flank face of the tool [25-27]. Hitomi and Thuereng [26] also showed that adhesion at the flank face could be prevented by the application of a lubricant and an increase in tool clearance angle.

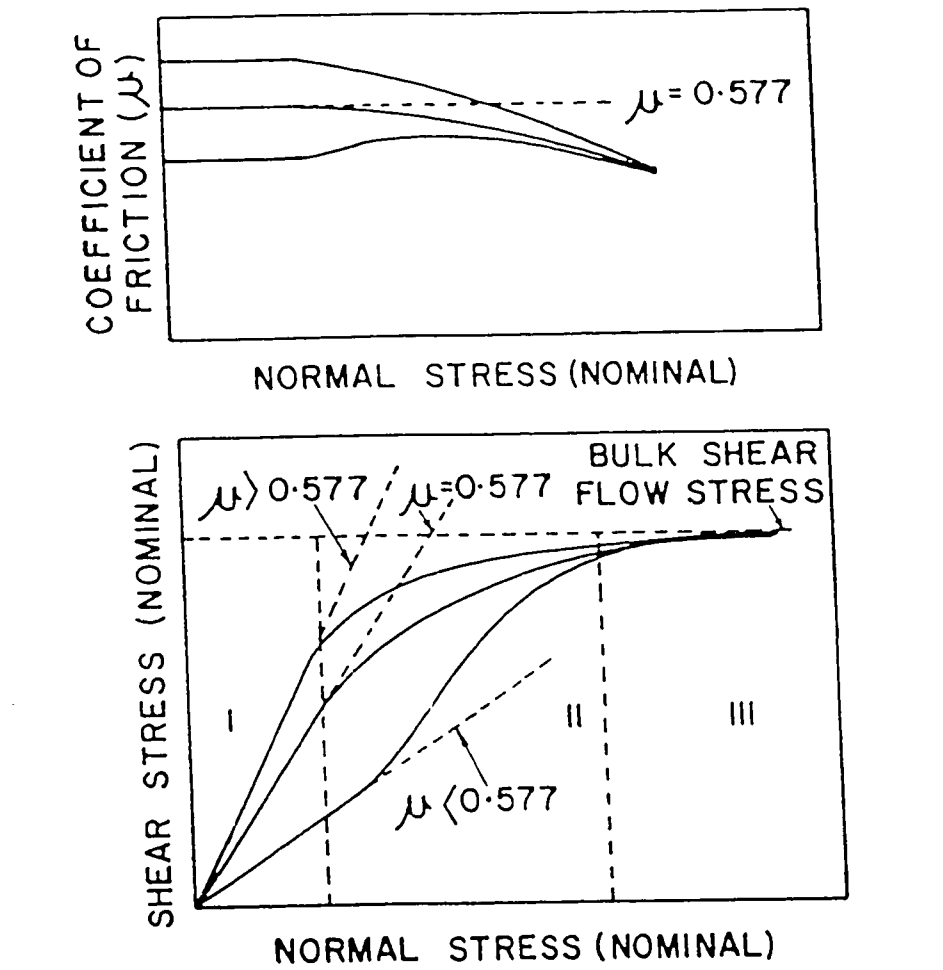

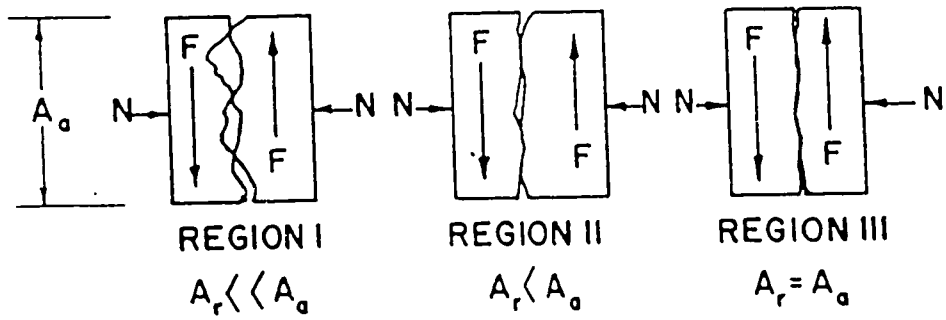

Fig. 2.4: A schematic representation of dry friction for pressures in the metal cutting range showing that for light pressures the coefficient of friction is independent of pressure and Amontons' law applies. As the pressure increases in clean surfaces sub-surface flow takes place when $F=A\tau$ and $\mu=0.577$ and F remains constant at large pressures unless τ is altered by phenomena such as work hardening. μ decreases with increase of pressure if τ remains constant. (After Thomsen [24]).

2.1.5.1 The Mechanics of Friction at the Tool-chip Interface

The severely work hardened chip which is formed by a shear process in the primary shear zone flows up the tool rake face under the action of large normal and shear stresses [25]. Assumption that the frictional condition in this region controls the geometry of the metal cutting process has led to the representation of the frictional behaviour by a single parameter β_f the mean angle of friction on the tool face. β_f is related to the mean normal and frictional forces by the expression tan β_f = F/N or tan β_f = μ where μ is the coefficient of friction on the tool rake face. A large proportion of previous theoretical work concerning the mechanics of metal cutting has dealt with the effect of the mean angle of friction β_f and the tool rake angle α on the shear angle ϕ. Many of the theoretical analyses predict a relationship between the angle parameter of the form:

$$\phi = A - B(\beta_f - \alpha) \qquad (2.5)$$

where A and B are positive constants. However, the above relationship can not be universal for all materials since experimental tests have found that the constants A and B are dependent on the material machined [28].

2.1.5.2 The Stress Distribution Effects on Frictional Conditions at the Tool-chip Interface

Zorev [29] reported that the real and apparent areas of contact between the tool and the chip were equal from an examination of the underside of the chip samples. Qualitative evidence to support the existence of sticking conditions at the tool-chip interface when machining with various carbide and steel cutting tools has been presented by Shaw [30], Trent [31] and Nakajama et al [32], using optical and electron microscopy. Wallace and Boothroyd [33] have shown that conditions of sticking friction, where the friction stress is constant and sliding friction, where the coefficient of friction is constant, exist simultaneously. These authors found that the average frictional stress approached its

maximum value asymptotically at the average normal stress increased. Constant frictional stress under sticking conditions is supported by the work of Takayama and Usui [34] and Chao and Trigger [35]. The work of Kato et al [36] showed the existence of both sliding and sticking conditions at the tool-chip interface and emphasized the importance of work hardening of the chip material in determining the length of the sticking region. The stress distribution and the corresponding frictional conditions at the tool-chip interface are illustrated in Fig. 2.5 [37].

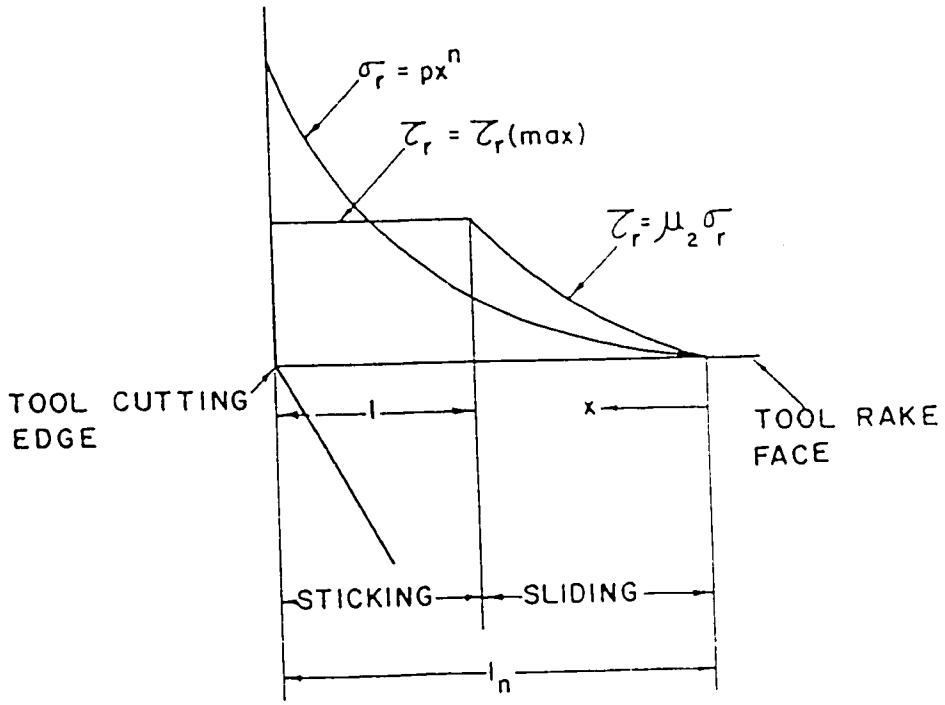

Fig. 2.5: Zorev's idealised model for tool rake stress distribution [37].

As shown in Fig. 2.5 the frictional stress is constant and equal to the flow stress of the chip material in the sticking region. The stress distribution is determined by both the strength of the chip material at the tool-chip interface and by the distribution over the tool-chip interface of the ratio of the real area to apparent area of contact between the chip and the tool [38]. At the area where sticking friction operates the shear stress is equal to the shear flow stress of the chip material under the

appropriate interfacial conditions. The mean normal stress can vary independently of the shear stress [28]. Under conditions of sticking friction deformation occurs in the sublayers of the chip and a stagnant or secondary shear zone is formed [39]. The velocity is zero at the tool-chip interface and equal to the chip velocity at the outmost boundary of the zone. This velocity gradient is accompanied by a gradient in shear strain. The shear strain rate should remain fairly constant unless there is severe shear localisation. The secondary shear zone can only form under high velocities which generate high interface temperatures. Under these conditions thermal softening dominates over strain hardening. At low cutting speeds where strain hardening dominates over thermal softening a built-up edge is formed [40]. In the low speed regime where the mean coefficient of friction increases with cutting speed, the flow stress increases at a higher rate than the normal stress due to dominating effects of strain hardening. In the high speed regime where thermal softening dominates over strain hardening the coefficient of friction decreases with increasing cutting speed because the flow stress decreases at a higher rate than the normal compressive stress.

2.1.5.3 The Effect of Cutting Conditions on Tool Rake Friction

The most extensive and self-consistent work on the influence of cutting conditions on tool-chip interface friction appears to be that of Zorev [41]. Under dry machining the mean coefficient of friction increases with increase in cutting speed. For certain ferrous materials, the mean coefficient of friction is shown to reach a maximum and then decrease continuously with further increase in cutting speed. For certain non-ferrous materials the mean coefficient of friction continues to increase but tends to become constant at high cutting speeds. Typical results produced by Zorev are shown in Fig. 2.6(a) and (b). Zorev [41] attributed the observations to the generation of surface contaminant oxide films which lower adhesion at the interface when machining at extremely low cutting speeds and to the existence of conditions of seizure at high cutting speeds. The increased coefficient of

friction produces a decrease in the shear angle and increase in cutting forces. An increase in tool rake angle produces an increase in the mean coefficient of friction [41-42]. An increase in the tool rake angle produces little change in the conditions of strain, strain rate and temperature at the tool-chip interface and hence little change in the shear flow stress of the chip material. However, by comparison an increase in the tool rake angle causes a large decrease in the normal stress. The coefficient of friction is low at low feeds due to the formation of a built-up edge which in turn increase the effective rake angle.

2.1.5.4 The Effect of Lubrication on Tool Rake Friction

Lubrication is achieved either through application of an external fluid or through the presence of inclusions of a lubricating nature in the workpiece. These inclusions are known as free cutting additives. The most common method of application is by flooding the cutting point with a lubricant fluid. A general view is that lubricating action occurs at the tool-chip interface through the formation of a film which tends to restrict metal to metal contact. However some confusion still exists concerning the true lubricating action of the cutting fluids. While Trent [31] has provided metallographic evidence to show that the lubricant can not penetrate the whole of the contact area, Williams et al [43] claim that cutting lubricants reduce frictional forces through reduction of the tool-chip contact length. Childs [44] has shown that while sticking friction conditions may prevail very close to the cutting edge of the tool in well lubricated cutting, the elastically stressed portion of the contact area which exists during unlubricated cutting is eliminated by lubrication. There is ample evidence to show that at high cutting speeds where conditions of seizure prevail at the tool-chip interface externally applied lubricants become ineffective as the atomic contact at the interface is inaccessible to external lubricants [39]. Therefore, the most viable method is in-situ lubrication of the interface from either the workpiece or the tool. One method of achieving in-situ lubrication of the

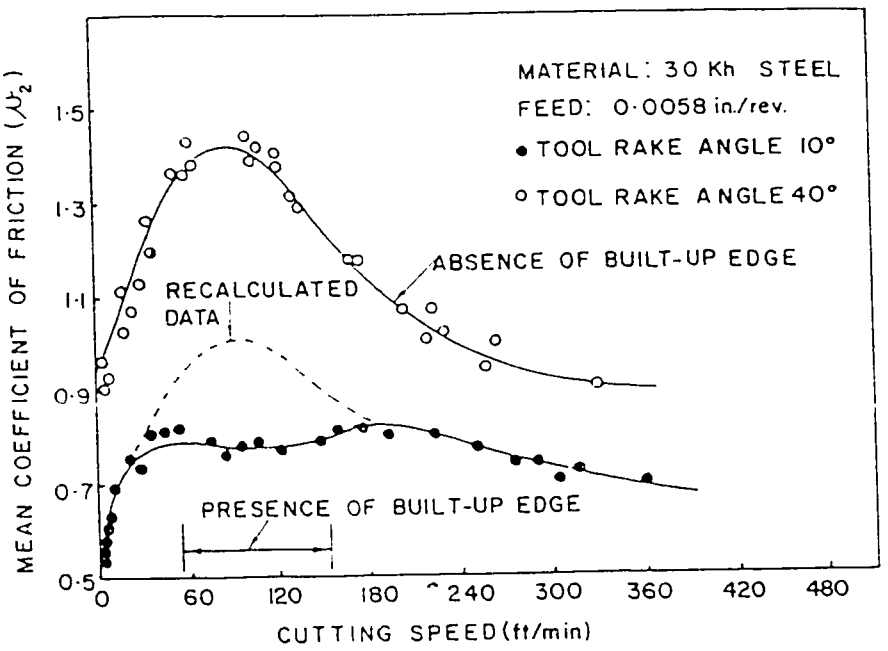

Fig. 2.6(a): Effect of cutting speed on mean coefficient of friction μ_2 on tool rake face. (After Zorev [41]).

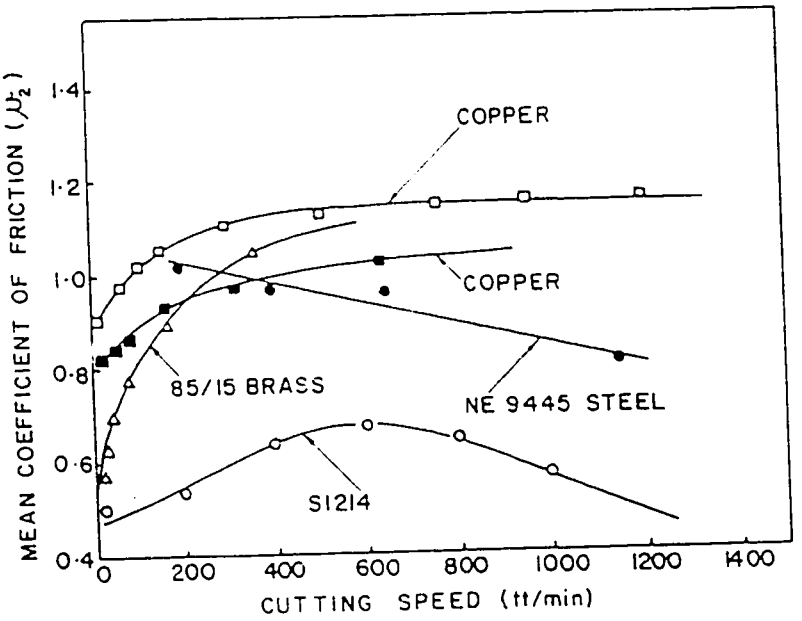

Fig. 2.6(b): Effect of cutting speed on mean coefficient of friction μ_2 on tool rake face. □ t_1 = 0.0381 in., α=20° tool- HSS. Δ t_1=0.020 in.,α =15°, tool-HSS. ■ t_1=0.020in., α=30°, tool-HSS. ● t_1=0.0037 in., α=10°, tool-carbide,○ t_1=0.0192 in., α=20°, tool-carbide. (After Bailey [28]).

tool-chip interface is by inclusion engineering of the workpiece with glassy phase inclusions which remain viscous under the prevailing strain, strain rate, pressure and temperature at the tool-chip interface. In order to succeed in inclusion engineering a precise definition of the tool-chip interfacial conditions as a function of cutting conditions and flow properties of the workpiece is required and is treated in the next section which deals with the definition of seizure in metal cutting.

2.1.6 The Definition of Seizure in Metal Cutting

At low cutting speeds the tribological phenomenon of sliding operates at the tool-chip interface [45]. As the cutting speed is increased, there is a transition from the tribological condition of sliding to that of seizure at the tool-chip interface [46]. Seizure has been defined as solid phase weld between the primary atomic bonds of absolutely clean metallic surfaces [5,47]. The essential feature of seizure is that atomic contact is established at the tool-chip interface and that relative motion occurs within the softer (chip) material. The layer of chip in contact with the tool is stationary and relative motion takes place in adjacent layers with the shear velocity gradually increasing until the bulk chip speed is obtained. These views were expressed by Trent [48], Wright & Trent [49] and Wright, Horne and Tabor [50], but quantitative evidence was not provided to support these views. The chip material of the seized region in the secondary shear zone is sheared under the action of compressive and shear forces acting on the surface of the rake face of the tool. Bowden and Tabor [5] used an equation first developed by Nadai [51] to relate the normal and shear stresses to the material flow stress in a seizure situation.

$$P^2 + 3s^2 = P_o^2 \qquad (2.6)$$

where P is the applied normal pressure, s is the tangential shearing stress (shear strength of the junction) and P_o is the yield pressure of the metal. Thus this model proposes that both compressive

pressure and shear strength of the junction determine the condition of flow in the slice of material adjacent to the welded interface as follows:

If P is initially equal to P_o at an area of contact A_o the material in the slice adjacent to the interface is already plastic and the smallest tangential stress s will be sufficient to cause further plastic flow. The smallest tangential stress produces a small but finite displacement as a result of which the area of contact increases to A. The normal pressure thus falls to a value less than P_o and is insufficient, in itself, to produce plastic flow. The tangential stress must now be increased to a finite value s such that the combined effect of P and s is again capable of producing plastic flow in the slice of material near the interface. According to the model, if the two surfaces are clean, there is a steady growth of the area of contact as s is increased, whilst plastic displacement on a minute scale occurs at the region of contact until the area of true contact approaches the geometric area and gross seizure occurs.

The recent progress in nanotribology has shown that the friction force is proportional to the actual rather than the apparent area of contact [9-10]. In this respect, it is important for the normal force to exceed the yield strength of the material in order that the asperities are deformed or squeezed to make the atomic contact. In this context, the concept of junction growth at the tool-chip interface invoked by Bowden and Tabor [5] is a useful approach to link the mechanics of metal cutting with material behaviour. In nanotribology the frictional force is directly proportional to the sliding velocity of the interface at the true contact points so long as the surfaces are not allowed to heat up and sliding speed is well below the speed of sound. In metal cutting, once seizure occurs the model originally proposed by Trent [52] applies wherein thermoplastic shear localised at the tool-chip interface raises the local temperature when thermally activated processes set in, causing inter-diffusion of solutes at the tool-chip interface. Thus it should be possible, using tungsten carbide tools, to correlate the onset of seizure predicted from force measurements with the onset of diffusional transport of tungsten from the tool into the chip. Experimental validation of the onset of seizure has been carried out using an

AISI 1045 grade steel by determining the lowest cutting speed at which measurable tungsten concentration penetration into the chip occurs as measured by the Secondary Ion Mass Spectrometric Analysis (SIMS). This is compared with the critical cutting speed for seizure at which the normal stress calculated from measured forces starts to exceed the yield strength of the workpiece material at the operating tool-chip interface temperature. The results are presented in section 4.1 and discussed in section 5.2.

2.2 The Mechanics and Mechanism of Chip Formation

The analysis of chip formation mechanism and micromechanisms of tool wear during high speed machining of a material requires understanding of the effect of several variables involved. The main variables can be grouped as: (1) Operating or metal cutting variables which include the rake angle, feed, depth of cut and cutting speed, (2) Initial material properties or characteristics which include flow properties, thermo-physical properties, and microstructure, and (3) System response parameters or phenomena which include the tool-chip interfacial conditions, shear plane angle, contact length, tool wear, microstructural evolution in the workpiece (i.e., tempering, dynamic recrystallisation or phase transformation) and the flow stress variation with strain, strain rate and temperature. The experimental observations found in the literature concerning the influence of metal cutting variables are as follows:

When the feed is increased the cutting forces, contact length, and the friction coefficient increase whereas normal stress decreases [53,54]. The effect of decreasing the normal stress is to reduce the flow stress [55] and the strain to fracture whereas the shear plane angle is increased [53]. The primary shear zone temperature decreases whereas the secondary shear zone temperature increases [56]. The overall result is to increase tool dissolution wear under condition of flow chip morphology and to promote the formation of discontinuous chips. Cook et al [55] have shown that reducing the

rake angle has the effect of increasing the normal stress which in turn increases the flow stress of the material. The cutting forces are increased. The same has recently been confirmed experimentally [56]. The strain is increased whereas the shear plane angle is reduced. The temperature at the tool-chip interface decreases while the temperature at the primary shear zone increases [56]. Reducing the rake angle contributes to the formation of discontinuous chips at low cutting speeds [55] and shear-localised chips at high cutting speeds [57-58]. The friction coefficient increases with increase of rake angle [28]. Increasing the cutting speed has the effect of increasing the shear plane angle, and reducing the contact length and cutting forces. The strain rate, temperature rise, tool wear and tendency to form transformed shear bands increase with cutting speed. The mean coefficient of friction at the rake face increases with increase in speed in the range of 0 to 200 m/min in most materials. Above this speed range the variation of the coefficient of friction with speed cannot be generalised. However, it depends on the mean normal and frictional stresses at the tool-chip interface.

The flow stress characteristics, the mechanism of chip formation and the micro mechanisms of tool wear at low and high cutting speeds are the subject of the present investigation and are reviewed separately in the sections that follow. The mechanics of chip formation are reviewed first.

2.2.1 The Mechanics of Chip Formation

After Ernst's [59] classical description of chip formation, Merchant [60] pioneered the mechanistic approaches to analysis of chip formation and developed expressions for cutting forces, cutting stresses and shear plane angle from his famous force circle, Fig. 2.7. The approach assumed continuous chip formation without a built-up edge with shear occurring in a very narrow zone which in the idealised limit becomes a plane. This model neglects thermo-mechanical effects on the flow stress of the workpiece material. Sliding or a coulomb friction law is assumed with a constant friction coefficient. Chip formation is considered to occur under shearing along a plane surface originating at

the tool tip and inclined with an angle ϕ with respect to the workpiece. The angle ϕ is known as the shear angle and attempts to determine it have been made by minimising the work produced by the cutting force. Alternative expressions for the shear plane angle were obtained by Lee and Shaffer [61] using the same shear plane model. Rowe and Spick [62] evaluated the shear plane angle by minimising the energy expended in metal cutting i.e. the energy at the shear plane plus the energy on the rake face, neglecting strain hardening of the workpiece. Later Hastings, Mathews and Oxley [63] proposed a shear zone model illustrated in Fig. 2.8 to replace the shear plane model. Seizure was assumed to occur at the tool-chip interface. A thermo-mechanical model was developed by Oxley [64] by accounting for effects of temperature, strain rate sensitivity and strain hardening on the workpiece material flow stress. These analyses show that the shear angle is not externally constrained, making determination of the shear plane angle a free boundary problem. These analyses are valid only for conditions where continuous chips are formed with sliding at the rake face of the tool. Finite element methods have been employed to attempt global analysis of the cutting process [65-68]. The analysis of the influence of some parameters using this method is more difficult than in simple specific analytical models. There appears to be no quantitative model at present that can predict the cutting forces, flow stress, strain and temperature fields, tool wear, surface state and stability condition from thermo-mechanical properties of workpiece and tool, the cutting conditions and friction law at the tool-chip interface. In addition the mechanistic approaches do not address the mechanism of chip formation. To model the cutting process an understanding of the thermo-mechanical behaviour of the workpiece is necessary. Strain rates in the order of 10^5 can be reached. Strains in the order of 3 and temperatures in the order of 400 - 500^{0}C can be reached at the primary shear zone. At the secondary shear zone further straining under high hydrostatic pressures can lead to strains and temperatures in the order of 100 and 1000^{0}C respectively. The shear flow stress depends on all these factors including deformation history and the damage rate.

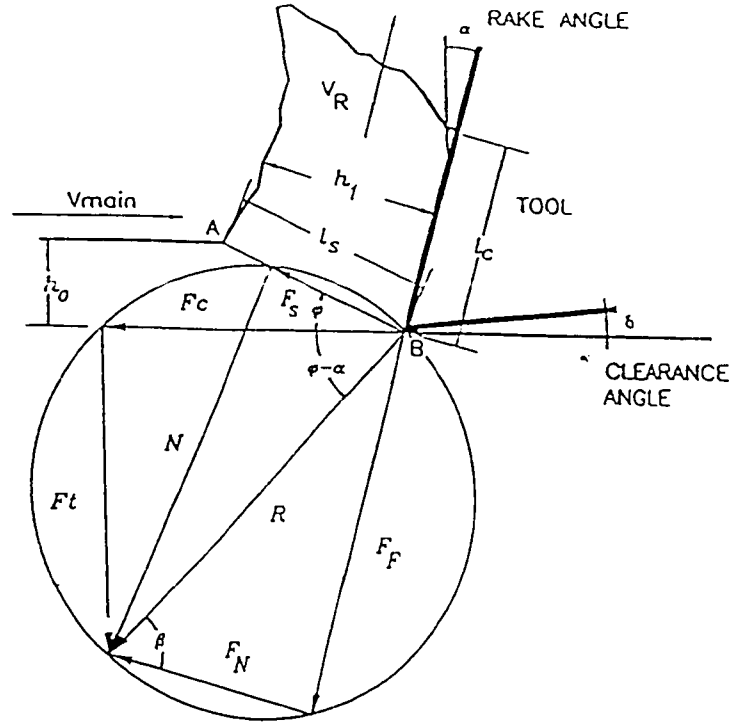

Fig. 2.7: The Merchant force circle [60].

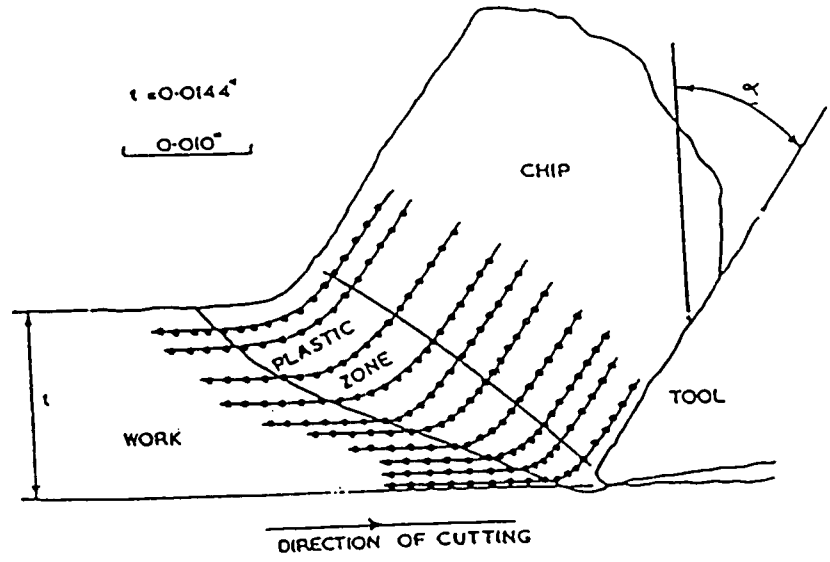

Fig. 2.8: The Matthews, Hastings and Oxley shear zone model in orthogonal cutting [63].

The pressure and sliding velocity at the tool-chip interface are high ~20 kbar and more than 2 m/s respectively at medium cutting speeds (100- 300 m/min) in steels. The high pressure and sliding velocity affect the friction conditions at the tool-chip interface. This is treated further in the experimental results and discussion sections devoted to the definition of seizure in metal cutting (section 5.2).

2.2.2 Mechanism of Chip Formation

The general mechanism of deformation in orthogonal cutting involves shearing at the primary shear zone where the chip is formed and the formation a secondary shear zone where the chip undergoes further shearing as it slides along the tool face accompanied by friction effects. The classical description of chip formation for most materials as cutting speed is increased within the conventional speed range (1 - 100 m/min) starts initially with a discontinuous chip (Type I) a continuous chip with a built-up edge (Type III) and finally a continuous chip (Type II) [59]. With further increase in speed, the chip formation process is affected by instabilities in the cutting process both at the primary and in the secondary shear zones, yielding chip segmentation. The sources of such instabilities have been a subject of great controversy and research [57-58,69-72].

At very low cutting speeds (<1 m/min) the mechanism of formation of discontinuous chips has been reported by Cook et al [55]. When the cutting speed is increased beyond the conventional speed range instabilities in shear occur, resulting in the formation of partially segmented chips. According to Komanduri and Brown [70], segmented chips form due to instabilities of the workpiece both in the primary and secondary shear zones, and the dynamic response of the machine tool structure contributes to their formation. Instability in the primary shear zone has been attributed to the negative

stress-strain characteristics of certain materials at large strains, involving void formation around second phase particles, their propagation into micro-cracks and coalescence of these cracks leading to partial fracture (i.e. geometrical instability). The instability at the secondary shear zone is due to stick-slip friction of the chip segment on the tool-face.

Sullivan, Wright and Smith [71] attributed the formation of segmented chips to seizure and strain rate hardening of the material at the rake face. In the first part of the contact length near the tool tip, the material strength increases due to work hardening so that the primary shear zone becomes the weaker region in which shear takes place. Due to temperature softening near the end of the secondary shear zone, the material at this region has a lower strength allowing flow to take place thus establishing stick-slip friction at the secondary shear zone with an attendant variation of the shear plane angle. The process is repeated with formation of a new segment. The analysis provided by Sullivan et al therefore introduced the flow stress and the material's strain rate sensitivity as key factors on which chip segmentation depends, while discounting the primary shear zone as the source of large scale heterogeneity. Shaw [72] has proposed that chip segmentation in 60/40 brass and hardened steel is caused by periodic gross fracture extending from the free surface of the chip toward the tool tip. There is insufficient quantitative experimental evidence in the literature to validate the mechanisms so far proposed.

Further increase in speed beyond the critical speed for adiabatic shear culminates in the formation of shear-localised chips due to catastrophic shear at the primary shear zone [57,69,72-74]. Lemaire and Backofen [58] investigated possible adiabatic instability in orthogonal machining of tempered martensitic steel (Fe-18.5Ni-0.52C) by observing the reverse transformation of martensite into austenite in the primary shear zone. The discontinuous chips formed exhibit white-etching bands between the segments, hence they are of the type described by Komanduri and Turkovich [57] to be shear-localised chips. The authors proposed the formation of this type of chips to involve localised

deformation confined to a narrow zone extending from the tip of the tool to the free surface of the test strip. They used Loewan and Shaw's [75] thermal model for continuous chip formation to calculate the shear zone temperature, taking average values of shear strain calculated from the chip thickness measurements. The temperatures obtained were below 200^{0}C which are far below the transformation temperature of the material (426^{0}C) and therefore insufficient to bring about the observed reversion of martensite to austenite. They suggested periodic release of the system stored elastic energy into the chip once the system becomes mechanically unstable as a potential energy source which raises the temperature in the adiabatic shear band beyond the transformation temperature of the material. This model based on experimental results at low cutting speeds where the frequency of chip segmentation is low and at or near the natural frequency of the system is a plausible explanation. However, the validity of the model under high cutting speeds where the frequency of oscillation is very high and far beyond the natural frequency of the system is doubtful. Due to inherent damping, the effect of overall machine tool response at that high frequencies of chip segmentation when machining at high cutting speeds should be minimal. The authors proposed three conditions upon which reversion of martensite to austenite depend: (1) deformation must be confined to a shear zone (2) temperatures in the shear zone must reach the level at which the criterion for adiabatic instability is met (3) rapid shearing during instability must raise the temperature further beyond the transformation temperature. The influence of pressure on phase transformation and the influence of phase transformation on adiabatic shear localisation was not addressed. It is not clear from Lemaire and Bakofen's results whether phase transformation causes adiabatic shear localisation or is incidental.

The shear-localised chip has been observed with difficult-to-machine materials such as AISI 4340 steel [69], Ti-6Al-4V [57] and Inconel 718 [74]. The formation of shear-localised chips may be caused by either (a) concentration of thermal energy in narrow bands because of poor thermo-physical properties of the workpiece material, or (b) concentration of thermal energy in narrow shear bands due

to insufficient time for dissipation of heat from these bands at the high strain rates encountered at high cutting speeds [70]. Two different mechanisms have been proposed to describe the formation of fully segmented chips at high cutting speeds. The first mechanism by Komanduri and Turkovich [57] proposes that the formation of fully segmented chips, which they referred to as shear-localised chips, begins with plastic instability, leading to strain localisation along a shear surface originating from the tool tip almost parallel to the cutting velocity vector and gradually curving until it meets the free surface. The formation of the chip is completed by gradual upsetting of the inclined wedge of the material ahead of the advancing tool. There is almost no relative motion between the bottom surface of the chip segment being formed and the tool face almost until the end of the flattening stage. Therefore rapid transfer of heat occurs at the tool tip. There is periodic development of concentrated shear band of very large strain accompanied by rapid shear i.e. adiabatic conditions prevail at the primary shear zone. An interesting feature of this model is that it proposes little or no secondary deformation along the rake face. Instead it proposes that the chip rolls over the tool face during the flattening stage. This implies that the formation of fully segmented chips does not involve seizure. If this is true then dissolution wear should be minimised at the tool-chip interface. The second mechanism by Shaw [72] proposed that adiabatic shear is not the root cause of chip segmentation at high cutting speeds. Instead Shaw proposed that chip segmentation at high cutting speeds occurs by periodic gross fracture extending from the free surface of the chip toward the tool tip. Thus the mechanism of formation of fully segmented chips at high cutting speeds and the influence of interfacial conditions on the mechanism does not appear to be resolved. The present work combines tool wear measurements and microstructural characterization of the chips to formulate the mechanisms of formation of segmented and shear-localised chips, and the resulting effect on tool wear mechanisms.

2.2.3 Flow Stress Characteristics in Metal Cutting

It has been shown in the previous section that the formation of partially segmented chips is caused by the varying frictional conditions at the tool-chip interface. In addition to the varying frictional conditions at the tool-chip interface major material related instabilities occurring at high cutting speeds are: (1) the response of the flow stress of the workpiece material to imposed cutting conditions (feed, speed, rake angle) i.e., its dependence on strain, strain rate, temperature and pressure, (2) the metallurgical and thermo-plastic characteristics of the workpiece material, and (3) the microstructural evolution accompanying thermoplastic shear localisation in the workpiece material under high strain, strain rate, temperature and pressure conditions (i.e., tempering, phase transformation and recrystallisation).

In metal cutting and other processes where plastic deformation of the metal occurs at high strain rates, the flow stress is a function of strain, strain rate and temperature. Any attempt to determine the stress strain curve must also deal with the dependence of the curve on strain rate and testing temperature. Zener and Hollomon [1] have developed an indirect method of determining the stress-strain relationship at very high strain rates by isolating the combined effect of high strain rates and temperatures. The principle of the method is based on a quantitative equivalence in the effects of changes of strain rate to changes in temperature. The authors have demonstrated that the effects of a large increase in strain rate upon the isothermal stress-strain relation may be obtained experimentally merely by lowering the temperature. Then the adiabatic stress-strain relation may be obtained by computation. The authors have shown that at room temperature and below, the isothermal stress-strain relation $\sigma(\epsilon)$ in steels depends upon strain rate and upon temperature T only through a single parameter P, i.e.

$$\sigma = \sigma(P,\epsilon) \tag{2.7}$$

On assuming that at room temperature and below only one type of rate, such as a rate of relaxation

affects the isothermal stress-strain curve and that this rate has a heat of activation, Zener and Hollomon expressed the parameter P as.

$$P = \dot{\varepsilon} e^{Q/RT} \tag{2.8}$$

Where Q is heat of activation $\dot{\epsilon}$ is strain rate, R is gas constant, and T is the temperature

The theory behind equations (2.7) and (2.8) is that if strain rate and temperature affect the stress-strain relation only through the parameter P, then when all stresses at a given strain rate are plotted against P, they should lie on a common curve. Zener and Hollomon confirmed this theory by using data for tensile strength and stress at a strain of 0.01, obtained at temperatures between 20°C and -190°C, for both cast steel and forged steel to illustrate the equivalence between the effect of strain rate and temperature. In each case, the data were found to lie upon a common curve. A plot of log σ against log P was found to give a linear relationship, i.e. $\sigma = P^r$ with r=0.0125 for a tempered pearlitic steel and 0.02 for mild steel. For the strain rates used (10^{-4} - 10^{4}) the authors expressed the stress as:

$$\sigma = e^{\psi RT} \tag{2.9}$$

Where q = rQ

The value of q for steels with carbon contents greater than 0.08% was found to be in the range of 90 to 120 cal/gm mole. The activation energy for shearing was also found to range between 70 and 130 cal/gm mole, for plastic strains between 0.01 and 0.6.

MacGregor and Fisher [76] have proposed a similar method which employs directly a velocity modified temperature in representing by means of a single variable the combined effect of strain rate and temperature on the stress strain relation. The velocity modified temperature T_{vm} is given as:

$$T_{vm} = T(1 - K \log(\dot{\epsilon}/\dot{\epsilon}_o)) \tag{2.10}$$

Where T is the test temperature K and $\dot{\epsilon}_o$ are constants, and $\dot{\epsilon}$ is the test strain rate.

Using this method, the stress corresponding to tests at very low ($5x10^{-4}$) strain rates and relatively

high ($500x10^{-5}$) strain rates may be found from tension tests at moderate strain rates and appropriately raised or lowered temperatures. The authors showed that the true stress in tension of SAE 1020 steel depends only on the true strain and the velocity modified temperature in the range $-70^0C<T<665^0C$ and for true strain rates $5x10^{-5}\ s^{-1}< \dot{\varepsilon}<500x10^{-5}\ s^{-1}$. The same was found for SAE 1045 steel and brass over smaller temperature ranges $-70^0C<T<370^0C$.

Kopalinsky and Oxley [53] have applied the velocity modified temperature model proposed by MacGregor and Fisher [76] to plane strain machining at high strain rates (>450 s^{-1}) and temperatures ranging between 0 - 1100^0C to determine the material flow stress as a function of T_{vm}. The velocity modified temperature is extensively used in engineering analysis of metal cutting to predict the flow stress at high strain rate and high temperature. Even though this method does not take into account the prior deformation history, (for example the possible increased sensitivity of flow stress to strain rate), the results obtained are relied upon.

2.2.3.1 Flow Stress Under High Strain Rates

In high speed machining strain rates in the order of 10^4 to 10^6 are reached in the workpiece material. Under these conditions of extremely high strain rates deformation may be localised thus localising the strain, strain rate and temperature rise in a narrow band surrounded by a relatively infinite body of material. Adiabatic conditions may prevail and in this case the adiabatic stress-strain curve is relevant in obtaining the flow stress. The theoretical analysis involves the solution of the coupled wave equation, heat equation and mechanical equation of state for the volume of material in which shear is localised.

The governing equations are respectively as follows [77]:

The wave equation: $$\rho\frac{\partial^2\gamma}{\partial t^2} = \frac{\partial^2\tau}{\partial y^2} \qquad (2.11a)$$

$$\textit{The heat equation:}\quad \beta\tau\frac{\partial\gamma}{\partial t} = \rho C\frac{\partial T}{\partial t} - \lambda\frac{\partial^2 T}{\partial y^2} \qquad (2.11b)$$

$$\textit{The mechanical equation of state:}\quad \tau = f(\gamma,\dot{\gamma},T) \qquad (2.11c)$$

Where ρ,λ,c,τ denotes density, thermal conductivity, specific heat, and flow stress of the material respectively; $\gamma,\dot{\gamma},T,t$ are shear strain, strain rate, temperature and time respectively, β is the fraction of plastic deformation energy converted into heat, and y is the spatial coordinate running perpendicular to and from the centre of the shear band. Dodd and Bai [77] have used the perturbation technique to predict the onset of instability, leading to shear localisation in a deforming material. The perturbation analysis is presented in section 2.2.5. Generally, shear bands are examined in post mortem test pieces. In steel they appear as white-etching lines of martensite and in other materials they appear as narrow bands. The shear bands observed in post-mortem samples are obviously representative of a late stage in their evolution and, as such, can be compared with the corresponding theory. Dodd and Bai [77] have obtained an approximate solution for the shear band thickness as follows:

Referring to equation 2.11b: as $t\to\infty$, this reduces to,

$$\beta\tau\dot{\gamma} \approx \lambda\frac{\partial^2 T}{\partial y^2} \qquad (2.12)$$

An estimate of the term $\lambda(\partial^2/\partial y^2)$ within a shear band is

$$\lambda\frac{\partial^2 T}{\partial y^2} \approx \lambda\frac{(T^* - T_o)}{\delta^2} \qquad (2.13)$$

δ is the shear band thickness. Usually, T_o, the temperature outside the shear band is significantly lower than T*, the temperature in the shear band; therefore, it is possible to make the approximation $\Delta T \approx T^*$. Substituting these simplifications into equation 2.12 gives the shear band thickness as:

$$\frac{\delta}{2} = \sqrt{\frac{\lambda \cdot T^{\cdot}}{\beta \tau^{\cdot} \dot{\gamma}^{\cdot}}} \qquad (2.14)$$

Where δ is the thickness of the shear band, and $^{\cdot}$ refers to values in the shear band. Equation 2.14 appears to be physically reasonable, because an increase in thermal conductivity λ and a decrease in the plastic-work rate would both tend to increase the band width. Besides the thermal conductivity, the band temperature T* and shear stress τ^* may also correspond to material parameter; at least this will be so for a transformation band. In a transformation band, the temperature T* is approximately the melting or transformation temperature, while τ^* is of the order of the flow stress. A characteristic strain rate $\dot{\gamma}^*$ can be defined for a given material only at high strain rates when the viscosity of the material may become important. If this is so, then $\dot{\gamma}^* \approx \tau^*/\eta$, and equation 2.14 becomes:

$$\frac{\delta}{2} = \frac{1}{\tau^{\cdot}} \sqrt{\lambda \eta T^{\cdot}} \qquad (2.15)$$

The theoretical values for the width of the shear band reported in reference [77] (Tables 7.1-7.3) show that the predictions by equation 2.14 and 2.15 are equal, giving $2\delta_{pred}$ = 0.1 - 0.11 mm for mild steel. The corresponding experimental value for mild steel is $2\delta_{expe}$ = 0.13-0.19 which therefore makes the widths predicted reasonably close approximations to experimental values. Thus from equation 2.15 it can be concluded that the thermoplastic shear band width should be a material characteristic.

In metal cutting δ can be measured directly from optical microstructures of the chips when

shear localisation occurs, τ^* can be calculated from measured cutting forces and $\dot{\gamma}^*$ can be calculated from the cutting speed and shear angle obtained from chip thickness measurements. Thus equations 2.14 and 2.15 are useful in calculating the temperature under metal cutting conditions where chip segmentation is caused by thermoplastic shear localisation.

2.2.3.2 Constitutive Description of Flow Stress

High-strain-rate plastic deformation is often described by constitutive equations that link stress with strain, strain rate and temperature. The stress can be expressed as given in equation 2.11c. However, plastic deformation is an irreversible and path-dependent process, and a number of parameters affect the development of the deformation structure and as a consequence, the mechanical response. The state of stress, strain rate and temperature affect the evolution of the microstructure. Thus the strain, current temperature and strain rate alone are often not sufficient to describe the stress. Depending on the strain rate, temperature and state of stress, a variety of deformation substructures form, thus the general term called "deformation history" [2] is added to equation 2.11c to give

$$\tau = f(\gamma, \dot{\gamma}, T, \text{"deformation history"}) \qquad (2.16)$$

Experimental determination of the variation of stress with any of these variables is usually accomplished by keeping all others constant except one whose variation with stress in then observed. The objective of a successful constitutive model is to combine all data, for example, as in the classic plot by Campbell and Ferguson [78] shown in Fig. 2.9, into a single equation having the capability of extrapolation and interpolation. The constitutive equations that have been developed fall into two categories.

(1) Empirical constitutive equations which have the work hardening term ϵ^n where n is the strain hardening index, the strain-rate hardening term where the strain-rate sensitivity is expressed as $(\dot{\epsilon}/\dot{\epsilon}_o)^M$;

$(1+a\dot{\epsilon})^M$; $(1+M \ln \dot{\epsilon}/\dot{\epsilon}_o)$, where $\dot{\epsilon}_o$, a and M are constants and the thermal softening which is represented by exponential or power-law functions [79-80].

Johnson and Cook [80] and Johnson et el [81] used these basic ingredients and proposed the following analytical expression,

$$\sigma = (\sigma_o + B\epsilon^n)(1 + C \ln \dot{\epsilon}/\dot{\epsilon}_o)[1-(T^*)^m] \qquad (2.17)$$

where σ_o, B, C, n, m are experimentally determined parameters and the term T* is calculated as:

$$T^* = \frac{T-T_r}{T_m-T_r}$$

where T, T_r and T_m are the current, reference temperature at which σ_o is measured (usually 298 K) and melting temperature respectively; $\dot{\epsilon}_o$ is a reference strain rate.

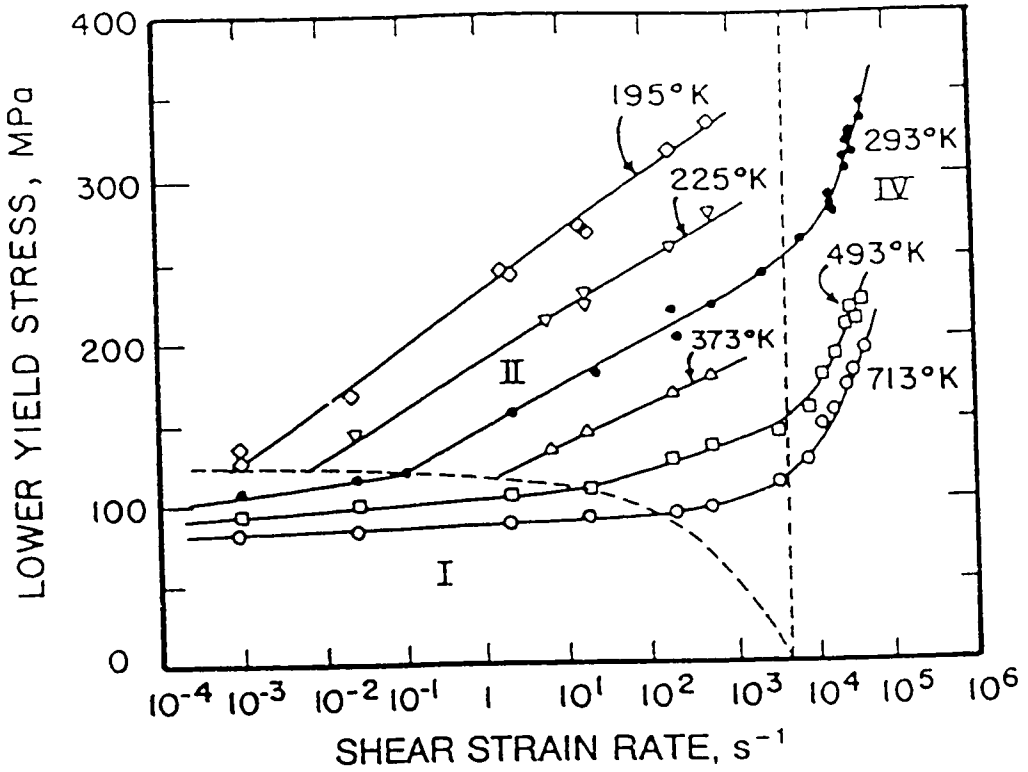

Fig. 2.9: Lower yield stress vs strain rate for mild steel. (After Campbell and Ferguson [78]).

The Johnson Cook equation is the highly useful and successful constitutive model. One of the problems with this equation is that all parameters are coupled by being multiplied by each other.

The response of materials at high strain rates is intimately connected with the evolution of the microstructure. This may involve the generation of defects, cracking, tempering, dynamic recrystallisation, phase transformations, lattice rotations and texturing and twinning. These and their mutual interplay establish the mechanical response of the material. This microstructural evolution is accompanied with marked changes in the thermo-mechanical response of the material which cause a sudden drop in the flow stress of the material in a localised shear zone. Fig. 2.10 shows the sudden drop in flow stress in shock-hardened copper attributed to dynamic recrystallisation [82]. In order to account for dynamic recrystallisation, Andrade et al [82] modified the Johnson Cook equation. They incorporated a reducer function H(T) into the constitutive equation:

$$\sigma = (\sigma_o + B\epsilon^n)(1 + C \ln \dot{\epsilon}/\dot{\epsilon}_o)[1 - (\frac{T - T_r}{T_m - T_r})^m] H(T) \qquad (2.18)$$

$$H(T) = \frac{1}{1 - [1 - \frac{(\sigma_f)_{rec}}{(\sigma_f)_{def}}] u(T)} \qquad (2.19)$$

u(T) is a step function of temperature defined as:

$$u(T) = 0 \text{ for } T < T_c$$

$$u(T) = 1 \text{ for } T > T_c \qquad (2.20)$$

Where T_c is the temperature at which the critical phenomenon (dynamic recrystallisation or phase transformation) occurs; $(\sigma_f)_{rec}$ and $(\sigma_f)_{def}$ are the flow stresses of the material just after and prior to dynamic recrystallisation respectively. The drastic drop in flow stress shown in Fig. 2.10 is attributed

to dynamic recrystallisation.

(2) The second group of equations are the microstucturally-based constitutive equations which are based on the micro mechanics of plastic deformation and are rooted in the thermally-activated motion of dislocations. The separation of short and long-range barriers as well as their shape yields the strain, strain-rate and temperature dependence of the flow stress.

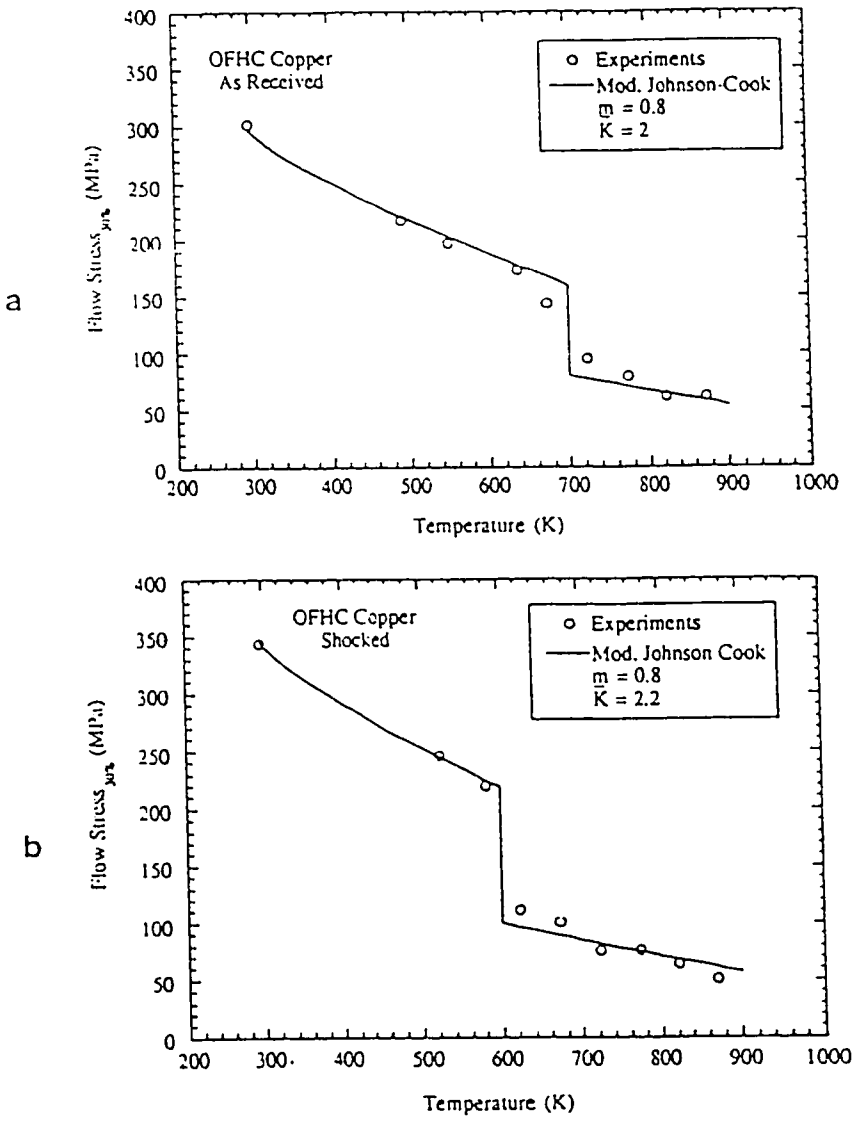

Fig. 2.10: Experimentally determined and computed flow stress (at a plastic strain of 0.3) as a function of temperature for (a) cold worked and (b) shocked copper. (After Andrade at al [82]).

The physically based constitutive equations follow the investigation of high strain-rate response of steels by Campbell [83], Lindholm [84] and Campbell and Harding [85]. The equations developed by Kocks et at. [86], Hoge and Mukherjee [87] Follansbee and Kocks [88], Zerilli and Armstrong [89] and Klepaczko [90] use this approach.

These forms of equations are based on thermal activation in dislocation glide, multiplication and annihilation. The rates of dislocation generation and annihilation are strain rate and temperature dependent. Zerilli and Amstrong based their model on the framework of thermally activated dislocation motion. They noticed that BCC metals exhibit much higher temperature and strain rate sensitivity than FCC metals. They observed that the activation area was dependent on strain for FCC metals and independent on strain for BCC metals. The activation area is the area swept by the dislocation in overcoming an obstacle. The Zerilli and Armstrong (ZA) model, based on thermally activated dislocation motion led to the conclusion that overcoming Peierls-Nabarro barriers was the principal thermal activation mechanism for BCC metals. The spacing of these obstacles is equal to the lattice spacing and is, obviously, not affected by plastic strain. On the other hand the activation area decreases with increasing strain for FCC metals. The athermal component of flow stress σ_G and a term that describes the flow stress dependence on grain size are included in the ZA equation [89] expressed as:

$$For\ FCC: \quad \sigma = \sigma_G + C_2\epsilon^{1/2}\exp(-C_3T+C_4T\ln\dot{\epsilon}) + Kd^{-1/2} \qquad (2.21a)$$

$$For\ BCC: \quad \sigma = \sigma_G + C_1\epsilon^{1/2}\exp(-C_3T+C_4T\ln\dot{\epsilon}) + C_5\epsilon^{n} + Kd^{-1/2} \qquad (2.21b)$$

where C_1, C_2, C_3, C_4, C_5, K are constants and d is the grain diameter.

The principal difference between the two equations resides on the fact that the plastic strain is uncoupled from the strain rate and temperature for BCC metals.

The mechanical threshold stress constitutive model (MTS) proposed by Follansbee [91] and Follansbee and Kocks [88] support the statement that structure evolution is rate sensitive. The MTS model uses the basic ingredients of thermally activated dislocation motion and focuses on the determination of the threshold stress (i.e the height of the barrier F_o, τ_o or σ_o, Fig. 2.11). This threshold is the flow stress of a certain structure at 0 K. The resulting equation is:

$$\left[\frac{\sigma}{G_{(T)}}\right]^{1/2} = \left[\frac{\sigma_o}{G_{(T)}}\right]^{1/2}\left[1 - \left(\frac{\kappa T}{Gb^3 g_o} \ln\frac{\dot{\epsilon}_o}{\dot{\epsilon}}\right)^{2/3}\right] \qquad (2.22)$$

where G(T) is the temperature dependence of shear modules, σ_o is the flow stress at 0 K, κ is Boltzmann's constant, g_o is a normalized total activation energy.

In conclusion the constitutive equations are complex but have been shown to give a reasonable fit to experimental data providing a means for extrapolating the flow stress behaviour beyond experimentally achievable conditions.

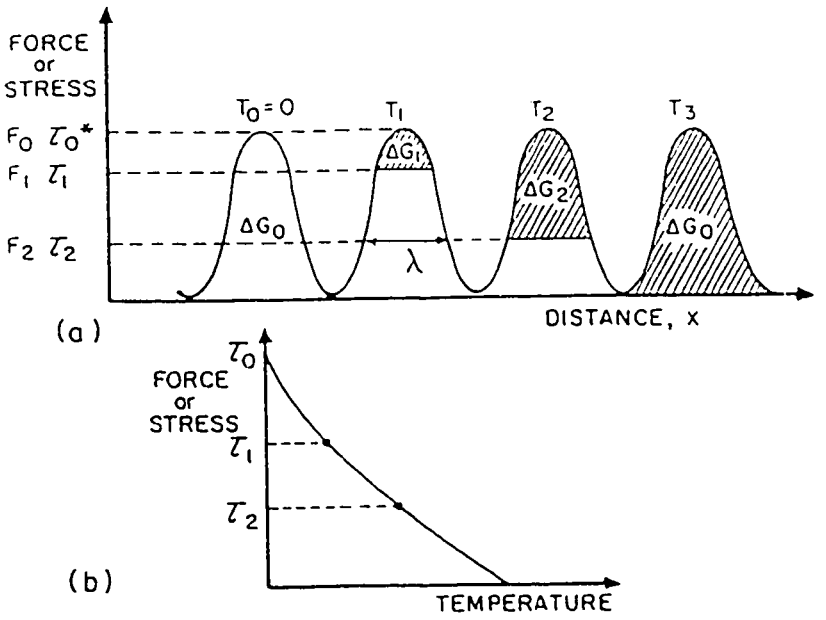

Fig. 2.11: (a) Overcoming of barriers by thermal energy; (b) stress required to overcome obstacles as a function of temperature. (After Meyers [2]).

2.2.3.3 The Effect of Stress on Dislocation Motion

High strain rate deformation mechanisms for metals may be governed by either dislocation glide, mechanical twinning or phase transformations. These mechanisms heavily depend on the strain rate which is given as:

$$\dot{\gamma} = \rho b v$$

where ρ, b, v are the density, length of burgers vector, and velocity of the dislocations respectively. The limiting strain rate is set up by the limiting velocity of the dislocation which in turn is set as the velocity of propagation of elastic shear waves. The dislocation velocity tends toward saturation as the shear wave velocity is approached. This has been shown [92] to occur when the stress approaches 10 GPa which is close to the theoretical strength is steels. If we set the upper limit for the velocity of elastic waves in a metal to be the speed of sound waves in a metal ~5000 m/s, the upper limit of the dislocation density in a deformed metal as $10^{11}cm^{-2}$ and a burgers vector of $2x10^{-8}$ cm, the strain rate obtained is of the order of 10^{8} /s. This is too high compared to the typical strain rates encountered in metal cutting which range between 10^{3} and 10^{6} /s. Dislocation glide mechanisms have been delineated [2] into three governing mechanisms. These mechanisms are thermally activated dislocation motion, phonon drag and relativistic effects.

(1) Thermally Activated Dislocation Motion

The obstacles which oppose dislocation motion include solute atoms, vacancies, small-angle grain boundaries, vacancy clusters, inclusions, precipitates and other dislocations. The Peierls-Nabarro forces oppose the movement at the atomic level. A force has to be applied to overcome an energy barrier in order to move a dislocation from one equilibrium atomic position to the next. The smaller narrower barriers are called short-range obstacles which, if strong, produce a rapidly varying glide stress. The larger wider barriers are called long-range obstacles for which the glide stress hardly varies with temperature and strain rate. The principal short-range barrier is the Peierls-Nabarro stress which

is important for BCC metals. For FCC and HCP metals, dislocation forests are the primary short-range barriers at lower temperatures. The different nature of these barriers is responsible for the major differences in temperature and strain rate sensitivity of the yield strength between FCC and BCC metals. Fig. 2.12 shows measured yield stresses at various fractions of the absolute melting point, T_m. The BCC metals are shown to exhibit a higher thermal sensitivity of the yield stress than FCC and HCP alloys. The activation energy required to overcome the short range barriers is expresses in terms of strain rate as [2]:

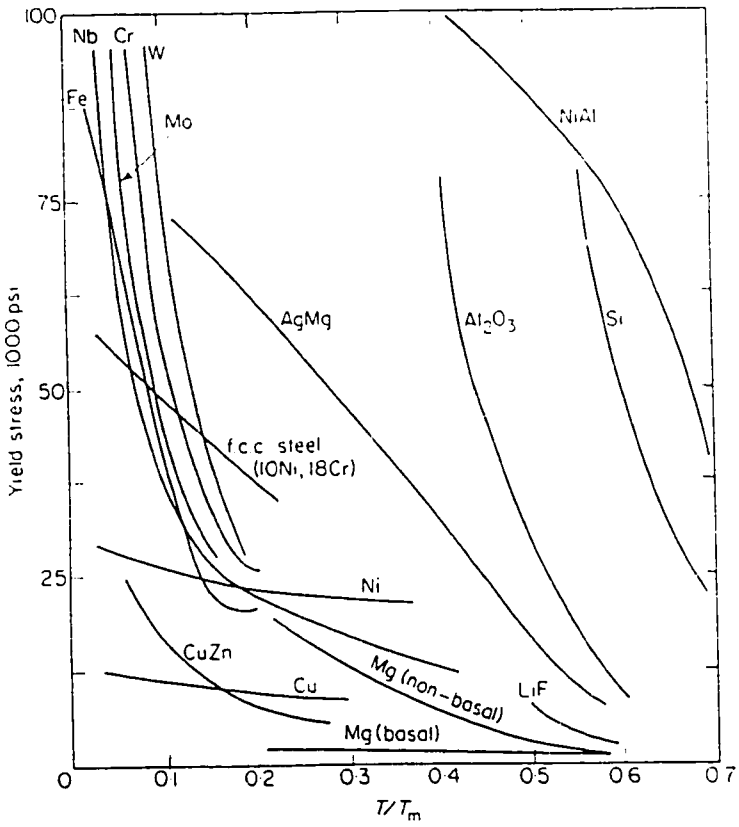

Fig. 2.12: Yield stress at various temperatures. [A.H Cottrell, The Mechanical properties of Matter, John Wiley and Sons, Inc. New York, 1964]

$$\Delta G = \kappa T \ln \frac{\dot{\epsilon}_o}{\dot{\epsilon}} \qquad (2.23)$$

where κ is Boltzmann constant T in the temperature $\dot{\epsilon}_0$ is a constant and $\dot{\epsilon}$ is the strain rate. This is the foundation for constitutive equations that are based on thermally assisted overcoming of obstacles.

(2) Dislocation Drag Mechanisms

Out of the total energy expanded in plastic deformation, 90% is dissipated by forces opposing the applied stresses. These forces can be expressed as a viscous behaviour of the solid. To a first approximation, the solid is assumed to act as a Newtonian viscous material with respect to the dislocation. Then under external stress, the dislocation will accelerate until it reaches a steady-state velocity. The stress is expressed as [93]:

$$\sigma = \frac{2B_c M_o}{\rho b^2}\dot{\epsilon} \qquad (2.24)$$

where B_c is the viscous damping coefficient, M_0 is an orientation factor [92]. Thus the flow stress is proportional to the strain rate when dislocation drag mechanisms are operative. Gillis et al [94] have expressed B_c as:

$$B_c = \frac{B_o}{1 - \upsilon^2/\upsilon_s^2} \qquad (2.25)$$

B_0 = viscosity at rest. υ_s is shear wave velocity. This implies that viscous drag decreases as the velocity increases.

The drag mechanisms that are not thermally activated are the interaction of the dislocation with thermal vibrations (phonon drag) and with electrons (electron viscosity). In addition relaxation

effects in the dislocation core are included [2]. For metals phonons cause drag at ambient and higher temperatures and electrons cause drag at low temperatures (<100K) [95]. The drag stress establishes a steady state velocity of about 0.5 the shear wave velocity.

(3) Relativistic Effects on Dislocation Motion

Relativistic effects start gaining importance when the dislocation velocity is in the range of 0.8 of the shear wave velocity [96-97]. Even though a supersonic dislocation was proposed by Eshelby [98], supersonic dislocations have neither been observed experimentally nor predicted analytically.

Summary

When the applied stress is lower than the threshold stress σ_0 (height of activation barrier), thermal activation controls the velocity of propagation. When the applied stress is higher than the short-range barrier height, drag (viscous and scattering) controls the resistance to dislocation motion. At higher velocities, in the range of 0.8 C_s relativistic effects start becoming important.

2.2.4. Metallurgical and Thermo-plastic Characteristics of the Workpiece Material

This section is devoted to a review of the material properties that affect the susceptibility of the material to thermoplastic shear localisation. Staker [99] illustrated the importance of strain hardening capacity of a material in adiabatic shearing by carrying out tests on 4340 steel specimens which had been subjected to different tempering temperatures. In this case, the composition of the steel and thermo-physical properties of the steel remain the same, but the microstructural and mechanical properties change, showing that the material condition influences its susceptibility to formation of adiabatic shear bands. The onset of adiabatic shear instability was found experimentally to take place at a critical true shear strain given by:

$$\gamma_c = \frac{-Cn}{\partial\tau/\partial T} \qquad (2.26)$$

where C is the volume specific heat, n is the strain hardening exponent and $\partial\tau/\partial T$ is the rate of change of flow stress with temperature. The volume specific heat has the same value for most ferrous metals and can be regarded as a constant independent of mechanical properties and heat treatment. The parameters n and $\partial\tau/\partial T$ were found to vary by nearly a factor of 3 with heat treatment the later term being more significant [99]. While the strain hardening exponent decreases with increase in strength [100], thermal softening increases with increase in strength. Thus high strength metals with large dependence of flow stress on temperature will exhibit instability at low strains.

The formation of shear-localised chips was first attributed to adiabatic shear by Recht [73]. He analysed adiabatic shearing during chip formation in high speed machining and developed a relationship, based on the thermo-plastic properties of the material, by which two materials could be compared relative to their sensitivity to adiabatic shearing. He obtained the relation by equating the plastic deformation work in shearing to the heat generated in the local volume of the shear band. The relation obtained is:

$$\frac{\dot{\varepsilon}_{c1}}{\dot{\varepsilon}_{c2}} = \frac{(\lambda\rho c)_1}{(\lambda\rho c)_2} \frac{[(\frac{\partial\tau}{\partial\varepsilon})_1 / (\frac{\partial\tau}{\partial T})_1]^2}{[(\frac{\partial\tau}{\partial\varepsilon})_2 / (\frac{\partial\tau}{\partial T})_2]^2} [\frac{\tau_{y2}}{\tau_{y1}}]^2 \qquad (2.27)$$

where λ, ρ, c, τ_y are the thermal conductivity, density, specific heat and shear yield strength of material respectively and ϵ, $\dot{\epsilon}_c$, T are the strain, critical strain rate for adiabatic shear to occur and temperature respectively with subscripts and superscripts 1 and 2 referring to material 1 and 2.

Titanium was found to be the most sensitive material having a critical speed for adiabatic slip of 1 sfm (0.3 m/min). A comparison of the critical strain rates for various metals with that of titanium assuming that the strain rate is directly proportional to the cutting speed enables the prediction of the critical cutting speed for adiabatic shear. This corresponds to the critical speed for chip segmentation

if it is assumed that chip segmentation is caused by adiabatic shear at the primary shear zone. The contribution from each of the terms in equation 2.27 in influencing the critical cutting speed for chip segmentation for various metals is summarised in Table 2.1.

Table 2.1: Contribution of thermophysical, thermoplastic and strength properties of various metals to the critical speed for adiabatic slip (chip segmentation) as compared with titanium.

Material	Density (kg/m^3)	Specific heat (J/kg K)	Thermal conduc-tivity (w/m K)	Ratio of thermo-physical properties	Thermal sensitivity ratio	Stre-ngth ratio	Strain rate ratio	Critical speed for adiabatic slip (m/min.)
Titanium RC-70	4405	502	14	1	1	1	1	.305
SAE 1020	7849	502	50	6.4	58	4.1	1522	457
SAE 310	7849	502	14	1.8	121	2.3	485	150
Ferritic Ductile Iron	7100	461	32	3.4	156	2	1061	323

The term containing the ratio of strain hardening to temperature softening (i.e. the thermal sensitivity ratio) has the greatest influence on the ratio of critical strain rates. Therefore any phenomenon that influences this term will have a major effect on thermoplastic shear localisation and chip segmentation. The critical strain rate for adiabatic shear localisation for mild steel SAE 1020 is predicted to be 1522 times that of Ti-6Al-4V alloy. This corresponds to a cutting speed of 457 m/min for the steel. For ferritic ductile iron the critical strain rate for the onset of thermoplastic shear localisation is predicted to be 1061 times that of Ti-6Al-4V, which corresponds to a cutting speed of 323 m/min.

Shear bands have been classified [101] as "transformed" and "deformed" on the basis of their appearance on metallographic observations. Deformed shear bands are manifested merely as zones

of intense shear deformation of the original microstructure. The formation of transformed shear bands requires high temperature rise at the section and ability of the material to undergo phase transformation. Thermal diffusivity, resistance to adiabatic shear localisation and ability to undergo phase transformation are used in classification of materials for their susceptibility to form transformed shear bands. Resistance to adiabatic shear deformation is evaluated using critical strain and critical strain rate criteria. Both the susceptibility of a given material to shear localisation and the resultant shear band structure depend on the initial microstructure. Timothy [102] has classified various metals by their general tendency to form transformed bands, deformed bands or no shear bands. Using thermal diffusivity, critical strain and critical strain rate criteria susceptibility of the different materials for adiabatic shear is mapped on a thermal diffusivity versus critical strain plot as shown in Fig. 2.13(a), and a thermal diffusivity versus critical strain rate plot as shown in Fig. 2.13(b). The critical strain for adiabatic shear to occur is given by:

$$\epsilon^c = -n\ C\ T_m/\psi_T\tau \tag{2.28}$$

where n is the hardening index, C is the volume specific heat, T_m, is the melting temperature, τ is the flow stress of the material, ψ_T is a function of the rate of softening of the material given as

$$\psi_T = \frac{T_m}{\tau}\left(\frac{\partial\tau}{\partial T}\right) \tag{2.29}$$

The relative critical strain rate at which each materials would exhibit the same thickness of the shear zone at a strain of 1.0 is given by [103]:

$$\lambda\ \rho\ C\ n^2\ T_m^2/\sigma_o \tag{2.30}$$

where λ is the thermal conductivity, ρ is the density, C is the specific heat, n is the hardening index,

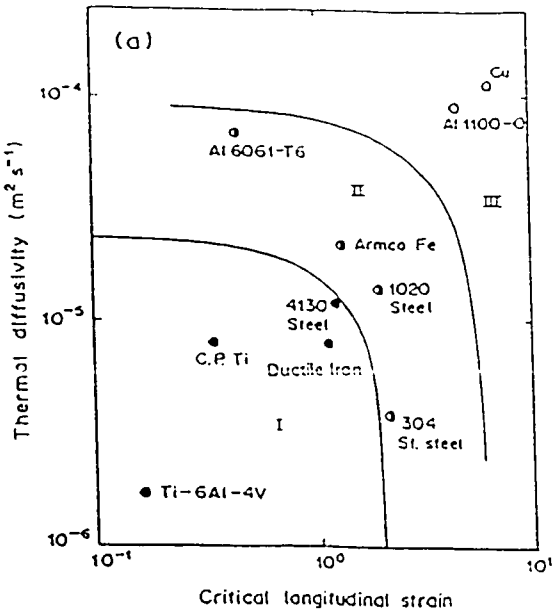

Fig. 2.13(a): Critical strain for adiabatic shear versus thermal diffusivity of material [102]. Solid symbols - metals tend to form "transformed" shear bands (region I): half-open symbols - metals tend to form "deformed" shear bands (region II): open symbols - metals do not tend to form discrete shear bands (region III). Ductile iron falls in the region of transformed shear bands.

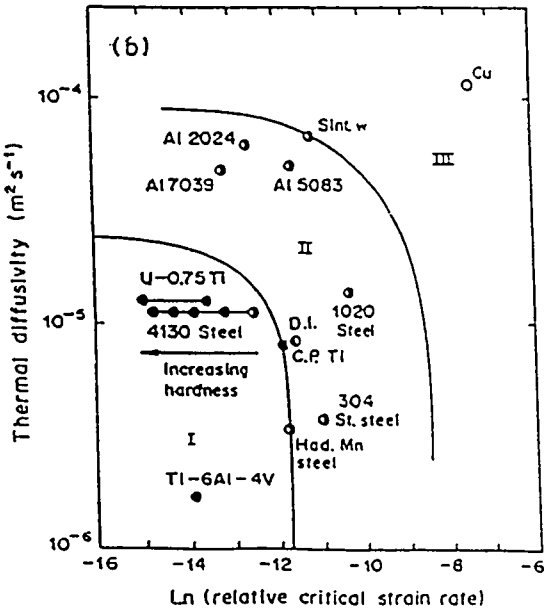

Fig. 2.13(b): Relative critical strain rate for adiabatic shear plotted against thermal diffusivity of material [102]. For symbols see Fig. 2.13(a). Ductile iron (DI) is at the limit of transformed shear band formation.

T_m is the difference between melting point and ambient temperature, $\sigma_o=\sqrt{3}\tau$ is the flow stress in tension. When ductile iron is mapped on the same diagram, it is obvious that it falls in the regime of materials with high susceptibility for shear localisation. However AISI 1020 steel with the same ferritic matrix falls in the region where it is only sensitive to formation of deformation shear bands.

The final widths and structure of adiabatic shear bands have been shown to be influenced by material properties [104-106]. A simple estimation of the shear band width has been given by Dodd and Bai [77,106], and Bai and co-workers [107] in equation 2.12. The equation shows the dependence of shear band thickness on thermo-physical properties of the material and strain rate.

2.2.5. Mechanism of Formation of Thermoplastic Shear Bands

Thermoplastic shear bands are formed when plastic flow is localised under loading conditions similar to shock or impact. The earliest observations of these forms of deformation were reported by Zener and Hollomon [1] who attributed the whole process to thermal softening and called it adiabatic shear. Since then, numerous others have reported similar observations in a range of materials [108-111]. The evidence accumulated over the past several years confirm the original proposal by Zener and Hollomon [1] that in crystalline solids, when the rate of work hardening of a material undergoing plastic deformation is less than the rate of thermal softening, the deformation may be localised in shear bands in which instability develops. The result is a considerable rise in temperature and drop in the flow stress of the material with an attendant change of other material properties; viz, thermal conductivity, and specific heat. Zener and Hollomon [1] assumed the process to be adiabatic and simply computed the adiabatic temperature rise in a material by converting the work of deformation into a temperature increase through the material heat capacity and density. Fig. 2.14 illustrates the effect of incorporating the deformation energy into the temperature rise. Shear stress-shear strain curves for commercially pure titanium are shown as a function of temperature. These relationships are

assumed to be linear as a first approximation. By converting 90% of the work of deformation into heat one obtains the adiabatic curve also included in Fig. 2.14. Whereas the isothermal curves show hardening, the adiabatic curve goes through a maximum (occurring at a stress of 280 Mpa, temperature of 400 K and strain of 1) and then decreases steadily. The point at which decrease of stress commences marks the onset of instability and the corresponding strain, strain rate and temperature are referred to as the instability values.

The development of a criterion for the onset of instability which leads to the formation of shear bands has been attempted by Recht [73], Culver [112, Bai [113] and others. Most of the analyses

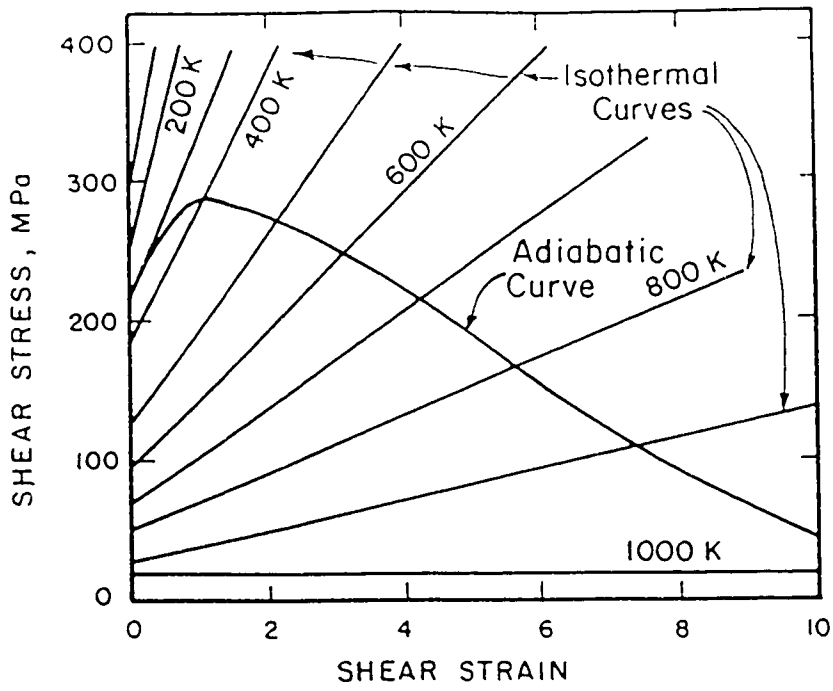

Fig. 2.14: Isothermal (straight lines) shear stress-strain response of commercial purity titanium between 100 and 1000 K; adiabatic shear stress-shear strain curve showing maximum at $\gamma = 1.0$. (After M.A.Meyers and H.R. Pak, Acta Metall., vol.34, p.2496, 1986)

culminate in the prediction of a critical strain for the onset of instability [112-114]. However, this is only after neglecting strain rate and deformation history effects and phase transformations in the volume of material subjected to localised shearing. Neglecting the strain rate and deformation history effects allows the onset of localisation to coincide with a maximum in the local flow stress and is referred to as the maximum stress criterion. Recht [73] analysed the case of high speed machining and obtained a condition for thermoplastic shear instability in terms of a critical strain rate. The material adjacent to the shear band is an efficient heat sink by diffusion. In order to contain the heat within the shear localised zone, attainment of both a critical strain and critical strain rate seems to be a more realistic condition for adiabatic shear instability.

Although it is true that unstable shear deformation may occur at a maximum in shear stress and along a thin zone, this approach is too simplistic. At instability, which is defined by the maximum in shear stress, homogeneous deformation will continue to occur in the specimen without the occurrence of shear localisation as long as no major perturbation is introduced. A perturbation in stress, strain or temperature, if it leads to a sudden drop in stress, is the onset of shear localisation. Thus localisation, not instability, marks the formation of a shear band. This has been illustrated by Wright and Walter [115] in the schematic shown in Fig. 2.15. As shown in the figure, homogeneous deformation continues after the instability point. When a perturbation is introduced a drastic fall in stress accompanied by a rise in strain rate and temperature marks the onset of localisation.

Localisation of plastic shear has received considerable theoretical attention, with most studies confining their attention to initiation of such a localisation phenomenon [73,77,113,116-120]. The general prediction is that the onset of localisation occurs after the occurrence of instability defined by a maximum in shear stress. An alternative approach emphasizes the coupling effects of strain hardening, strain-rate hardening and thermal softening in the linear instability and the linear perturbation analyses [118-120].

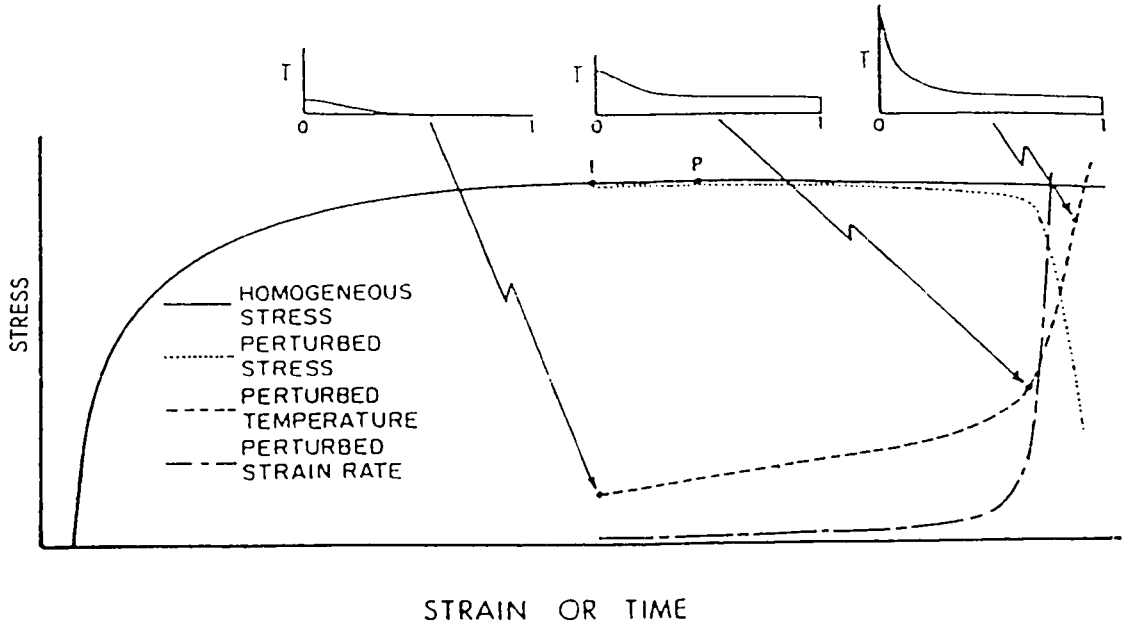

Fig. 2.15: Sketch showing the evolution of stress, maximum temperature, and maximum strain rate; small temperature perturbation introduced just before peak stress. (After Wright and Walter J.Mech. Phys. Solids,Vol.35, pp.701-720, 1987).

The growth of infinitesimal inhomogeneities from homogeneous simple shearing are investigated using this method. The problem is to identify the criterion for the marginal instability of thermoplastic shear using linear perturbation analysis technique. The question is: when does the homogeneous deformation become unstable and give way to inhomogeneous shear deformation? This problem has been examined by Clifton and co-workers [118], Bai [119] and by Anand and co-workers [120]. The approach is to linearize the governing equations about the unperturbed homogeneous shear deformation. The analysis by Bai [119] and Bai and Dodd [77] considers strain hardening, thermal softening and strain sensitivity and heat conduction and investigates the growth of infinitesimal perturbations (inhomogeities) from homogeneous simple shearing. The governing equations for thermoplastic shear localisation are obtained from the fundamental equations concerning conservation of mass, momentum and energy as well as the constitutive equation. Heat conduction is governed by Fourier's law. The equations are: (1) The wave equation describing the propagation of a shear wave

through the material, equation 2.11a; (2) Fourier's heat conduction equation which describes the conduction of heat in the deforming material, equation 2.11b, and (3) The mechanical equation of state which relates the flow stress to the strain, strain rate and temperature of the deforming zone, equation 2.11c. The differential form of equation 2.11c is given as:

$$d\tau = Q d\gamma + R d\dot{\gamma} - P dT \qquad (2.31)$$

where,

$$Q = \left(\frac{\partial \tau}{\partial \gamma}\right)_{\dot{\gamma},T} \; ; \quad R = \left(\frac{\partial \tau}{\partial \dot{\gamma}}\right)_{\gamma,T} ; \quad P = \left(\frac{\partial \tau}{\partial T}\right)_{\gamma,\dot{\gamma}} \qquad (2.32)$$

and τ, γ, $\dot{\gamma}$, T are the stress, strain, strain rate and temperature of an element undergoing deformation. The physical meaning of each of these terms is as follows: Q= the isothermal strain hardening rate at constant strain rate; R= the isothermal strain-rate hardening at constant strain; P= the rate of thermal softening at constant strain and strain rate.

The infinitesimal perturbations considered are:

$$(\gamma', \tau', T') \ll (\gamma^h, \tau^h, T^h) \qquad (2.33)$$

Substitution of the perturbations into the governing equations 2.11a and 2.11b and only retaining first order terms gives the following linearized perturbed equations:

$$\rho \frac{\partial^2 \gamma'}{\partial t^2} = \frac{\partial^2 \tau'}{\partial y^2} \qquad (2.34a)$$

$$\beta \tau^h \frac{\partial \gamma'}{\partial t} + \beta \tau' \dot{\gamma}^h = \rho C \frac{\partial T'}{\partial t} - \lambda \frac{\partial^2 T'}{\partial y^2} \qquad (2.34b)$$

We now examine the equations for the following type of solution:

$$\tau' = \tau^{\bullet} \exp(\alpha t + i\Lambda y) \qquad (2.35a)$$

$$\gamma' = \gamma^{\bullet} \exp(\alpha t + i\Lambda y) \qquad (2.35b)$$

$$T' = T^{\bullet} \exp(\alpha t + i\Lambda y) \qquad (2.35c)$$

where the amplitude $\tau^{\bullet}, \gamma^{\bullet}, T^{\bullet}$ and the values of the growth rate α and the wave number Λ are undetermined.

Combining equations 2.31, 2.34 and 2.35 gives a system of homogeneous algebraic equations for $\tau^{\bullet}$ and $T^{\bullet}$:

$$\{\rho\alpha^2 + (Q + R\alpha)\Lambda^2\}\tau^{\bullet} - P\Lambda^2 T^{\bullet} = 0 \qquad (2.36a)$$

$$\{\beta\tau^h\alpha + \beta\,\dot{\gamma}^h(Q + R\alpha)\}^{\bullet} - (\beta\,\dot{\gamma}^h P + \rho c\alpha + \lambda\Lambda^2)T^{\bullet} = 0 \qquad (2.36b)$$

For non-zero solutions for $\tau^{\bullet}$ and $T^{\bullet}$ the determinant of the coefficients in equations (2.36) should be zero. This leads to the characteristic equation:

$$\{\rho^2 c\alpha^3 + \rho\{\beta P\,\dot{\gamma}^h + (\lambda + cR)\Lambda^2\}\alpha^2 + (\lambda R\Lambda^2 + \rho cQ - \beta\tau^h P)\Lambda^2\alpha + \lambda Q\Lambda^4 = 0 \qquad (2.37)$$

If the eigenvalue of α has a positive real part, this implies that instability is possible. For positive α:

$$B > 1 + 2\sqrt{C} \qquad (2.38)$$

Where

$$B = \beta\tau^h P/\rho cQ, \quad C = \beta\Lambda P\,\dot{\gamma}^h/\rho c^2 Q = B/Pr$$

C can be evaluated for metal approximately as:

$$C = \beta\Lambda P\,\dot{\gamma}^h/\rho c^2 Q \approx (10^2 \times 10^6)/(10^3 \times 10^6 \times 10^8)\dot{\gamma}^h \approx 10\text{-}9\,\dot{\gamma}^h \ll 1$$

then it follows that the criterion for instability simplifies to

$$B > 1$$

which is identical to the maximum shear stress criterion stated as : thermoplastic shear instability will occur when the local rate of change of temperature has a negative effect on strength which is equal to or greater than the positive effect of hardening i.e. when $d\tau = 0$ which makes the assumptions of

negligible strain-rate sensitivity, adiabatic deformation and power-law hardening, $\tau = \tau_o \gamma^n$, and expresses the critical strain for instability to occur as:

$$\gamma_c = \frac{n\rho c}{-\left(\frac{\partial \tau}{\partial T}\right)_{\gamma,\dot{\gamma}}} \qquad (2.39)$$

where n is the strain hardening index.

For the adiabatic case, $\lambda=0$. The characteristic equation for this case is:

$$\{\rho^2 c\alpha^2 + \rho\{\beta P\, \dot{\gamma}^h + cR\Lambda^2\}\alpha - (\beta\tau^h P - \rho cQ)\Lambda^2 = 0 \qquad (2.40)$$

The criterion is $B>1$ and the maximum growth rate of the instability is

$$\alpha = (\beta\tau^h P - \rho cQ)/\rho cR \qquad (2.41)$$

which occurs for disturbances with a short wavelength, $\Lambda \to \infty$.

The conclusion from this analysis is that thermal softening accelerates the growth of inhomogeneities, whereas strain-hardening retards the growth.

Since neither the principle of the maximum in the shear stress nor the perturbation technique describe the shear localisation itself, Bai and Dodd [77] considered the fundamental problem of how to define localisation and discover the fundamental mechanism operative in the occurrence of adiabatic shear bands. The localisation analysis is a lengthy process and will not be reproduced here. However, a major result of the localisation analysis is the indication that the start of localisation is not consistent with instability. In addition assuming the constitutive equation:

$$\tau = A\gamma^n \dot{\gamma}^m \theta^{-\nu} \qquad (2.42)$$

and using these methods of analysis, Dodd and Bai [77] showed that thermal softening accelerates growth of inhomogeneities, whereas strain hardening and strain rate hardening retards the growth. The

localisation requires that

$$n+m-\nu<0 \qquad (2.43)$$

However, linear perturbation carried out on the state variables using the same constitutive equation leads to the instability condition:

$$m+n-\nu > 0 \quad with \qquad n-\nu < 0 \qquad (2.44)$$

Therefore, there is a gap between instability and localisation.

The formation and evolution of adiabatic shear bands is generally accepted [77] to be a multi-stage process which is considered to occur as follows: (1) homogenous shear deformation (2) instability leading to inhomogeneous deformation (3) the emergence of a localised shear zone (4) formation of a fully developed localised shear zone and (5) shear fracture along the shear zones.

Coffey [121] has proposed a descriptive mechanism for shear localisation. According to this mechanism the transition features involved in the formation of adiabatic shear bands are instability and localisation. The initial point when instability gives way to localisation is an isothermal and momentum dominant process controlled by rate dependant diffusion, or viscosity. At this stage, the lattice responds through the existence of dislocation sources which produce copious quantities of dislocations. The dislocations are constrained to move along nearly adjacent slip planes with velocities nearly equal to the shear wave speed. This rapid movement of dislocations can cause multi phonon processes to occur leading to rapid molecular vibrations and even electronic excitation. The dislocations soon encounter obstacles and form a dynamic pile-up. The back stress from this pile-up will temporarily cause the source to shift production to other nearby slip planes. In this way, a shear band composed of dynamic pile-ups on nearly simultaneously active slip planes is formed. This has been estimated [77,121] to occur as early as a few nano-seconds after shock arrival. Significant

temperature increase does not occur until later times (~μ seconds) because of the absence of internal molecular vibrational states. Deformation at this stage is therefore quite unconnected with temperature and is fairly isothermal. The later stage is the coupling of heat diffusion and quasi-static shear localised deformation work. A similar conclusion has been reached by Drew & Flaherty [122] through finite element simulations.

The preceding analyses neglect the contribution from the microstructural changes to the onset of shear localisation. In fact the localisation analysis by the perturbation technique, presented by Dodd and Bai [77] concludes that there is a gap between instability and localisation. The next section is devoted to the role of microstructural evolution in thermoplastic shear localisation.

2.2.5.1 The Role of Phase Transformation in Thermoplastic Shear Localisation

It has been pointed out that the mechanism for chip segmentation in high speed machining involves thermoplastic shear localisation. It has also been shown that theoretical analysis neglecting microstructural changes leaves a gap between shear instability and shear localisation [77]. It is therefore important to enquire into the causes of thermoplastic shear localisation. Meyers [2] has recently clarified that the mechanism of shear localisation involves two stages; first, instability occurs at a maximum of the shear stress; then localisation follows if there is a major microstructural change involving a sudden drop in the shear stress. Meyers [2] attributed shear localisation to a microstructural evolution in the shear band involving dynamic recrystallisation. The present study examines if phase transformation is another phenomenon that is capable of introducing localised softening in the material while undergoing high strain rates deformation. Timothy [102] reviewed the structure of transformed shear bands and concluded that the role of phase transformations themselves in promoting their formation may be incidental. Lemaire and Backofen [58] observed reversion of an Fe-18.5Ni-0.52C martensitic steel to austenite in the chips obtained during orthogonal

machining. The authors attributed the reversion of martensite to austenite to shear localisation as caused by the adiabatic rise in temperature beyond the phase transition temperature A_s. In materials with phase transformation temperature higher than recrystallisation temperature, dynamic recrystallisation would control shear localisation. In materials whose phase transformation temperature falls below the recrystallisation temperature, phase transformation would control shear localisation. An intermediate situation would exist in which a transformed shear band forms at the centre of a deformation shear band depicting a contribution from both phase transformation and dynamic recrystallisation to shear localisation. Thus the major microstructural changes accentuating shear localisation may be classified into three categories; dynamic recrystallisation alone, the combination of dynamic recrystallisation with phase transformation and phase transformation alone. The low strain rate (10^{-3}/s) deformation of cold worked and shocked copper as a function of temperature has been used in an attempt to demonstrate the role of dynamic recrystallisation in shear localisation [82]. The case of combined effects of recrystallisation and phase transformation appears to be the most confusing is several investigations that have been made to establish the structure of adiabatic shear bands in steels [123-128]. It is generally agreed that transformed shear bands (white-etching bands) in steel have a very fine-grained, highly dislocated microstructure. Based on TEM observations and X-ray diffraction measurements body-centred tetragonal structures [127] and retained austenite [123,129] have been reported in the white-etching bands formed during high strain rate deformation of steels. Greenwood and Johnson [130] have provided experimental evidence which shows that phase transformation could accentuate instability in shear localisation.

2.2.5.2 Effect of Hydrostatic Pressure on Phase Transformation Temperature

A high compressive stress has been reported [102] to promote phase transformation during the occurrence of adiabatic shear localisation. The pressure effect on phase transformation is governed

by volume change accompanying phase transformation. Hydrostatic pressures of 10 Kbar and above have been reported [131] to reduce the transformation temperature of a martensitic Fe-28.4at%Ni-0.5at%C alloy at a rate or about 4°C per Kbar. The metal cutting variables determine the temperature rise leading up to the phase transformation temperature. The pressure effect influences the phase transformation temperature. The influence of metal cutting variables through the specific cutting pressure on phase transformation temperature is significant if there is volume change accompanying phase transformation. This important aspect is ignored in metal cutting literature pertaining to formation of shear localised chips.

In orthogonal cutting, the specific cutting pressure or hydrostatic pressure is obtained by dividing the measured cutting force F_z by the area of cut (i.e. feed x depth of cut). Under typical machining conditions hydrostatic pressures of 20 Kbar are encountered. The specific cutting pressure increases with decrease of feed [53]. The experimental results from the machining of a martensitic Fe-18.5Ni-0.5C steel show that as the rake angle is reduced, the type of chips formed change from type 1 characterised by absence of newly formed austenite and an irregular fracture along the sheared edge of the chip, to type 2 and 3 which contained an austenite band half the length and on the full length of the sheared edge respectively [58].The effect of reducing the rake angle is to increase the cutting force and reduce the shear plane angle [55-57]. This has the effect of increasing the hydrostatic pressure at the primary shear plane. Thus reducing the rake angle increases the cutting forces and the hydrostatic pressure which in turn leads to adiabatic shear localisation. Hence the role of hydrostatic pressure should not be ignored when dealing with adiabatic shear localisation.

2.2.6 Fracture Mechanism in Metal Cutting

The general mechanism of fracture of ductile solids has been observed [132,133] to be the result of growth and coalescence of microscopic voids. Models have been proposed to predict the

growth of voids in deforming materials. The models use methods of continuum plasticity and deal with the expansion of pre-existing voids under a particular state of stress. As proposed by McClintock [132] the changes in size, shape and spacing of the holes in ductile fracture by growth of holes depends on the entire history of stress, strain and rotation. McClintock considered the growth of long cylindrical holes parallel to the tensile axis and having an initial spacing of λ_o and diameter d_o. The integration of the growth law gives the fracture strain as:

$$\epsilon_f = \frac{2}{\sqrt{3}} \frac{\ln F_{co}}{\sinh(\sqrt{3}\sigma_r/(\sigma_z - \sigma_r))} \qquad (2.45)$$

where F_{co} is the relative growth factor due to c holes growing together in the o direction given by

$$F_{co} = \frac{d}{d_o} \cdot \frac{\lambda_o}{\lambda} \qquad (2.46)$$

at the onset of coalescence. For cylindrical holes with elliptical cross-sections in a strain hardening

$$\epsilon_f = (1-n) \frac{\ln F_{co}}{\sinh((1-n)(\sigma_1+\sigma_2)/(2\bar{\sigma}/\sqrt{3}))} \qquad (2.47)$$

material the fracture strain is given by:

where σ_1 and σ_2 are the two unequal transverse stress components. The ratio $\sigma_1 + \sigma_2/\bar{\sigma}$ characterises the stress triaxiality.

In order to calculate the damage rate and accumulated damage at a point the stress and strain history at that point is required. McClintok's fracture criterion has been used [134] to show that damage accumulation in the process can be expressed as:

$$A_{co} = \ln F_{co} = \int_0^{\varepsilon} d(\ln F_{co}) \qquad (2.48)$$

The accumulated damage can be denoted as:

$$A_{co} = \ln F_{co}^{f} = \ln \lambda_o/d_o \qquad (2.49)$$

where λ_o and d_o are initial void spacing and void dimensions along the o direction.

The left hand side in equation 2.48 and 2.49 is a constant for a material and is defined as the critical accumulated damage (CAD), A_{co}. This observation has been used [134] to develop a method for measuring the critical accumulated damage to fracture. Another model to describe the growth of voids is by Rice and Tracey [133]. The model describes the growth of an isolated spherical void of initial radius R_o in a non-hardening material by an analytical solution of the growth rate given by:

$$\dot{R}_i = R_o(a\dot{\epsilon}_i^{\infty} + (\frac{2}{3}\dot{\epsilon}_j^{\infty}\dot{\epsilon}_j^{\infty})\ D) \qquad (2.50)$$

where R_i = growth rate in the principal direction i

$\dot{\epsilon}_i^{\infty}$ = remote strain rate in that direction

a = amplification factor, varying between 5/3 for a strong hardening or very low triaxiality in a non-hardening material, and 2 for higher triaxiality of the latter case.

For a non-hardening material D is given by;

$$D = 0.56\ \sinh(\sqrt{\frac{3}{2}}\frac{\sigma_m^{\infty}}{\tau_o}) \qquad (2.51)$$

where σ_m^{∞} = remote mean stress component and τ_o = shear yield stress.

For a strong linear hardening material,

$$D = \sqrt{\frac{3}{4}}\frac{\sigma_m}{\tau_o} \qquad (2.52)$$

The first term in equation 2.50 refers to a change in shape of a void, and the second term to a change in its volume. The deformations transform initially spherical surfaces into infinitesimally neighbouring ellipsoids. For the particular case of a non-linear hardening the approximate equation for growth rates is given by,

$$\dot{R}_o = \dot{\gamma}(a + b\frac{P}{k})R_0 \qquad (2.53)$$

This represents the growth of voids under the conditions where they are acted upon by a remote hydrostatic (tensile or compressive) pressure P in the material with a shear yield stress of k. In this case a is a material constant which is the amplification factor of the remote strain rate field and is assumed to be initially equal to 1.5. b is a constant affecting the stress triaxiality and is equal to ½√2 for a hardening material. This model emphasizes the determining influence of the stress state i.e. the P/k ratio on the growth of voids in a deforming material. In metal cutting the P/k ratio is influenced by metal cutting variables.

2.2.6.1 Shear Band Induced Damage Accumulation and Fracture

There is evidence of accumulation of damage which accompanies grain distortion under conditions of shear loading [135-138]. Giovanola [137] reported metallographic evidence of the characteristic white etching bands and voids in tool steel RC 50 under torsional loading. Similar evidence has been provided by Xu et al [139]. In situations of combined compression and shear deformation it has been proposed [137] that thermoplastic shear bands form in two stages: (1) In the

first stage shear banding is initiated by local perturbation in a uniform strain field. This perturbation is said to develop with increasing strain because of imbalance between thermal softening and strain hardening. This observation was also made by Culver [112] and Bai [113] and others. (2) The second stage of localisation occurs due to nucleation and growth of micro voids, which corresponds to shear fracture of the band. It is therefore clear that the mechanisms which lead to the first stage of localisation and the second stage of localisation are basically different and must be modelled separately. A thermo-mechanical instability model describing the dominating effect of thermal softening is consistent with the observed first stage of localisation, whereas the second stage of localisation is related to shear fracture by microvoid nucleation and growth which can be modelled by considering the dominating effects of geometrical softening. This will be discussed in another section.

2.3. Temperature in Metal Cutting

Plastic deformation at low strain rates may be treated as an isothermal process. However, high-strain-rate deformation encountered in metal cutting is often adiabatic, and the deformation work is transformed into heat with the attendant temperature increase of the shear zones. The temperature can have a profound effect on the mechanical response of the material because of thermal softening which may lead to shear localisation. In metals many of the dislocation mechanisms of plastic deformation are thermally activated and are governed by Arrhenius-type activation equations. Therefore, any variation in temperature will change the rate at which deformation will occur.

Increasing the temperature has the same effect on the flow stress as decreasing the applied strain rate i.e. the level of the stress-strain curve is decreased and the fracture strain is increased. Zener and Hollomon [1] proposed the parameter, known as the Zener-Hollomon parameter given in equation 2.8 which is a form of temperature corrected strain rate. McGregor and Fisher [76] used an alternative

approach which they called the velocity modified temperature given in equation 2.10. The velocity modified temperature approach has been used successfully by Oxley and co-workers [64]. The temperature rise associated with plastic deformation can be directly obtained from the constitutive equation by considering that a fraction of plastic deformation energy β is converted into heat. Following the experiment work of Manson et al [140] the fraction of plastic deformation energy converted into heat β is about 0.9 (this implies that 10% of the work of deformation is stored in the material as defects) for 2024 Al and 4340 steel. For Ti-6Al-4V alloy a drop from 1 to 0.6 occurs as the strain is increased from 0.05 to 0.2. It has been suggested [2] that the low fraction occurs in cases where dislocations are not the primary carriers of plastic strain. Twinning and martensitic phase transformations are proposed as possible contributory factors. Thus the temperature rise can be expressed as:

$$\Delta T = \frac{\beta}{\rho c} \int_0^{\epsilon_f} \sigma \, d\epsilon \qquad (2.54)$$

where ρ is the density, C is the specific heat ϵ_f in the final strain and σ is the flow stress. The constitutive relation for σ (i.e. relations expressed in equation 2.14 or 2.18) can be substituted into the above equation which can be evaluated numerically or otherwise to obtain the temperature rise.

In addition to affecting the chip formation process, the role of temperature in metal cutting is to promote dissolution wear of the tool at high cutting speeds (52,141-142). For this reason determination of the tool-chip interface temperature has been one of the major subjects for research in metal cutting. Experimental methods used to measure the tool-chip interface temperature include: (1) Tool-Workpiece thermocouple method [143], (2) Inserted thermocouple], (3) Radiation method [145-146] and (4) Changes in hardness and microstructure due to material transformations [147]. The use of these methods has demonstrated that the equilibrium values of temperature are reached almost

instantaneously after the start of the cut and that the maximum temperature occurs on the rake face of the tool some distance away from the cutting edge of the tool. Typical temperature distributions obtained by using the method of microstructural changes are shown in Fig. 2.16 for cast irons and 2.17 for steels. As shown the maximum temperature occurs close to the cutting edge of the tool during the machining of ductile iron. The high temperature gradients usually encountered near the tool-chip interface render all of these methods grossly inaccurate. An alternative has been the estimation of the temperature analytically using measured cutting parameters.

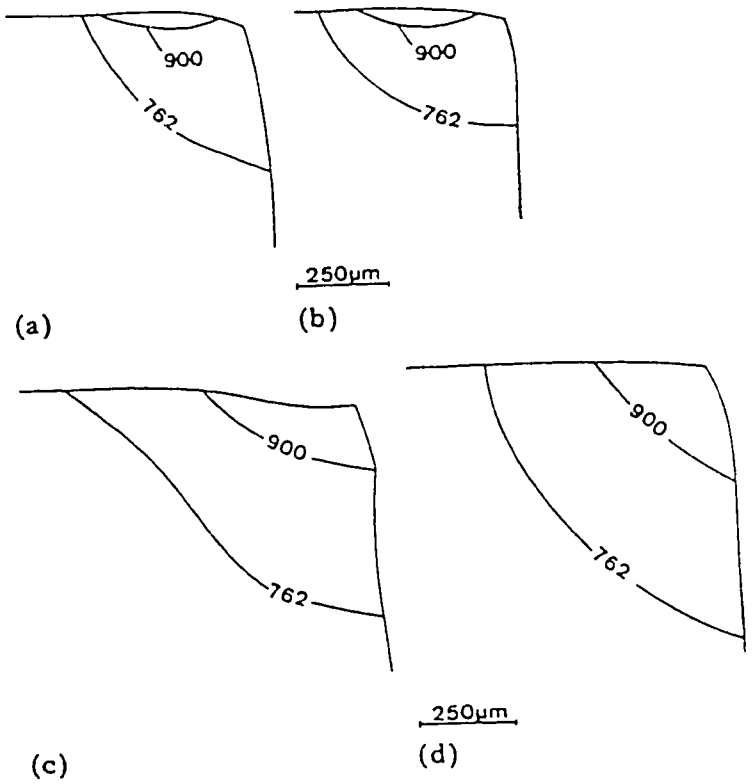

Fig. 2.16: Temperature maps (in °C) derived from iron-bonded carbide tools used at 200 m/min: (a) uncoated carbide used on gray cast iron, (b) TiN-coated carbide used on gray cast iron, (c) uncoated carbide used on ductile iron, (d) TiN-coated carbide used on ductile iron. (After Dearnley [147].

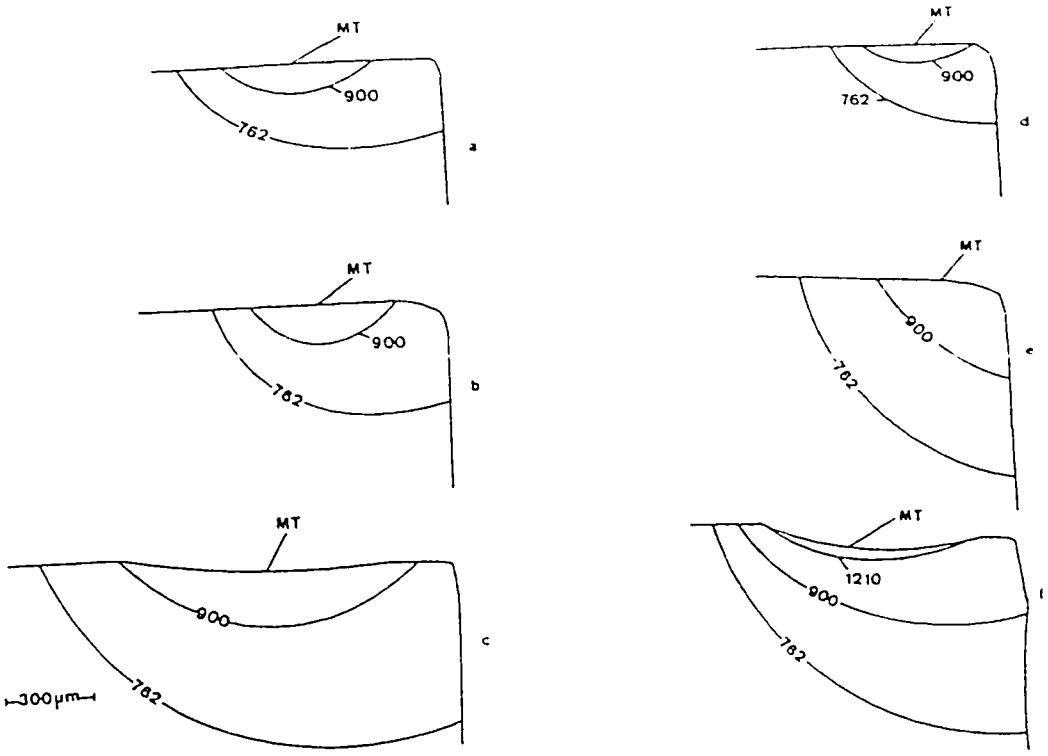

Fig. 2.17: Temperature maps (in °C) derived from iron-bonded carbide tools: (a) and (b) TiN-coated carbide used to cut AISI 1042 steel at 180 and 240 m/min. Respectively for 30 s.,(c) uncoated carbide used to cut AISI 1042 steel at 240 m/min. for 30 s., (d) and (e) TiN-coated carbide used to cut AISI 4340 steel at 180 and 240 m/min. Respectively for 10 s., (f) uncoated carbide used to cut AISI 4340 steel at 240 m/min. for 10 s. (After Dearnley [147].

Attempts to determine cutting temperatures analytically are reported by Chao and Trigger [148], Loewan and Shaw [75], Boothroyd [145] and Tay et al [149] and others. Under conditions of flow chip formation the estimation of the tool-chip interface temperature is defined as the problem of solving the Fourier's heat conduction equation for the tool-chip interface. For orthogonal cutting the two-dimensional steady state energy equation is written as:

$$\rho c[u\frac{\partial T}{\partial x} + v\frac{\partial T}{\partial y}] - \lambda[\frac{\partial^2 T}{\partial x^2} + \frac{\partial^2 T}{\partial y^2}] - Q = 0 \qquad (2.55)$$

where ρ, c, λ, T are the density, specific heat, thermal conductivity and temperature respectively; Q

is the rate of heat generation per unit volume; x and y are the Cartesian coordinates, and u and v are the velocity components in the x and y directions. Since deformation first occurs at the primary shear zone and then at the secondary shear zone, the analysis involves partitioning of heat and solution for temperature rise at the primary shear zone and then the partitioning of heat and solution for temperature at the secondary shear zone. By using the procedure of Block's partition principle Loewan and Shaw [75] arrived at expressions for the fraction of heat taken by the chip at the primary and secondary shear zone. The expressions predict an increase of the fraction of heat taken by the chip with increase of cutting speed. The authors obtained expressions for the average temperature at the primary shear zone and the tool-chip interface. The analytical expression for the tool-chip interface temperature can be simplified as:

$$T_s - T_o = \frac{\tau_{sp}}{J}\sqrt{\frac{V_C\, t_1\, \overline{\gamma}}{\rho_2\, C_2\, \lambda_2}}\left\{A\, f(T,\gamma\ \dot{\gamma}) + B\right\} \qquad (2.56)$$

where T_s is the interface temperature, τ_{sp} mean shear stress at the shear plane A,B are essentially constants, ρ_2,C_2,λ_2 are the workpiece density, specific heat and thermal conductivity respectively at the interface temperature. Equation 2.56 shows that the temperature increases with increase of cutting speed and feed and is dependent on the workpiece material properties. The variation of flow stress as affected by temperature and compressive stress at the tool-chip interface is not accounted for in this model.

Chao and Trigger [148] used a numerical method to calculate the temperature distribution along the length of the contact zone. The method assumes friction contact at the tool-chip interface which cannot be applied to high speed machining where the conditions of seizure prevail. Boothroyd [145] obtained an empirical expression for the maximum interface temperature from a compilation of experimental data for steel. Tay et al [149] used the finite element method to evaluate the

temperature distributions in the workpiece, chip and tool during orthogonal cutting using experimentally determined flow fields and cutting forces. The analysis assumes that the shear stress at the tool-chip interface (which depends on the strength of the material) is constant while in fact it varies along the contact length due to variation of the chip material flow stress and the compressive stress. A more accurate approach in the analysis is to consider the effect of frictional conditions and temperature rise on the flow stress and the temperature dependence of thermo-physical properties of the workpiece material.

In the present work the variation of flow stress with temperature is considered in a finite element analysis for the prediction of tool-chip interface temperature distribution.

2.4. Micromechanisms of Tool Wear

The major tool wear micro mechanisms may be broadly classified as physical and chemical: the physical wear processes that operate during metal cutting include chipping wear, abrasive wear, adhesive (or attrition) wear, plastic deformation (delamination and ploughing); the chemical wear processes involve oxidation wear, corrosion wear and dissolution wear. The review of these wear mechanisms has been the subject of many authors notably Suh [6], Trent [48]. It is now well known that each of these wear mechanism can operate as the dominant tool wear mechanism under specific cutting conditions.

At low cutting speeds (< 100 m/min in AISI 1020 steel and ferritic ductile iron) abrasive wear dominates when the conditions at the tool-chip interface are essentially sliding. When weak adhesion occurs between the tool and the workpiece, adhesive wear occurs by the mechanical removal of tool material when the adhesive junctions are broken as the chip flows over the tool. Trent [48] referred to this wear mechanism as "attrition wear". At moderate and higher cutting speeds the adhesion between the tool and the chip increases with the cutting speed until seizure occurs at the tool-chip

interface when the real area of contact approaches the apparent area of contact. Once seizure has occurred, intense shear localisation can occur, leading to thermoplastic shear deformation of a thin layer of the chip material adjacent to the tool-chip interface. It is now accepted that many features of the metal cutting operation are strongly influenced by this thin layer known as the secondary shear zone or flow zone [52]. Intense shear localisation and deformation in the secondary shear zone raises the temperature of the tool-chip interface. For instance, when machining steel at moderate cutting speeds (100 - 200 m/min) temperatures in the range of 1000^{0}C can be achieved at the tool-chip interface. In addition when the thermal diffusivity of the workpiece is low, the plastic heat generated from the deforming workpiece is concentrated at the tool tip. Under this conditions, the yield strength of the tool material may be lowered sufficiently to permit plastic deformation [150]. Experimental observations suggest that plastic deformation causes failure in carbide tools, ceramic tools and coated tools subsequent to chemical wear. The second and most important wear mechanism emerging from the occurrence of seizure and its attendant thermoplastic shear localisation is chemical instability wear. Chemical instability wear could occur by dissolution, corrosion or oxidation depending on the tool and workpiece combination and the nature of the cutting process i.e. whether the cutting is continuous or interrupted. When seizure occurs under continuous cutting conditions, for example, as in the majority of turning operations dissolution wear is the dominant wear mechanism at moderate and high cutting speeds. This form of wear is characterized by rapid cratering at the rake face of the tool which, upon weakening of the cutting edge, leads to catastrophic failure of the tool by plastic deformation or chipping of the cutting edge. Different views have been held regarding the mechanism of transport in dissolution wear. The diffusional model proposed by Trent [46,48] relies on a diffusional flux of the dissolved tool constituent and the existence of a concentration gradient of the tool constituent atoms from the interface into the body of the chip. The convective flow model proposed by Kramer [142] assumed dissolved tool constituents to be transported by a convective flow of material, next to

the tool-chip interface, into the chip. Experimental evidence for a diffusional mechanism has since been published [151]. The concentration depth profiles for tungsten and cobalt obtained from SIMS analysis of the tool-chip interface show a diffusion profile thus providing the evidence for a diffusional mechanism of transport. However, quantitative analysis of diffusional transport at the tool-chip interface suggests that enhanced diffusion ought to operate to reconcile with the experimentally measured values of tungsten.

Details of the model based on diffusion transport have been described [3]. The model is a refinement of Bhattacharyya's [152] model of diffusion wear to improve on the determination of interfacial concentration (which is based on the workpiece material microstructural transformation), and the influence of plastic deformation on diffusivity. Average interface temperatures obtained from Boothroyd's [145] model were used in the numerical calculation of dissolution wear. Even though the temperature estimated from Boothroyd's model is exaggerated the measured dissolution wear was much higher than the predicted wear suggesting that the lattice diffusion coefficient was enhanced by about two orders of magnitude.

2.4.1 The Effect of Phase Transformation on Tool Crater Wear

The importance of adiabatic shear banding in metal cutting was first noted by Recht [73] who attributed a localised rise of the shear zone temperature to adiabatic shearing. Since Recht's pioneering work of adiabatic shear in the primary shear zone, little has been done to extend the work to analyse the role of adiabatic shear bands at the secondary shear zone. This is because the chip-tool contact phenomenon was treated as a case of sliding friction. However, at high speeds of cutting, it has been reckoned that seizure conditions prevail at the tool-chip interface [52]. Under these conditions, the chip can undergo localised deformation characterised by deformed shear bands away from the interface and transformed shear bands close to the interface or deformed shear bands in the whole

section if the speed does not exceed the critical speed for the formation of transformed shear bands. Timothy [102] has reviewed the nature and occurrence of transformed shear bands and concluded that the initiation and propagation of adiabatic shear bands is favoured by predominantly compressive loading conditions. The high temperature and high compressive stress state of the secondary shear zone promotes the formation of high temperature high pressure phases. Timothy suggested that modification of the initial microstructure within the brief time-scale of events (typically micro-seconds) may be achieved by rapid diffusion of various atomic species at elevated temperature, possible phase transformations and enhanced dissolution of phases resulting from the localised shear deformation itself. If phase transformation occurs martensitically the product has a high dislocation density which is capable of enhancing diffusion by dislocation pipe diffusion. Dislocation pipe diffusion is reckoned to be about five orders of magnitude higher than lattice diffusion [153,154]. Thus enhanced dissolution and diffusion in the resulting transformed shear band at the secondary shear zone can lead to a high wear rate of the tool by a diffusion mechanism. These observations are drawn from the quantitative investigations on tool crater wear carried out by Ingle [3]. During the machining of AISI 1045 steel diffusion wear of a cemented carbide tool (K11) did not take place at cutting speeds of 25, 50 and 100 m/min. At these speeds, there was no modification of the microstructure in the underside of the chip. Dissolution wear of the K11 tool was detected at 150 m/min and increased with cutting speed. At 240 m/min, modification of the microstructure occurred in a region of the shear band less than 5 μm thickness closest to the tool-chip interface and a deformed shear band farther away from the tool-chip interface formed the remaining 7 μm of the total thickness of the shear bands. The modification of the microstructure in the shear band correlate with the enhanced dissolution wear of the tool. An experimental program was designed in the present work to study the role of phase transformation in enhancing diffusion wear of the tool and in the formation of segmented chips during high speed machining.

CHAPTER 3

EXPERIMENTAL PROCEDURES

3.1 Tool Materials

Most of the cutting experiments were conducted using Kennametal grade of uncoated cemented carbide tool (grade K1). Tool wear testing was carried out using the uncoated carbide tool, TiN/TiC multi layer cemented carbide coated tool (KC 250), HfN coated K1 tool, and TiN/TiC based cermet tool (KT 125). The nominal compositions of the tools are given in Table 3.1 [155]. The tool geometry was a triangular insert (Kennametal TPG 432) with nose radius of 0.794 mm (1/32 in) and clearance angle of 11°.

Table 3.1: Constitution of tools [155].

Type of tool	Coating	Coating thickness (um)	Nominal composition of the uncoated and substrate for the coated cemented carbide (Wt%)		
			WC	Co	Ta(Nb)C
Uncoated (K-1)	NA	NA	85	11	4
Coated (KC250)	TiN TiC	1-2 5-8	85	11	4
Coated (HfN)	HfN	5-8	11	11	4
Cermet (KT125)	NA	NA	Approx. 15% TiN, 55% TiC and 30% (W,Ta,Nb)C & Co		

3.2. Workpiece Materials

The choice of workpiece materials was based on the matrix microstructure and thermal

softening sensitivity during high strain rate deformation involving rapid heating and cooling. These factors influence chip morphologies and the corresponding tool wear mechanisms.

3.2.1 Workpiece Materials for Tribology, Chip Morphology and Tool Wear Investigations

An AISI 1045 steel was used to investigate the tribological condition at the tool-chip interface. The material was found useful for this purpose because its flow stress as a function of testing temperature is available in the literature. Some aspects of the tribological condition at the tool-chip interface were also investigated with AISI 1080 steel, which was also used to investigate the effect of phase transformation on tool crater wear. The microstructures of these workpiece materials are shown in Figs 3.1 and 3.2 and their compositions are given in Table 3.2. AISI 1020 steel was selected for investigation of the mechanism of tool wear and the role of phase transformation in tool crater wear under flow chip morphology. Fig. 3.3 shows the microstructure of the AISI 1020 steel used for the cutting experiments. A ferritic ductile iron with a matrix microstructure similar to that of AISI 1020 steel, but having a dispersion of graphite nodules was used in the cutting experiments. The microstructure is shown in the optical micrograph in Fig. 3.4. It was possible to investigate the effect of dispersing soft second phase particles in the matrix on the chip morphology and tool wear using ferritic ductile iron. Ductile iron has a lower thermal diffusivity than AISI 1020 steel. The effect of a low thermal diffusivity and phase transformation on tool wear is discussed in section 5.4.3. The role of second phase particles (graphite) in shear localisation is discussed in section 5.7.3. The compositions of these workpieces are given in Table 3.2.

3.2.2. Iron-Nickel-Carbon (Fe-Ni-C) Alloys

Iron-Nickel-Carbon alloys were selected for an experimental programme designed to investigate the role of phase transformation in thermoplastic shear localisation and tool wear. Four

Iron-Nickel-Carbon alloys with 0.1wt%C and varying nickel content ranging from 1.4 wt%Ni to 28.86wt%Ni were chosen as suitable specimens for this study. By varying the nickel content in this range the martensite-austenite transformation temperature was varied from 400- 760^{0}C. The alloys were made from electrolytic iron and nickel under the controlled atmosphere of argon. The phase transformation temperatures for Fe-Ni and Fe-Ni-C alloys as well as the effect of deformation and pressure are well documented [156-160]. The chemical compositions and phase transformation temperatures for the alloys are given in Table 3.3(a) and 3.3(b) respectively. The calculation of the phase transformation temperature for the Fe-Ni-C alloys is based on the work of Kaufman and Cohen [156], Rao, Russell and Winchell [157] and Kaufman, Leyenaar and Harvey [159] as detailed in Appendix A. The microstructural change accompanying phase transformation was used to map the temperature distribution. Since the alloys soften with temperature rise, the critical speed for segmentation of the chip was low and hence the chip morphology could be varied over a moderate range of cutting speeds. The effect of shear localisation in the primary shear zone on the chip morphology, temperature distribution and the location of the crater wear could be investigated.

Table 3.2: Chemical composition of workpieces (wt%)

Element	Ductile iron	AISI 1020 Steel	AISI 1045 Steel	AISI 1080 Steel
C	3.60	0.17	0.44	0.81
Mn	0.23	1.21	0.71	0.84
Mo	0.001	0.08	0.05	
Si	2.43	0.22	0.25	0.24
Cr	0.01	0.18	0.15	
Ni	0.01	0.15	0.14	
S	0.01	0.001	0.017	0.004
P	0.10	0.014	0.008	0.016
Mg	0.04			

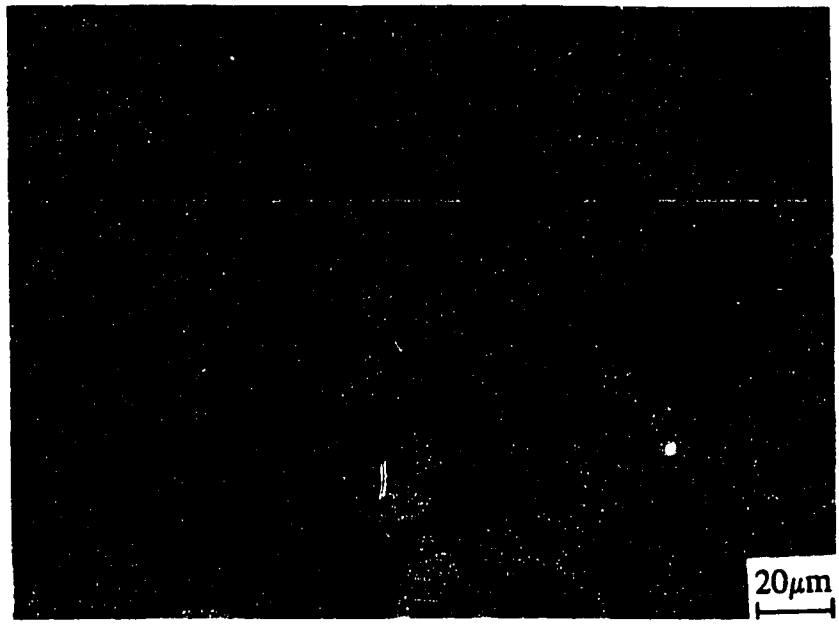

Fig. 3.1: Optical photograph showing the microstructure of AISI 1045 steel workpiece (Etched in 2% Nital).

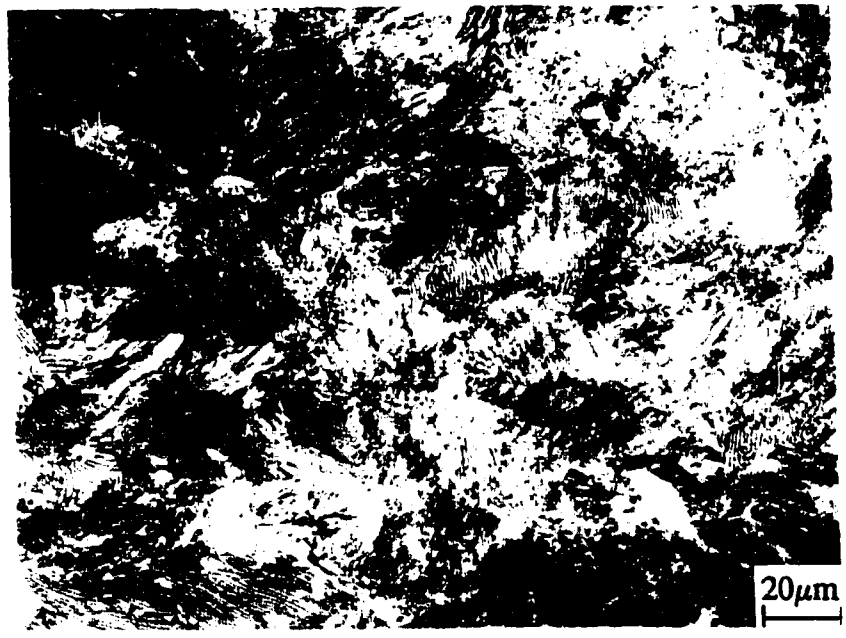

Fig. 3.2: Optical photograph showing the microstructure of AISI 1080 steel workpiece (Etched in 4% picric acid).

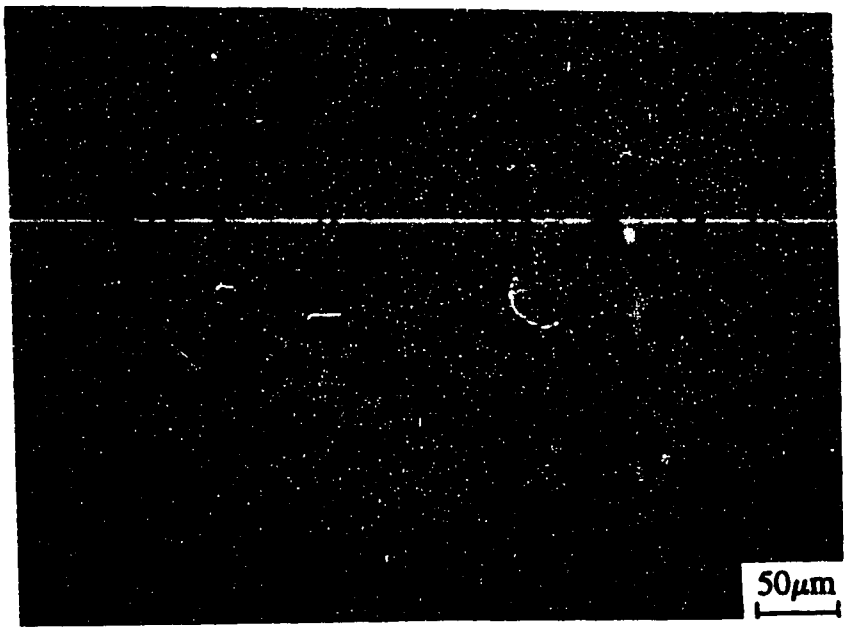

Fig. 3.3: Optical photograph showing the microstructure of AISI 1020 steel workpiece (Etched in 2% Nital).

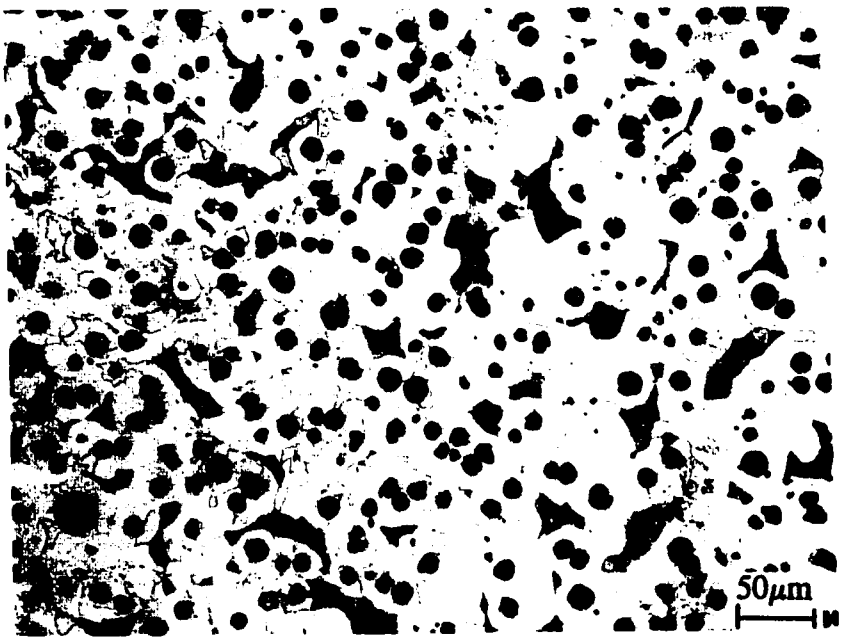

Fig. 3.4: Optical photograph showing the microstructure of ferritic ductile iron workpiece (Etched in 2% Nital).

Table 3.3(a): Chemical composition of Fe-Ni-C alloys.

Sample Number	Chemical composition (wt%)		
	Ni	C	Al
367	1.4	0.090	0.037
368	9.7	0.104	0.100
369	18.9	0.105	0.038
370	28.9	0.100	0.036

Table 3.3(b): Phase transformation temperatures and microstructural constituents of the quenched Fe-Ni-C alloys.

Sample Number	Estimated phase transformation temperature		Microstructural constituents of quenched alloy
	Ms (^{0}C)	As (^{0}C)	
367	476	760	Ferrite + Pearlite + Martensite
368	324	620	Martensitic + some bainite
369	205	530	Martensitic
370	-40	400	Martensitic

3.2.3 Heat Treatment of Fe-Ni-C Alloys

All Fe-Ni-C alloys were heat treated to obtain martensitic structures at room temperature before performing the cutting tests. The Fe-28.9%Ni-0.1%C and Fe-18.9%Ni-0.1%C alloys were homogenised in a helium atmosphere at 1000^{0}C for twenty four hours and then furnace cooled. The microstructure of the furnace cooled (annealed) Fe-28.9%Ni-0.1%C alloy is austenitic (Fig. 3.5). In order to induce a martensitic structure, the alloys were quenched below the Ms temperature in liquid nitrogen (-195^{0}C) and held for 168 hours for transformation to martensite to take place. On warming to room temperature the martensitic microstructure is retained. Figs. 3.6 and 3.7 show the microstructure of the martensitic Fe-28.9%Ni-0.1%C and Fe-18.9Ni%-0.1%C alloys respectively.

The Fe-9.7Ni-0.1C and Fe-1.4Ni-0.1C alloys were heated to 1000 ^{0}C at 100 ^{0}C/hour under an argon atmosphere, held at 1000^{0}C for for six hours and then quenched from 1000^{0}C into brine (9% NaCl in water) to obtain martensitic structures. The microstructures of the as-quenched 9.7wt%Ni and 1.4wt%Ni alloys are shown in Figs 3.8 and 3.9 respectively. The effect eliminating phase transformation by annealing heat treatment on the critical speed for chip segmentation was investigated by performing cutting experiment on austenitic Fe-28.9wt%Ni-0.1wt%C alloy under the same cutting conditions used for the martensitic alloy. The effect of phase transformation temperature on the critical cutting speed for chip segmentation was investigated by keeping all other cutting variables constant and cutting martensitic Fe-Ni-C alloys with different nickel content.

3.3. Cutting Experiments

The cutting experiments involved turning of round bars on a continuous speed MAZAK lathe. The cutting was performed dry (without use of cutting fluids) under the following cutting conditions:

Cutting speed: (a) varied from 1 to 500 m/min for Fe-Ni-C alloys, AISI 1045 steel and AISI 1080 steel.

(b) varied from 100 to 350 m/min for AISI 1020 steel and ferritic ductile iron.

Feed rate: 0.259 mm/rev.

Depth of cut: 2.0 mm

Rake angle: positive 5^{0}

Cutting time: varied from 1 to 30 seconds

Orthogonal cutting is achieved when (1) the cutting edge of the tool is straight and perpendicular to the cutting velocity vector, (2) the depth of cut is at least five times the feed.

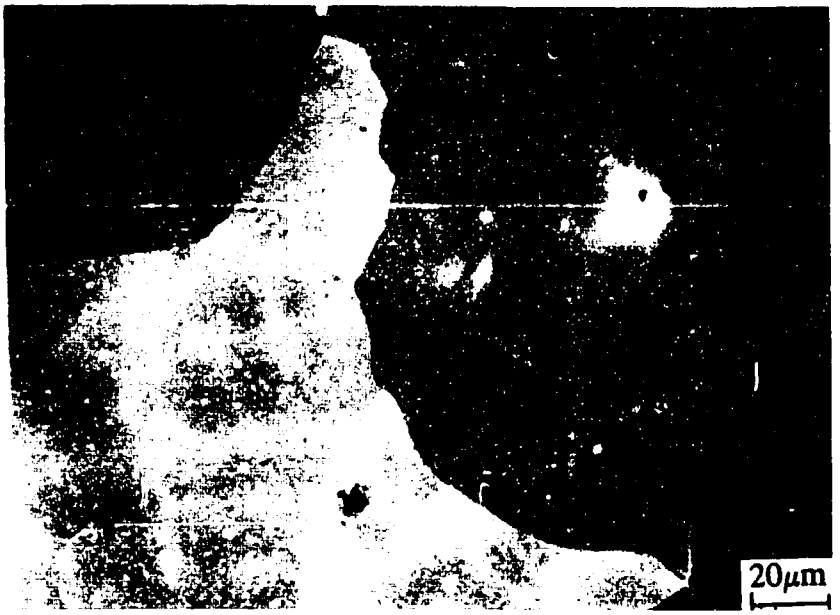

Fig. 3.5: Optical micrograph showing the microstructure of austenite in annealed Fe-28.9%Ni-0.10%C alloy before machining.

Fig. 3.6: Optical micrograph showing the microstructure of martensite in quenched Fe-28.9%Ni-0.10%C alloy before machining.

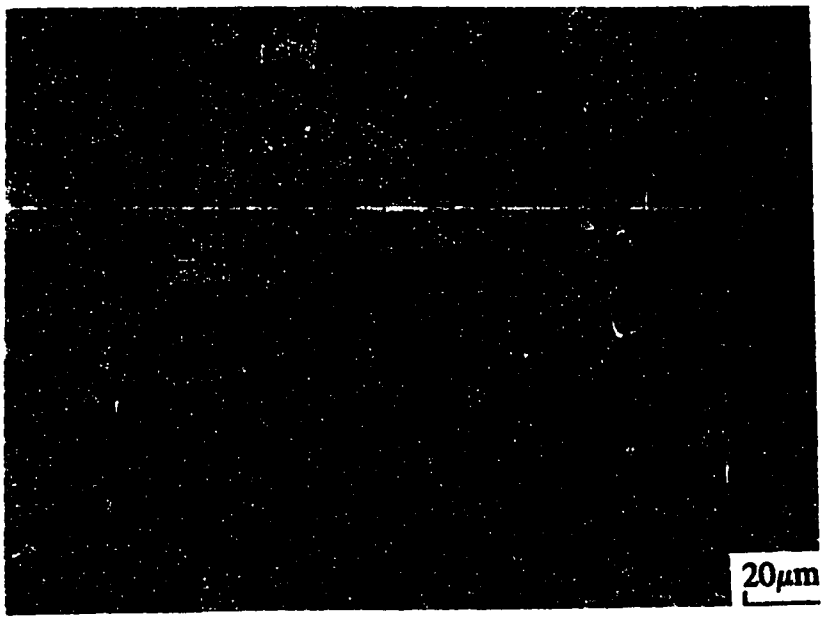

Fig. 3.7: Optical micrograph showing the microstructure of martensite in quenched Fe-18.9%Ni-0.10%C alloy before machining.

Fig. 3.8: Optical micrograph showing the microstructure of quenched Fe-9.7%Ni-0.10%C alloy before machining, with evidence of martensite and bainite.

Fig. 3.9: Optical micrograph showing the microstructure of quenched Fe-1.4%Ni-0.10%C alloy before machining, with evidence of ferrite, pearlite and islands of martensite.

Under orthogonal cutting conditions the chip forming process is two dimensional (i.e. the chip is produced under plane strain) and the chip flows up the tool face in a direction perpendicular to the cutting edge. This implies that there is no spread of material parallel to the cutting edge and the width of the chip is equal to the depth of cut. Under the conditions of plane strain there are only two forces (the cutting force Fz and the feed force Fx) and Merchant's model [60] is applicable in calculating the stresses acting at the primary and secondary shear zone. The depth of cut used was approximately seven times the feed and a straight cutting edge was used and kept perpendicular to the cutting velocity vector. Thus as a first approximation orthogonal cutting is assumed in the process.

3.3.1 On-line Measurement of Cutting Forces

Even though efforts were made to ensure orthogonal cutting conditions , the finite nose radius of the tool of 0.794 mm representing about 40% of the depth of cut made the cutting semi-orthogonal.

Consequently a third component of force , the radial force, was included in the force measurement. The three components of cutting forces exerted on the tool during a semi-orthogonal cutting process are shown in Fig. 3.10. In order to apply Merchant's model [60] for calculating the stresses from measured forces the radial force Fy and the feed force Fx were resolved to give a resultant force F_t which is perpendicular to the cutting force Fz. The calculation of stresses from cutting forces is presented in Appendix B. The most widely used dynamometers for measurement of forces during turning processes employ transducing elements which convert mechanical deformation into electrical signals which are then digitized through computer interfacing. The details regarding the construction of various types of dynamometers have been discussed by Bhattacharyya [152].

On-line measurement of cutting forces was accomplished by the use of a 3-component piezo-electric transducer type dynamometer. The dynamometer was developed in McMaster by Lai [161]. In piezo-electric crystals the centres of the positive and negative charges are not located at the centre of the unit cell of the crystal lattice. For this reason they possess a permanent electric dipole. An externally applied force causes displacement of the ions to take place. This leads to a change in length of the electric dipole. The dynamometer design is such that the cutting forces subject the piezo-electric crystal to compression loading, which causes an excess charge density on the ends of the quartz crystal. The piezo-electric crystal (transducer) of the dynamometer responds in proportion to the components of force, Fx in the feed direction, Fz in the tool face and Fy in the radial direction of the workpiece with induced charges which are picked up by electrodes and fed into charge amplifiers. The amplified output is fed to an Analog to Digital Converter (ADC) through a low pass filter that smooth the signal. A data acquisition frequency of 100 HZ was used. This is four times the maximum frequency of the machine tool (25 HZ when operated at the maximum speed of about 1600 rpm). Data acquisition was accomplished using the GLOBAL LAB software. Using this set up, it was possible to measure the three components of forces in semi-orthogonal cutting to an accuracy of ±10 newton.

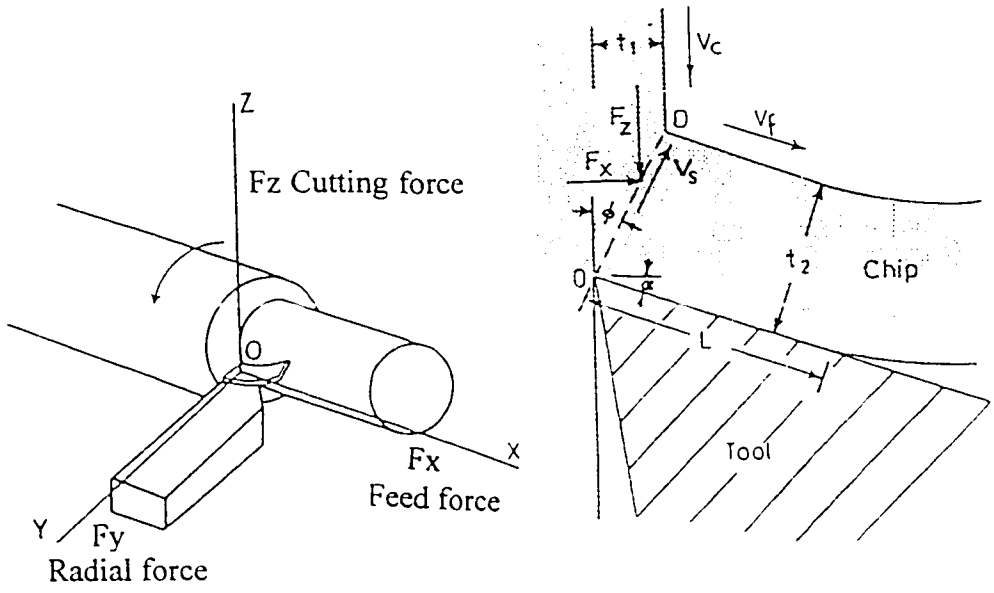

Fig. 3.10: Components of cutting forces acting on the tool in semi-orthogonal cutting.

3.3.2. Tool-Chip Interface Temperature Using Ultrasonic Technique

An ultrasonic method developed by N.D.Patel and M.A.Elbastawi [162] was used to measure the average tool-chip interface temperature. The ultrasonic sensor film having a 70-100 MHZ frequency range was deposited on a cemented carbide tool (K1) using a CVD process. Measurement of temperature is achieved through the dependence of the ultrasonic transit time on temperature. The experimental procedure involves the use of a modified tool holder with a 50 ohm coaxial wire connected to a copper wire of 2 mm diameter to excite the high frequency piezo-electric film deposited on the carbide tool face (opposite to the cutting face). A 100 MHZ ultrasonic system was used to generate the high frequency signal with beam diameter of 2 mm (sensor size 2 mm) in the carbide tool. The on-line information of transit time (100 Pico-second) and amplitude is displayed on a computer interfaced with the ultrasonic system as cutting progress. The transit time as a function of temperature was calibrated using a standard heat source. An accuracy of ± 25^{0}C was achieved with the carbide tool

and a 100 MHZ ultrasonic process control system model FU-1100.

3.3.3 Chip Thickness and Shear Plane Angle

The thickness of the chips was measured using a point-to-point micrometer gauge. For each measurement an average of ten readings was taken. Then the shear plane angle was calculated from Merchant's [60] shear plane model as:

$$\tan \phi = \frac{r \cos \alpha}{1 - r \sin \alpha} \qquad (3.1)$$

where ϕ is the shear plane angle, r is the chip thickness ratio and α is the rake angle.

3.4 Optical and Scanning Electron Microscopy (SEM) of Chips and Tools

The chips were mounted and polished so as to show details of the microstructure in the sections parallel to the chip flow direction. The etchant used was 2% nital for most of the alloys, except for the high nickel alloys that were etched in a mixture containing equal parts by volume of reagent grade (68-70 %) nitric acid, reagent grade (36.5-38%) hydrochloric acid and water. The chips were polished and etched, and examined under the optical microscope and scanning electron microscope (SEM). The fracture surfaces of the chips were examined on the SEM. The tool wear was characterised using optical and scanning electron microscopes.

3.4.1 Measurement of Contact Length

The tool-chip contact lengths were determined by taking a photograph of the contact area on the rake face of the tool with an optical microscope at low magnification (50X). The average of ten readings, from different locations, of the length from the cutting edge to the point where the chip

leaves intimate contact with the tool was taken as the contact length. Fig. 3.11 shows a typical optical photograph of the cutting edge of a cemented carbide tool grade K1 used to machine AISI 1020 steel at 300 m/min for 20 seconds.

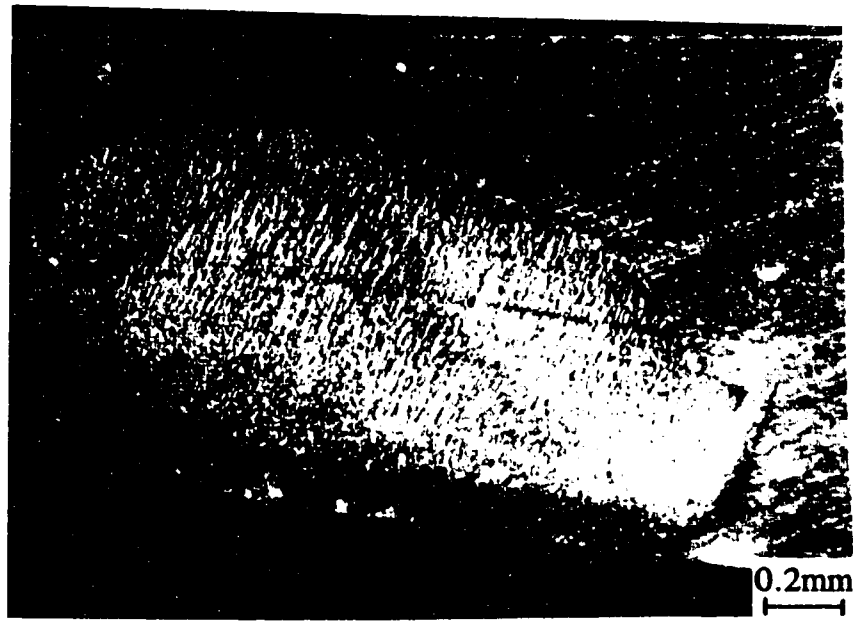

Fig. 3.11: Typical optical photograph of the cutting edge of a cemented carbide tool used to machine AISI 1020 steel for 20 seconds.

3.4.2 Measurement of Shear Band Thickness

The secondary shear zone in both steel and ductile iron was found to exhibit shear bands at the bottom of the chip. The thickness of the zone was delineated as the distance from the bottom face of the chip to the point where the lines of maximum grain elongation start curving upwards, see Fig. 3.12. The Fe-Ni-C alloys exhibited the so-called white etching (transformed) bands that are easily delineated in an optical micrograph. The thickness of the shear bands was measured directly from the optical micrographs.

Fig. 3.12: An optical micrograph taken from a section parallel to the chip flow direction of an AISI 1045 chip, showing the typical dimensions of the secondary shear zone from which the thickness is measured.

3.4.3 Vickers Microhardness Measurement

The thickness of the shear bands formed in the Fe-Ni-C alloys ranged from 30 to 50 μm. Therefore the load used for the hardness measurements was selected such that the indentations were smaller than the shear band thickness. The Vickers microhardness tests were conducted using 50g weight. The hardness was measured at the centre of the shear bands. Since the microstructural evolution in the shear band would depend on the temperature gradients within the shear band, the hardness values obtained from the measurements are interpreted as average values. The tests were carried out on polished specimens cut from the Fe-Ni-C workpieces and on polished sections of the chips obtained from machining. Micro-hardness measurements on the chips were carried out on the primary shear band, A, the chip body, B, and the secondary shear band, C, shown in Fig. 3.13.

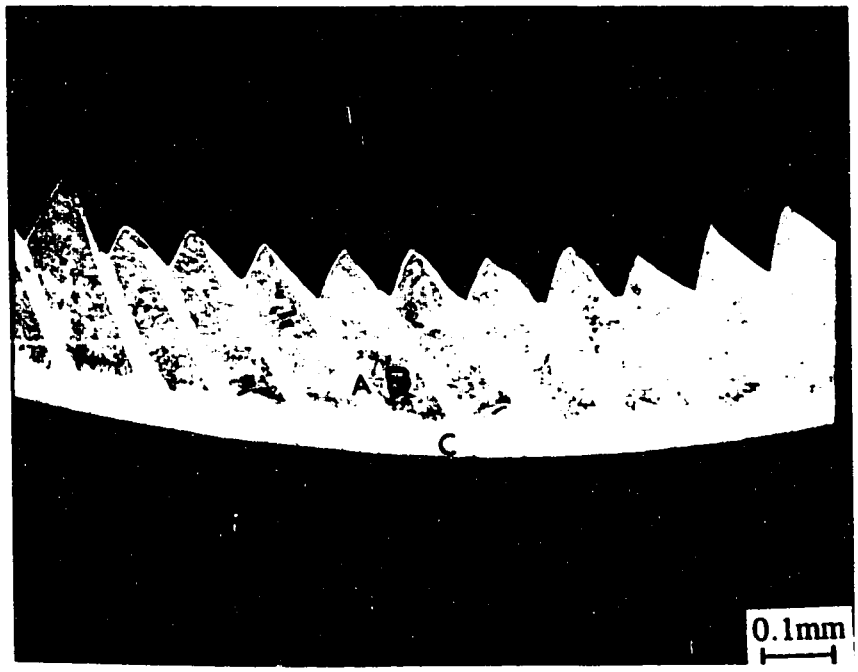

Fig. 3.13: Optical photograph showing the microstructure of an Fe-28.9Ni-C alloy chip obtained at a cutting speed of 400 m/min. The regions at the primary and secondary shear bands and the chip body where the micro-hardness tests were made are indicated as A, C and B respectively.

3.5 Quantification of Tool Wear

Concentrations of the tool material in the chip resulting from wear are very low i.e. in parts per million (ppm). Therefore limit of detection required is in ppm by weight and the precision needed for the concentration of the elements of the tool material (W, Co, Ti, Hf) present in the chip material is ±0.1 ppm by weight. Therefore the technique to be used must be sensitive to very small changes in concentration. Several techniques are available for multi-elemental or single element analysis including Instrumental Neutron Activation Analysis (INAA), Inductively Coupled Plasma Mass Spectrometry (ICP-MS), X-ray Fluorescence Spectrometry (XRF), Atomic Emission Spectroscopy and Graphite Furnace Atomic Absorption Spectrometry (GF-AAS). Each of the techniques has its own limitations on the range of elements which can be determined in an iron matrix and also on the concentration levels at which minute concentrations of the elements can be determined. Emission

spectroscopy is limited to general composition determination and cannot be used for analysis of the minute elemental concentrations encountered in tool wear. XRF has its sensitivity limited to 50 ppm which renders it unsuitable for the present application. The two techniques INAA and ICP-MS have reasonably high sensitivities for the present analysis and their application is discussed below.

3.5.1 Instrumental Neutron Activation Analysis (INAA)Technique

The technique of INAA is well established. Successful application of this technique in the analysis of minute concentrations of tungsten and cobalt dissolved in the chips during the wear of cemented carbide tools has been reported [3.151]. Detailed account of the principle and instrumentation of INAA used in characterising chemical and physical wear is given by Ingle [3].

Crater wear of cemented carbide tools is measured quantitatively by determining the tungsten and tungsten carbide content of the chips, using instrumental neutron activation analysis. All the chips generated at a given cutting speed for a given time are collected and irradiated in a neutron flux of 10^{12} neutrons/cm^2s. The total amount of tungsten carried into the chips, (tungsten atomically dissolved in the matrix plus tungsten present as tungsten carbide) is determined using standards of known composition. The chips are then dissolved in concentrated hydrochloric acid and filtered through 0.1-0.2 μm filters. The tungsten carbide retained in the undissolved residue is determined by the analysis of the filters using INAA to determine the mechanical wear. The tungsten atomically dissolved in the matrix (i.e. dissolution wear) is taken as the difference between the total tungsten in the chips and the tungsten tied up as tungsten carbide (mechanical wear).

3.5.2 Inductively Coupled Plasma Mass Spectrometry (ICP-MS)

Since INAA is not suitable for analysis of elements with short half-life like titanium, the technique of ICP-MS was developed to enable quantitative analysis of titanium based tools.

Inductively Coupled Plasma Mass spectrometry (ICP-MS) is a new technique for elemental and isotopic analysis which combines the elegance of the ICP for atomizing and ionizing injected samples with the power of sensitivity and selectivity of mass spectrometry. There have been numerous reviews and general studies on ICP-MS, the most complete being those by Douglas and Houk [163], Houk and Thompson [164] and Gray [165]. Date and Gray [166] and Jarvis, Gray and Williams [167] have discussed the range of applications of ICP-MS. The main attractive features offered by ICP-MS are:

1. Detection limits of 10 ng/L or better are obtained, particularly for heavy elements such as rare earths [164,166].
2. Isotope ratios can be determined quickly and routinely by isotope dilution.
3. The mass spectra observed from analyte elements are simple (i.e. primarily M^+ ions), and overlap interferences caused by other species are readily predictable.
4. High sensitivity of the ICP-MS.
5. Sample throughput is high, largely because sample introduction and ionisation occur outside the vacuum chamber. For instance, quantitative determination of 10 elements in one sample would typically take one to three minutes including the rinse cycle.

In metallurgical applications, the use of ICP-MS in the analysis of iron materials has been reported [164,165], however, ICP-MS has not been applied in quantitative investigations.

In the present work ICP-MS was developed for quantitative determination of the minute concentrations of tungsten, hafnium, and titanium dissolved in cast iron and steel chips during high speed machining of the materials with coated and uncoated cemented carbide tools. The technique was used to quantify Ti which could not be accurately quantified by INAA, hence enabling wear of TiN/TiC-coated tools and TiN/TiC cermets to be determined quantitatively for the first time. For the analysis of ductile iron and steel, a detection limit of 100 ng/L (100 pptr) in solution, i.e. 0.1 ppm in the solid, was obtained with 4-7% relative standard deviation (RSD) at 95% confidence for elements

Ti, W and Hf. This detection limit of 0.1 ppm is better than that of INAA (1 ppm with ±0.1 accuracy).

3.5.3 Quantitative Analysis by ICP-MS

The technique of ICP-MS was calibrated using INAA by analysis of identical specimens using both techniques. Table 3.4 shows the comparison of the results obtained by the two techniques on identical specimens, i.e. chips collected at the 20th second during the machining of ductile iron with a cemented carbide tool (K-1). The concentrations of tungsten measured using both techniques agree closely, confirming that ICP-MS is a quantitative tool, even more powerful than INAA for the separation of physical and chemical wear during machining. ICP-MS has lower detection limits and higher sensitivity that INAA, see Table 3.5. The rest of this section is devoted to describing the procedure followed in quantitative analysis of the concentrations of tool material elements transferred into the chips by wear during the cutting process.

Table 3.4: Comparison of the results from ductile iron chips obtained by ICP-MS and INAA

Cutting speed (m/min)	W pick-up from ICP-MS (ppm)	W pick-up from INAA (ppm)
100	2.0±0.2	1.9±0.5
200	3.1±0.3	2.8±0.5
300	7.2±0.4	6.6±0.5

Table 3.5: Comparison of sensitivity and detection limits for ICP-MS and INAA.

Element	Detection limit (ppm)		Precision (ppm)	
	ICP-MS	INAA	ICP-MS	INAA
Tungsten	0.1	1.0	±0.005	±0.1
Hafnium	0.1	0.7	±0.005	±0.1
Titanium	0.1	*	±0.005	*

* Ti could not be analysed with INAA because of its short half-life.

(i) Sample Preparation

The machined chips were collected at the end of the 10th, 20th and 30th second of cut for use in quantitative analysis. The chips were rinsed in acetone to remove any contaminants. Portions of chips from each sample (1000±0.005 mg weighed to the nearest 0.0001 mg) were weighed into clean PTFE bottles and dissolved in 15 mol. sub-boiling nitric acid. The solutions were diluted with deionised water (18 $MQ.cm^{-1}$) to a known weight (1000+0.005 g weighed to the nearest 0.0001 g) i.e. 0.1%. Undissolved material which contained mechanically transferred tool material was filtered off using 0.1 μm filter papers. Two aliquots from each sample were transferred into plastic test tubes. One was spiked with a known amount of W,Hf,Ti standards to a final spike concentration of 2 to 10 ppb. The aliquots were analysed by ICP-MS to obtain quantitative values of concentration of atomically dissolved tungsten in the chips, which is a measure of the dissolution wear. Aqua regia plus hydrofluoric acid mixture was used to prepare the solution from which the total amount of tungsten in the chips was determined. The difference between the total tungsten (crater wear) and the atomically dissolved tungsten in the chips (dissolution wear) gives the amount of mechanical wear. The same procedure for ICP-MS was followed in quantifying wear for TiN/TiC coated tools. The chips were first dissolved in 2.5 mol HCl to obtain a measure of dissolution wear and then aqua regia to obtain the total wear. The difference of these two measurements gave the amount of mechanical wear. Only dissolution wear was quantified for the HfN coated tool because a solvent for HfN was not available.

(ii) Sample Introduction System

The liquid samples are introduced into the ICP by nebulization. The nebulizing gas used is argon. Before the sample is injected into the ICP it is mixed with a rhodium internal standard at a pre-set flow rate. The range of conditions at which the ICP-MS was operated are shown in Table 3.6.

(iii) The Inductively Coupled Plasma

The sample is carried via a laminar flow of argon into the axial channel where atomization and ionization occur. Ionization for most elements is efficient at 7500 K [164]. The ionization conditions are not overly energetic, so relatively few (<10%) doubly charged ions are formed. Thus the mass spectra from the analytes in the ICP show primarily singly charged, monatomic, positive ions.

(iv) Sampling Ions from the ICP.

The ICP operates at atmospheric pressure while the mass spectrometer operates at high vacuum, therefore the ions are extracted into a vacuum system before they are mass analysed. A cooled cone with a sampling orifice in the tip is inserted directly into the ICP, the base of the cone being sealed to the vacuum system. Ions are entrained into the flow of neutral gas through the orifice. The central potion of the jet flows through a skimmer into a high vacuum region where the mean free path is long enough for ions to be collected and transmitted by an ion lens.

(v) Ion focusing, mass analysis, and detection.

The ions are focused and transmitted to the mass analyser by electrostatic ion lenses. The mass analyser is of the quadruple variety. The quadruple rapidly scans a limited mass range of interest and stores the accumulated spectrum in a multichannel analyser. The mass resolved ions leaving the analyser are detected by channeltron electron multipliers capable of counting ion pulses at rates above 10^6 counts/s and have natural background count rates of below 1 count/s.

(vi) Data Handling

Due to the fast scan capability of the quadruple, pulse-counting ion detection is normally used. In order for the data handling system to accept a fast pulse train, normal pulse-counting electronics

is employed. The peak dwell time during each sweep across a mass range of 100 or more peaks may be as little as 100 micro-seconds. The analyser is stepped across the peaks of interest in a repeated cycle, and the accumulated counts for each successive dwell on a peak are added together in the appropriate computer memory location. For any sample 10 peaks are analysed and the average intensity and standard deviation are computer outputs.

3.5.4 Principle of Quantitative Analysis by ICP-MS

The concentration of the analyte element is given by:

$$\frac{C_a}{I_{un}} = \frac{C_{as}}{I_s} \qquad (3.2)$$

where C_a is the concentration of analyte in solution, C_{as} is the concentration of analyte in spike (standard), I_{un} is the intensity of unspiked aliquot, and I_s is the intensity due to spike.

For determination of elemental concentrations, normalisation of analyte ion count to an internal standard is used to correct for the gradual decrease of extraction efficiency of analyte ions caused by progressive solid condensation near the orifice, which remains an operational problem up to now.

3.5.5 Detection Limit of ICP-MS

Analytical calibration curves obtained in an integration mode show a working range covering 2 to 3 orders of magnitude with detection limit of 0.1 ppm in the solid for Ti, W and Hf with 4-7% relative standard deviation (RSD) at 95% confidence. The data were obtained from reference solutions containing only one element.

Table 3.6: The ICP-MS Instrumental Operating Parameters.

Instrument		Perkin Elmer Sciex Elan 250
Nebulisation		
	peristaltic pump	Gilson, uptake rate 1 $mL.min^{-1}$
	nebuliser	Cetac Ultrasonic U5000
Plasma		
	Fassel type torch	
	RF frequency	27 MHZ
	Forward RF power	1.2 kW
	Reflected RF power	0 W
Gas flows		
	Plasma	13 $L.min^{-1}$
	auxiliary	0.5 $L.min^{-1}$
	nebuliser	0.5 $L.min^{-1}$
Cones		
	sampling cone	nickel; 1.1 mm orifice
	skimmer cone	Nickel 0.9 mm orifice
Vacuum pressures		
	expansion	10 - 1 Torr
	intermediate	$2.1x10^{-5}$ Torr
	analyser	$2.1x10^{-5}$ Torr
Scanning conditions		Quantitative mode
	Elemental masses analysed	^{103}Rh (Internal standard) ^{54}Fe ^{184}W ^{59}Co ^{48}Ti ^{178}Hf
Measurements/peak		10 measurements/peak
Total measurement time		1 second
Dwell time		100 millisecond

3.6 Measurement of Crater Depth Profiles

Among the methods available for crater wear measurement, crater depth profile measurement is the only one which gives a more quantitative indication of the extent of crater wear with respect to the position on the cutting tool. On-line measurement of the crater depth profile during the cutting operation without detaching the tool from the tool post is still not possible. Measurement of the crater wear depth profile was carried out after the cutting process using two techniques.

3.6.1 The Talysurf Surface Roughness Tester

The Talysurf roughness tester consists of the surface measuring instrument itself, a measuring stand and a profile recorder. The stylus is mounted on an armature which is pointed at the contact limit of an E-shaped soft iron head. The outer limbs of the head are provided with two induction coils and a small air gap is left between the armature and the outer limbs of the head. A downward movement of the stylus results in a decrease of the air gap of the primary coil and an equal increase of the air gap at the secondary coil. The impendence of the coils vary proportionally to the size of the air gap whose variation is proportional to the displacement of the stylus. The position of the stylus, therefore, controls the modulation of the carrier. This method of carrier modulation enables true graphs of the surface topography to be obtained. A cylindrical skid is provided as a datum and the pick-up unit is moved across the test surface by means of a motor and a gear box. This provides different measuring speeds for recording, indicating the average value or for measuring the root mean square (r.m.s.) values.

A Mitutoyo Surface roughness Tester (Surftest 211 series 178), which utilises the same principle as the Talysurf but gives a digital output reading, was used in the measurement of crater depth profiles. A diamond stylus having a four-sided pyramid shape and a tip radius less that 2.5μm was used. The sensitivity of this tester is 0.05 μm. The crest spacing limit is 5 μm. The metre was set

to measure the parameter R_{max}. This is the largest "single peak-to-valley-height Zi" occurring over the evaluation length (lm), e.g., Z4 in Fig. 3.14. In order to obtain a single peak in the entire contact length (length of crater) on the tool (~1 mm) or depth of cut (width of crater) used (~2 mm), the evaluation length was set at least five times these lengths i.e., 2x5 = 10 mm for the depth of cut of 2 mm. Readings of R_{max} were taken at various positions away from the cutting edge giving a depth profile of the crater.

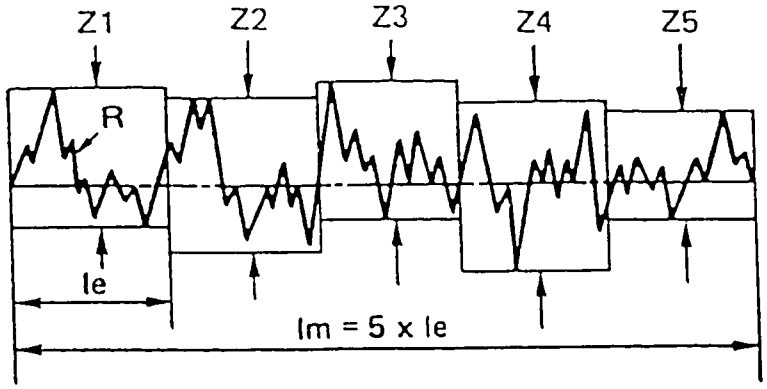

$$Rz = (Z1 + Z2 + Z3 + Z4 + Z5)/5$$
$$Rmax = Zi\ max$$

Fig. 3.14: A schematic illustration of the crater depth profile measurement, by the measurement of R_{max} defined as the largest "single peak-to-valley-height, Z_i" occurring over the evaluation length (lm) e.g. Z4 in the diagram.

3.6.2 Crater Depth Profile by Ultrasonic Technique

The crater depth profiles along the contact length were measured using an ultrasonic technique in order to supplement the quantitative tool wear measurement. The tool was immersed in water in order to use the ultrasonic technique. The transit time as a function of depth was calibrated using a standard specimen and the known velocity of sound in water. An accuracy of ±0.075 μm was achieved using a 100 MHZ ultrasonic process control system model FU-1100. By changing the position of the ultrasonic sound source along the contact length and moving it across the width of the

crater, measurements of the maximum depth of crater were obtained at known positions along the contact length. This enabled measurement of the profile for the maximum depth of crater as a function of cutting speed.

3.7 Secondary Ion Mass Spectrometry (SIMS)

In secondary ion mass spectrometry (SIMS), an energetic beam of focused ions is directed at a sample surface in a high or ultrahigh vacuum environment. The transfer of momentum from the impinging primary ions to the sample surface causes sputtering of the surface atoms and molecules. Some of the sputtered species are ejected with positive or negative charges; these are termed secondary ions. The secondary ions are then mass analysed using a double-focusing mass spectrometer or an energy filtered quadruple mass spectrometer.

If the rate of sputtering is relatively low, a complete mass spectrum can be recorded to provide a surface analysis of the outermost 5 nm of the sample. This is often termed static SIMS. The most important interaction of the incident ion and the solid surface is the transfer of momentum from the incident ion to the target atoms. The primary ion penetrates the solid surface, travels some distance (termed the mean free path), then collides with the target atom. This collision displaces the target atom from its lattice site, where it collides with a neighbouring atom that in turn collides with its neighbour. This collision cascade continues until the energy transfer is insufficient to displace target atoms from their lattice positions.

The sputtering, or ejection, of target atoms and molecules occurs because much of the momentum transfer is redirected toward the surface by the recoil of target atoms within the collision cascade. The ejection of target atoms due to a single binary collision between the primary ion and surface atom occurs more frequently. The energy of the incident ions ranges between 1 to 20 keV. In most SIMS experiments, Cs^+, O_2^+, O^-, and Ar^+ primary ion species are used in the energy range

from 2 to 20 keV at angles of incidence between 45^0 and 90^0.

An important parameter required for interpretation of depth profiles is the sputtering rate. In practice, the sputter rate is determined for a given set of operating conditions and the material of interest by measuring the depth of the sputtered crater. The crater depth can be measured using optical interferometry or profilometry.

3.7.1 Quantitative Analysis by SIMS

The relationship between the secondary ion current I_i^+ (that is, the positive secondary ion count rate for a monoisotopic element I) and the concentration of I in the specimen is:

$$I_i^+ = I_p.S.\gamma_i^+.C_i.\eta \qquad (3.3)$$

where I_p is the primary ion beam current, S is the sputter yield, γ_i^+ is the ionization efficiency for I^+, C_i is the atomic fraction of I, and η is an instrumental factor that characterizes the collection, transmission, and detection efficiency of the instrument, that is, the ratio of ions I^+ ions emitted to ions I^+ detected. Clearly, the problem in quantitative SIMS analysis is that the measured signal I_i^+ depends not only on the concentration of I in the specimen, but also on the specimen matrix (S, γ_i^+) and the electronic properties of the surface (γ_i^+).

In the present analysis, the infinite velocity method for quantitative SIMS was used to quantify the SIMS results [168]. SIMS has a sensitivity of the order of <0.1 ppm with a depth resolution of < 1 nm.

3.7.2 SIMS Analysis of Rough Surfaces

Surface irregularities, when sputtered, will replicate into underlayers. In this case, the sputter

rate is obtained from a control sample of the same matrix composition but having a smooth surface for which an accurate crater depth can be obtained. In this way, the problem of surface irregularity in the chips was overcome.

3.8 X-Ray SEM and TEM Analysis of Shear Bands

Optical metallography could only reveal the presence of thermoplastic shear bands in Fe-Ni-C alloys with high nickel contents. This bands were observed as white etching bands with no further details from optical metallography. In order to facilitate interpretation of the results the structure and grain size of the phase formed in the shear bands had to be determined. X-ray diffraction, SEM and TEM techniques were used to complement optical metallography.

3.8.1 X-ray Diffraction Analysis

X-ray diffraction for structure and phase determination is well established [169]. No special specimen preparations was required. The chips were flattened by compression and the secondary shear zone was analysed.

3.8.2 SEM Analysis

The sample preparation for SEM analysis of the shear bands was similar to that for optical metallography. An exception for SEM samples is that they were mounted on transoptic resin which was later dissolved off by immersing for several hours in dichloromethane after polishing and etching. The finish polishing was carried out with 0.04 μm colloidal silica. The samples were etched in a 2ml H_2O_2.100ml HCl solution to reveal the microstructure of the shear bands. The samples were examined on a Phillips SEM microscope at high magnification.

3.8.3 TEM Analysis

The segmented nature of the chips rendered the conventional method of specimen preparation for TEM examination difficult. Nonetheless attempts were made to glue the chips in a substrate for punching out a 3 mm diameter disc. Mechanical polishing was carried out in a diamond paste. This was followed by ion thinning. In order to confirm that ion beam thinning at low temperature does not introduce artefacts, alternative techniques of specimen preparation for TEM examination are in progress.

CHAPTER 4

EXPERIMENTAL RESULTS

4.1 Investigations on the Tribological Condition at the Tool-Chip Interface

When metal surfaces are placed in contact they touch only at the tips of their asperities. In these regions the pressure is always high enough to produce plastic flow. The two contacting surfaces form welded junctions that have a specific shear strength. Plastic yielding in the junctions must occur (according to plasticity theory) as a result of combined normal and tangential stresses according to the yield criterion reviewed in section 2.1.4. In metal cutting the compressive and shear stress vary with cutting speed. Therefore the conditions at the tool-chip interface were investigated by performing cutting experiments on AISI 1045 steel and AISI 1080 steel at cutting speeds ranging from 1 m/min to 350 m/min in air and with a jet of helium directed at the cutting point. The use of a helium jet was intended to prevent the formation of oxides which contaminate the interface and reduce seizure. Using Merchant's model [60], the stresses at the tool-chip interface were calculated from the measured cutting forces as a function of cutting speed. The primary shear zone temperature was calculated from measured cutting forces using Loewen and Shaw's model [75]. The measured cutting forces, contact lengths and the calculated values of stresses and temperature in the primary and secondary shear zones are summarised in Table 4.1(a) for AISI 1045 steel and in Table 4.1(b) for AISI 1080 steel.

Figs. 4.1(a) and 4.1(b) show the variation of the measured cutting forces and contact length with the cutting speed respectively, during the machining of AISI 1045 steel. The corresponding results for AISI 1080 steel are shown in Figs. 4.2(a) and 4.2(b). There is a rapid increase in forces in

the low cutting speed range (1 to 10 m/min) followed by a rapid drop in an intermediate speed range (10 to 75 m/min) and then a rise between 75 and 125 m/min. before they remain almost constant with speed. The contact length variation with cutting speed exhibits a minimum at the point where the cutting force is minimum. The values of Po calculated using equation 2.6 and the stresses calculated from the measured cutting forces are plotted as a function of temperature in Fig. 4.3. The cutting speeds are annotated on the figure. The variation of the yield strength for AISI 1045 steel with test temperature is plotted on the same diagram, using the data-base from Simmons and Cross [170]. As depicted in Fig. 4.3 junction growth commences at a cutting speed of approximately 10 m/min according to the plasticity theory advanced by Tabor [47]. Fig. 4.4 shows a schematic used to illustrate the mechanism of formation of a built up edge. An increase in temperature in the secondary shear zone (zone Q) above the temperature of the chip body material (zone P) occurs. This creates an instant when the material at zone Q becomes stronger than that at zone P. This condition is known as the blue brittle range of the steel which occurs at temperatures between 150 and 350 ^{0}C. The blue brittle behaviour of the material occurs as a result of dynamic strain aging which is the process in which during plastic deformation solute atoms diffuse fast enough into the stress field of dislocations [171, 172]. The material exhibits a high rate of strain hardening and decrease in strain rate sensitivity. The result is an increase in strength and decrease in the ductility of the metal. This process is also known as the Portevin Le Chatelier effect [171]. Under this condition shear and flow of the chip material takes place at zone P as the material in zone Q remains stationary forming what is referred to as a built up edge. The effect of the built up edge is to cause an artificial increase in the rake angle which in turn leads to a decrease in the observed cutting forces and contact length. The built up edge is maximum at the point where the cutting forces and contact length are minimum Figs. 4.1 and 4.2. Thus the formation of a built up edge occurs under conditions of low speed low temperature regime of metal cutting in which strain hardening dominates over thermal softening in the chip material.

Table 4.1(a): Experimental cutting forces and the stresses and temperature calculated from the cutting forces in the machining of AISI 1045 steel.

Cutting Speed (M/Min)	Measured Cutting Forces			Contact Length (mm)	Calculated temperatures		Calculated Stresses at the Primary Shear Zone		Calculated Stresses at the Secondary Shear Zone		
	Fx (N)	Fy (N)	Fz (N)		Primary Shear zone (^{0}C)	Secondary Shear Zone (^{0}C)	Shear Stress (Mpa)	Normal Stress (Mpa)	Normal Stress, P (Mpa)	Shear Stress, s (Mpa)	Po from Tabor's equation, $P^2+3s^2=P_o^2$
1	176	67	353	1.11	48	52	159	159	151	98	227
5	340	203	777	1.30	127	175	426	519	284	178	419
10	699	317	1336	1.18	229	392	727	1065	536	374	841
25	651	310	1256	0.99	259	550	692	1064	600	418	940
50	614	252	1168	0.84	283	663	628	868	658	454	1025
75	483	200	1065	0.74	287	679	603	746	686	414	992
100	488	204	1131	0.76	319	792	650	774	711	412	1007
150	400	157	1101	0.78	333	858	681	751	679	335	894
240	380	166	1097	0.86	343	950	691	845	615	296	801
350	338	182	1062	0.85	341	1041	704	857	602	279	772

Table 4.1(b): Experimental cutting forces and the stresses and temperature calculated from the cutting forces in the machining of AISI 1080 steel.

Cutting Speed	Measured Cutting Forces			Contact Length	Calculated temperatures		Calculated Stresses at the Primary Shear Zone		Calculated Stresses at the Secondary Shear Zone		
(m/min)	Fx (N)	Fy (N)	Fz (N)	(mm)	Primary Shear zone (^{0}C)	Secondary Shear Zone (^{0}C)	Shear Stress (Mpa)	Normal Stress (Mpa)	Normal Stress, P (Mpa)	Shear Stress, s (Mpa)	Po from Tabor's equation, $P^2+3s^2=P_o^2$
5	736	318	1618	1.01	223	299	948	1294	763	465	1110
10	802	370	1641	0.92	267	323	896	1164	846	556	1282
25	843	309	1558	0.65	297	440	862	1357	1133	792	1780
50	617	192	1310	0.55	290	466	786	1242	1135	689	1648
75	490	157	1235	0.52	307	573	792	1102	1140	596	1538
100	423	147	1169	0.51	306	660	775	1064	1104	537	1443
150	360	159	1191	0.53	335	741	829	1089	1087	468	1356
200	364	215	1200	0.58	345	751	817	1060	999	453	1271
275	747	446	1282	0.64	268	771	619	1573	939	764	1623
350	789	356	1287	0.63	261	798	607	1643	957	773	1646

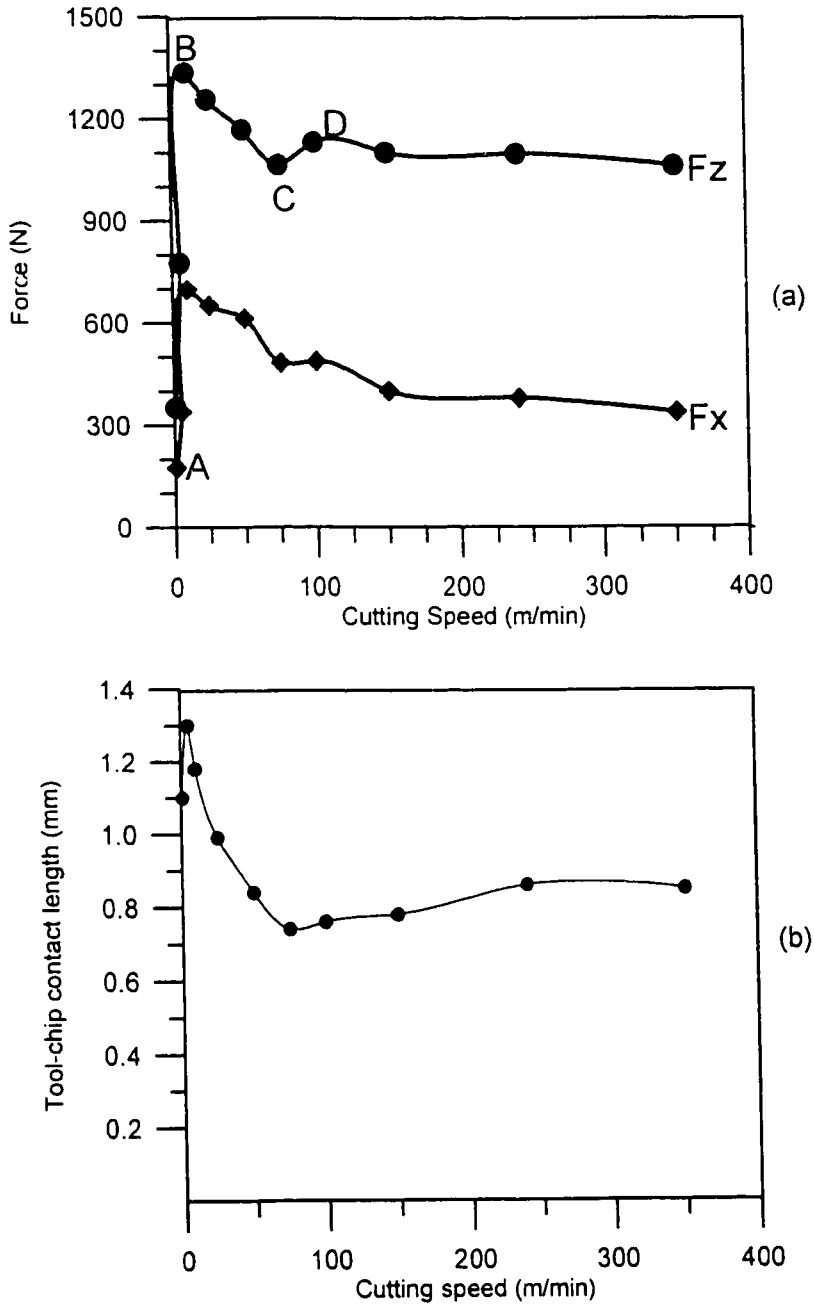

Fig. 4.1: Variation of measured (a) cutting force (Fz) and feed force (Fx) and (b) tool-chip contact length, as a function of cutting speed during machining of AISI 1045 steel with a cemented carbide tool (K1).

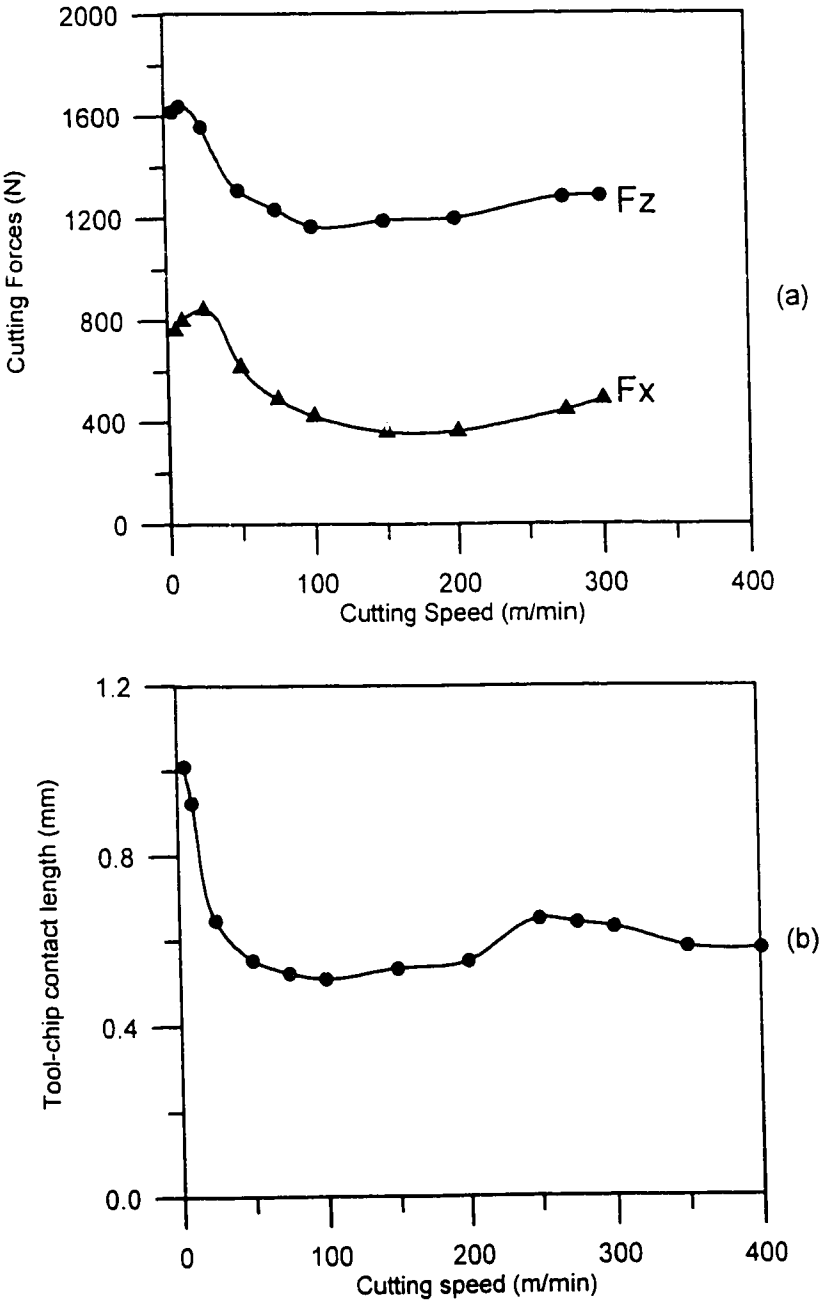

Fig. 4.2: Variation of measured (a) cutting force (Fz) and feed force (Fx) and (b) tool-chip contact length, as a function of cutting speed during machining of AISI 1080 steel with a cemented carbide tool (K1).

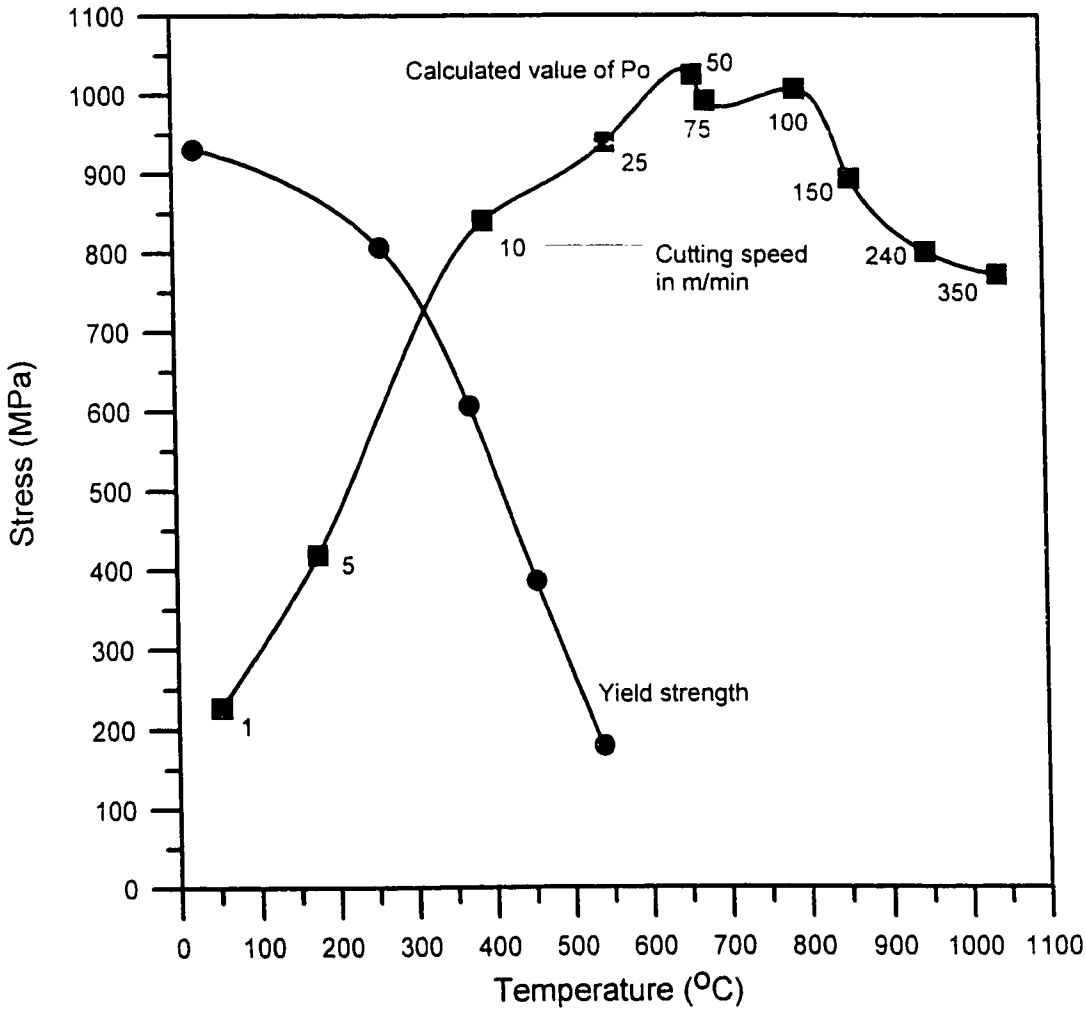

Fig. 4.3: A plot of the values of P_0 calculated from Tabor's equation as a function of temperature.

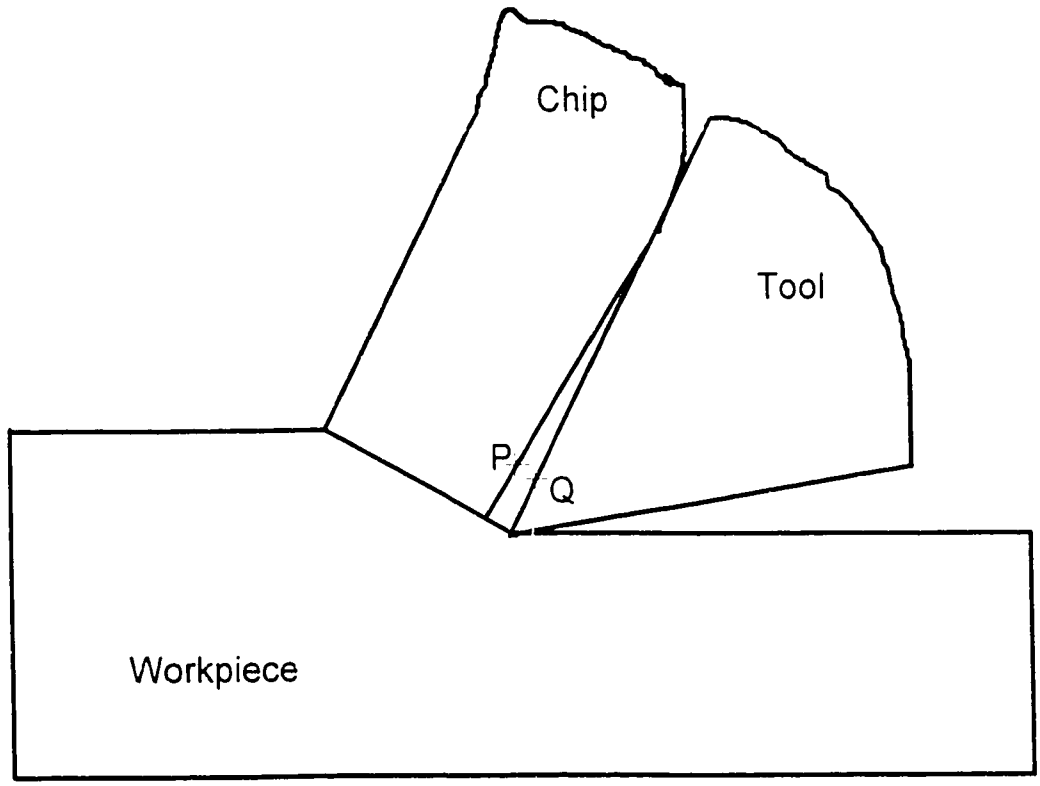

Fig. 4.4: A schematic of ther deformation zones in a turning operation illustrating the formation of a built up edge.

Between 75 m/min and 100 m/min the effects of thermal softening on the yield strength offset the effects of strain hardening in the material closest to the tool-chip interface which in turn becomes softer than the adjacent chip body material. The result is a decrease in size of the built up edge as the cutting speed increases from 75 m/min to 100 m/min at which it disappears. As the built up edge grows smaller the cutting force increases due to the attendant decrease of the effective rake angle but slightly due to the weakening effect brought about by thermal softening.

Fig. 4.5 shows the variation of the calculated compressive stress at the tool-chip interface with the calculated primary shear zone temperature during the machining of AISI 1045 steel. The cutting speeds are annotated on the curve. The variation of the yield strength for AISI 1045 steel with temperature is plotted on the same diagram, using the data-base from Simmons and Cross [170]. It can be seen that at 100 m/min. the normal stress is 710 MPa, which is equalled by the yield strength of the AISI 1045 steel at 320^{0}C, corresponding to the chip body temperature at the same cutting speed of 100 m/min. Thus, according to the physical model for seizure, asperities will be squeezed to make atomic contact, rendering the true contact area equal to that of apparent contact area at 100 m/min. and above. Once seizure sets in, thermoplastic shear will be localised at the tool-chip interface, causing the local temperature to rise. Thermally activated processes will set in, causing interdiffusion of solute elements at the tool-chip interface. By measuring the concentration profile of solute elements in the chip using a highly sensitive technique, it is possible to confirm seizure. Secondary Ion Mass Spectrometry (SIMS) was chosen as a sensitive technique to characterise the concentration profiles of tungsten and cobalt in the chips. The technique is sensitive to detect the concentration of tungsten in the order of 0.1 ppm in depth resolution of 1nm. The chips obtained at each cutting speed were analysed using SIMS. Figs. 4.6(a) and 4.6(b) show diffusion profiles of tungsten and cobalt for chips obtained at different cutting speeds. The lowest cutting speed at which measurable diffusion of tungsten into the chips is obtained turns out to be 100 m/min., which is in accord with the

prediction from the physical model for seizure based on atomic contact.

At cutting speeds above 100 m/min, the contact length continues to increase albeit slow as the cutting speed of 240 m/min is approached, Fig. 4.1(b). A secondary shear zone forms in the chip. The micrographs in Figs. 4.7(a) and 4.7(b) show the secondary shear zone formed in the chips obtained from AISI 1045 steel and AISI 1080 steel respectively. The experimental evidence suggests that junction growth reaches a maximum in this region leading to complete seizure between the tool and chip. Further temperature rise as a result of seizure and thermoplastic shear deformation is accompanied with occurrence of phase transformation in the thin layer of material adjacent to the tool-chip interface which appears as a white etching layer. The consequences of phase transformation is the mechanical weakening of the chip material and enhanced diffusivity due to dislocation generation. This zone is first thick and then becomes thinner as the speed is increased. The thickness of the zone corresponds to the layer that is partially or completely transformed.

The effect of increasing the feed from 0.17 mm/rev to 0.26 mm/rev is demonstrated in Fig. 4.8(a) and 4.8(b). Increasing the feed has the effect of lowering the cutting speed at which the built up edge and flow zone start forming. This has the effect of reducing the normal pressure on the tool face hence delaying the onset of built up edge and flow zone formation to higher cutting speeds. Fig. 4.9 is a plot of the measured contact length as a function of cutting speed during machining of AISI 1045 steel in air and with a jet of helium directed at the cutting point. The jet of helium was used in order to shield the tool-chip contact from oxygen. The presence of oxygen is expected to form oxides which would prevent seizure from occurring and reduce the contact length. However as shown in Fig. 9 the contact length remained the same in both cases when machining at cutting speeds above 25 m/min. This suggests that at high cutting speeds external lubricants would not have a chance of accessing the tool-chip interface.

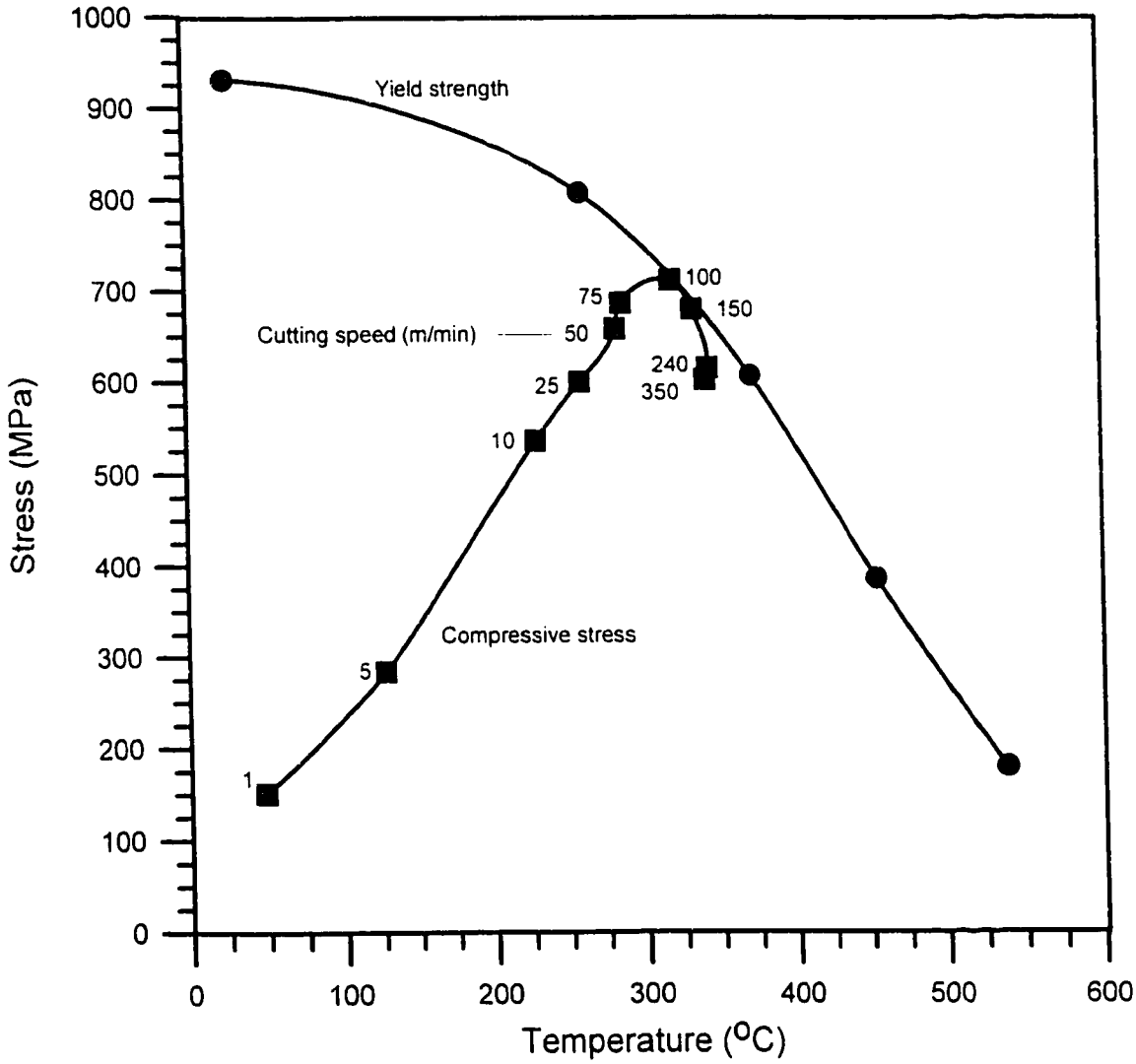

Fig. 4.5: (A) The variation of the calculated compressive stress at the tool-chip interface with the calculated primary shear zone temperature during machining of AISI 1045 steel. (B) The variation of the yield strength of AISI 1045 steel with temperature.

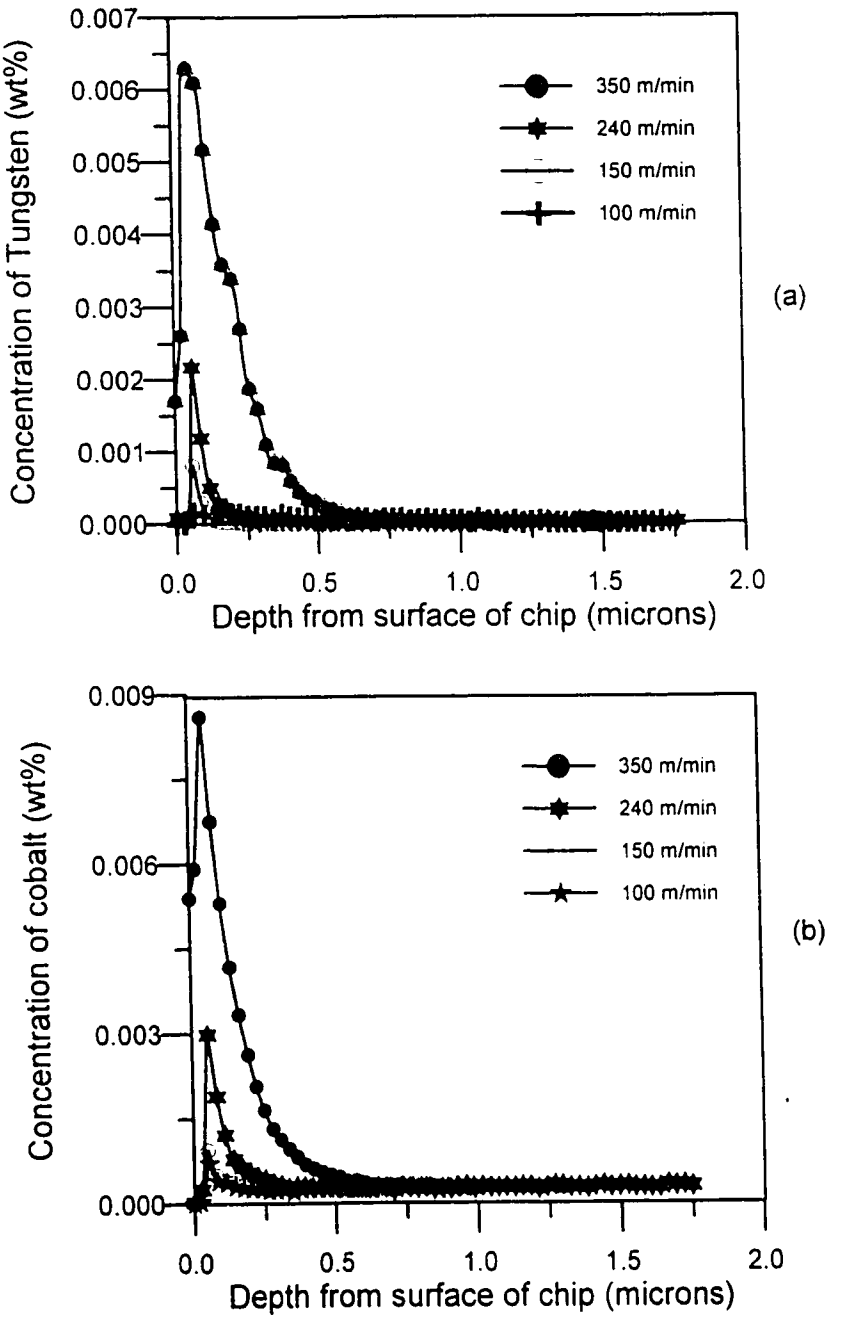

Fig. 4.6: Concentration profiles for (a) tungsten and (b) cobalt obtained from SIMS analysis of chips generated at each of the cutting speeds ranging from 25 m/min. to 350 m/min. during machining of AISI 1045 steel with a cemented tungsten carbide (K1) tool.

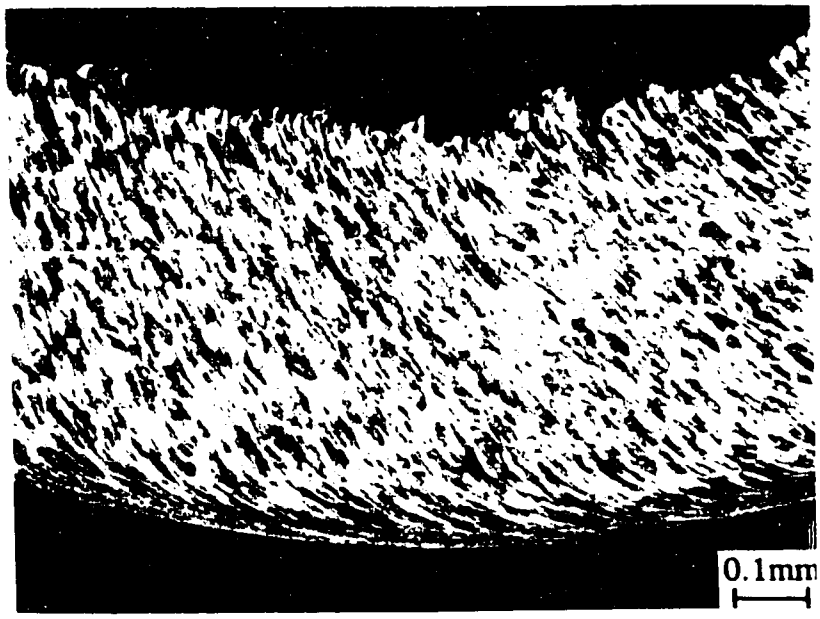

(a)

(b)

Fig. 4.7: The secondary shear zone formed in the chips obtained from (a) AISI 1045 steel (b) AISI 1080 steel.

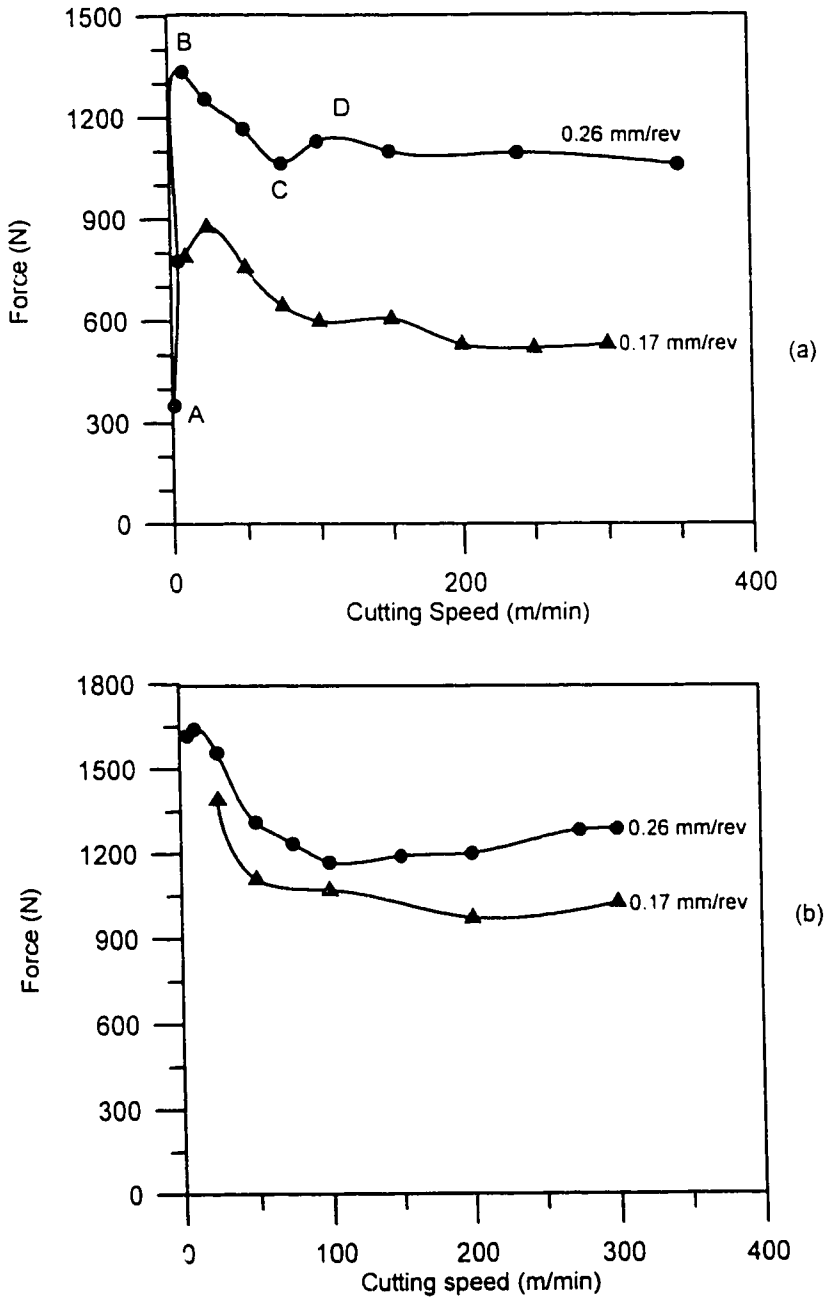

Fig. 4.8: Variation of the cutting force (Fz) with cutting speed for different feed rates during machining of (a) AISI 1045 steel and (b) AISI 1080 steel.

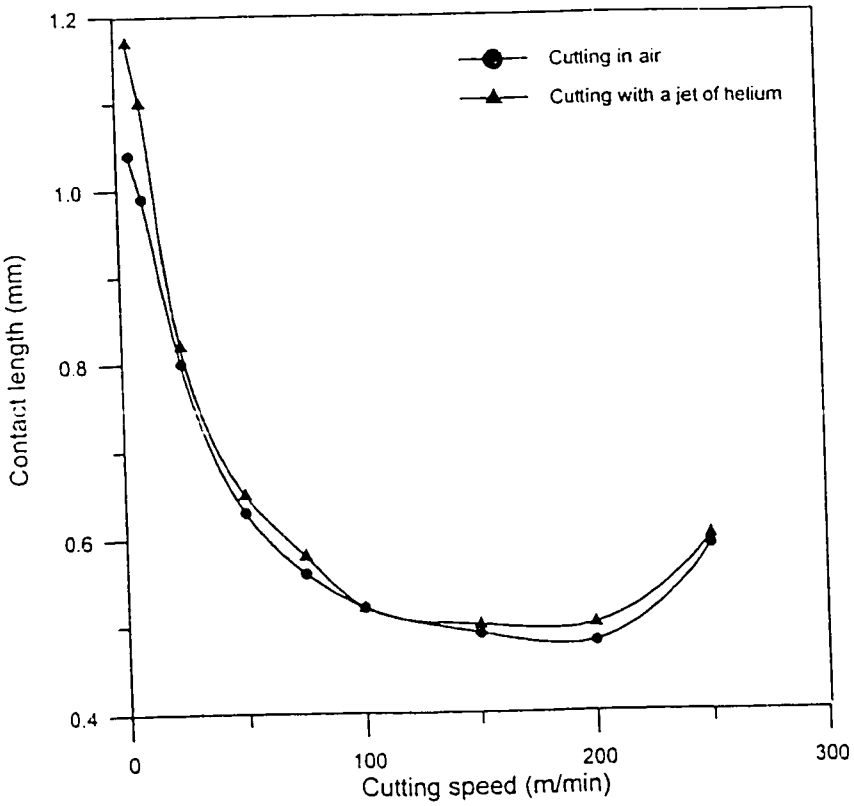

Fig. 4.9: Measured contact length as a function of cutting speed during machining of AISI 1045 steel in air and with a jet of helium gas directed at the cutting point.

4.2 Experimental Results on Ductile Iron and AISI 1020 Steel

4.2.1 Metal Cutting Data Base for Ductile Iron and AISI 1020 Steel

Table 4.2 summarises the measured cutting forces, contact length, thickness of the secondary shear zone and the shear plane angle, calculated from the measured chip thickness, as a function of the cutting speed during machining of ductile iron and AISI 1020 steel using uncoated cemented carbide (K1) tool, TiN/TiC coated (KC250) and HfN coated K1 tool. The cutting speeds used were 100, 200 and 300 m/min. In this speed range, the cutting forces, contact length and secondary shear zone thickness decrease with increase in cutting speed, whereas the shear plane angle increases. The decrease in cutting forces with increase of cutting speed is more in ductile iron than in steel. There are two differences in material properties between ductile iron and AISI 1020 steel that can be used to account for this observation. The first is that ductile iron has a lower thermal diffusivity (8×10^{-6} m^2/s)

than AISI 1020 steel whose value is 12.7×10^{-6} m^2/s. Therefore ductile iron concentrates the heat generated by plastic deformation at the shear zones more than AISI 1020 steel leading to formation of adiabatic shear bands and hence reduced cutting forces. The second is that ductile iron has a dispersion of soft graphite second phase particles which can cause geometrical softening which aids in chip segmentation. The high values of shear plane angle and chip thickness ratio correspond to lower strains in the chip and reduced energy consumption. As the cutting speed is increased the contact length is decreased. The increase of shear plane angle corresponds with the increase in the material flow stress by strain hardening and strain rate hardening. When the flow stress increases the system tends to minimise the cutting energy by increasing the shear plane angle. The effect of coating is to decrease both contact length and cutting forces. Coating with HfN was found to reduce the contact length in ductile iron more than coating with TiN/TiC, however, this decrease is small and much less than that observed in AISI 1020 steel. Table 4.3 shows the values of stresses and maximum temperature calculated from the measured values in Table 4.2. The normal stress and the maximum tool-chip interface temperature increase with increase in cutting speed. The effect of coating is to decrease both normal stress and maximum tool-chip interface temperature.

Table 4.4 shows the calculated and measured average tool-chip interface temperature as a function of cutting speed for both ductile iron and AISI 1020 steel when machining with uncoated cemented carbide (K1) tool. The average tool-chip interface temperature was measured by the ultrasonic technique. The theoretical calculation of the average tool-chip interface temperature was accomplished by finite element analysis as described in Appendix C. The measured and calculated average temperatures show close agreement. The average temperature increases with increase in cutting speed but the increase is slight at cutting speeds above 200 m/min. The effect of coating is to decrease the calculated temperature by about 70^0C.

Table 4.2: Experimental data from turning of ferritic ductile iron and AISI 1020 steel using uncoated cemented carbide tool grade K1,TiN/TiC coated tool grade KC250 and HfN-coated K1 tool.

Workpiece Material	Tool	Cutting Speed (m/min)	Cutting forces			Tool-chip Contact length (mm)	Thickness of secondary shear zone (μm)	Shear plane angle (deg.)
			Fx (N)	Fy (N)	Fz (N)			
Ductile Iron	K1	100	546	318	1065	0.62	25	32
Ductile Iron	K1	200	472	212	925	0.54	22	33
Ductile Iron	K1	300	376	162	826	0.45	15	34
Ductile Iron	KC250	100	374	175	845	0.61	26	31
Ductile Iron	KC250	200	322	149	779	0.50	23	33
Ductile Iron	KC250	300	292	120	708	0.42	15	35
Ductile Iron	K1-HfN	100	404	---	815	0.59	--	33
Ductile Iron	K1-HfN	200	308	---	801	0.45	--	36
Ductile Iron	K1-HfN	300	271	---	778	0.38	--	37
AISI 1020 steel	K1	100	466	188	973	1.12	46	20
AISI 1020 steel	K1	200	393	172	936	0.93	34	22
AISI 1020 steel	K1	300	385	160	921	0.90	38	23
AISI 1020 steel	KC250	100	387	166	879	0.57	28	21
AISI 1020 steel	KC250	200	331	158	864	0.44	24	24
AISI 1020 steel	KC250	300	329	140	850	0.40	20	26

Table 4.3: The strain rate and calculated stresses and temperature from turning of ferritic ductile iron and AISI 1020 steel using a uncoated cemented carbide tool grade K1, TiN/TiC coated tool grade KC250 and HfN-coated K1 tool.

Worpiece Material	Tool	Cutting Speed (m/min)	Stresses at the primary shear zone		Stresses at the secondary shear zone		Strain rate at secondary shear zone x10^4 /s	Calculated maximum tool-chip interface temperature (^{0}C)
			Normal stress (Mpa)	Shear stress (Mpa)	Normal stress (Mpa)	Shear stress (Mpa)		
Ductile Iron	K1	100	1117	582	811	583	3.9	829
Ductile Iron	K1	200	979	520	812	552	9.2	950
Ductile Iron	K1	300	650	493	874	534	20.3	982
Ductile Iron	KC250	100	788	509	661	398	3.8	778
Ductile Iron	KC250	200	768	484	745	422	9.0	882
Ductile Iron	KC250	300	734	441	807	448	21.9	912
Ductile Iron	K1-HfN	100	835	488	658	401	--	--
Ductile Iron	K1-HfN	200	803	531	858	419	--	--
Ductile Iron	K1-HfN	300	782	533	989	445	--	--
AISI 1020 steel	K1	100	525	488	413	261	1.3	840
AISI 1020 steel	K1	200	554	517	482	274	3.9	960
AISI 1020 steel	K1	300	570	520	489	275	7.6	991
AISI 1020 steel	KC250	100	499	467	786	435	2.3	771
AISI 1020 steel	KC250	200	524	407	941	501	6.0	807
AISI 1020 steel	KC250	300	584	513	1019	538	11.7	834

Table 4.4: Experimental and calculated average tool-chip interface temperatures during machining of ferritic ductile iron and AISI 1020 steel using a cemented carbide (K1) tool.

Workpiece material	Cutting speed (m/min)	Measured average tool-chip interface temperature (^{0}C)	Calculated average tool-chip interface temperature (^{0}C)	Austenite start temperature of workpiece (^{0}C)
Ferritic ductile iron	100	555±25	637	835
	200	760±25	780	
	300	845±25	870	
AISI 1020 steel	200	855±25	790	840
	300	940±25	856	

4.2.2 Microstructure of the Chips Obtained from Ductile Iron

When ductile iron was machined using uncoated cemented carbide tool continuous chips were formed at 100 m/min, Fig. 4.10(a) and partially segmented chips at 200 m/min, Fig. 4.10(b). At 300 m/min the segments are partially separated, Fig. 4.10(c). Fully segmented chips were observed at 350 m/min, Fig. 4.10(d). Fig. 4.10(e) is an SEM image showing the section parallel to the chip flow direction of a typical chip obtained at 300 m/min during the machining of ductile iron using a K1 tool. A 10 μm thick deformation shear band is evident at the interface. The graphite spherulite is extruded into a very thin slab inside the shear band indicating that deformation is highly localised. Formation of the shear band is indicative of extreme shear localisation which leads to high tool-chip interface temperatures. The creation of lattice defects and high temperature in the shear band could contribute to enhanced diffusion at the tool-chip interface thus increasing dissolution wear of the tool.

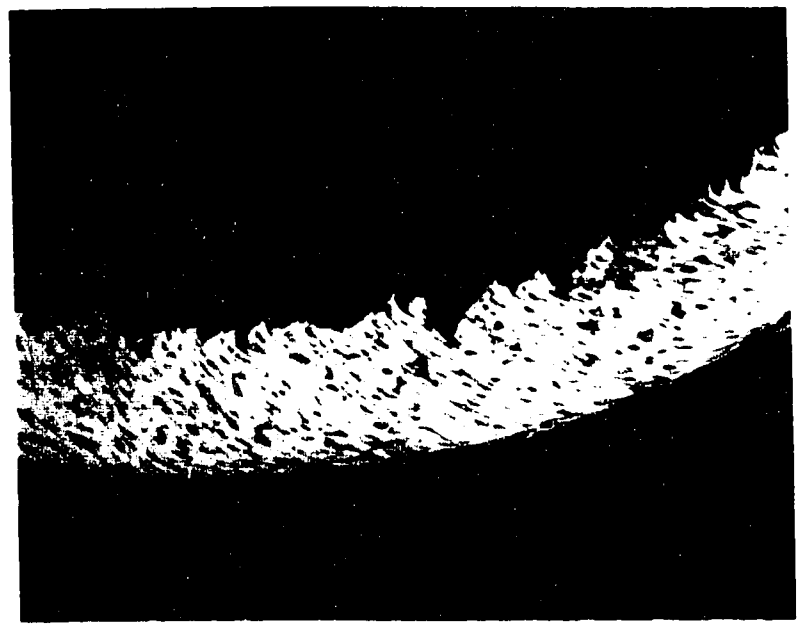

Fig. 4.10(a): An optical micrograph showing a section parallel to the chip flow direction of a continuous chip obtained from machining ductile iron with cemented carbide tool (K1) at a cutting speed of 100 m/min. Etched in 2% nital. (Mag. 50X)

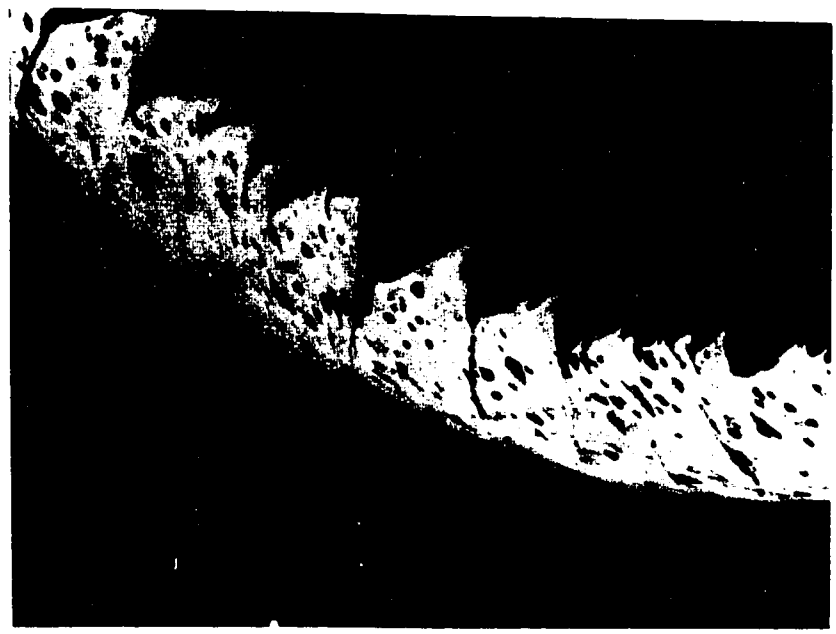

Fig. 4.10(b): An optical micrograph showing a section parallel to the chip flow direction of a partially segmented chip obtained from machining ductile iron with cemented carbide tool (K1) at a cutting speed of 200 m/min. Etched in 2% nital. (Mag.50X)

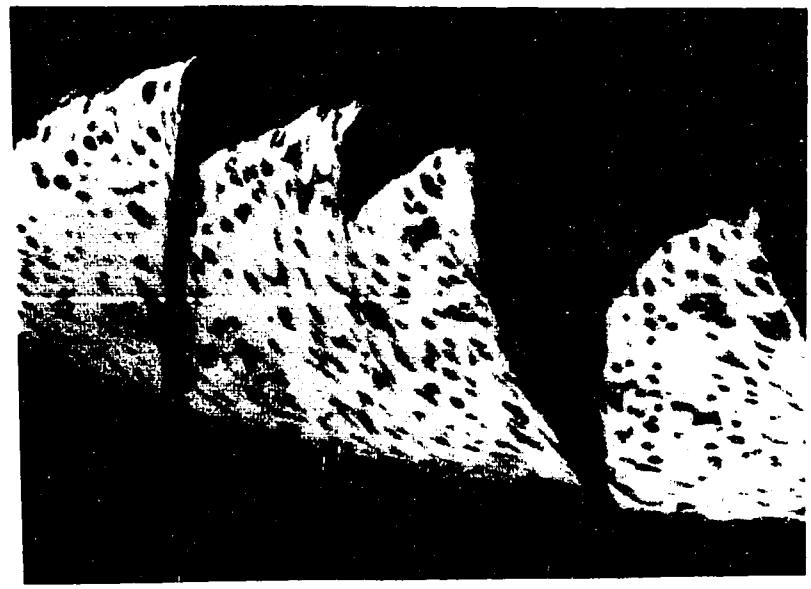

Fig. 4.10(c): An optical micrograph showing a section parallel to the chip flow direction of the chip obtained from machining ductile iron with cemented carbide tool (K1) at a cutting speed of 300 m/min, showing partial separation of the segments. Etched in 2% nital. (Mag. 50X)

Fig. 4.10(d): An optical micrograph showing a section parallel to the chip flow direction of a fully segmented chip obtained from machining ductile iron with cemented carbide tool (K1) at a cutting speed of 350 m/min. Etched in 2% nital. (Mag. 64X)

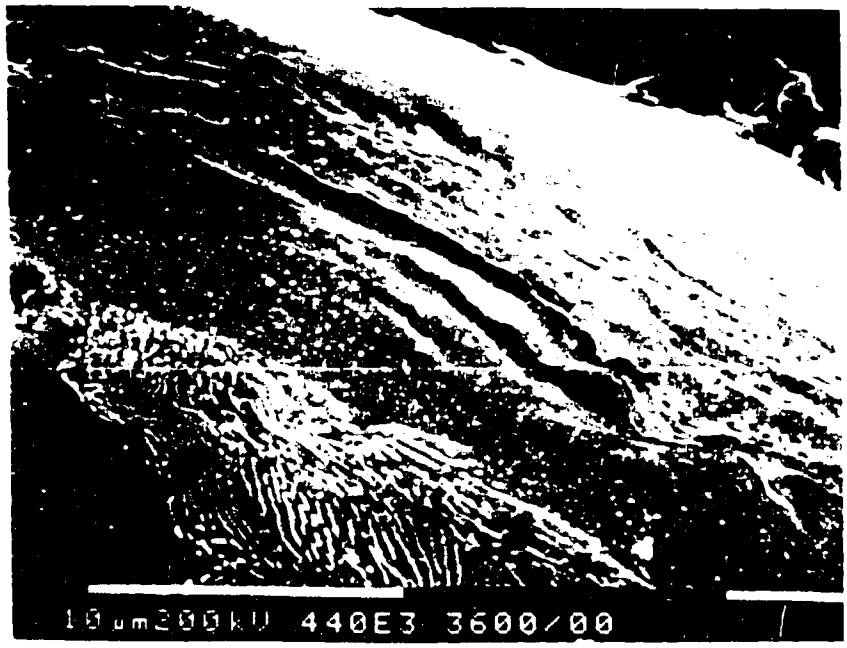

Fig. 4.10(e): SEM image of the chip segments machined from ductile iron using a cemented carbide tool (K1) at 300 m/min, showing a deformation shear band in which the graphite spheroid is extruded into a very thin slab indicating large strain in the shear band.

4.2.3 Optical and SEM Microscopy of the Chips Obtained from Ductile Iron at 350 m/min

Fig. 4.11(a) is an SEM image of the chips produced at 350 m/min showing the top free surface and the trailing face of the primary shear zone. The free surface of the chip has tool marks with intense deformation from ploughing of the flank edge. Extensive voids are seen near the bottom of the primary shear plane of the chip. The trailing face of the primary shear zone shows intense void growth near the bottom of the chip. Figs. 4.11(b) is an SEM image of the section parallel to the chip flow direction. Localised deformation at the primary shear zone is indicated by the deformation of the graphite spheroids into plates, aligned along the shear band. The graphite spheroid in the body of the chips suffer little or no deformation. The graphite spheroid within the shear band exhibits large strains which indicates that there is intense shear localisation in very narrow shear bands at the primary shear zone under the action of a high compressive pressure. The shear band runs through the chip thickness. Fig. 4.11(c) is an SEM image of a section parallel to the chip, showing seizure at the tool-chip interface and heterogeneous deformation at the secondary and primary shear zones.

Fig. 4.11(a): SEM image of the chip segments machined from ductile iron using a cemented carbide tool (K1) at 350 m/min, showing the trailing face and the free surface of the chip. Extensive void growth can be seen on the trailing face near the bottom of the chip.

Even though the chips are fully segmented, there is seizure which leads to intense deformation localised in very narrow shear bands in the secondary shear zone. The graphite in the secondary shear band is deformed and elongated into a narrow strip indicating that large strains (~8) are reached in the shear band due to the action of a high compressive pressure. The section parallel to the chip flow direction shows that the deformation shear band apparently extends from the bottom to the free surface of the chip. Fully and partially developed cracks culminating in periodic fracture coincide with the shear bands. These observations suggest that deformation at the primary shear zone is probably that of adiabatic shear localisation which culminates in the formation of deformed shear bands. The cracks coinciding with the shear bands are responsible for formation of fully segmented chips. However a new observation made from the present work is that the segmented elements of the chips appear to seize to the tool during the upsetting of the segments.

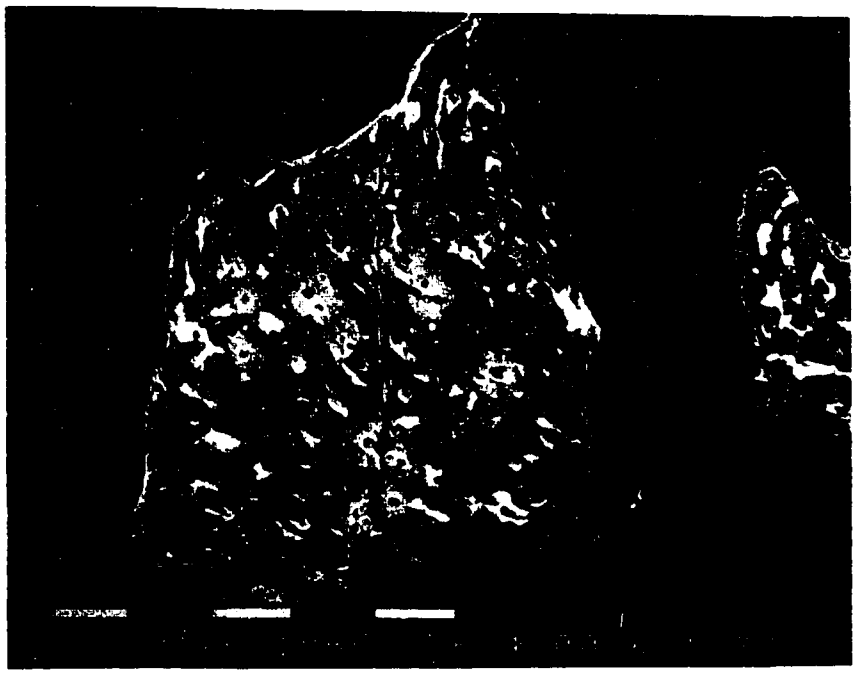

Fig. 4.11(b): SEM image a section parallel to the chip flow direction, showing localised deformation at the primary shear zone. The elongated graphite indicated deformation in the shear band. The shear band runs through thickness of the chip, apparently commencing from the bottom.

Fig. 4.11(c): SEM image of a section parallel to the chip flow direction, showing intense deformation of the secondary shear zone and heterogeneous deformation at the primary shear zone.

4.3 Micromechanisms of Tool Wear in AISI 1020 Steel and Ductile Iron

The results reported in section 4.1 suggest that at cutting speeds above 100 m/min in steel, the tribological phenomenon of seizure occurs at the tool-chip interface. Seizure leads to atomic transfer at the tool-chip interface resulting in dissolution wear. A quantitative tool wear data base has been established using ICP-MS technique. Tables 4.5, 4.6, and 4.7 show the measured concentration rise of W, Ti and Hf in ductile iron chips resulting from mechanical and dissolution wear at each cutting speed for uncoated cemented carbide (K1) tool, TiN/TiC coated and HfN coated tools respectively. The corresponding values for steel are given in Tables 4.8 and 4.9 respectively. Tool wear was measured after machining for 20 seconds. In both ductile iron and AISI 1020 steel, the contribution of dissolution wear to the total wear increases with speed and is dominant at high cutting speeds. The effect of coating is to decrease dissolution wear, in both ductile iron and steel. Hafnium nitride is more effective than TiN/TiC in minimising tool dissolution wear.

Table 4.5: Contribution of mechanical and dissolution wear (as measured by the tungsten concentration rise) to the total wear of K-1 tool measured after 20 seconds machining of ductile iron.

Cutting speed (m/min)	Total wear (ppm of W)	Mechanical wear (ppm of W)	Dissolution wear (ppm of W)	Percent dissolution wear
100	2.0±0.2	0.9±0.01	1.1±0.2	55
200	3.1±0.2	1.1±0.01	2.0±0.2	65
300	7.2±0.3	1.3±0.01	5.9±0.3	82

Table 4.6: Contribution of mechanical and dissolution wear (as measured by the titanium concentration rise) to the total wear of KC250 tool measured after 20 seconds machining of ductile iron.

Cutting speed (m/min)	Total wear (ppm of Ti)	Mechanical wear (ppm of Ti)	Dissolution wear (ppm of Ti)	Percent dissolution wear
100	1.0±0.1	0.6±0.01	0.4±0.1	40
200	2.8±0.2	1.1±0.01	1.7±0.2	61
300	5.8±0.3	1.3±0.01	4.5±0.3	78

Table 4.7: Dissolution wear of HfN coated cemented carbide tool (as measured by the Hafnium concentration rise in the chips) after 20 seconds machining of ductile iron.

Cutting speed (m/min)	Dissolution Wear (ppm of Hf)
100	0.1±0.01
200	0.2±0.02
300	0.4±0.03

Table 4.8: Contribution of mechanical and dissolution wear (as measured by the tungsten concentration rise) to the total wear of K-1 tool measured after 20 seconds machining of low carbon steel.

Cutting speed (m/min)	Total wear (ppm of W)	Mechanical wear (ppm of W)	Dissolution wear (ppm of W)	Percent dissolution wear
100	2.7±0.2	0.4±0.01	2.3±0.2	85
200	4.4±0.3	0.3±0.01	4.1±0.3	93
300	8.8±0.4	0.4±0.01	8.4±0.4	96

Table 4.9: Contribution of mechanical and dissolution wear (as measured by the titanium concentration rise)to the total wear of KC250 tool measured after 20 seconds machining of low carbon steel.

Cutting speed (m/min)	Total wear (ppm of Ti)	Mechanical wear (ppm of Ti)	Dissolution wear (ppm of Ti)	Percent dissolution wear
100	0.7±0.1	0.5±0.01	0.2±0.05	29
200	2.2±0.1	0.8±0.01	1.4±0.1	64
300	4.3±0.3	1.3±0.01	3.0±0.2	70

4.3.1 Effect of Coating on Dissolution Wear

Fig. 4.12(a) and 4.12(b) are bar charts showing mechanical and dissolution wear as measured by the titanium concentration rise in the chips at the end of 20 seconds of machining ductile iron and steel respectively with TiN/TiC coated cemented carbide tool (KC250). Dissolution wear is still significant in the case of ductile iron when TiN/TiC coated tools are used whereas in the case of steel the coating is effective in reducing dissolution wear. Fig. 4.13 is a bar chart showing the effect of hafnium nitride coating on dissolution wear in comparison with uncoated cemented carbide tool (K-1) and TiN/TiC coated (KC250) tool. The equilibrium solubility of hafnium nitride in austenite is 10 million times less than that of tungsten carbide at 1127^{0}C. Thus hafnium nitride coating is very effective in minimising tool dissolution wear.

4.3.2 The Tool-chip Interface Temperature Distribution and Crater Depth Profiles

Figs. 4.14 and 4.15 are SEM pictures of the cutting edges for the K-1 tool after machining ductile iron and steel respectively for 20 seconds at a cutting speed of 300 m/min. Seizure at the tool-chip interface leads to diffusion wear resulting in formation of the craters. The crater is located closer

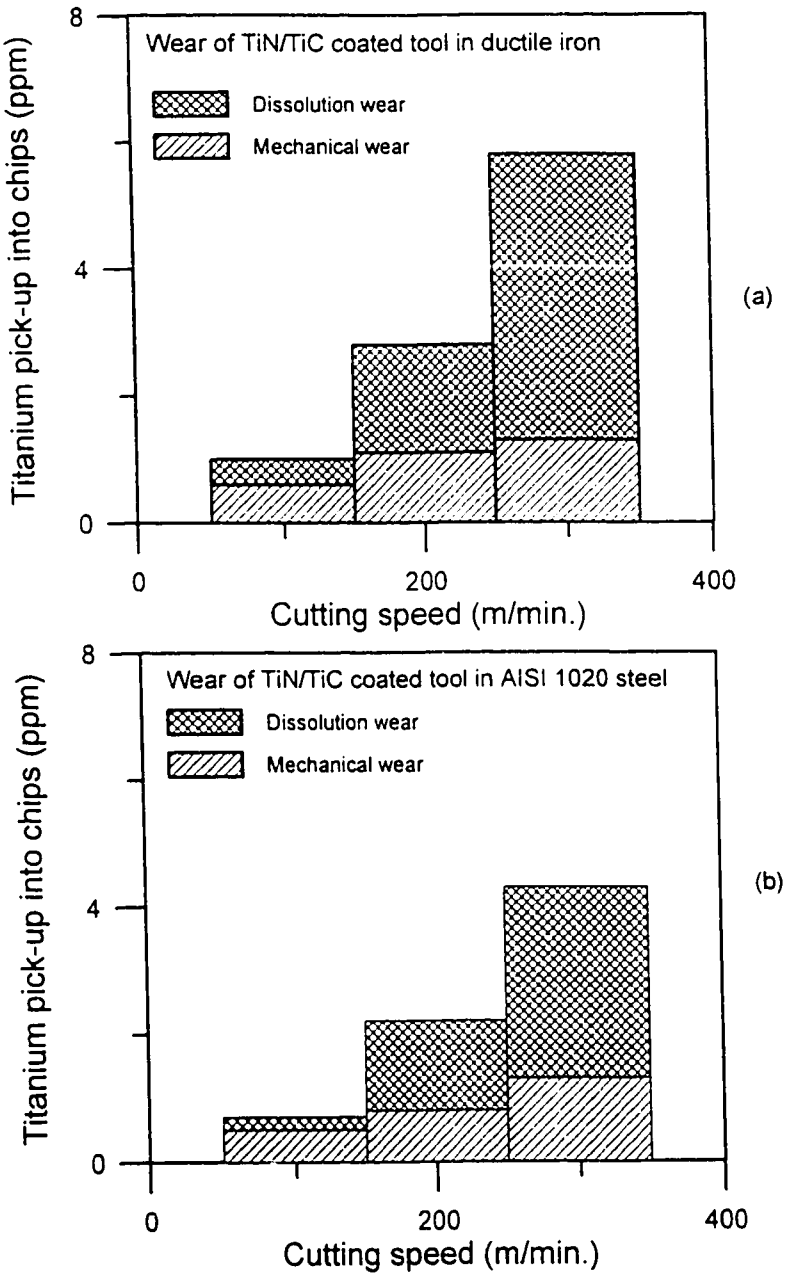

Fig.4.12: Bar chart showing mechanical and dissolution wear as measured by the titanium concentration rise in the chips at the end of 20 seconds of machining (a) ferritic ductile iron (b) AISI 1020 steel, with TiN/TiC-coated cemented carbide tool (KC250).

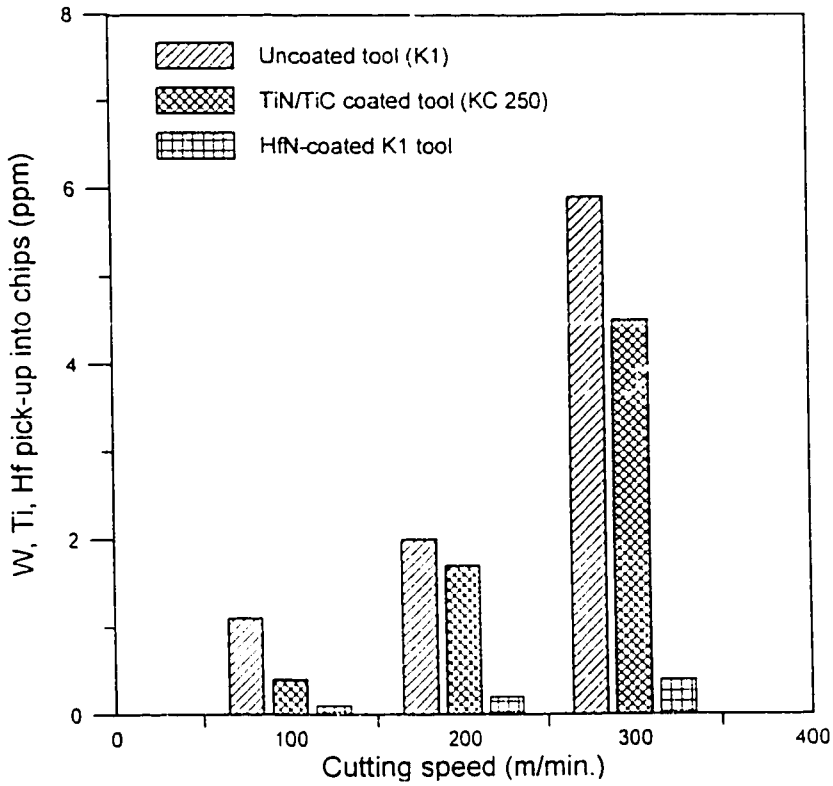

Fig. 4.13: A bar chart showing dissolution wear as measured by solute concentration rise (W,Ti and Hf respectively) in the chips at the end of 20 seconds of machining ferritic ductile iron with uncoated cemented carbide (K-1), TiN/TiC-coated cemented carbide tool (KC250) and HfN coated K-1 tools.

to the tool cutting edge in machining ductile iron than in steel. This is because chip segmentation at the primary shear zone in ductile iron concentrates the heat generated by plastic deformation near the cutting edge of the tool causing high temperature rise and tool wear near the cutting edge of the tool.

Fig. 4.16(a) shows the depth profiles of craters formed during machining of ductile iron with uncoated cemented carbide tool. The crater moves closer to the cutting edge as the cutting speed is increased, eventually damaging the cutting edge at a cutting speed of 300 m/min. Typical results from the present model for the calculation of tool-chip interface temperature distribution as a function of position on the rake face are shown in Fig. 4.16(b) for ductile iron when machining with uncoated cemented carbide (K1) tool. The temperature increases from the tool tip to a maximum at the point

where the chip loses intimate contact with the tool. Fig. 4.17(a) and 4.17(b) show the measured depth profiles of craters formed on the rake face of the tool and the calculated tool-chip interface temperature distribution as a function of position on the rake face of the tool during machining of AISI 1020 steel with K1 tool. The crater is located farther away from the cutting edge in AISI 1020 steel right from the start of cutting. With increase in cutting speed, even though the crater draws close to the cutting edge of the tool the cutting edge is not damaged even at high cutting speeds in steel. Fig. 4.18(a) shows the measured crater depth profile during machining of AISI 1080 steel. The crater moves closer to the cutting edge of the tool with increase in cutting speed. Fig. 4.18(b) shows the calculated tool-chip interface temperature distribution along the length of tool-chip contact for AISI 1080 steel. It is interesting to compare the crater depth profiles with the predicted temperature profiles. The maximum depth of the crater does not occur at the maximum temperature. Instead the maximum depth of the craters formed on the tools used to machine ductile iron and the steels coincides with the phase transformation temperature of each material. This suggests the occurrence of phase transformation and its contribution to enhancement of diffusion. Fig. 4.19 shows the effect of coating the tool with hafnium nitride on the location of the crater as the cutting speed is increased. The effect of coating is to minimise tool crater wear and also to draw the crater away from the cutting edge. This should help to preserve the cutting edge for longer periods of time hence increasing tool life. Table 4.10 summarises the results from crater depth profile and temperature measurements. The calculated temperatures are included in the same table. As shown the maximum calculated temperature is higher than the phase transformation temperature for cutting speeds greater than 100 m/min. The location of the maximum depth of the crater moves closer to the cutting edge of the tool with increase in cutting speed.

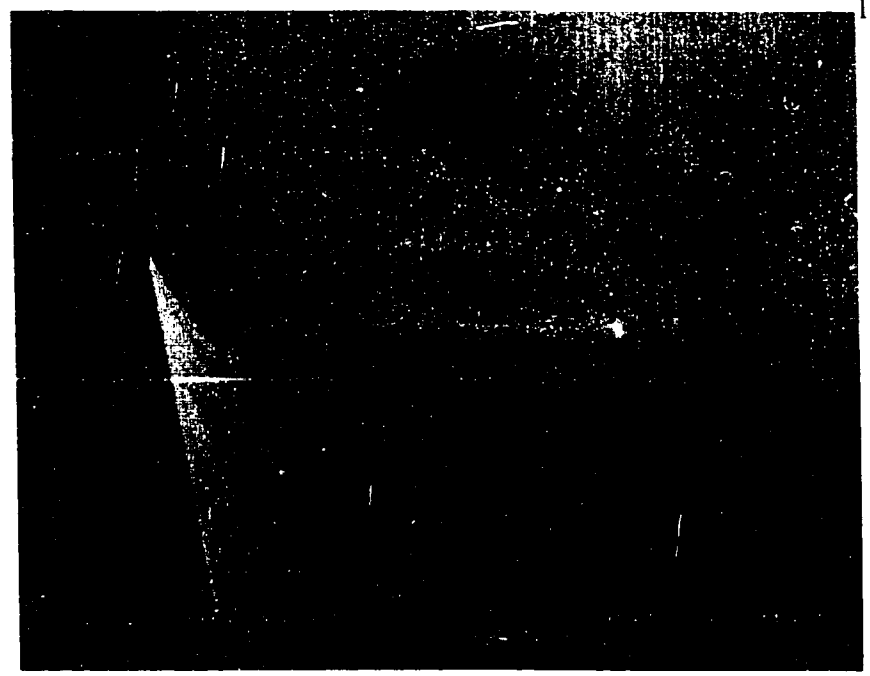

Fig. 4.14: SEM image of the crater observed on the K1 cemented carbide tool after machining of ductile iron at 300 m/min for 20 seconds. Note the crater localised nearer to the cutting edge of the tool leading to damage of the tool and loss of surface finish.

Fig. 4.15: SEM image of the crater observed on the K1 cemented carbide tool after 20 seconds machining of steel at 300 m/min. Note the crater occurring farther away from the cutting edge of the tool.

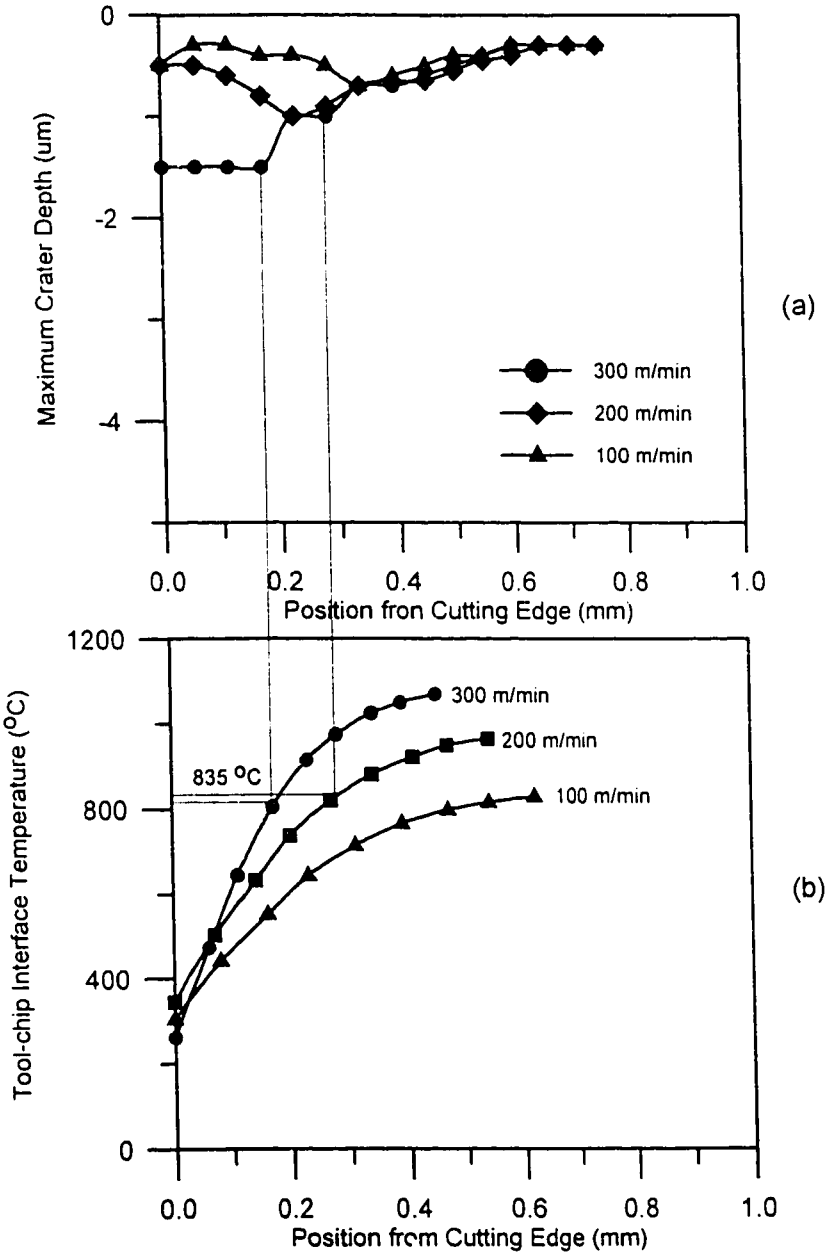

Fig.4.16: (a) The measured depth profiles of the crater (b) predicted tool-chip interface temperature distribution along the contact length, after machining ferritic ductile iron for 20 seconds with a cemented carbide tool (K1) for cutting speeds 100, 200, and 300 m/min. respectively.

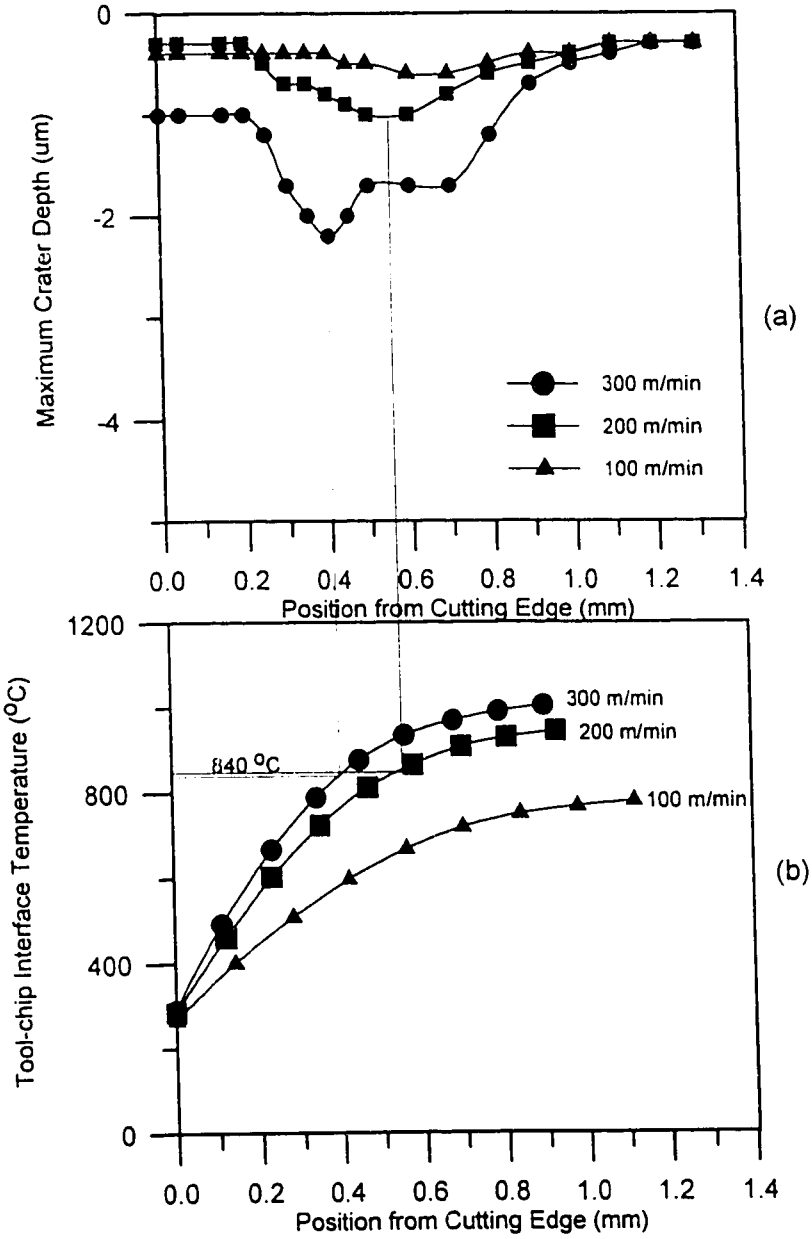

Fig.4.17: (a) The measured depth profiles of the crater (b) predicted tool-chip interface temperature distribution along the contact length, after machining AISI 1020 steel for 20 seconds with a cemented carbide tool (K1) for cutting speeds 100, 200, and 300 m/min. respectively.

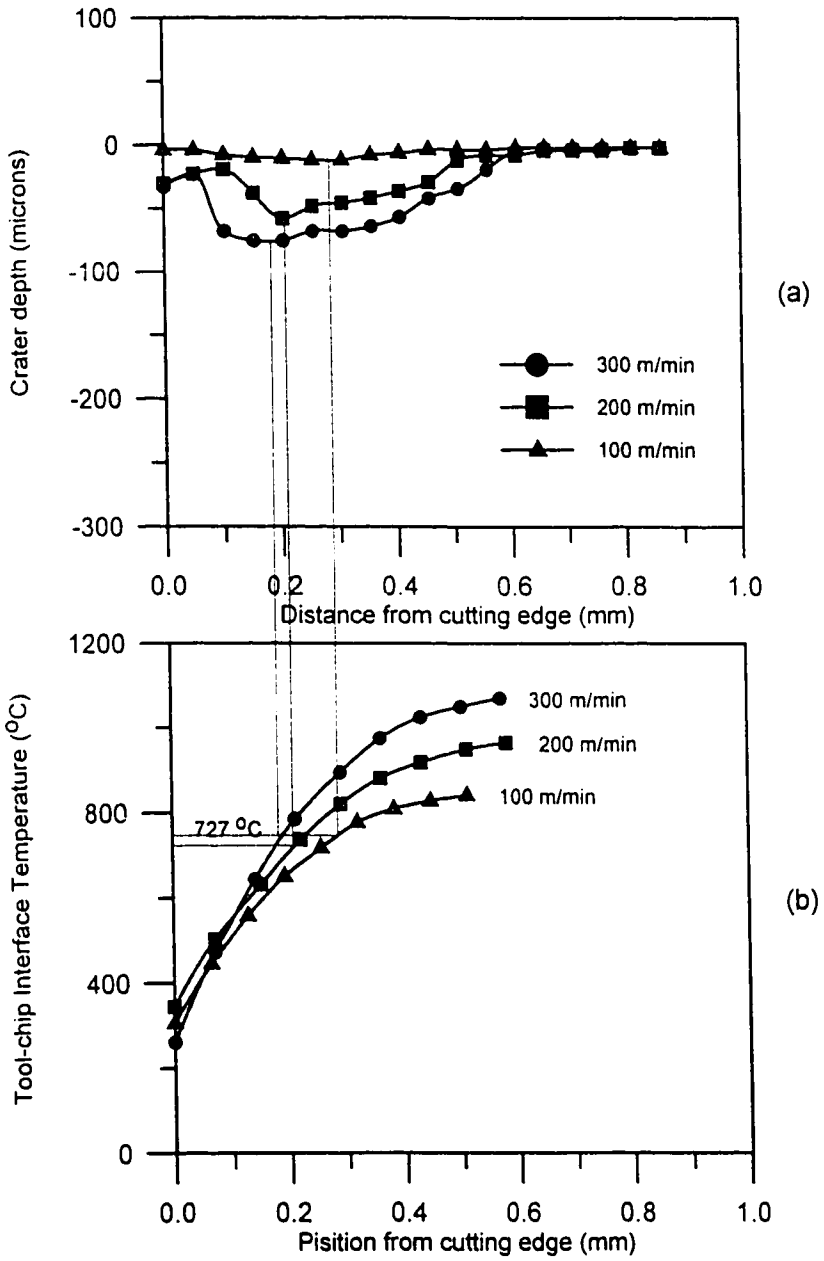

Fig.4.18: (a) The measured depth profiles of the crater (b) predicted tool-chip interface temperature distribution along the contact length, after machining AISI 1080 steel for 20 seconds with a cemented carbide tool (K1) for cutting speeds 100, 200 and 300 m/min. respectively.

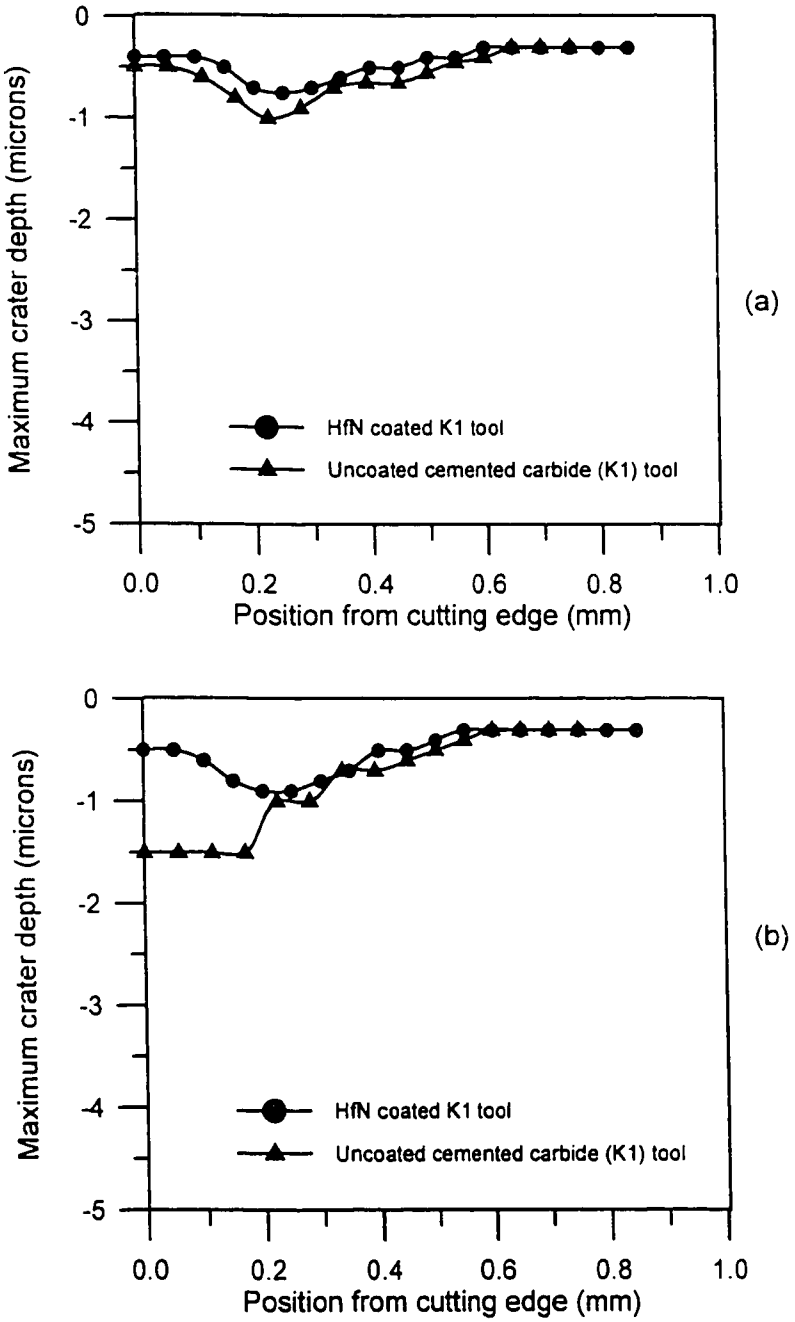

Fig. 4.19: Comparison of the measured crater depth profile for uncoated and HfN-coated cemented carbide (k1) tool when machining ferritic ductile iron at cutting speed of (a) 200 m/min. and (b) 300 m/min.

Table 4.10: Data from crater depth profile and temprature measurements and calculated tool-chip interface tempratures for ferritic ductile iron and AISI 1020 steel and AISI 1080 steel.

Work piece Material	Tool	Cutting Speed (m/min)	Measured average tool-chip interface temperature (^{0}C)	Calculated average tool-chip iterface temperature (^{0}C)	Calculated maximum tool-chip interface temperature (^{0}C)	Calculated temperature at position of maximum crater depth (^{0}C)	Phrase transformation temprature of material (^{0}C)	Location of maximum depth of crater from cutting edge (mm)
Dutile Iron	K1	100	555	637	829	740	835	0.34
Dutile Iron	K1	200	760	780	950	825		0.24
Dutile Iron	K1	300	845	870	982	833		0.17
Dutile Iron	K1-HfN	100	---	---	--	---		0.38
Dutile Iron	K1-HfN	200	---	---	--	---		0.30
Dutile Iron	K1-HfN	300	---	---	--	---		0.25
AISI 1020 steel	K1	100	---	---	840	710	840	0.65
AISI 1020 steel	K1	200	855	790	960	840		0.55
AISI 1020 steel	K1	300	940	856	991	835		0.41
AISI 1080 steel	K1	100	---	660	841	726	727	0.28
AISI 1080 steel	K1	200	---	751	965	729		0.21
AISI 1080 steel	K1	300	---	798	1070	730		0.19

4.4 Effect of Phase Transformation on Chip Segmentation

The purpose of this section is to present as comprehensive as possible, a study into the mechanism of chip segmentation and its influence on tool wear and surface finish at high cutting speeds. Fe-Ni-C alloys were used in their quenched (hardened) condition in order to obtain a wide range of chip morphologies within a narrow speed range achievable in the laboratory. The study was aimed at answering the basic question: Is phase transformation the cause or the effect of shear localisation in metal cutting of hardened alloy steels. The study investigated as throughly as possible the role of thermal softening due to phase transformation in causing shear localisation; the effect of the phase transformation temperature on the critical speed for chip segmentation; the effect of eliminating thermal softening due to phase transformation on chip morphology and tool wear; and the effects of metal cutting variables (speed, feed, depth of cut and lubricants) on chip morphology and tool wear during high speed machining. In addition an attempt is made to provide a comprehensive data base on force, contact length, chip thickness, and shear band thickness measurements and the values of stresses and temperature calculated from these measured parameters.

4.4.1 The Evidence of Phase Transformation in the Chips

Figs. 4.20 and 4.21 are optical micrographs of the cross sectional view of typical chips obtained during machining of Fe-28.9%Ni-0.1%C alloy at cutting speeds of 1 m/min and 400 m/min respectively. An interesting feature is that a discontinuous chip of the type whose mechanism of formation has been described by Cook et al [55] is observed at this low cutting speed. Deformation in the primary shear zone is homogeneous and the structure remains martensitic. At 400 m/min a fully segmented chip is formed exhibiting a white etching transformation shear band in the primary shear zone, in addition to the transformation shear band in the secondary shear zone occurring parallel to the tool-chip contact. This is indicative of heterogeneous deformation in both primary and secondary

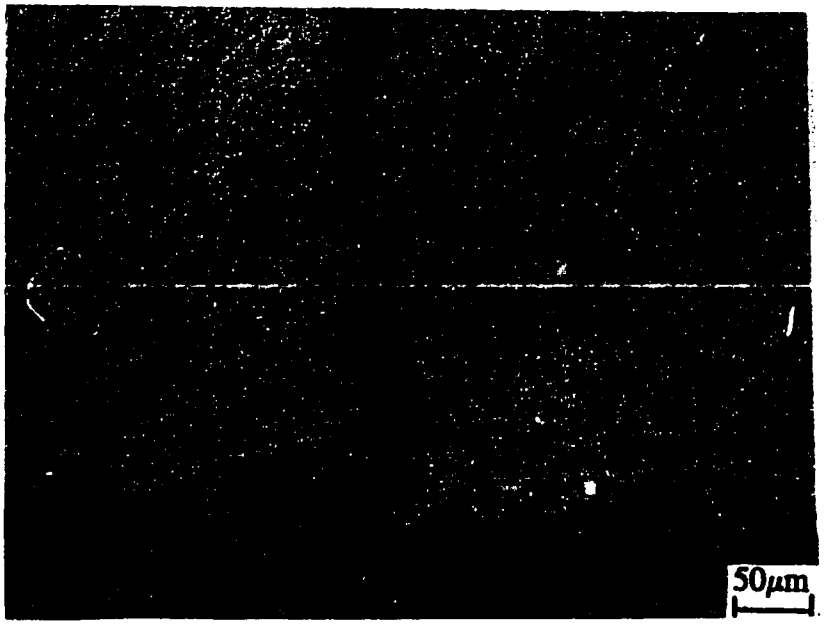

Fig. 4.20: Optical micrograph of a discontinuous chip obtained at a cutting speed of 1 m/min., during the machining of martensitic Fe-28.9Ni-0.1C alloy. Note that there are no phase changes of the microstructure.

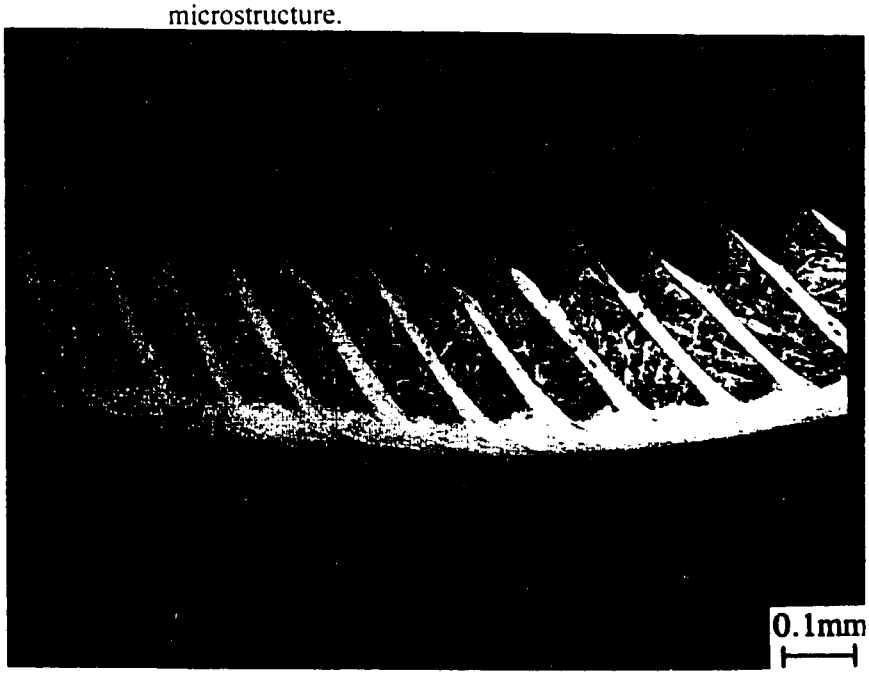

Fig. 4.21: Optical micrograph of a fully segmented chip obtained at a cutting speed of 400 m/min., showing transformation shear bands enveloping the chip segments during machining of Fe-28.9%Ni-0.10%C alloy. The white band is the region that has undergone phase transformation from martensite to austenite at 400°C.

shear zones. The individual segments are surrounded with the white etching band. These white etching regions could not be resolved with optical or SEM microscopy. The white etching regions are confirmed by X-ray diffraction analysis to be formed by the reversion of martensite into austenite, and hence are referred to as transformation shear bands. Fig. 4.22 is an X-ray result illustrating the presence of austenite in the shear bands formed at a cutting speed of 400 m/min and its absence in the chips formed at 1 m/min.

4.4.2 Microhardness of the Chips

The variations in the hardness in various regions of the chip, i.e., the chip body, the primary shear bands and the secondary shear bands were determined. Table 4.11 summarises the results from microhardness measurements carried out on the Fe-Ni-C alloys. The hardness results for Fe-28.9Ni-0.1C alloy are presented in both annealed (austenitic) and quenched (martensitic) conditions. The hardness of the austenitic workpiece is 151 VHN. Due to strain hardening the hardness of the chips obtained at a cutting speed of 5 m/min. is more than three times the hardness of the workpiece. Heterogeneous deformation at the secondary shear zone is indicated by the higher hardness of 484 VHN at the secondary shear zone compared to 421 VHN at the primary shear zone. At a cutting speed of 75 m/min thermal softening starts to dominate over strain hardening and causes reduction in hardness at both primary and secondary shear zone. In this case heterogeneous deformation in the secondary shear zone is shown by the lower hardness value of 333 VHN compared to 385 VHN in the primary shear zone. In this case the effect of thermal softening is more in the secondary shear zone than in the primary shear zone. At higher strain rates obtained at a higher cutting speed of 350 m/min., the secondary shear zone experiences more softening due to higher temperature rise in this region. The hardness is lowered to 303 VHN.

The hardness of the martensitic workpiece was 374 VHN. At 1 m/min (i.e low strain rates

~10/s) homogeneous deformation dominated by strain hardening occurs in the primary shear zone raising the hardness to 603 VHN. Further deformation in the secondary shear zone is heterogeneous with dominating strain hardening which raises the hardness to 675 VHN. At 400 m/min (i.e. high strain rate $\sim 10^5$/s) deformation is heterogeneous with thermoplastic shear localisation at both primary and secondary shear zones. The hardness of the primary and secondary shear bands are 402 and 369 VHN respectively. The hardness in the chip body where the microstructure remains unchanged is 473 VHN.

In the Fe-18.9%Ni-0.1%C and Fe-9.7%Ni-0.1%C alloys the thermoplastic shear bands which undergo reversion of martensite to austenite are rapidly quenched by the surrounding material to form a more refined martensitic structure which is harder. Hence the shear bands are harder than the original martensite. In the Fe-1.4%Ni-0.1C alloy heterogeneous deformation in the secondary shear zone at low cutting speeds where strain hardening is dominant over thermal softening leads to a higher hardness at the secondary shear zone than the primary shear zone. A lower hardness occurs at higher cutting speeds suggesting that thermal softening is more dominant.

4.4.3 The Effect of Cutting Speed on Chip Morphology and Tool Wear

The optical micrographs in Figs. 4.23-4.32) show the change in chip morphology as a function of cutting speed during machining of quenched martensitic Fe-28.9%Ni-0.10%C alloy and the corresponding changes in tool wear. The following observations are made concerning change in chip morphology with increase of cutting speed:

(i) At 1 m/min discontinuous chips which do not show any phase changes are formed. The cracks appear to start from the bottom of the chips and propagate to the free surface. Deformation is homogeneous in the chip body.

(ii) At 5 m/min the chips formed appear to undergo inhomogeneous deformation in the

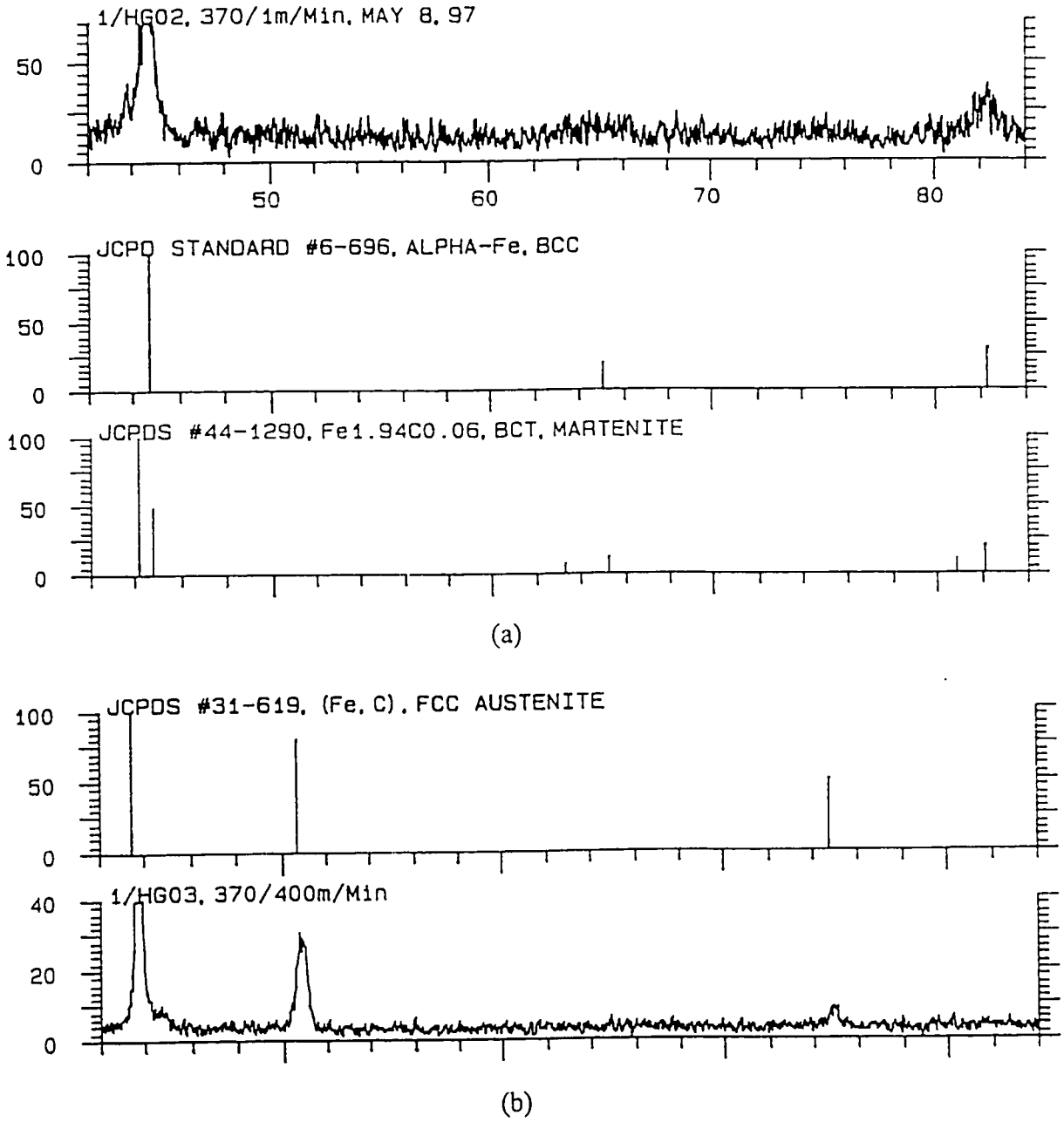

Fig. 4.22: X-ray diffraction intensities taken from the chips obtained during machining of martensitic Fe-28.9%Ni-0.10%C alloy at (a) 1 m/min showing that the microstructure mains body centred tetragonal (bct) (b) 400 m/min showing that the martensitic microstructure reverts to austenite in the white etching shear bands formed at high cutting speeds where fully segmented chips are formed.

Table 4.11: Vickers micro-hardness values measured from the chips obtained in the machining of Fe-Ni-C alloys with varying nickel content.

Material and heat treatment condition	Cutting speed (m/min)	(A) Primary shear zone (or band) hardness (VHN_{50})	(B) Chip body hardness (VHN_{50})	(C) Secondary shear zone (or band) hardness (VHN_{50})
Fe-28.9Ni-0.1C (Quenched Martensitic)	Workpiece	374±29		
	1	603±23	603±23	675±17
	400	402±26	473±28	369±15
Fe-28.9Ni-0.1C (Annealed Austentic)	Workpiece	151±14		
	5	421±24	421±24	484±19
	75	385±18	385±18	333±25
	350	362±22	362±22	303±27
Fe-18.9Ni-0.1C (Quenched Martensitic)	Workpiece	454±26		
	1	689±36	689±36	755±33
	75	554±21	554±21	608±23
	350	640±28	443±24	554±29
Fe-9.7Ni-0.1C (Quenched Martensitic)	Workpiece	396±15		
	1	640±23	640±23	701±25
	75	460±41	460±41	438±11
	150	524±15	453±25	358±16
	400	584±16	412±23	466±21
Fe-1.4Ni-0.1C (Quenched)	Workpiece	223±29		
	1	593±19	593±19	549±31
	75	362±17	362±17	381±26
	400	317±14	317±14	303±21

primary shear zone. There is a thin white layer formed at the bottom i.e., the secondary shear zone. White layers of transformed martensite are also observed running from the bottom of the chip into the body of the chip but not through the whole thickness of the chip.

(iii) At 10 m/min deformation in the primary shear zone is inhomogeneous. At the secondary shear zone deformation is localised with formation of a transformation shear band. Phase transformation appears to occur between the chip segments formed. The thickness of the zone is larger and it runs through the thickness of the chip.

(vi) At 25 to 50 m/min the chip morphology is continuous with homogeneous deformation in the primary shear zone and the structure is martensitic; the secondary shear zone exhibits a white etching transformation shear band even at this low cutting speed, indicative of heterogeneous deformation in the secondary shear zone. The white etching regions are confirmed by X-ray studies to be austenite, and hence are referred to as transformation shear bands. The corresponding tool crater wear is shown in the SEM photographs the cutting edges of the tools. The development of seizure region of tool-chip contact can be distinguished but no significant wear is noted because of the short cutting time.

(v) Figs. 4.28(a) shows the chip morphology at a cutting speed of 75 m/min. The chips exhibit partial segmentation. White etching transformation shear band is seen corresponding to the primary shear zone, in addition to the transformation shear band in the secondary shear zone occurring parallel to the tool-chip contact. The corresponding tool wear at 75 m/min. in Fig. 4.28(b) shows the onset of crater wear. Fig. 4.29(a) shows a fully segmented chip morphology at a cutting speed of 150 m/min. and the corresponding tool wear in Fig. 4.29(b) shows pronounced crater wear at the end of 10 seconds of machining. Note the degree of segmentation of the chip increasing with cutting speed and the crater draws closer to the cutting edge. Fig. 4.32(a) shows the fully segmented chip morphology obtained at the highest cutting speed of 456 m/min. used in the present investigation. At 456 m/min

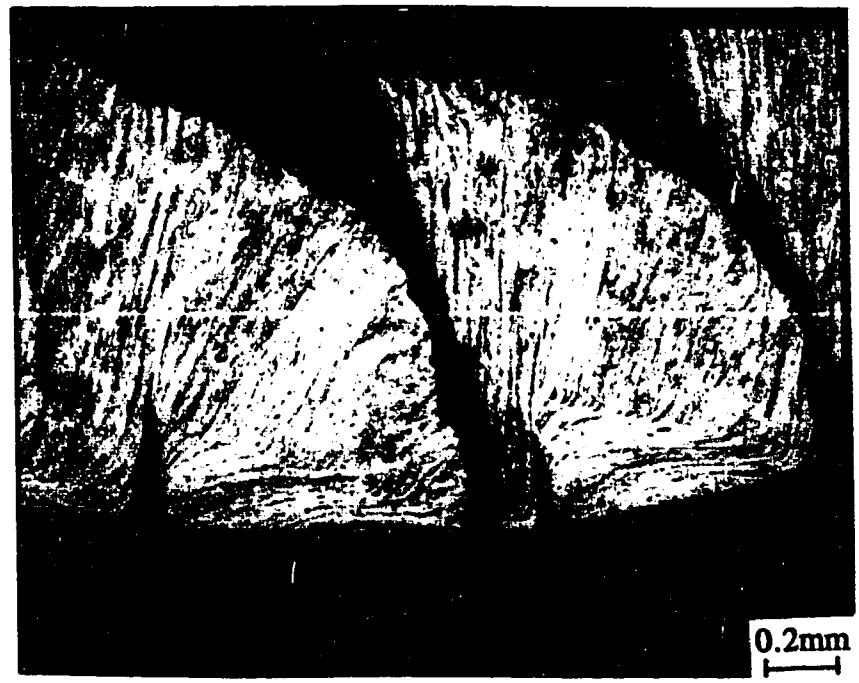

Fig. 4.23(a): Optical micrograph of a discontinuous chip formed during machining of Fe-28.9%Ni-0.10%C alloy at a cutting speed of 1 m/min.

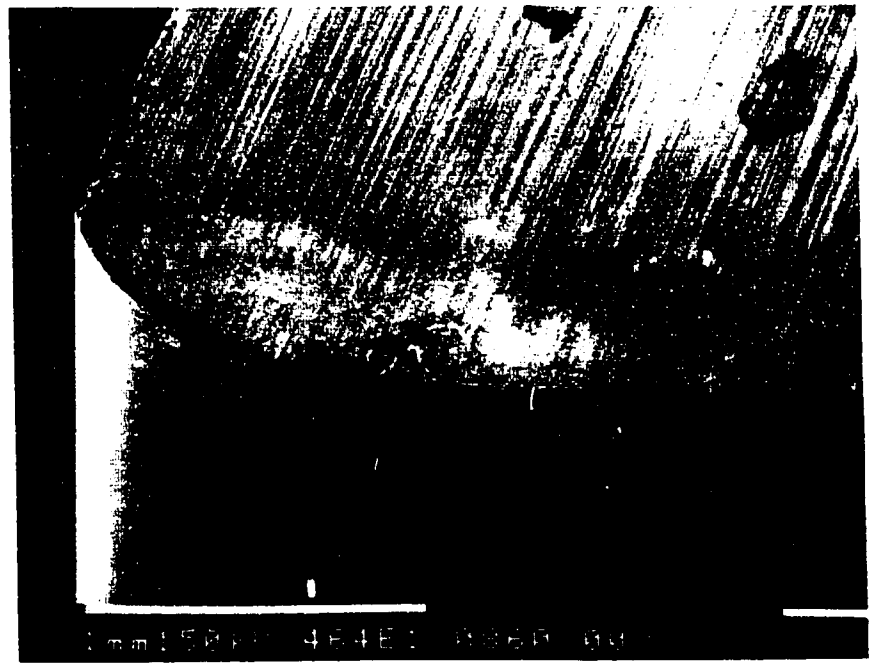

Fig.4.23(b): SEM picture of the tool rake face after 30 seconds machining of Fe-28.9%Ni-0.10%C alloy at 1 m/min.

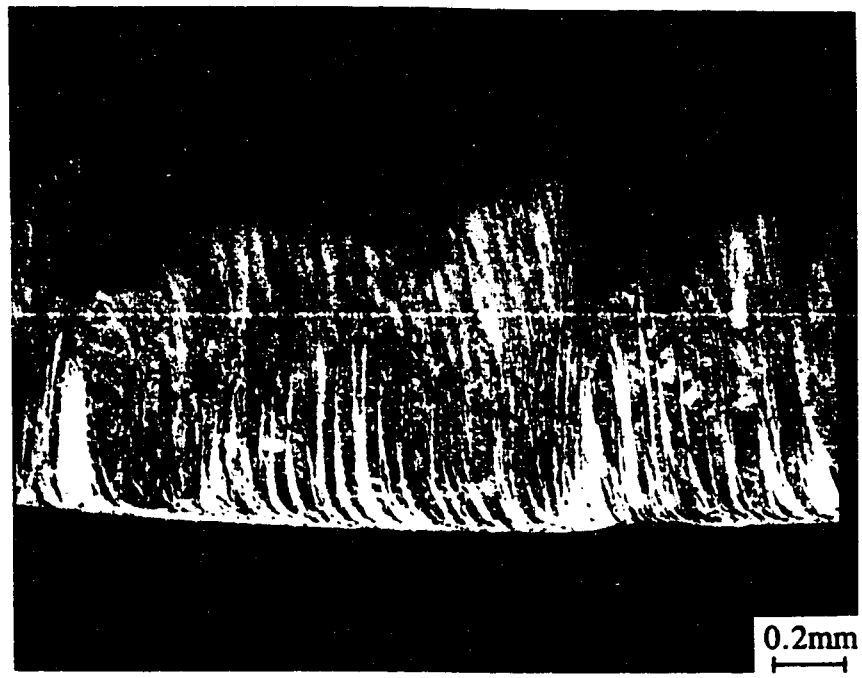

Fig.4.24(a) Optical micrograph showing the morphology of the chips formed during machining of Fe-28.9%Ni-0.10%C alloy at 5 m/min. Note the phase changes in thin bands running from the bottom of the chip and ending in the chip body.

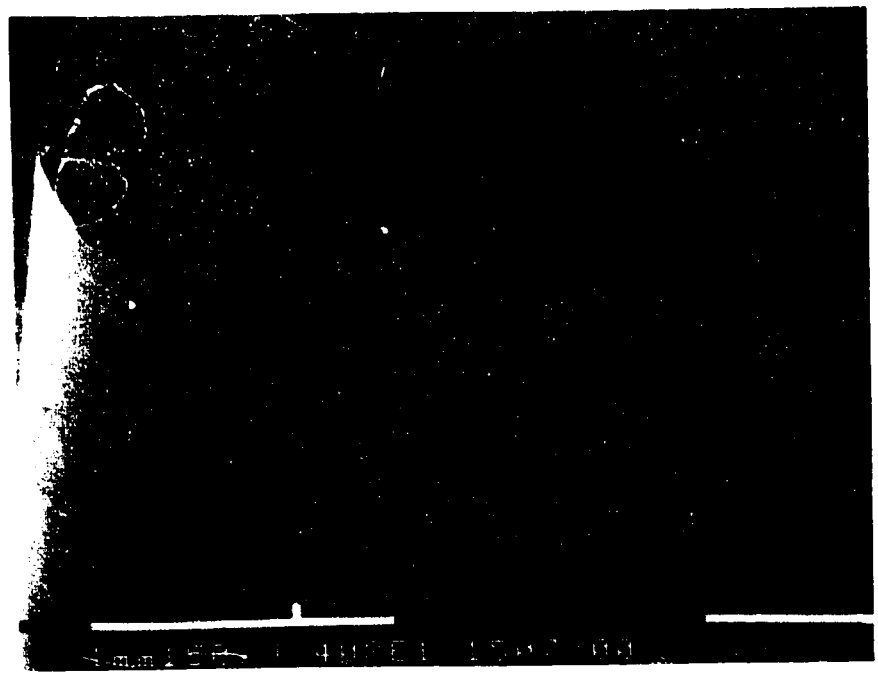

Fig.4.24(b): SEM picture of the tool rake face after 30 seconds machining of Fe-28.9%Ni-0.10%C alloy at 5 m/min.

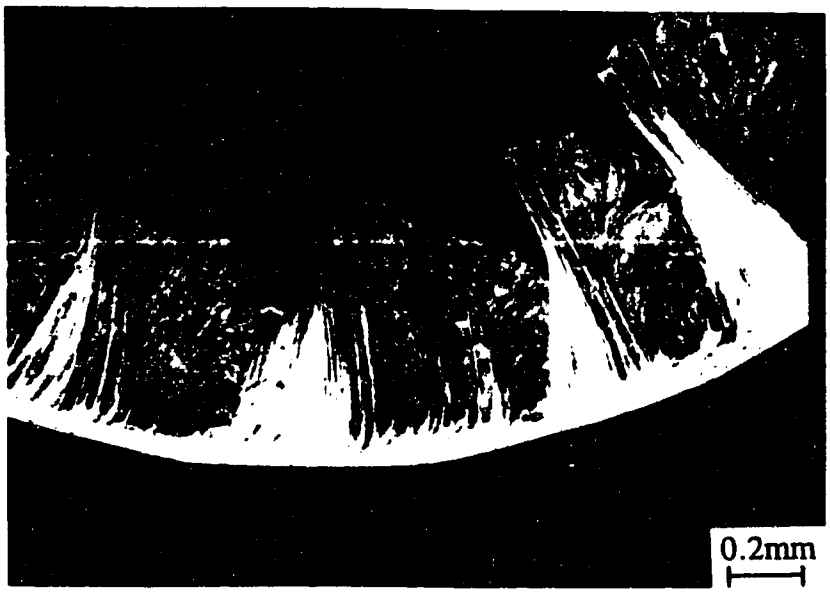

Fig.4.25(a) Optical micrograph showing the morphology of the chips formed during machining of Fe-28.9%Ni-0.10%C alloy at 10 m/min. Note the phase changes in thick bands running through the thickness of the chip.

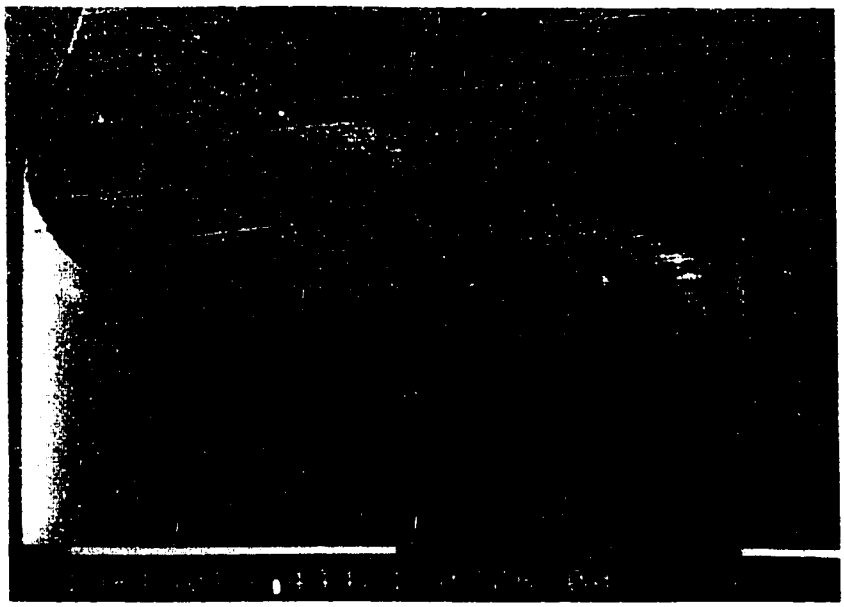

Fig.4.25(b): SEM picture of a tool rake face after 10 seconds machining of Fe-28.9%Ni-0.10%C alloy at 10 m/min.

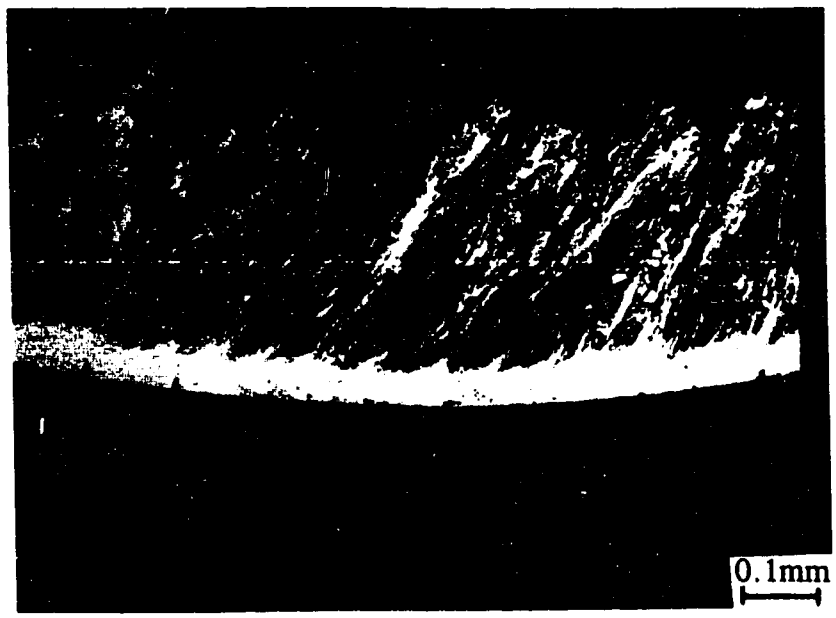

Fig. 4.26(a): Optical micrograph of a continuous or flow chip obtained at a cutting speed of 25 m/min, showing a transformation shear band located at and parallel to the tool-chip interface at a low cutting speed in Fe-28.9%Ni-0.10%C alloy. The white band is the region that has undergone phase transformation from martensite to austenite at 400°C.

Fig. 4.26(b): SEM picture of tool crater wear obtained at the end of 10 seconds machining of an Fe-28.9%Ni-0.10%C alloy at a cutting speed of 25 m/min.

Fig. 4.27(a): Optical micrograph of a continuous chip obtained at a cutting speed of 50 m/min., showing transformation shear band located parallel to the tool-chip interface during machining of Fe-28.9%Ni-0.10%C alloy. The white band is the region that has undergone phase transformation from martensite to austenite at 400°C.

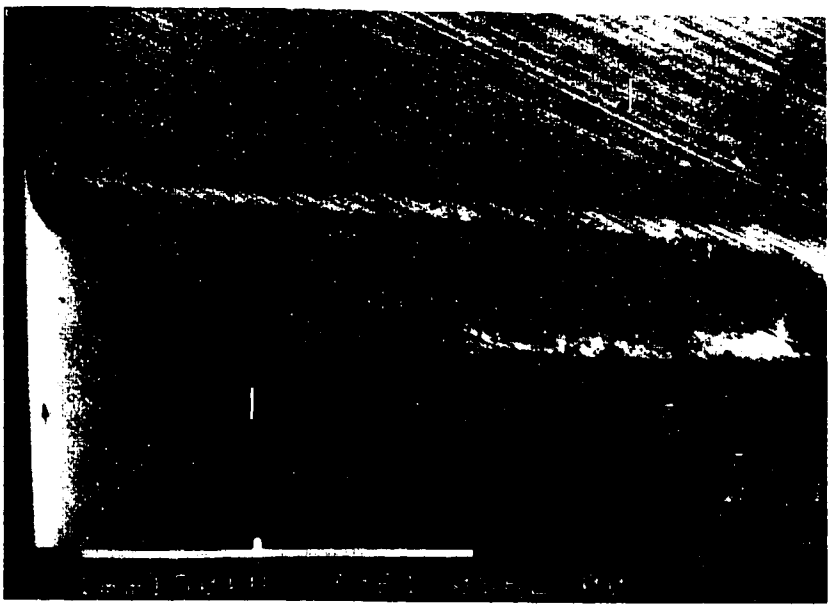

Fig. 4.27(b): SEM picture of tool crater wear obtained at the end of 10 seconds machining an Fe-28.9%Ni-0.10%C alloy at a cutting speed of 50 m/min. Note the location of the crater at some distance (0.33 mm) from the cutting edge.

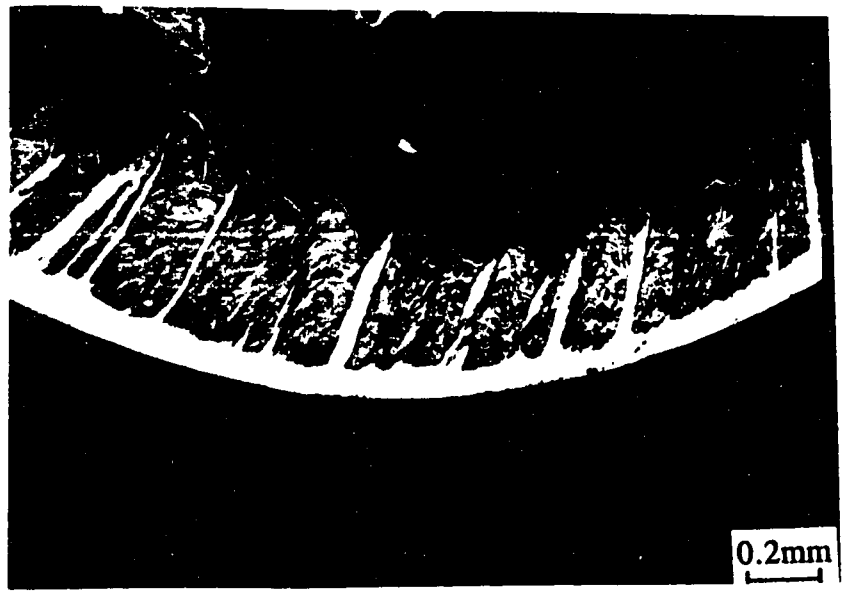

Fig. 4.28(a): Optical micrograph of a partially segmented chip obtained at a cutting speed of 75 m/min., showing transformation shear band located parallel and at an angle to the tool-chip interface during machining of Fe-28.9%Ni-0.10%C alloy. The white band is the region that has undergone phase transformation from martensite to austenite at 400°C.

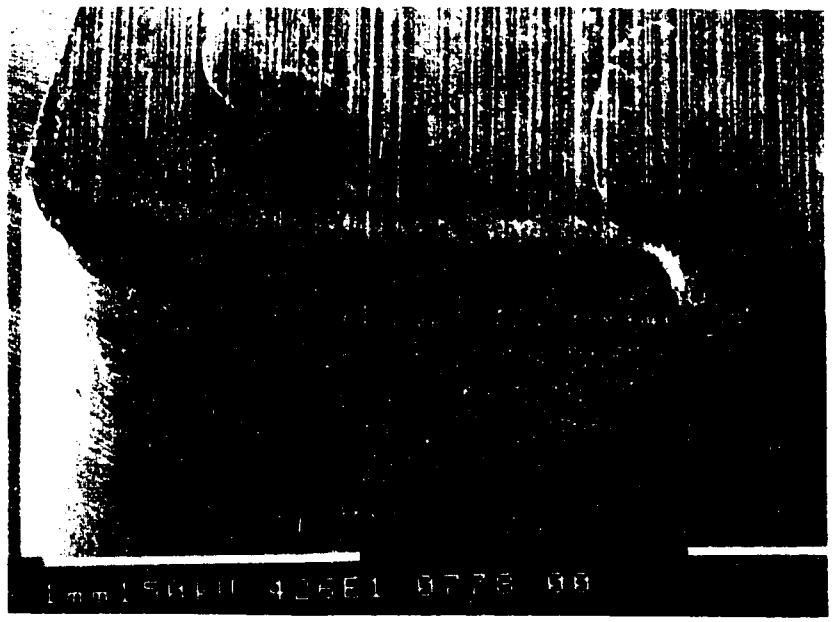

Fig. 4.28(b): SEM picture of tool crater wear obtained at the end of 10 seconds machining an Fe-28.9%Ni-0.10%C alloy at a cutting speed of 75 m/min. Note the location of the crater at some distance (0.28 mm) from the cutting edge.

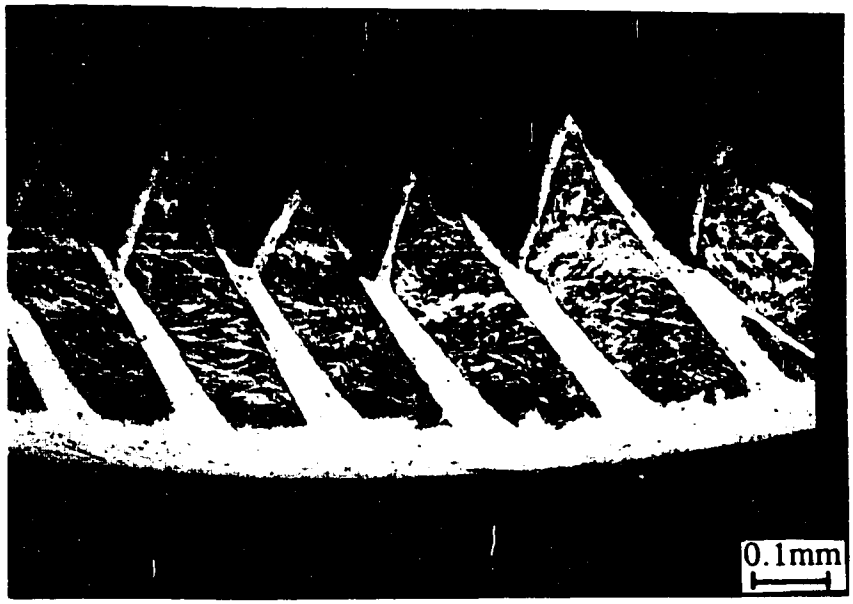

Fig. 4.29(a): Optical micrograph of a fully segmented chip obtained at a cutting speed of 150 m/min., showing transformation shear band enveloping the segmented chip in Fe-28.9%Ni-0.10%C alloy. The white region that has undergone phase transformation from martensite to austenite at 400°C.

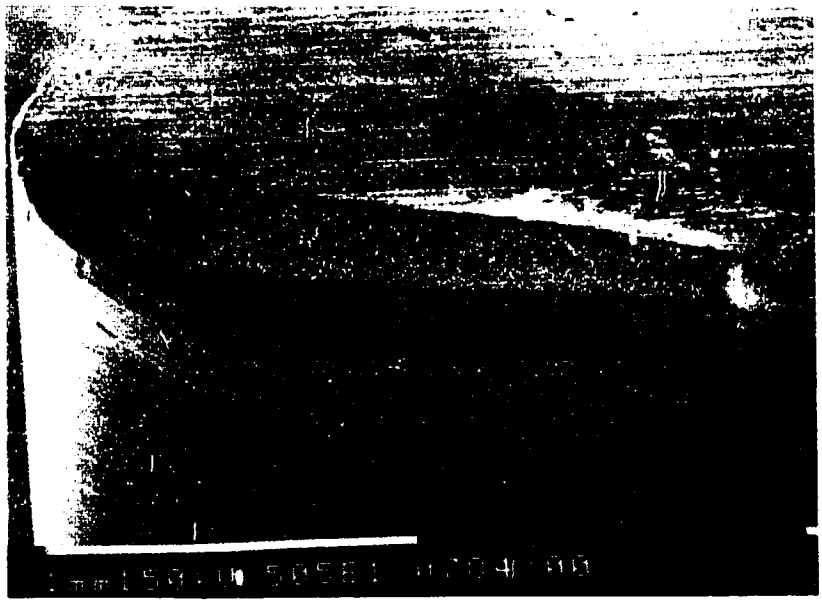

Fig. 4.29(b): SEM picture of tool crater wear obtained at the end of 10 seconds machining of an Fe-28.9%Ni-0.10%C alloy at a cutting speed of 150 m/min. Note the location of the crater closer to the cutting edge of the tool (0.18 mm away).

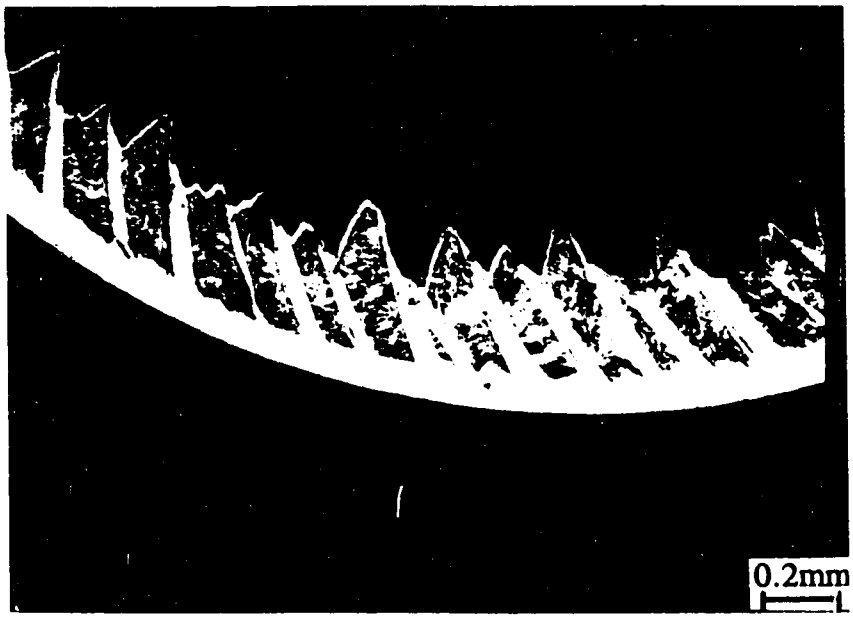

Fig. 4.30(a): Optical micrograph of a fully segmented chip obtained at a cutting speed of 250 m/min., showing transformation shear band enveloping the segmented chip in Fe-28.9%Ni-0.10%C alloy. The white region that has undergone phase transformation from martensite to austenite at 400°C.

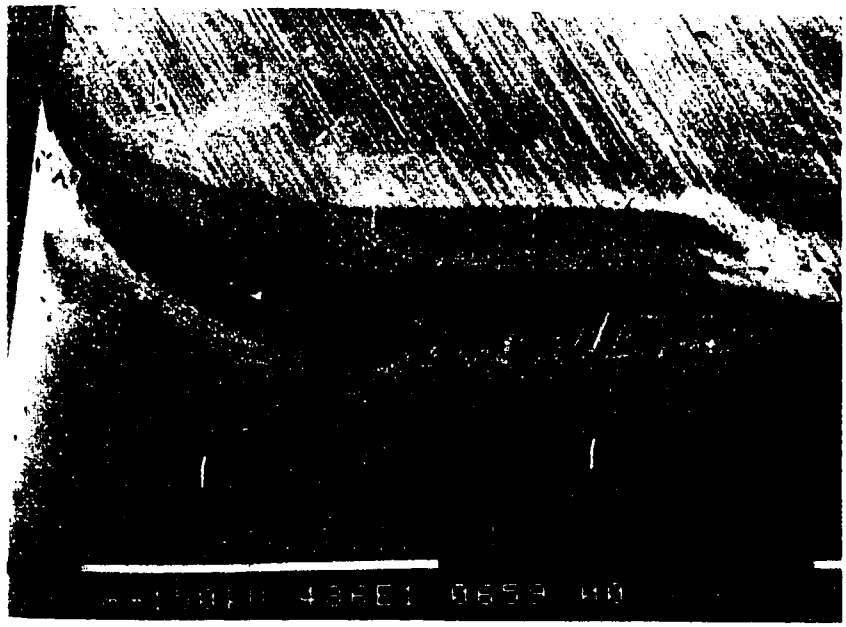

Fig. 4.30(b): SEM picture of tool crater wear obtained at the end of 1 second machining of an Fe-28.9%Ni-0.10%C alloy at a cutting speed of 250 m/min. Note the location of the crater closer to the cutting edge of the tool (0.12 mm away).

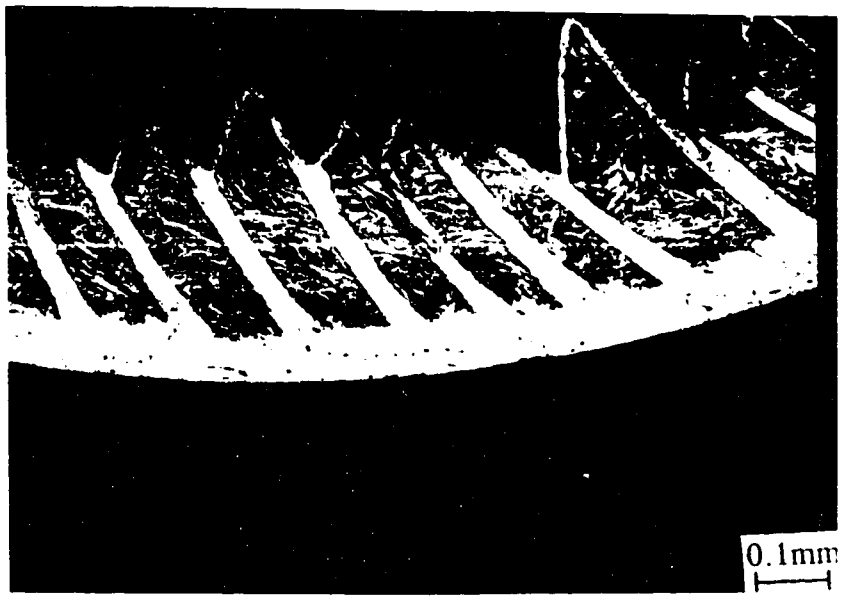

Fig. 4.31(a): Optical micrograph of a fully segmented chip obtained at a cutting speed of 350 m/min., showing transformation shear band enveloping the segmented chip in Fe-28.9%Ni-0.10%C alloy. The white region that has undergone phase transformation from martensite to austenite at 400°C.

Fig. 4.31(b): SEM picture of tool crater wear obtained at the end of 1 seconds machining of an Fe-28.9%Ni-0.10%C alloy at a cutting speed of 350 m/min. Note the location of the crater closer to the cutting edge of the tool (0.12 mm away).

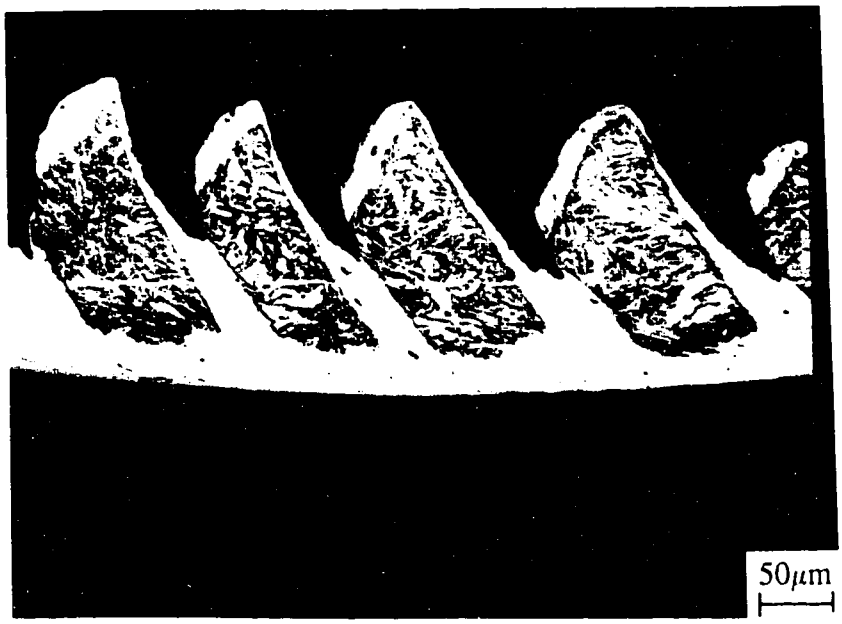

Fig. 4.32(a): Optical micrograph of a fully segmented chip obtained at a cutting speed of 456 m/min., showing transformation shear band enveloping the segmented chip in the machining of Fe-28.9%Ni-0.10%C alloy. The white band is the region that has undergone phase transformation from martensite to austenite at 400°C.

Fig. 4.32(b): SEM picture of tool crater wear obtained at the end of 1 second machining of an Fe-28.9%Ni-0.10%C alloy at a cutting speed of 456 m/min. Note the location of the crater closest to the cutting edge of the tool (0.12 mm away), leads to damage of the cutting edge of the tool.

the chip segments are almost separated through the whole thickness. Fig. 4.32(b) is an SEM picture of the tool crater wear. The crater is localised nearest to the cutting edge, damaging the tool cutting edge and extending into flank face as well. It should be pointed out that even though the onset of segmentation of the chip takes place at 75 m/min., the crater is located some distance away from the cutting edge. With increase in cutting speed up to 350 m/min., the degree of segmentation of the chip increases progressively and the crater moves closer to the cutting edge. However, at 456 m/min., the chips are segmented to a remarkable degree and the crater appears to be localised at the cutting edge itself. The loss of cutting edge of the tool impairs the surface finish. Figs. 4.33 and 4.34 show the morphology of the surface of martensitic Fe-28.9%Ni-0.10%C alloy workpiece after machining at cutting speeds of 25 and 400 m/min, respectively. At 25 m/min the surface finish is smooth without any microstructural change. At 400 m/min., the machined surface of workpiece exhibits microstructural features characteristic transformed region and the surface finish is rough.

Table 4.12(a) shows a summary of the measured cutting forces and contact length and the calculated stresses as a function of cutting speed during the machining of quenched martensitic Fe-28.9%Ni-0.10%C alloy. The stresses in the shear zones were calculated using Merchant's model [60] for the mechanics of metal cutting. Table 4.12(b) is a summary of the calculated values for the strain rate and temperature in the primary shear zone as a function of cutting speed. The primary shear zone temperature has been calculated using Loewen and Shaw's [75] model for conditions of continuous chip morphology and Dodd and Bai's [77] method for estimating the temperature in a shear band for the cases when segmented chips are formed as a result of instability and thermoplastic shear localisation. The expression developed by Dodd and Bai [77] relates the thickness of the shear band to the temperature, flow stress, strain rate and thermal conductivity as given in equation 2.14. The shear band thickness δ was measured from the optical micrographs of the chips shown in Figs. 4.23(a)- 4.32(a).

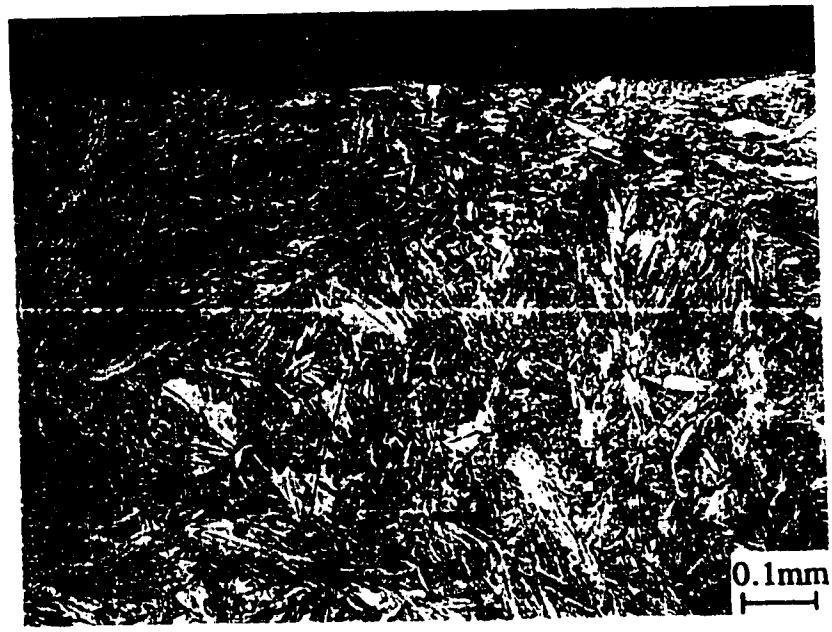

Fig. 4.33: Optical micrograph taken from the cross-section of a Fe-28.9%Ni-0.10%C alloy after machining the workpiece at a cutting speed of 25 m/min. Note the absence of a white (transformed) layer on the surface.

Fig. 4.34: Optical micrograph taken from the cross-section of a Fe-28.9%Ni-0.10%C alloy after machining the workpiece at a cutting speed of 400 m/min. Note the formation of a white (transformed) layer on the surface and the rough surface finish compared with the surface finish at 25 m/min.

Thermo-physical properties data for the Fe-Ni-C alloys was obtained from references [173] and [174]. The value of τ used is the same value calculated at the primary shear zone B. The fraction of plastic work converted into heat was assumed to be 0.9. It is shown that temperature in the shear band exceeds the phase transformation temperature of the workpiece. The phase transformation temperature corrected for the effects of pressure is ~ 360^{0}C. The deformation time and the time taken for the heat from plastic work to diffusion from the shear zone are included in the table. The deformation time t_D is calculated as $t_D = \delta/Vs$ where δ is the shear zone or shear band thickness and Vs is the shear velocity in the primary shear zone. The time for heat diffusion t_H was calculated as $\delta \approx 2\sqrt{\alpha t_H}$ where δ is the shear zone thickness and α is the thermal diffusivity of the alloy.

The results for the other three alloys viz; Fe-18.9Ni-0.1C, Fe-9.7Ni-0.1C and Fe-1.4Ni-0.1C alloys are summarised in Tables 4.13, 4.14 and 4.15 respectively.

4.4.4 The effect of Thermal Softening on Critical Speed for Chip Segmentation

The effect of increasing the nickel content is to decrease the martensite to austenite phase transformation temperature. Since thermal softening accompanies martensite to austenite phase transformation, shear instability will be localised by thermal softening accompanying phase transformation. Shear localisation in the primary shear zone, in turn, promotes chip segmentation.

Figs. 4.35-4.40 show the change in chip morphology and the corresponding tool wear as a function of cutting speed during the machining of quenched Fe-18.9%Ni-0.10%C alloy. The onset for full chip segmentation in this alloy occurs at 150 m/min as shown in Fig. 4.39 (a). Fig. 4.39(b) shows the corresponding tool crater wear, located at about 0.2 mm from the cutting edge of the tool.

Table 4.12(a): Measured cutting forces and contact length and calculated stresses as a function of cutting speed during machining of as-quenched Fe-28.9Ni-0.1C alloy.

Cutting speed	Cutting forces			Shear angle	Tool-chip interface Contact length	Calculated Stresses at the Primary shear zone		Calculated stresses at the secondary shear zone	
(m/min)	Fx (N)	Fy (N)	Fz (N)	(deg.)	(mm)	Normal stress (Mpa)	Shear stress (Mpa)	Normal stress (Mpa)	Shear Stress (Mpa)
1	776	243	1445	14.4	0.94	551	575	728	498
5	941	297	1794	18.8	0.90	941	859	945	633
10	881	233	1545	25.2	0.76	1219	830	960	868
25	624	168	1282	30.0	0.63	1159	760	969	600
50	440	124	1144	31.1	0.56	979	741	982	496
75	376	114	1077	33.0	0.54	964	724	962	450
100	374	108	1053	33.7	0.60	966	698	938	399
150	411	120	1039	34.4	0.61	1026	671	818	424
200	511	152	1048	35.8	0.61	1180	607	817	510
250	549	152	1020	36.6	0.51	1287	536	947	643
300	589	157	987	39.1	0.52	1438	420	894	667
350*	758	235	1015	42.8	0.47	1669	270	1002	935
400*	892	276	1194	46.2	0.43	2101	213	1289	1202

* The experimental values at these cutting speeds are subject to higher uncertainties.

Table 4.12(b): Calculated values of temperature , deformation time and heat diffusion time as a function of cutting speed during machining of as-quenched Fe-28.9Ni-0.1C alloy.

Cutting speed (m/min)	Shear Velocity (m/s)	Measured shear zone thickness (μm)	Strain rate (/s)	Fraction of heat retained in shear zone	Calculated temperature rise using Dodd and Bai's model (^{0}C)	Deformation time (μs)	Heat diffusion time (μs)
1	0.02	--	38	0.30	181	6549	1070
5	0.09	--	250	0.51	360	1289	1070
10	0.18	--	683	0.63	330	623	1070
25	0.46	--	2078	0.74	310	241	1070
50	0.92	--	4333	0.76	319	119	1070
75	1.41	47	16343	0.78	384	33	195
100	1.89	46	22832	0.81	502	24	186
150	2.86	45	35890	0.82	623	16	178
200	3.87	42	53843	0.84	742	11	155
250	4.87	38	76464	0.86	792	8	127
300	6.02	35	108390	0.90	834	6	108
350	7.35	34	146968	0.92	866	5	102
400	8.83	32	199085	0.93	883	4	90

Table 4.13(a): Measured cutting forces and contact length and calculated stresses as a function of cutting speed during machining of as-quenched Fe-18.9Ni-0.1C alloy.

Cutting speed	Cutting forces			Shear angle	Tool-chip interface Contact length	Calculated Stresses at the Primary shear zone		Calculated stresses at the secondary shear zone	
(m/min)	Fx (N)	Fy (N)	Fz (N)	(deg.)	(mm)	Normal stress (Mpa)	Shear stress (Mpa)	Normal stress (Mpa)	Shear Stress (Mpa)
1	854	422	2088	12.7	1.16	589	776	861	487
5	761	377	1961	13.8	0.95	595	784	989	535
10	895	333	1833	21.7	0.84	1117	964	1037	661
25	631	228	1481	23.7	0.76	939	843	932	525
50	457	179	1301	27.4	0.71	919	825	883	424
75	375	135	1143	31.8	0.50	957	775	1104	497
100	436	148	1165	37.4	0.46	1259	757	1218	609
150	540	142	1094	40.5	0.41	1423	588	1270	795
200	631	160	1148	41.0	0.37	1576	556	1469	1012
250	673	205	1036	42.0	0.31	1571	386	1566	1276
300	842	269	1156	43.0	0.29	1889	319	1853	1692
350	806	189	1145	45.1	0.27	1908	303	1979	1712

Table 4.13(b): Calculated values of temperature , deformation time and heat diffusion time as a function of cutting speed during machining of as-quenched Fe-18.9Ni-0.1C alloy.

Cutting speed (m/min)	Shear Velocity (m/s)	Measured shear zone thickness (μm)	Strain rate (/s)	Fraction of heat retained in shear zone	Calculated temperature rise using Dodd and Bai's model (^{0}C)	Deformation time (μs)	Heat diffusion time (μs)
1	0.02	110	33	0.24	230	6578	631
5	0.08	110	182	0.42	289	1312	631
10	0.17	110	582	0.56	333	636	631
25	0.44	110	1598	0.68	350	252	631
50	0.90	110	3749	0.76	373	123	631
75	1.40	110	6670	0.80	396	79	631
100	1.97	110	10837	0.83	403	56	631
150	3.06	48	41391	0.90	504	16	120
200	4.10	38	70864	0.91	514	9	75
250	5.20	36	96603	0.94	552	7	67
300	6.32	34	126790	0.95	558	5	60
350	7.60	32	168165	0.96	579	4	53

Table 4.14(a): Measured cutting forces and contact length and calculated stresses as a function of cutting speed during machining of as-quenched Fe-9.7Ni-0.1C alloy.

Cutting speed	Cutting forces			Shear angle	Tool-chip interface Contact length	Calculated Stresses at the Primary shear zone		Calculated stresses at the secondary shear zone	
(m/min)	Fx (N)	Fy (N)	Fz (N)	(deg.)	(mm)	Normal stress (Mpa)	Shear stress (Mpa)	Normal stress (Mpa)	Shear Stress (Mpa)
1	1423	898	2404	22.4	1.25	1818	1163	899	754
5	604	359	1533	24.8	1.00	1037	888	733	417
10	924	452	1730	19.8	0.98	1016	837	834	600
25	748	390	1482	23.7	0.90	1062	790	779	539
50	423	182	1066	30.5	0.73	919	671	700	378
75	392	176	986	33.7	0.54	969	623	875	476
100	354	167	950	33.7	0.51	913	614	894	463
150	313	154	913	33.7	0.50	853	606	879	427
200	362	161	962	33.7	0.40	925	622	1155	598
250	524	244	964	35.1	0.41	1140	507	1110	805
300	516	229	983	35.8	0.42	1166	527	1107	771
350	760	274	1021	36.0	0.41	1423	398	1155	1090
400	896	401	1023	36.8	0.40	1618	267	1167	1334

Table 4.14(b): Calculated values of temperature , deformation time and heat diffusion time as a function of cutting speed during machining of as-quenched Fe-9.7Ni-0.1C alloy.

Cutting speed (m/min)	Shear Velocity (m/s)	Measured shear zone thickness (μm)	Strain rate (/s)	Fraction of heat retained in shear zone	Calculated temperature rise using Dodd and Bai's model (^{0}C)	Deformation time (μs)	Heat diffusion time μs)
1	0.02	--	60	0.26	204	6334	417
5	0.09	--	336	0.45	249	1249	417
10	0.17	--	528	0.51	321	642	417
25	0.44	--	1598	0.64	328	252	417
50	0.92	--	4236	0.74	267	120	417
75	1.42	--	7147	0.78	248	78	417
100	1.89	--	9529	0.80	251	58	417
150	2.84	--	14294	0.83	258	39	417
200	3.79	--	19059	0.85	271	29	417
250	4.80	48	57474	0.90	524	23	79
300	5.80	42	80764	0.93	563	19	61
350	7.17	35	134201	0.94	576	15	42
400	8.42	31	184815	0.94	615	13	33

Table 4.15(a): Measured cutting forces and contact length and calculated stresses as a function of cutting speed during machining of as-quenched Fe-1.4Ni-0.1C alloy.

Cutting speed	Cutting forces			Shear angle	Tool-chip interface Contact length	Calculated Stresses at the Primary shear zone		Calculated stresses at the secondary shear zone	
(m/min)	Fx (N)	Fy (N)	Fz (N)	(deg.)	(mm)	Normal stress (Mpa)	Shear stress (Mpa)	Normal stress (Mpa)	Shear Stress (Mpa)
1	1660	871	2566	12.4	1.80	987	872	665	581
5	2939	1756	3564	8.4	1.70	1102	853	956	1094
10	852	497	1882	9.9	1.60	430	559	559	358
25	1231	586	1961	12.6	1.50	740	681	612	510
50	1080	472	1690	15.5	1.30	819	678	608	508
75	806	340	1395	19.6	1.20	837	661	547	414
100	633	253	1192	18.1	1.10	611	553	513	356
150	470	185	1041	30.5	0.88	944	628	564	337
200	477	183	1062	31.1	0.99	983	644	512	304
250	424	161	1031	31.8	0.60	945	648	823	451
300	567	213	1102	30.5	0.63	1059	629	829	555
350	426	168	979	31.0	0.64	892	600	731	423
475	583	241	1076	32.0	0.56	1131	592	908	645

Table 4.15(b): Calculated values of temperature , deformation time and heat diffusion time as a function of cutting speed during machining of as-quenched Fe-1.4Ni-0.1C alloy.

Cutting speed (m/min)	Shear Velocity (m/s)	Estimated shear zone thickness (μm)	Strain rate (/s)	Fraction of heat retained in shear zone	Calculated temperature rise using Dodd and Bai's model (^{0}C)	Deformation time (μs)	Heat diffusion time (μs)
1	0.02	110	33	0.18	2	6583	280
5	0.08	110	110	0.29	7	1325	280
10	0.17	110	260	0.38	14	661	280
25	0.42	110	829	0.53	30	263	280
50	0.84	110	2047	0.63	52	131	280
75	1.29	110	3917	0.70	71	86	280
100	1.70	110	4805	0.72	84	65	280
150	2.76	110	12707	0.80	118	40	280
200	3.70	110	17330	0.82	140	30	280
250	4.65	110	22234	0.84	160	24	280
300	5.52	110	25413	0.85	177	20	280
350	6.47	110	30214	0.85	192	17	280
475	7.45	110	35839	0.86	209	15	280

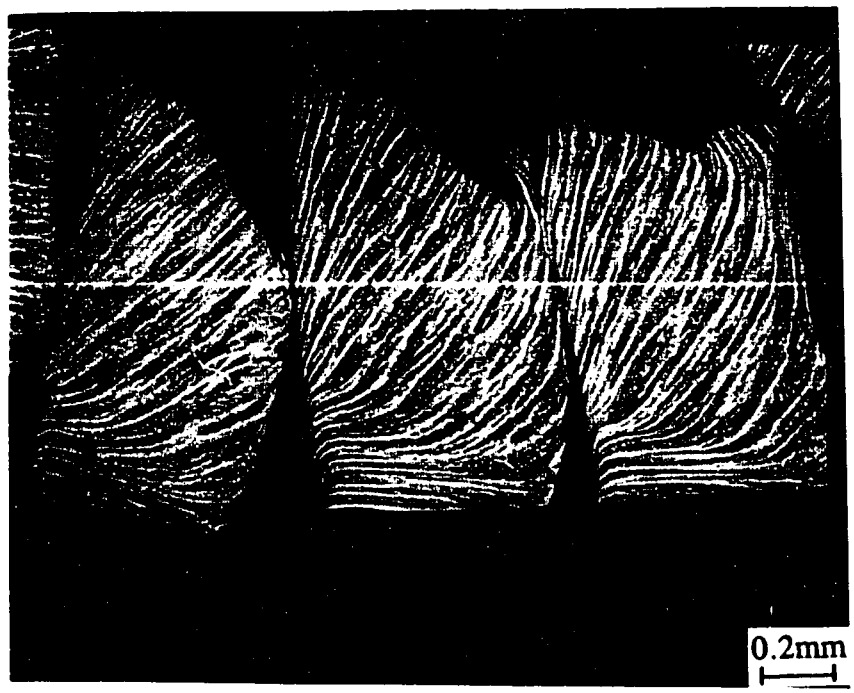

Fig. 4.35(a): Optical micrograph of a discontinuous chip formed during machining of Fe-18.9%Ni-0.10%C alloy at a cutting speed of 1 m/min.

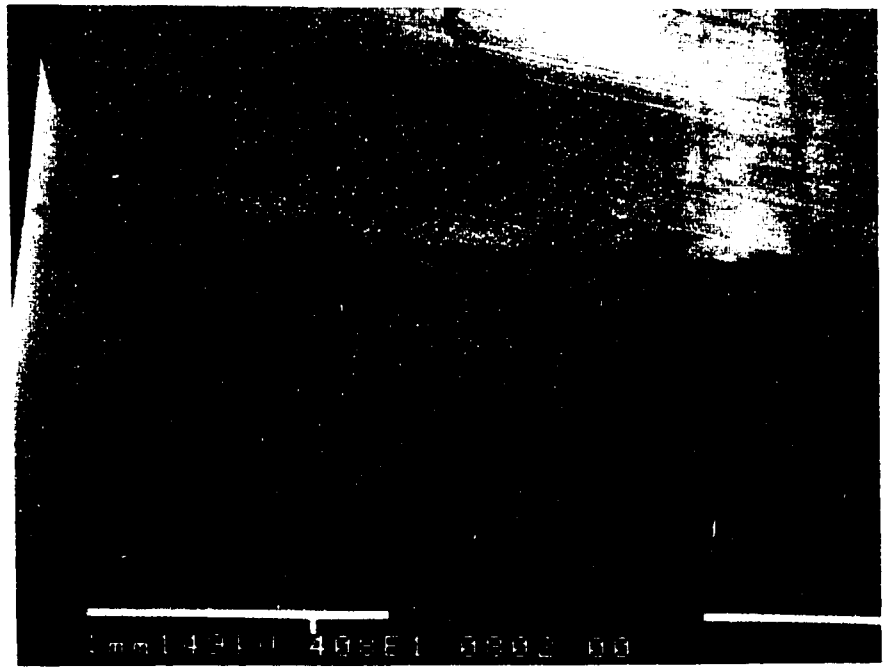

Fig.4.35(b): SEM picture of a tool rake face after 30 seconds machining of Fe-18.9%Ni-0.10%C alloy at 1 m/min.

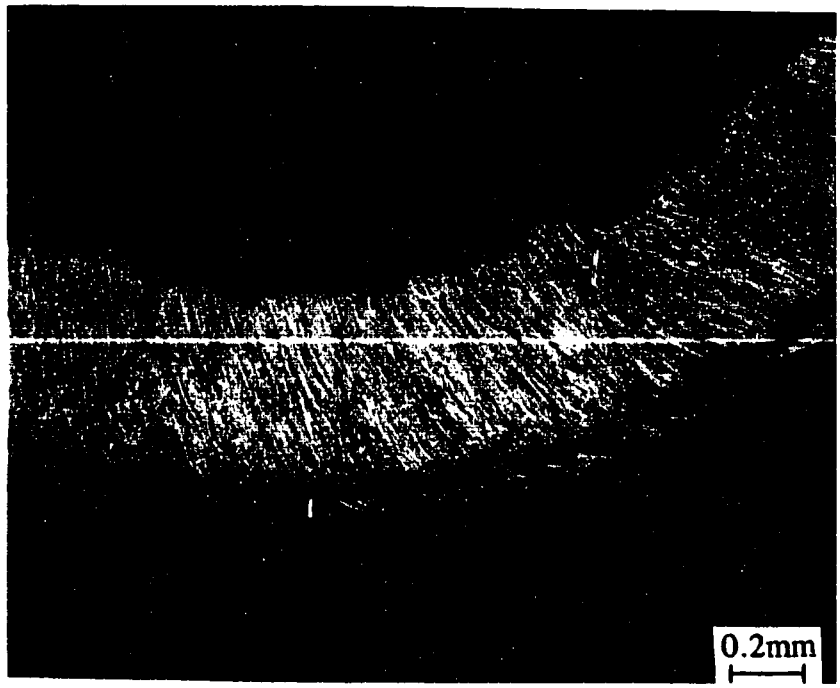

Fig. 4.36(a): Optical micrograph of a continuous or flow chip obtained at a cutting speed of 50 m/min, showing a transformation shear band located at and parallel to the tool-chip interface at a low cutting speed in Fe-18.9%Ni-0.10%C alloy. The white band is the region that has undergone phase transformation from martensite to austenite at 530°C.

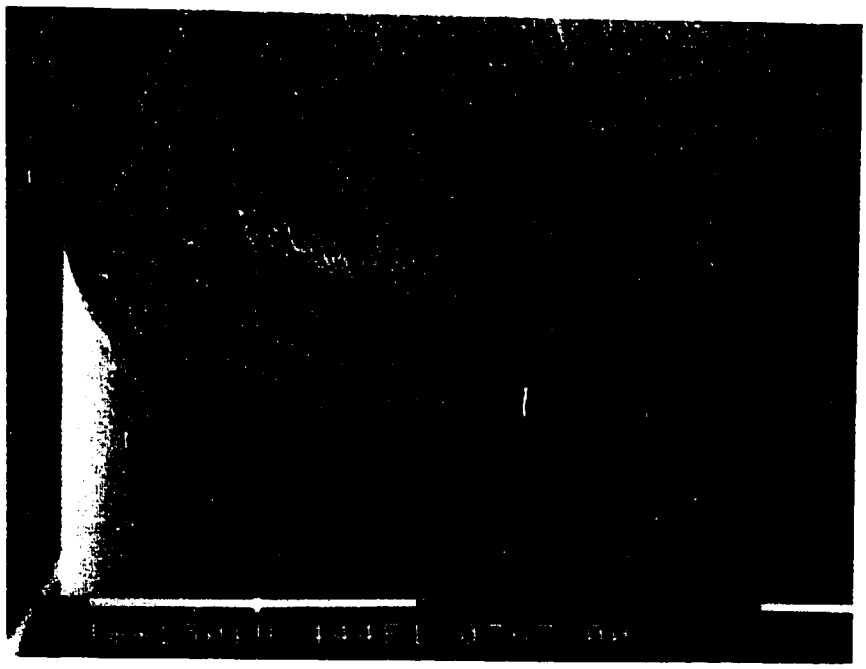

Fig. 4.36(b): SEM picture of tool crater wear obtained at the end of 10 seconds machining of an Fe-18.9%Ni-0.10%C alloy at a cutting speed of 50 m/min.

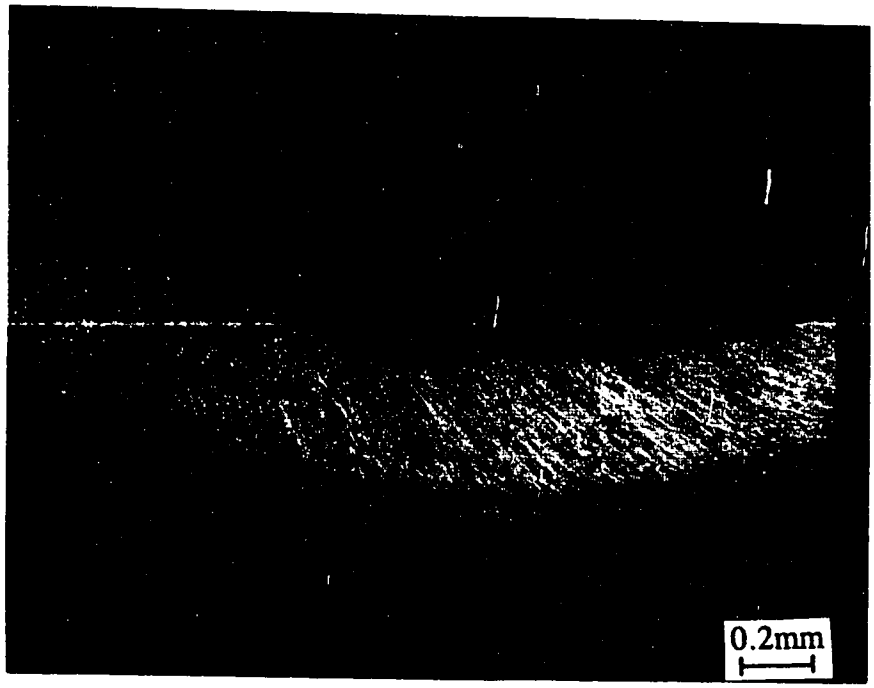

Fig. 4.37(a): Optical micrograph of a continuous chip obtained at a cutting speed of 75 m/min., showing transformation shear band located parallel to the tool-chip interface during machining of Fe-18.9%Ni-0.10%C alloy. The white band is the region that has undergone phase transformation from martensite to austenite at 530°C.

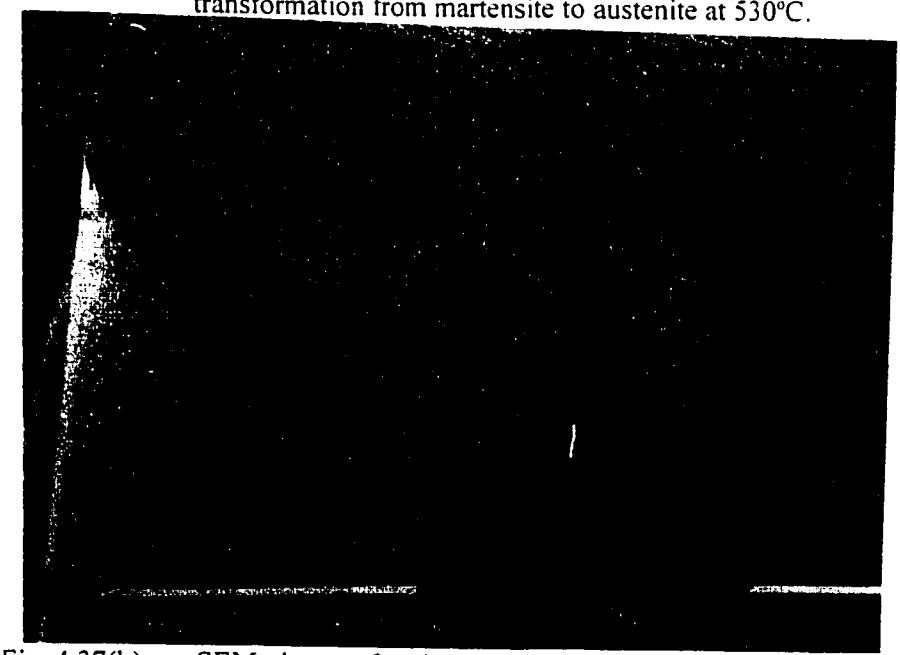

Fig. 4.37(b): SEM picture of tool crater wear obtained at the end of 10 seconds machining an Fe-18.9%Ni-0.10%C alloy at a cutting speed of 75 m/min. Note the location of the crater at some distance (0.34 mm) from the cutting edge.

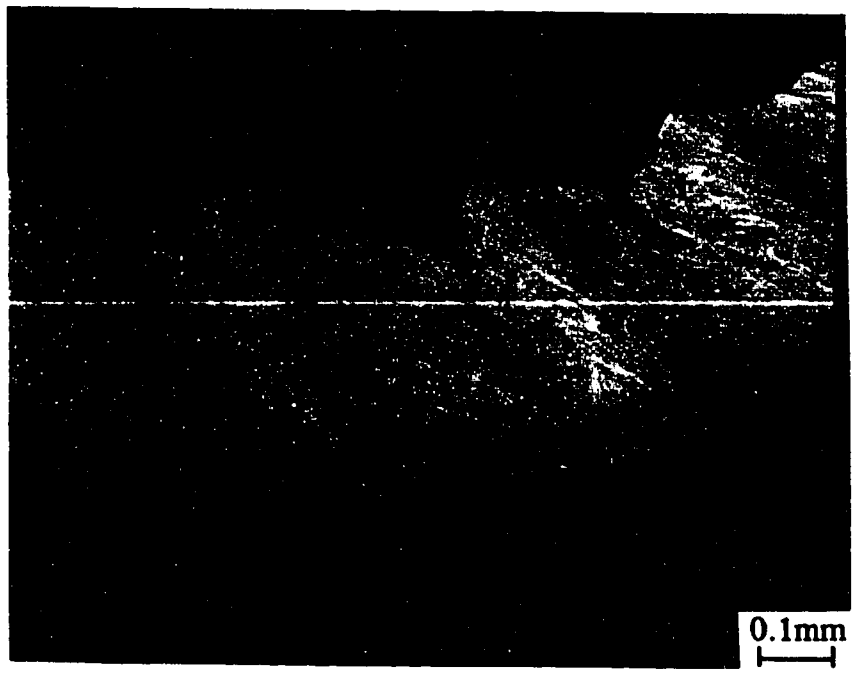

Fig. 4.38(a): Optical micrograph of a continuous chip obtained at a cutting speed of 100 m/min.,showing transformation shear band located parallel to the tool-chip interface during machining of Fe-18.9%Ni-0.10%C alloy. The white band is the region that has undergone phase transformation from martensite to austenite at 530°C.

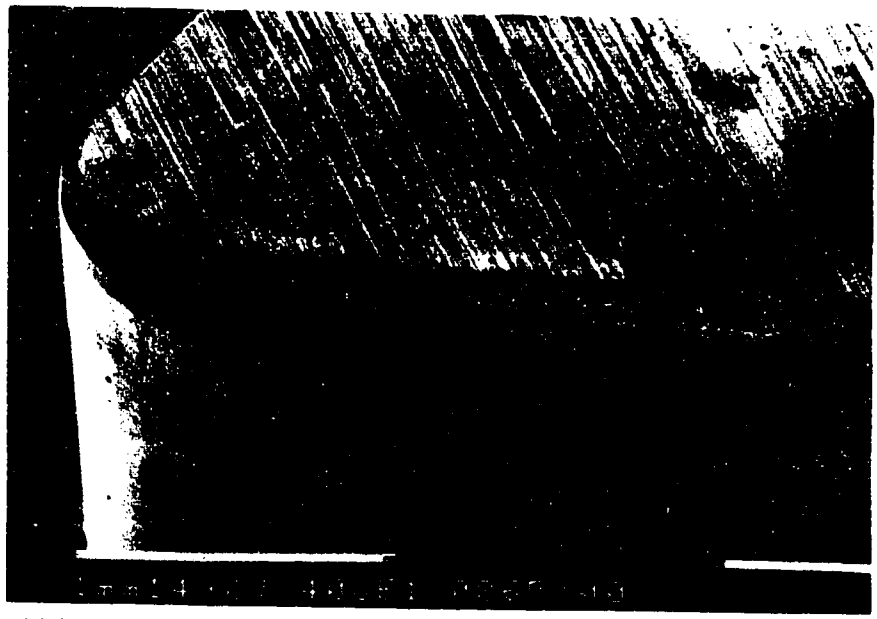

Fig. 4.38(b): SEM picture of tool crater wear obtained at the end of 10 seconds machining an Fe-28.9%Ni-0.10%C alloy at a cutting speed of 100 m/min. Note the location of the crater at some distance (0.24 mm) from the cutting edge.

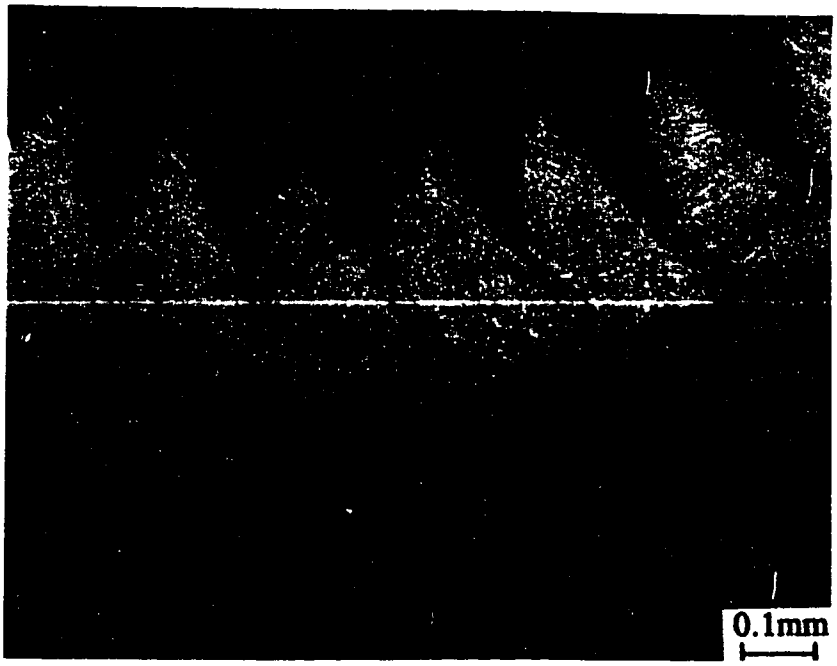

Fig. 4.39(a): Optical micrograph of a fully segmented chip obtained at a cutting speed of 150 m/min., showing transformation shear band enveloping the segmented chip at the critical cutting speed for chip segmentation of 150 m/min in Fe-18.9%Ni-0.10%C alloy. The shear bands have undergone phase transformation from martensite to austenite at 530°C.

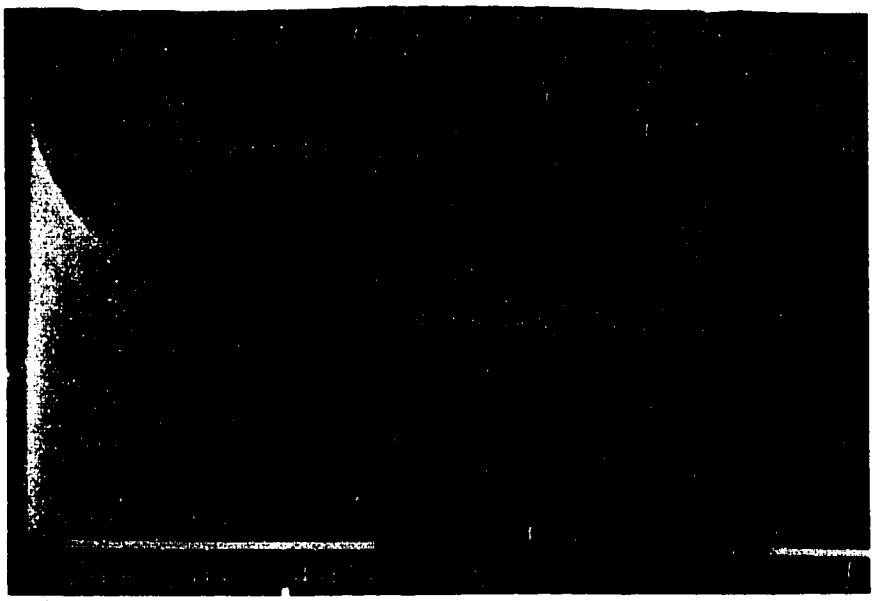

Fig. 4.39(b): SEM picture of tool crater wear obtained at the end of 5 seconds machining of an Fe-18.9%Ni-0.10%C alloy at a cutting speed of 150 m/min. Note the location of the crater closer to the cutting edge of the tool (0.2 mm away).

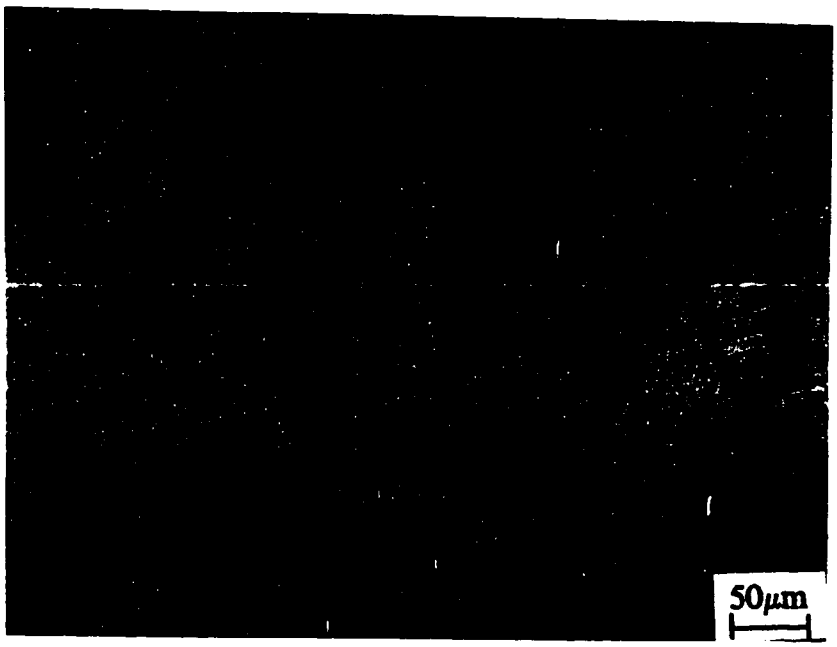

Fig. 4.40(a): Optical micrograph of a fully segmented chip obtained at a cutting speed of 350 m/min.,showing transformation shear band enveloping the segmented chip at the critical cutting speed for chip segmentation of 150 m/min in Fe-18.9%Ni-0.10%C alloy. The shear bands have undergone phase transformation from martensite to austenite at 530°C.

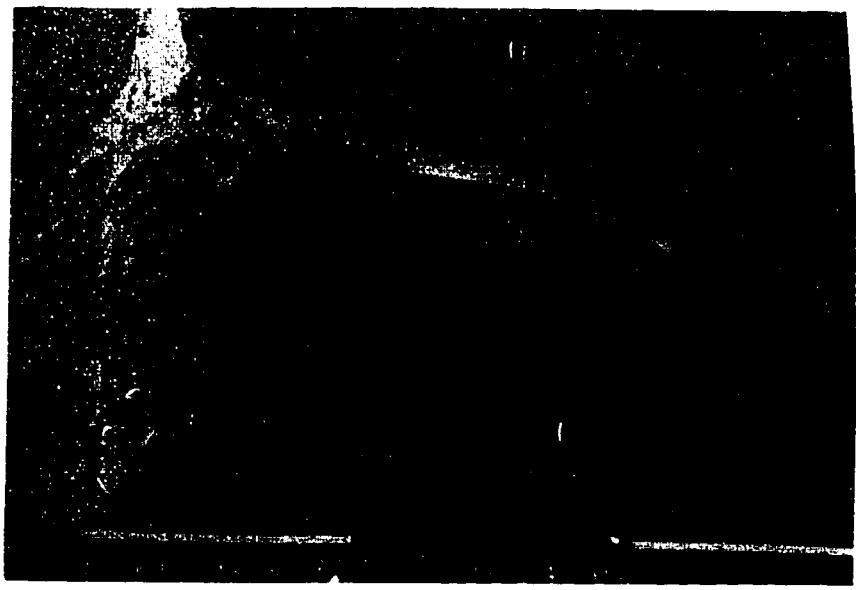

Fig. 4.40(b): SEM picture of tool crater wear obtained at the end of 1 second machining of an Fe-18.9%Ni-0.10%C alloy at a cutting speed of 150 m/min. Note the location of the crater closer to the cutting edge of the tool (0.12 mm away).

Figs. 4.41 - 4.47 show the change in chip morphology and corresponding tool wear as a function of cutting speed during the machining of quenched Fe-9.7%Ni-0.10%C alloy. At a cutting speed of 50 m/min there is no modification of the microstructure in the primary and secondary shear zones and the crater wear is minimal. At 100 m/min modification of the microstructure occurs in the secondary shear zone probably due to phase transformation from martensite to austenite which, upon rapid cooling reverts back to martensitic but with refined structure. The features shown at 150 m/min. mark the onset of instabilities at the primary shear zone and partial chip segmentation but a deformation shear band is not formed until 250 m/min. The shear bands formed at the primary shear zone exhibit microstructural changes which are attributed to early stage tempering of martensite. The crater is located closer to the cutting edge of the tool. The intensity of segmentation increases with increase in cutting speed. At 350 m/min. the chips are almost fully segmented and damage occurs to the cutting edge of the tool. As shown in Fig. 4.46(a) a transformation shear band is formed at the centre of the deformation shear band causing the onset of full chip segmentation at 400 m/min for the Fe-9.7%Ni-0.10%C alloy. Fig. 4.46(b) shows the damage to the cutting edge of the tool from fully segmented chips. Figs. 4.47-4.50 show change in chip morphology and the corresponding tool wear as a function of cutting speed during the machining of quenched Fe-1.4Ni-0.1C alloy. Homogeneous deformation in the primary shear zone occurs throughout the cutting speed range used, 5 - 475 m/min. Heterogeneous deformation in the secondary shear zone commences at a cutting speed of 100 m/min., but crater wear does not start until a cutting speed of 250 m/min. is reached where a white layer appears. This indicates that the secondary shear zone reaches the phase transformation temperature (760 ^{o}C) at 250 m/min. The crater intensifies and moves closer to the cutting edge with increase in cutting speed and decrease in contact length. As shown in Fig. 4.50(a) the chip morphology remains continuous up to the highest cutting speed used (475 m/min) during the machining of quenched Fe-1.4Ni-0.1C alloy.

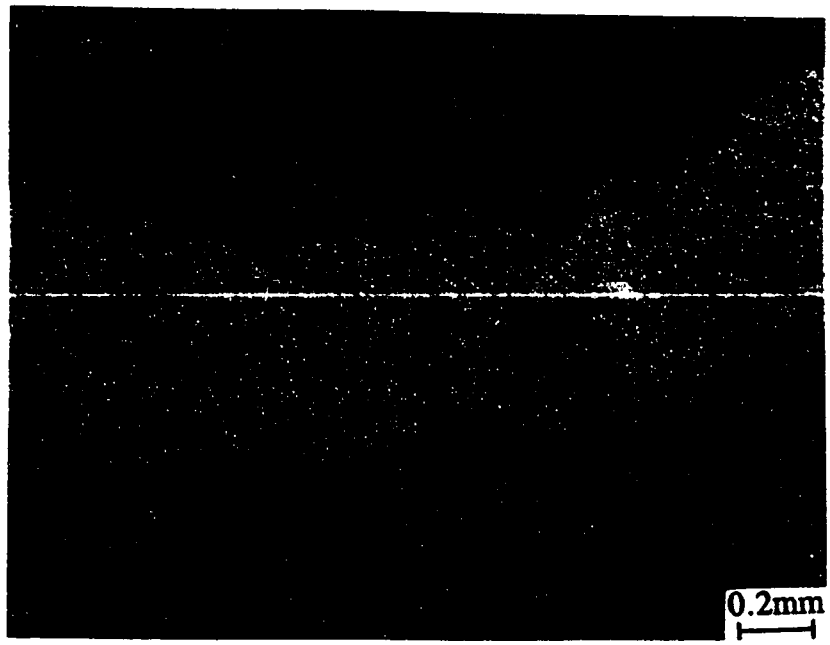

Fig. 4.41(a): Optical micrograph of a continuous chip obtained at a cutting speed of 50 m/min., during machining of Fe-9.7%Ni-0.1%C alloy.

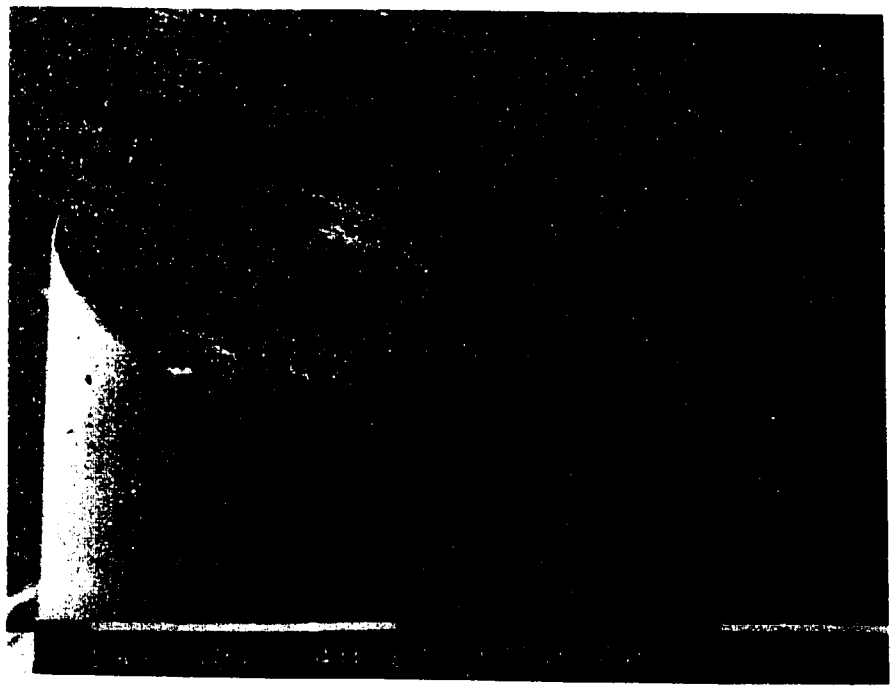

Fig. 4.41(b): SEM picture of tool crater wear obtained at the end of 10 seconds machining of an Fe-9.7%Ni-0.10%C alloy at a cutting speed of 50 m/min. with a cemented carbide tool.

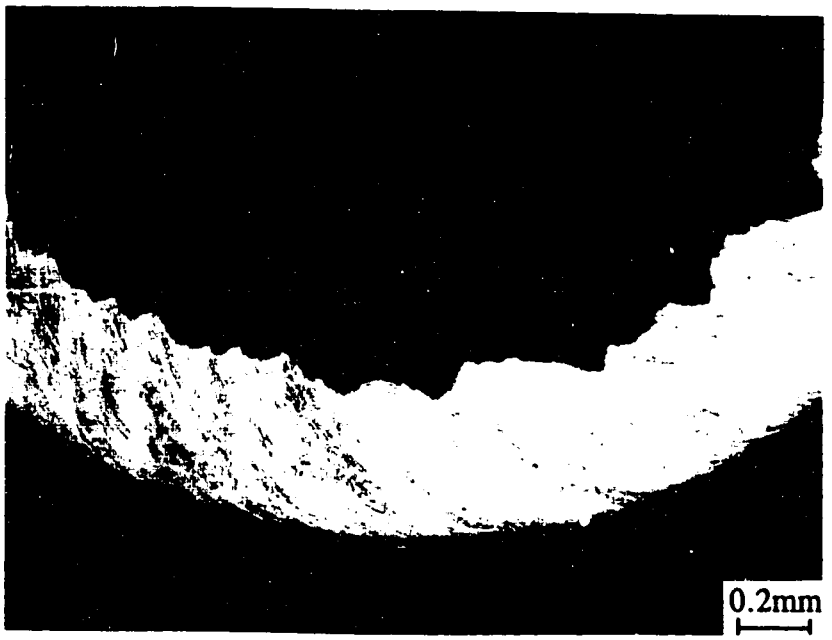

Fig. 4.42(a): Optical micrograph of a continuous chip obtained at a cutting speed of 100 m/min., during machining of Fe-9.7%Ni-0.1%C alloy. The dark band is the region that undergoes phase transformation from martensite to austenite and back to refined martensite.

Fig. 4.42(b): SEM picture of tool crater wear obtained at the end of 5 seconds machining of an Fe-9.7%Ni-0.10%C alloy at a cutting speed of 100 m/min. with a cemented carbide tool. Note the location of the crater far away from the cutting edge of the tool (0.25 mm away).

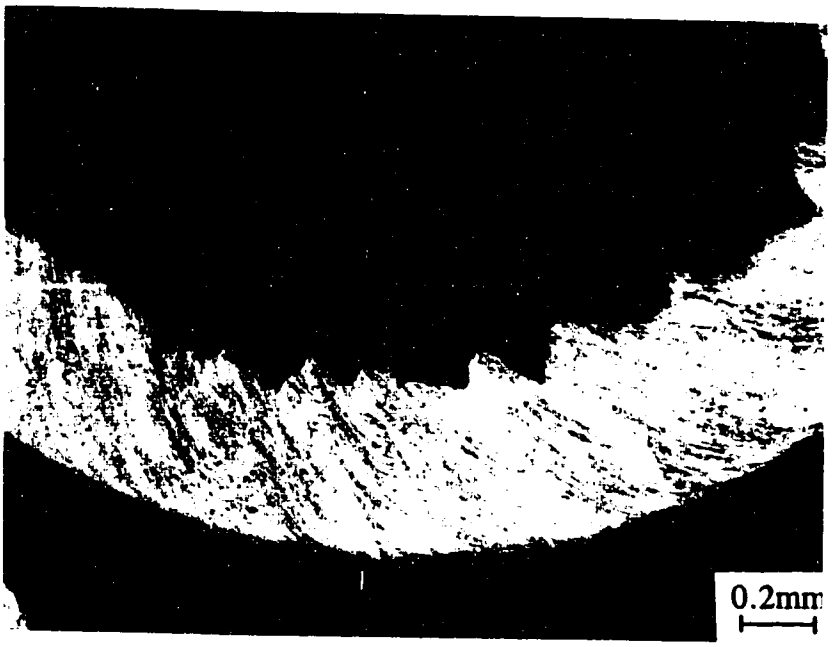

Fig. 4.43(a): Optical micrograph of a continuous chip obtained at a cutting speed of 150 m/min., during machining of Fe-9.7%Ni-0.1%C alloy. Note the onset of instability at the primary shear zone. The dark band is the region that undergoes phase transformation from martensite to austenite and back to refined martensite.

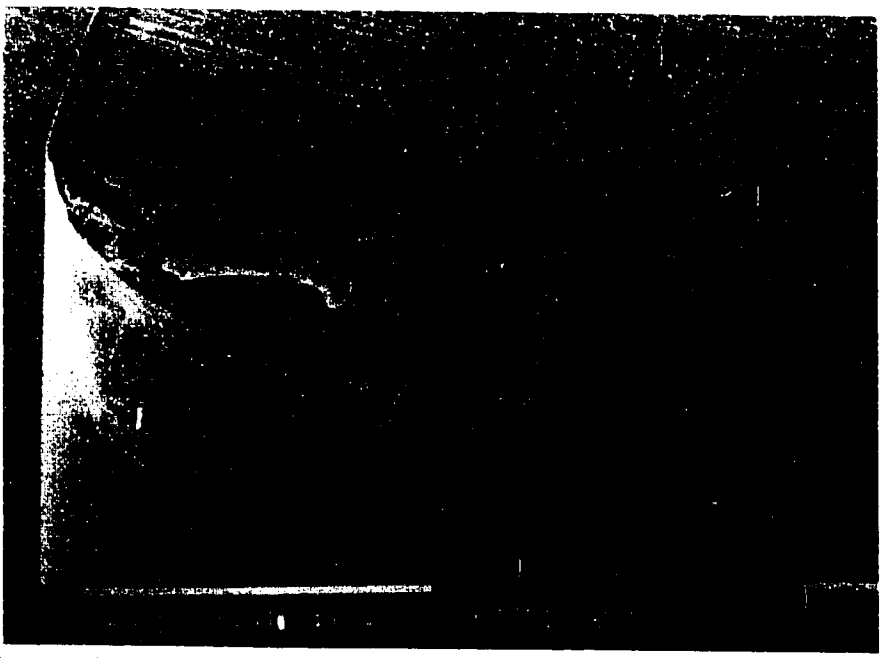

Fig. 4.43(b): SEM picture of tool crater wear obtained at the end of 1 second machining of an Fe-9.7%Ni-0.10%C alloy at a cutting speed of 150 m/min. with a cemented carbide tool. Note the location of the crater closer to the cutting edge of the tool (0.21 mm away).

Fig. 4.44(a): Optical micrograph of a partially segmented chip obtained at a cutting speed of 250 m/min., during machining of Fe-9.7%Ni-0.1%C alloy. Note the instability at the primary shear zone. The microstructure of the band in the primary shear zone is the region that undergoes tempering giving rise to instability and localisation.

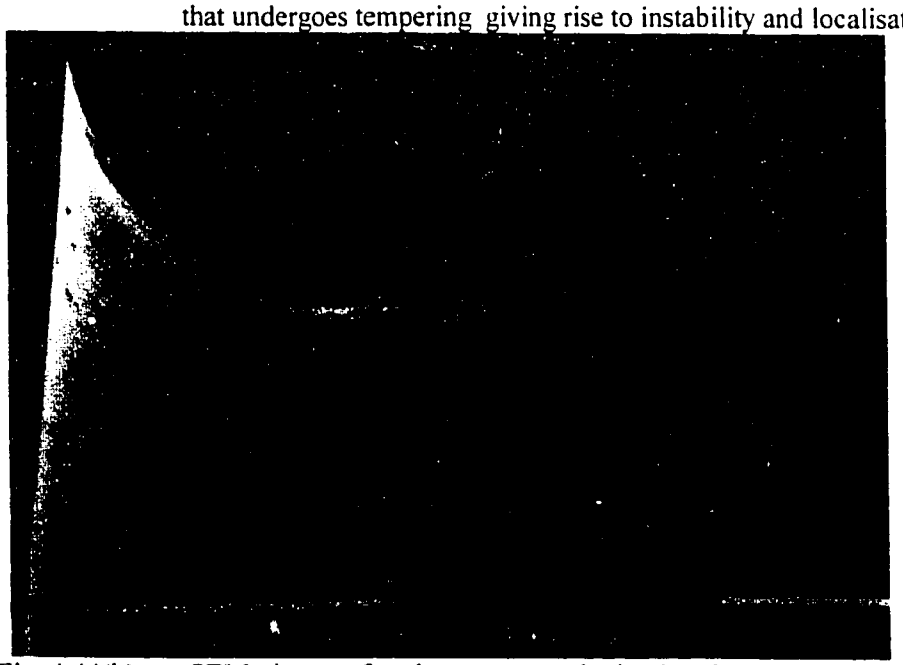

Fig. 4.44(b): SEM picture of tool crater wear obtained at the end of 1 second machining of an Fe-9.7%Ni-0.10%C alloy at a cutting speed of 250 m/min. with a cemented carbide tool. Note the location of the crater closer to the cutting edge of the tool (0.19 mm away).

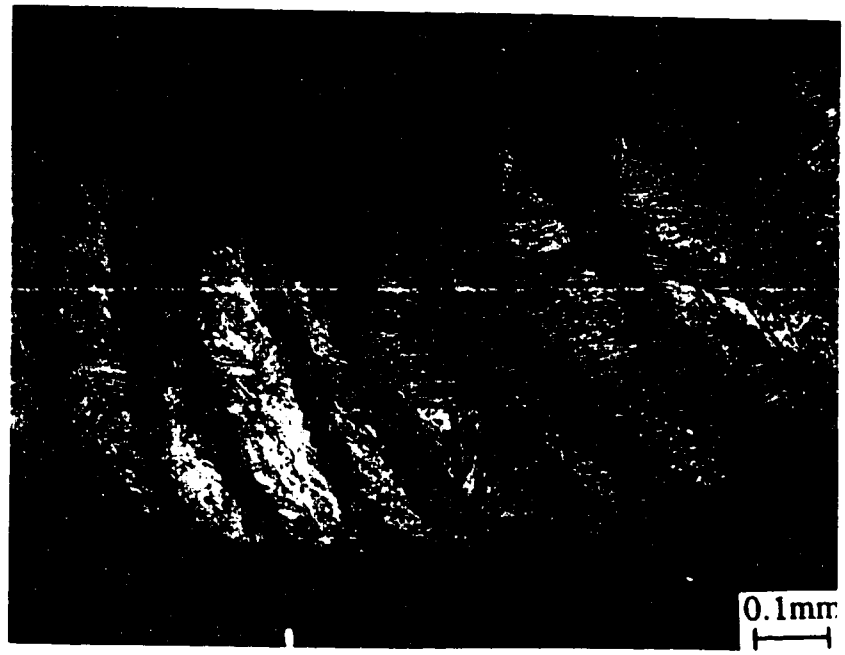

Fig. 4.45(a): Optical micrograph of a partially segmented chip obtained at a cutting speed of 350 m/min., during machining of Fe-9.7%Ni-0.1%C alloy. Note the instability at the primary shear zone. The microstructure of the band in the primary shear zone is the region that undergoes tempering of martensite giving rise to instability and localisation.

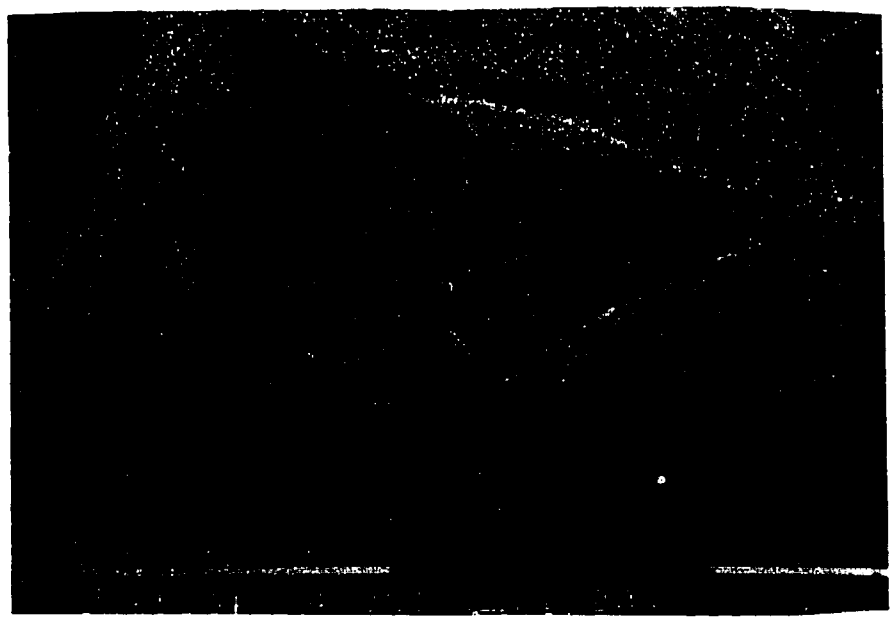

Fig. 4.45(b): SEM picture of tool crater wear obtained at the end of 1 second machining of an Fe-9.7%Ni-0.10%C alloy at a cutting speed of 350 m/min. with a cemented carbide tool. Note the damage of the cutting edge due to location of the crater closest to the cutting edge of the tool (0.16 mm away).

Fig. 4.46(a): Optical micrograph of a fully segmented chip obtained at a cutting speed of 400 m/min, showing transformation shear band at the centre of the deformation shear band and enveloping the segmented chip at the critical cutting speed for chip segmentation of 400 m/min in Fe-9.7%Ni-0.10%C alloy. The shear bands have undergone phase transformation from martensite to austenite at 620°C indicating the temperature in the primary shear zone.

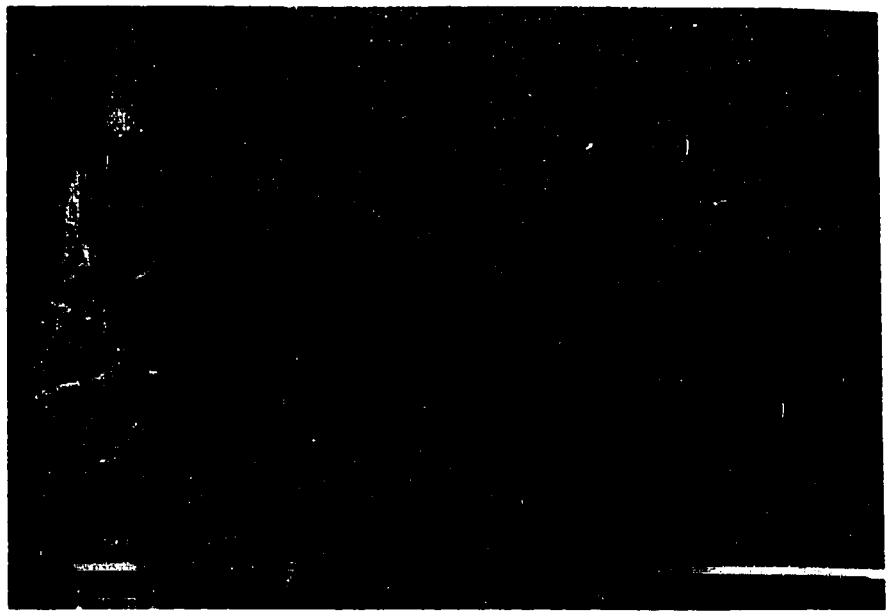

Fig. 4.46(b): SEM picture of tool crater wear obtained at the end of 1 second machining of an Fe-9.7%Ni-0.10%C alloy at a cutting speed of 400 m/min. Note the damage of the cutting edge of the tool caused by location of the crater at the cutting edge.

Fig. 4.47(a): Optical micrograph of a continuous chip obtained at a cutting speed of 100 m/min., during machining of Fe-1.4%Ni-0.1%C alloy.

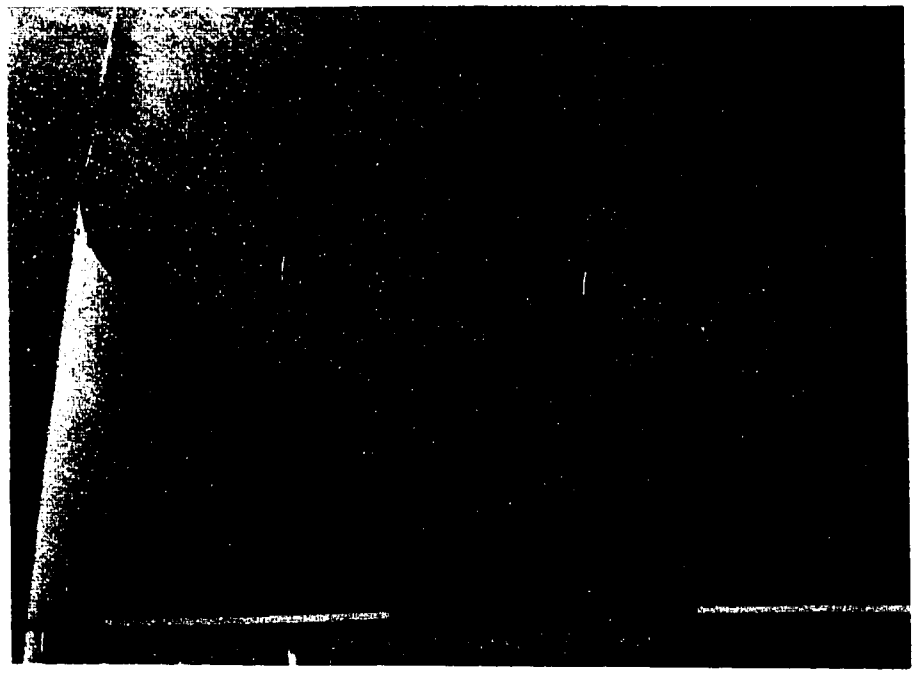

Fig. 4.47(b): SEM picture of tool crater wear obtained at the end of 10 seconds machining of an Fe-1.4%Ni-0.10%C alloy at a cutting speed of 100 m/min. with a cemented carbide tool.

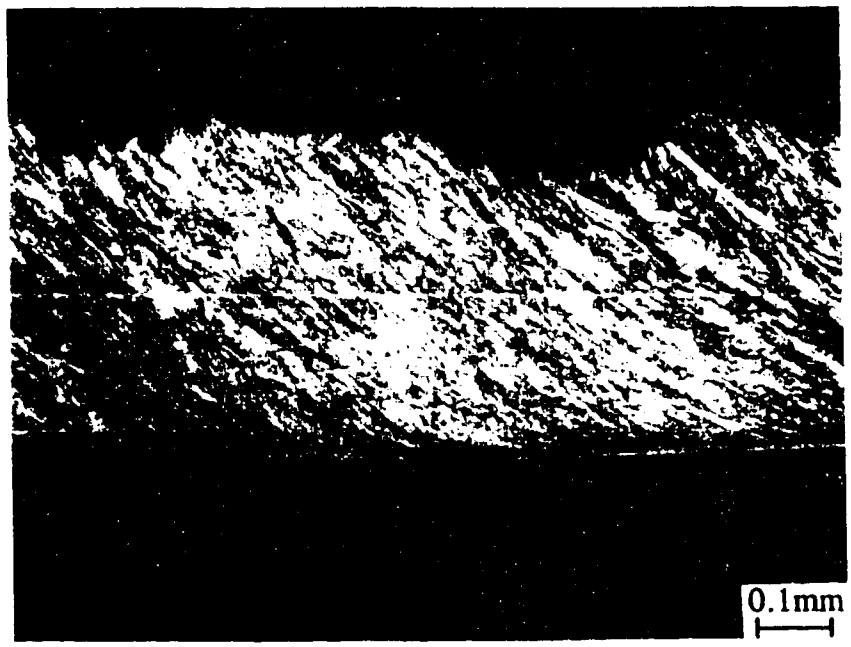

Fig. 4.48(a): Optical micrograph of a continuous chip obtained at a cutting speed of 250 m/min., during machining of Fe-1.4%Ni-0.1%C alloy. The dark band is the region that undergoes phase transformation from martensite to austenite and back to refined martensite.

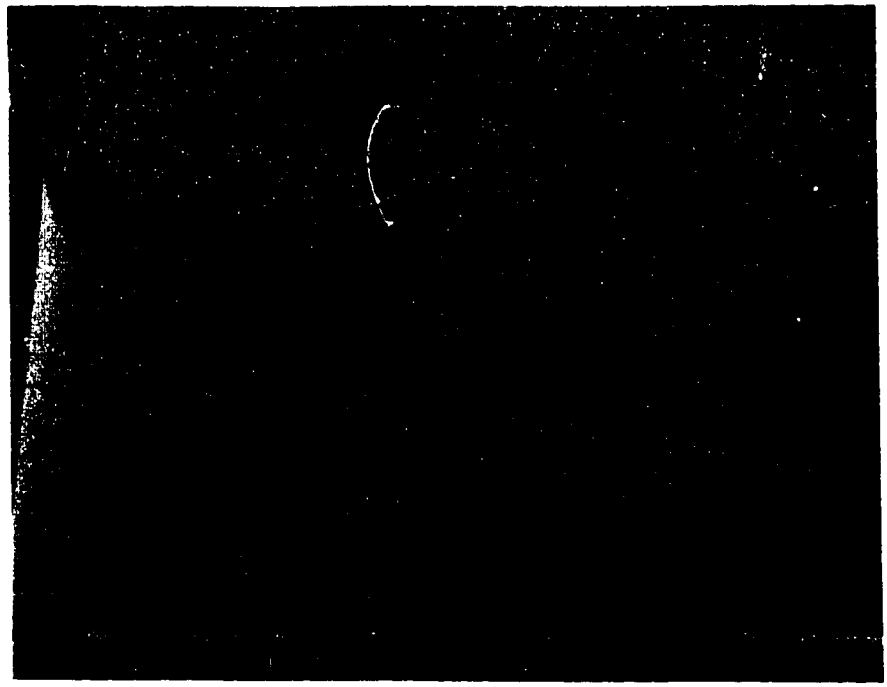

Fig. 4.48(b): SEM picture of tool crater wear obtained at the end of 10 seconds machining of an Fe-1.4%Ni-0.10%C alloy at a cutting speed of 250 m/min. with a cemented carbide tool.

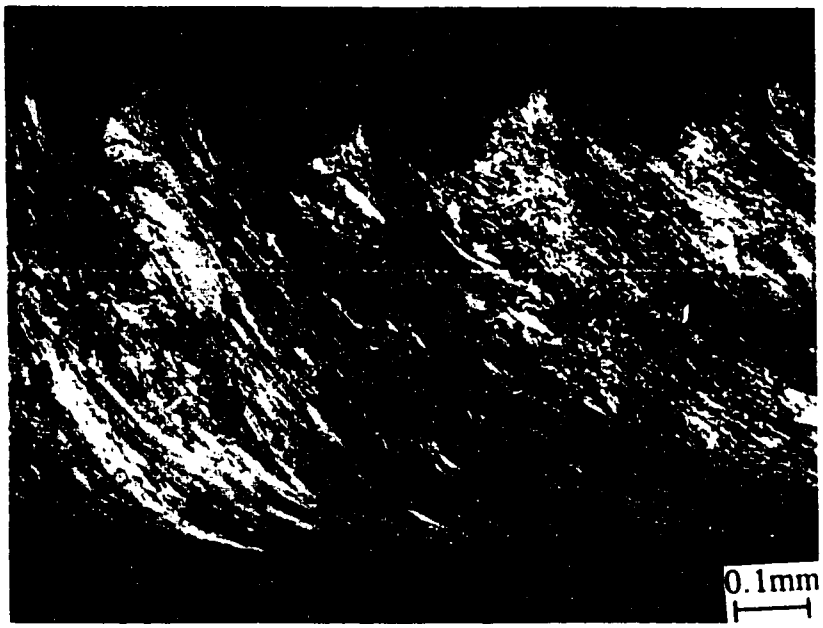

Fig. 4.49(a): Optical micrograph of a continuous chip obtained at a cutting speed of 350 m/min., during machining of Fe-1.4%Ni-0.1%C alloy. The dark band is the region that undergoes phase transformation from martensite to austenite and back to refined martensite.

Fig. 4.49(b): SEM picture of tool crater wear obtained at the end of 3 seconds machining of an Fe-1.4%Ni-0.10%C alloy at a cutting speed of 350 m/min. with a cemented carbide tool.

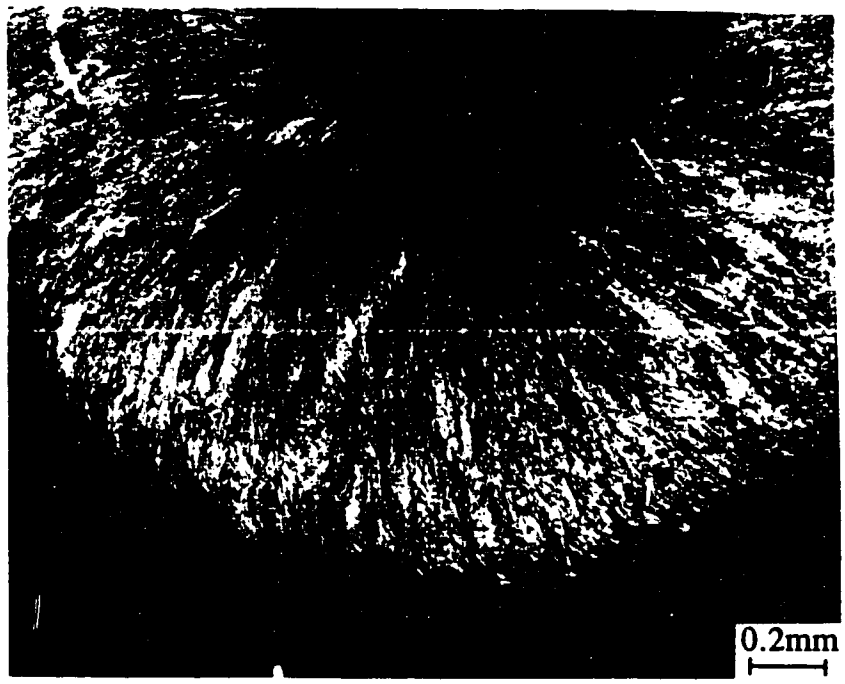

Fig. 4.50(a): Optical micrograph of a continuous chip obtained at a cutting speed of 475 m/min., during machining of Fe-1.4%Ni-0.1%C alloy. The dark band is the region that undergoes phase transformation from martensite to austenite and back to refined martensite.

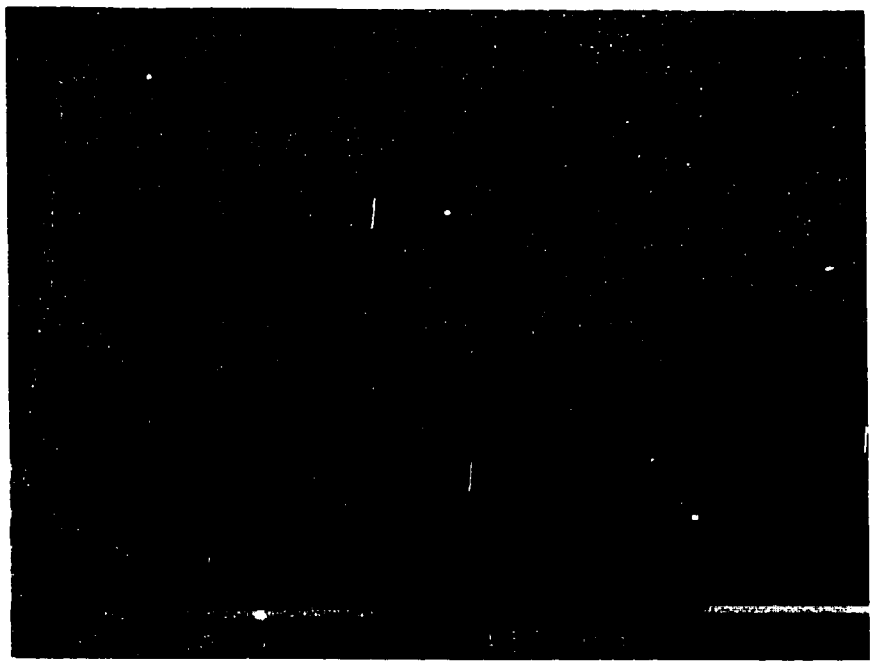

Fig. 4.50(b): SEM picture of tool crater wear obtained at the end of 3 seconds machining of an Fe-1.4%Ni-0.10%C alloy at a cutting speed of 475 m/min. with a cemented carbide tool.

Table 4.16 gives a summary of the critical speed for chip segmentation and estimated phase transformation temperature as a function of nickel content. The critical speed for chip segmentation increases with decrease in nickel content and increase in phase transformation temperature.

Table 4.16: The martensite to austenite phase transformation temperature and critical speed for chip segmentation as functions of nickel content in Fe-Ni-C alloys.

Alloy Chemistry (wt%)	Fe-28.9Ni-0.1C	Fe-18.9Ni-0.1C	Fe-9.7Ni-0.1C	Fe-1.4Ni-0.1C
Austenite start temperature (°C)	400	530	620	760
Critical speed for chip segmentation (m/min)	75	150	400	>475*
Chip morphology	Fully segmented	Fully segmented	Fully segmented	No segmentation

* The chips are not segmented at 475 m/min

4.4.5 The Effect of Eliminating Thermal Softening Chip Morphology and Tool Wear

Thermal softening accompanies martensite to austenite phase transformation. By annealing Fe-28.9%Ni-0.10%C alloy a stable austenite phase is formed and hence the thermal softening due to phase transformation is eliminated and its consequence on shear localisation on the primary shear zone is examined. Figs. 4.51-4.53 show the flow chip morphology obtained from machining of austenitic Fe-28.9%Ni-0.10%C alloy at cutting speeds ranging from 75 to 350 m/min. The morphology of the chips remained continuous even at cutting speeds above 75 m/min. where the martensitic phase of the same alloy gave fully segmented chips, compare with Figs. 4.28(a)-4.32(a). The corresponding crater wear of the tools used in machining the austenitic alloy are shown in the adjacent photographs. Table 4.17 shows the positions of the craters formed on the tool as a function of the cutting speed and heat treatment condition of the alloys.

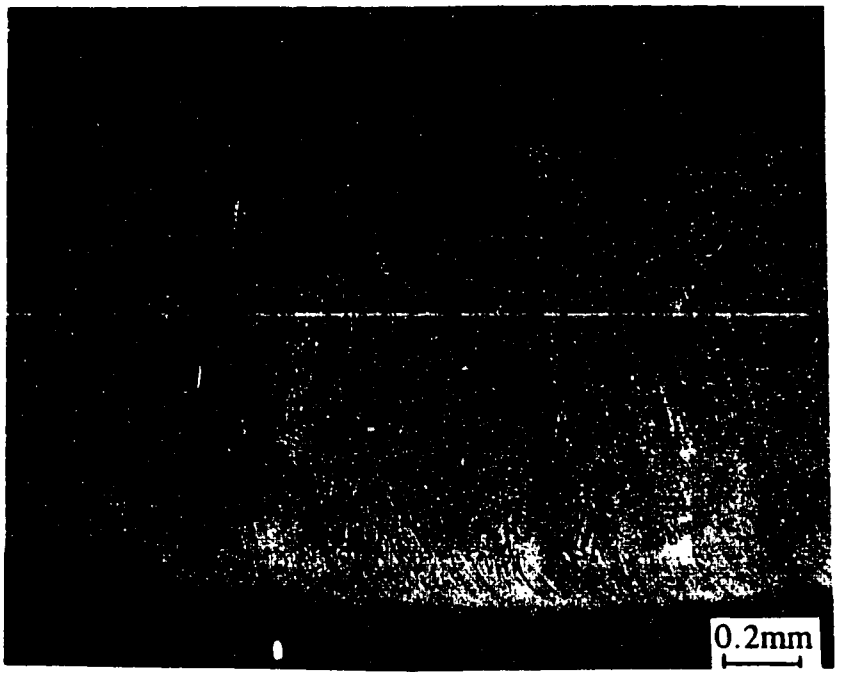

Fig. 4.51(a): Optical micrograph of a continuous or flow chip obtained at a cutting speed of 75 m/min., showing that in the absence of thermoplastic shear localisation and phase transformation in austenitic Fe-28.9%Ni-0.10%C alloy, continuous of flow chips are formed at a cutting speed that gives fully segmented chips if the alloy is martensitic.

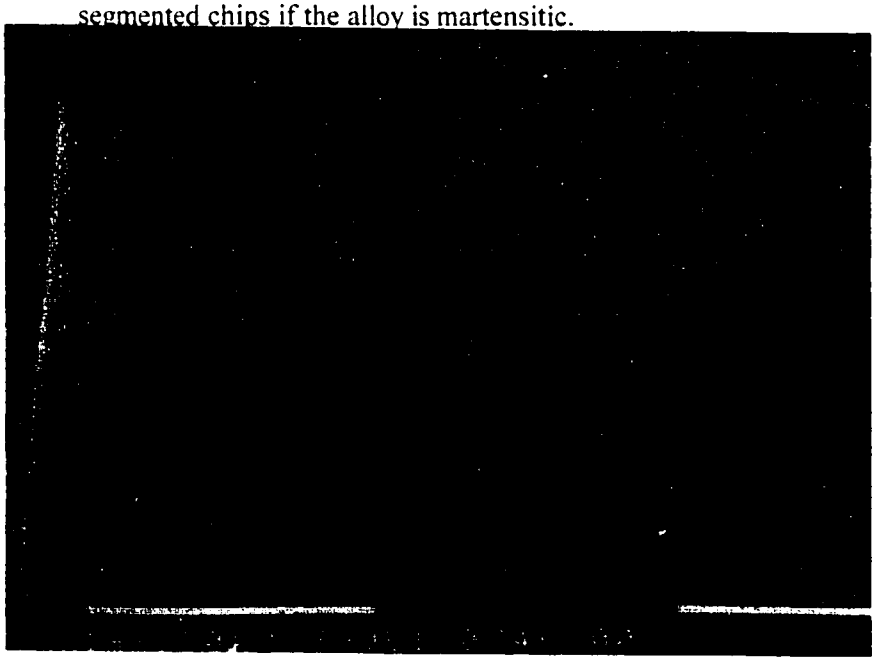

Fig. 4.51(b): SEM picture of tool crater wear obtained at the end of 10 seconds machining of an Fe-28.9%Ni-0.10%C alloy at a cutting speed of 75 m/min. Note the location of the crater at a distance (0.76 mm) from the cutting edge which is larger than in the case of the martensitic alloy (0.28 mm) at the same cutting speed of 75 m/min.

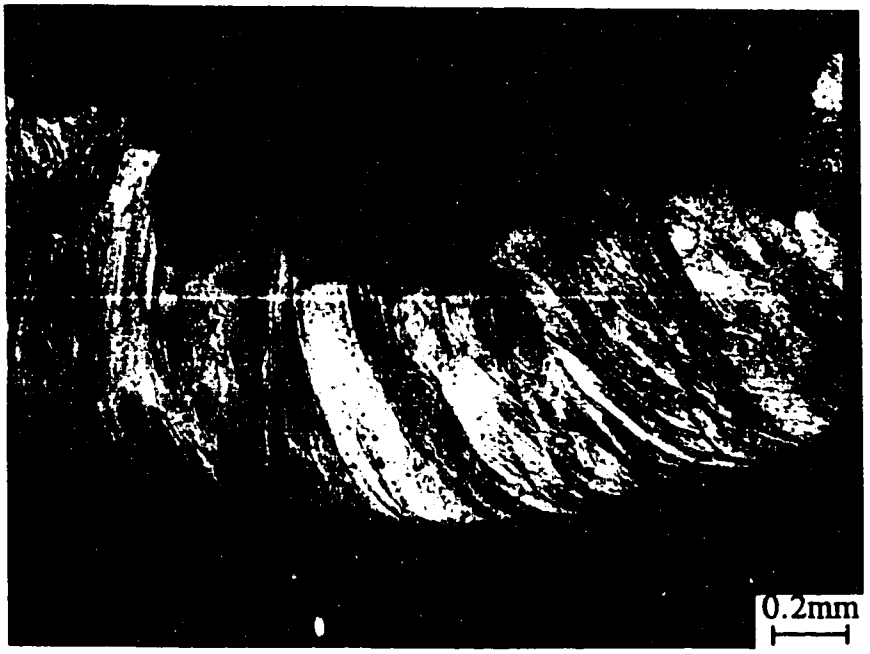

Fig. 4.52(a): Optical micrograph of a continuous or flow chip obtained at a cutting speed of 150 m/min., showing that in the absence of thermoplastic shear localisation and phase transformation in austenitic Fe-28.9%Ni-0.10%C alloy, continuous of flow chips are formed at a cutting speed that gives fully segmented chips if the alloy is martensitic.

Fig. 4.52(b): SEM picture of tool crater wear obtained at the end of 10 seconds machining of an Fe-28.9%Ni-0.10%C alloy at a cutting speed of 150 m/min. Note the location of the crater at a distance (0.48 mm) from the cutting edge which is larger than in the case of the martensitic alloy (0.18 mm) at the same cutting speed of 150 m/min.

Fig. 4.53(a): Optical micrograph of a continuous or flow chip obtained at a cutting speed of 350 m/min., showing that in the absence of thermoplastic shear localisation and phase transformation in austenitic Fe-28.9%Ni-0.10%C alloy, continuous of flow chips are formed at a cutting speed that gives fully segmented chips if the alloy is martensitic.

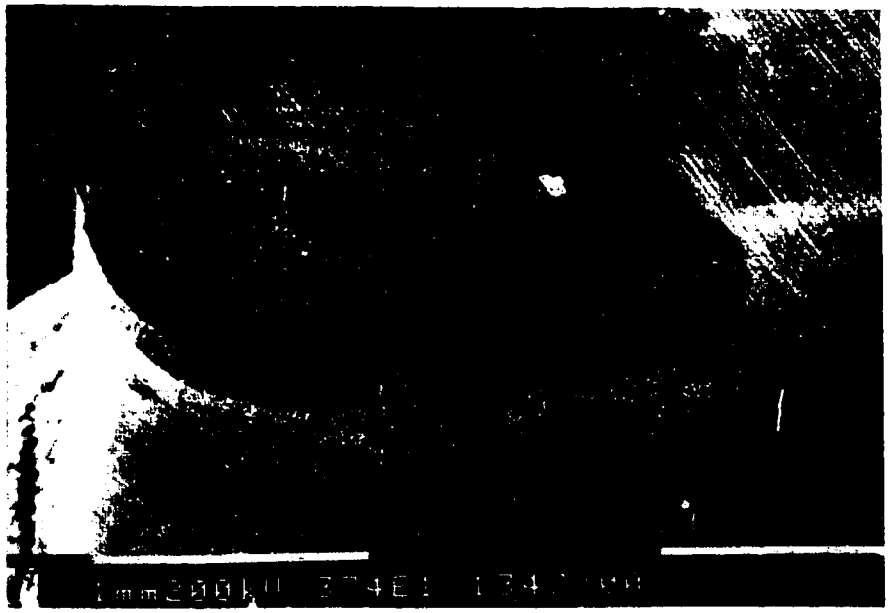

Fig. 4.53(b): SEM picture of tool crater wear obtained at the end of 2 seconds machining of an Fe-28.9%Ni-0.10%C alloy at a cutting speed of 350 m/min. Note the location of the crater at a distance (0.24 mm) from the cutting edge which is larger than in the case of the martensitic alloy (0.12 mm) at the same cutting speed of 350 m/min.

Table 4.17. Measured values of contact length and position of craters from cutting edge of tool as a function of cutting speed during machining of quenched Fe-Ni-C alloys.

Alloy	Cutting Speed (m/min)	Cutting time (s)	Contact Length (mm)	Position of crater from cutting edge (mm)
Fe-28.9Ni-0.1C (Quenched Martensitic)	50	10	0.58	0.33
	75	10	0.54	0.28
	100	10	0.60	0.24
	150	10	0.61	0.18
	200	10	0.61	--
	250	1	0.51	0.12
	300	2	0.52	0.12
Fe-28.9Ni-0.1C (Annealed Austentic)	50	10	1.28	0.98
	75	10	1.16	0.76
	100	10	0.97	0.64
	150	10	0.74	0.48
	200	10	0.73	0.40
	250	2	0.74	0.36
	300	2	0.76	0.32
Fe-18.9Ni-0.1C (Quenched Martensitic)	50	10	0.71	0.46
	75	10	0.50	0.34
	100	10	0.46	0.24
	150	5	0.41	0.20
	200	1	0.37	0.18
	250	1	0.31	0.12
	300	1	0.29	0.12
Fe-9.7Ni-0.1C (Quenched Martensitic)	50	10	0.73	0.48
	75	10	0.54	0.36
	100	5	0.51	0.25
	150	1	0.50	0.21
	200	1	0.40	0.19
	250	1	0.41	0.19
	300	1	0.42	0.18

At 150 m/min. the crater formed on the tool used to machine the austenitic alloy is located 0.48 mm from the cutting edge in comparison with 0.18 mm when machining the martensitic phase of the same alloy. Fig. 4.53(a) shows the flow chip morphology obtained from machining of austenitic Fe-28.9%Ni-0.10%C alloy at a cutting speed of 350 m/min. As shown in the corresponding crater wear of the tool, the crater has moved to 0.24 mm from the cutting in comparison with 0.12 mm when machining martensitic phase of the same alloy under identical cutting conditions. Continuous or flow chips are formed up to the maximum speed used in the present investigation (450 m/min), i.e., chip segmentation is suppressed by suppressing thermal softening of martensite occurring either by tempering of martensite or by martensite to austenite phase transformation. In consequence, flow chip morphology results and the contact length is increased and the crater is drawn farther away from the cutting edge of the tool. Thus the cutting edge of the tool is preserved, resulting in a good surface finish and a prolonged tool life.

4.4.6 Effect of Feed on Chip Segmentation

The changes in chip morphology were investigated as a function of feed during machining of martensitic Fe-28.9%Ni-0.1%C alloy at a constant speed of 400 m/min and depth of cut of 2.0 mm. Fig. 4.54-4.58 show the change in chip morphology and the corresponding tool wear as a function of feed during the machining of martensitic Fe-28.9%Ni-0.1%C alloy at a constant speed of 400 m/min and depth of cut of 2.0 mm. A continuous chip morphology corresponds to a low feed of 0.055 mm/rev at a cutting speed of 400 m/min. The corresponding tool crater wear shows that the contact length is small and the crater is localised near the cutting edge. When the feed is 0.107 mm/rev (0.0042 in/rev), partially segmented chips are formed with larger portions of the segments undergoing the martensite to austenite phase transformation leaving isolated islands of untransformed martensite (Fig. 4.55(a)). At a feed of 0.206 mm/rev, partially segmented chips are formed with individual

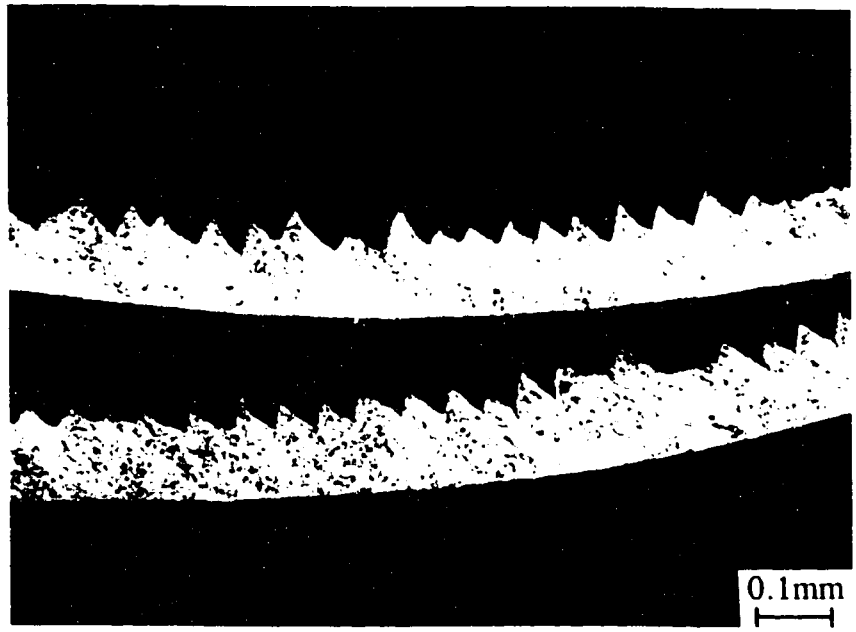

Fig. 4.54(a): Optical micrograph of a continuous or flow chip obtained at a feed of 0.055 mm/rev and a cutting speed of 400 m/min in Fe-28.9%Ni-0.10%C.

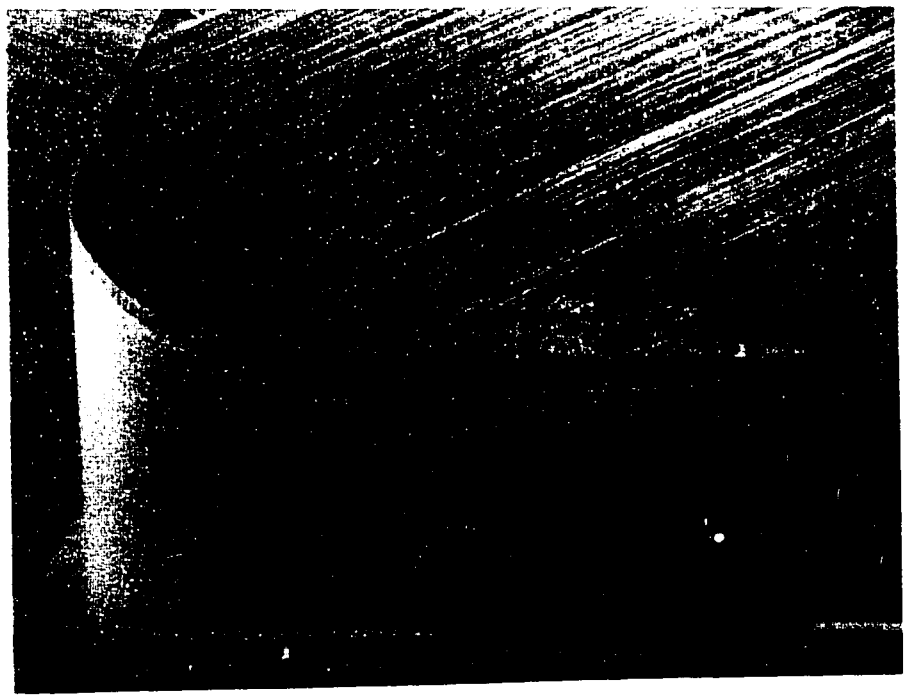

Fig. 4.54(b): SEM picture of tool crater wear, obtained at a feed of 0.055 mm/rev and a cutting speed of 400 m/min in Fe-28.9%Ni-0.10%C.

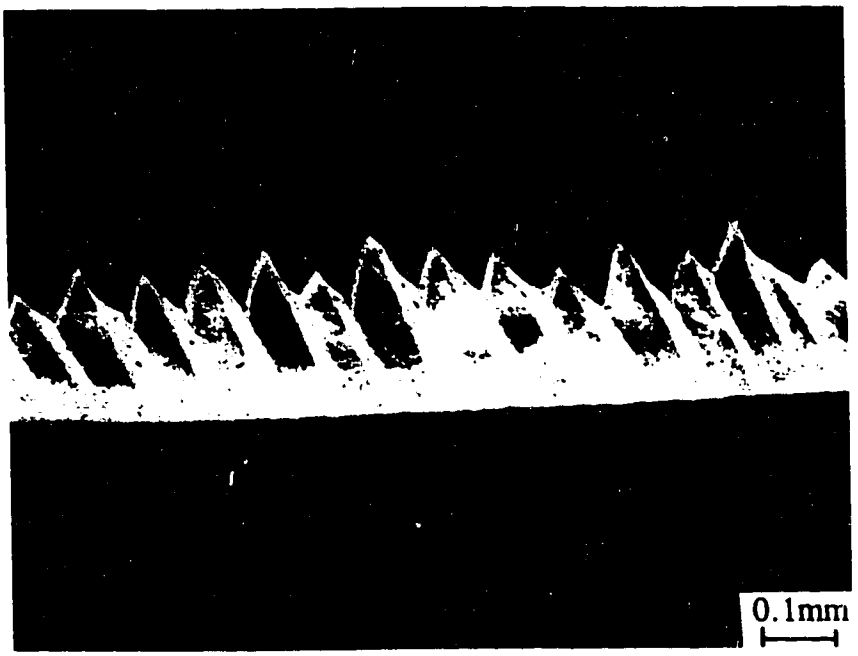

Fig. 4.55(a): Optical micrograph of a fully segmented chip obtained at a feed of 0.107 mm/rev and a cutting speed of 400 m/min in Fe-28.9%Ni-0.10%C.

Fig. 4.55(b): SEM picture of tool crater wear, obtained at a feed of 0.107 mm/rev and a cutting speed of 400 m/min in Fe-28.9%Ni-0.10%C.

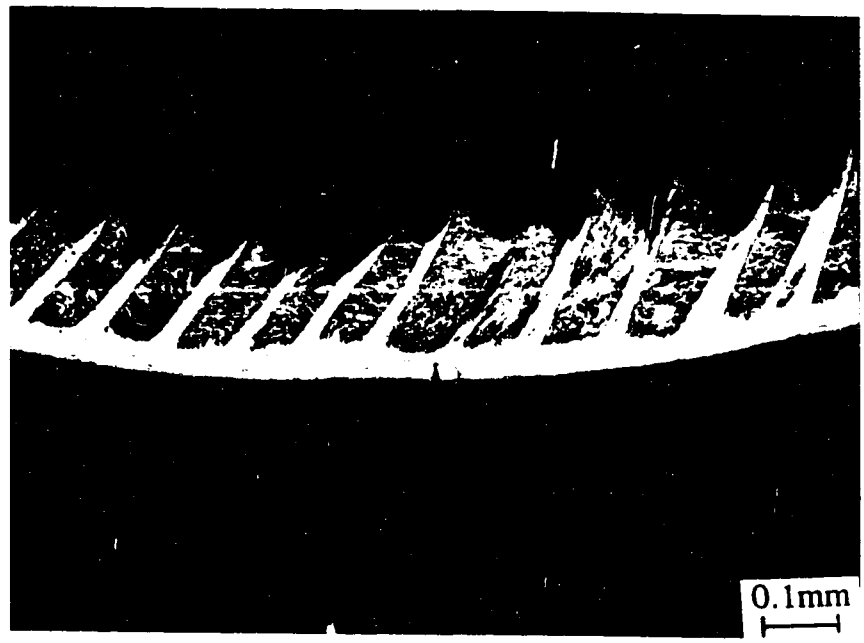

Fig. 4.56(a): Optical micrograph of a fully segmented chip obtained at a feed of 0.206 mm/rev and a cutting speed of 400 m/min in Fe-28.9%Ni-0.10%C.

Fig. 4.56(b): SEM picture of tool crater wear, obtained at a feed of 0.206 mm/rev and a cutting speed of 400 m/min in Fe-28.9%Ni-0.10%C.

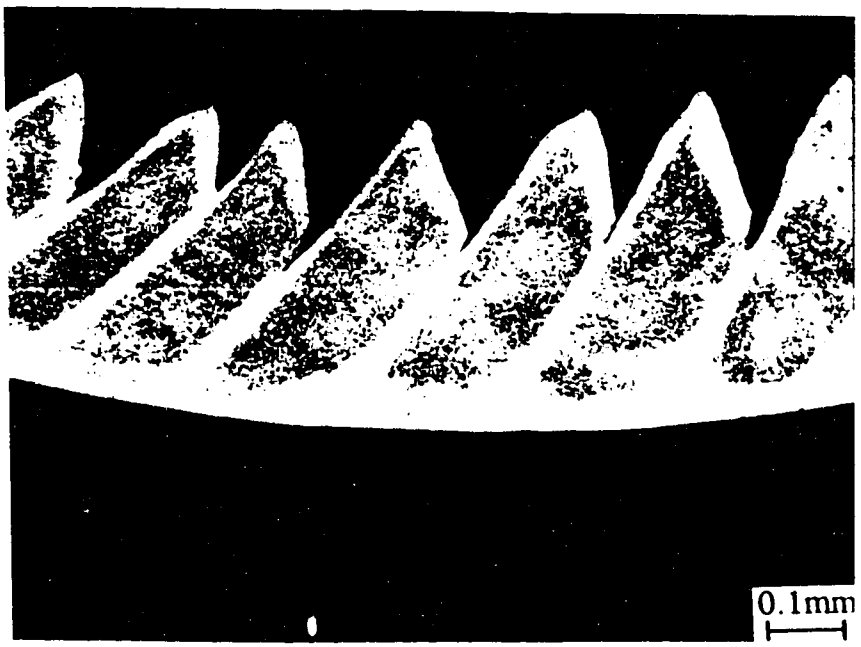

Fig. 4.57(a): Optical micrograph of a fully segmented chip obtained at a feed of 0.305 mm/rev and a cutting speed of 400 m/min in Fe-28.9%Ni-0.10%C.

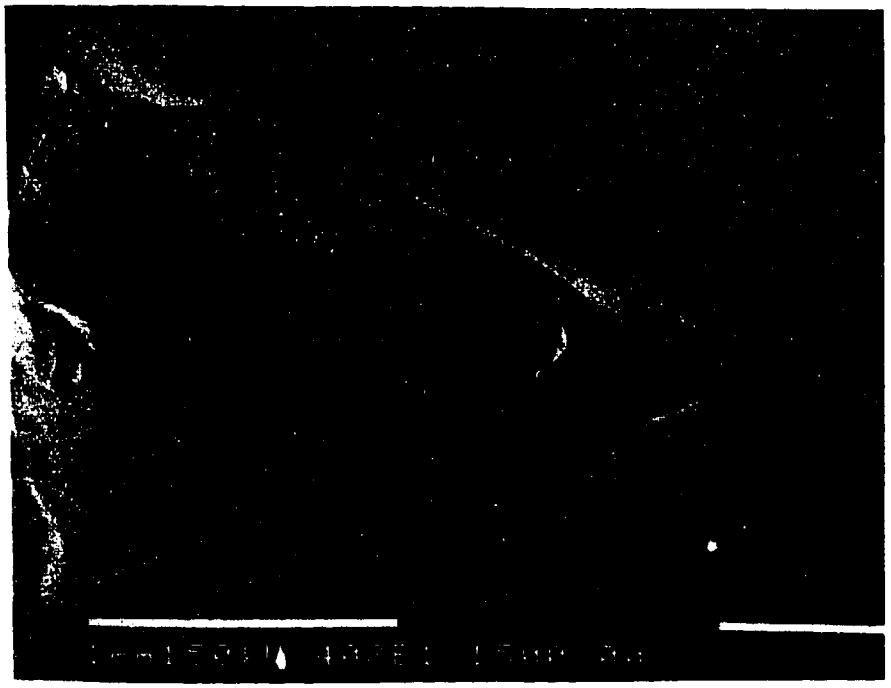

Fig. 4.57(b): SEM picture of tool crater wear, obtained at a feed of 0.305 mm/rev and a cutting speed of 400 m/min in Fe-28.9%Ni-0.10%C. Note the damage of the tool.

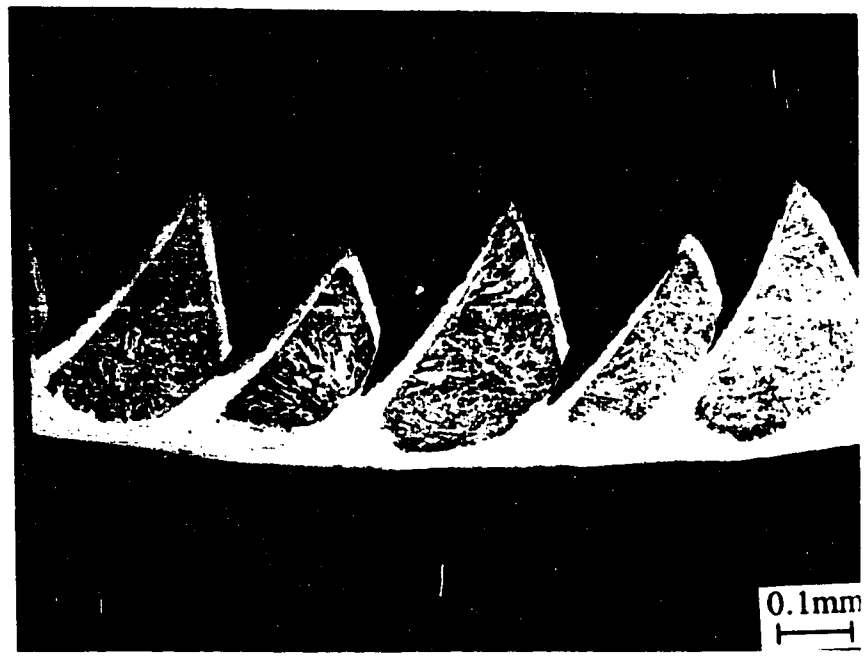

Fig. 4.58(a): Optical micrograph of a fully segmented chip obtained at a feed of 0.397 mm/rev and a cutting speed of 400 m/min in Fe-28.9%Ni-0.10%C.

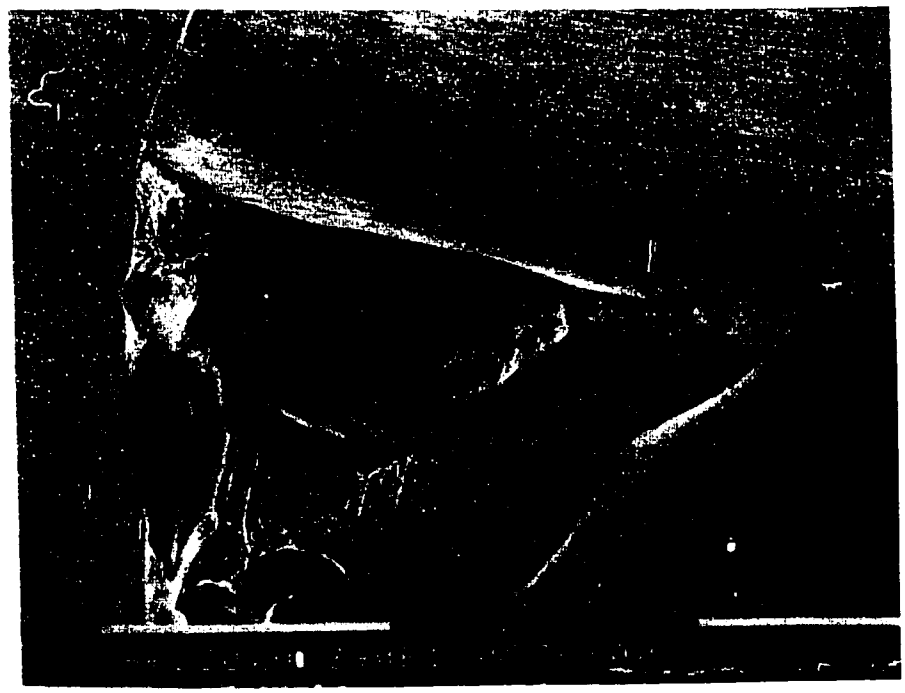

Fig. 4.58(b): SEM picture of tool crater wear, obtained at a feed of 0.397 mm/rev and a cutting speed of 400 m/min in Fe-28.9%Ni-0.10%C. Note the extensive damage of the tool.

segments bounded by the transformation shear bands which occur at the primary shear zone (Fig. 4.56(a)). Further increase of the feed through 0.259 mm/rev, and 0.305 mm/rev shows increased shear localisation and chip segmentation until full separation of the chip segments commences at a feed of 0.397 mm/rev as shown in Fig. 4.58(a). A low feed and high speed combination lowers the contact length and localises the crater closer to the cutting edge. Table 4.18 shows that the measured cutting forces increase with increase in feed. The calculated hydrostatic pressure and the chip body temperature increase with decrease in the feed. At a low feed phase transformation is predicted by the calculated temperature which is above the phase transformation temperature of the alloy.

Table 4.18: Measured cutting forces, calculated hydrostatic pressure and primary shear zone temperature as a function of feed in machining of hardened Fe-28.9Ni-0.1C alloy.

Feed (mm/rev)	Feed force (N)	Radial force (N)	Cutting force (N)	Hydrostatic pressure (Mpa)	Temperature in the chip body (^{0}C)	Temperature in the primary shear band (^{0}C)	Estimated A_r temperature corrected for pressure (^{0}C)
0.055	172	52	296	2691	418	---	292
0.107	335	118	492	2299	280	682	308
0.206	506	210	740	1796	115	708	328

A similar series of experiments were carried out in Fe-18.9%Ni-0.10%C alloy at a constant speed of 350 m/min and depth of cut of 2.0 mm. Figs. 4.59-4.63 show the change in chip morphology and the corresponding tool wear as a function of feed during the machining of martensitic Fe-18.9%Ni-0.1%C alloy at a constant cutting speed of 350 m/min and depth of cut of 2.0 mm. A continuous chip morphology corresponding to a low feed of 0.055 mm/rev. is formed at a cutting speed of 350 m/min. The corresponding tool crater wear shows a small contact length and the crater is localised near the cutting edge. The degree of chip segmentation and the intensity of crater wear increase with increase

in feed. Fig. 4.63(a) shows high degree of segmentation in the chip morphology corresponding to a high feed of 0.397 mm/rev at the same cutting speed of 350 m/min with the corresponding tool crater wear in Fig. 4.63(b) showing extensive damage to the tool cutting edge. Table 4.19 shows that the measured cutting forces increase with increase in feed. The the calculated hydrostatic pressure and the chip body temperature increase with decrease in the feed. The predicted chip body temperature falls below the phase transformation temperature of the Fe-18.9Ni-0.1 alloy even at the lowest feed used (0.055 mm/rev).

Figs. 4.64-4.67 show the changes in chip morphology and the corresponding tool wear as a function of feed during machining of martensitic Fe-9.7%Ni-0.1%C alloy at a constant speed of 400 m/min and depth of cut of 2.0 mm. The effect of reducing the feed is found to increase the tendency to form continuous chips.

4.4.7 The Effect of Depth of Cut on Chip Morphology and Tool Wear

The depth cut was varied from 0.1 mm (0.004 in) to 2.0 mm(0.08 in) at a constant speed and feed of 300 m/mm and 0.259 mm/rev (0.01 in/rev) respectively. Fig. 4.68- 4.70 show the morphology of the chips as a function of depth of cut, and the corresponding craters formed on the tool. The chips are segmented with each segment being enveloped in the transformation shear bands, at the primary and secondary shear zones in all depths of cut used. Table 4.20 shows the values of energy expended, shear stress, strain rate and temperature at the primary shear zone calculated from the measured cutting forces for each of the depths of cut used. The cutting forces increase but the shear stress decreases with increase in the depth of cut. However, the chip morphology remains the same over the wide range of depths of cut. At lower depths of cut, the crater is located closest to the tool cutting edge.

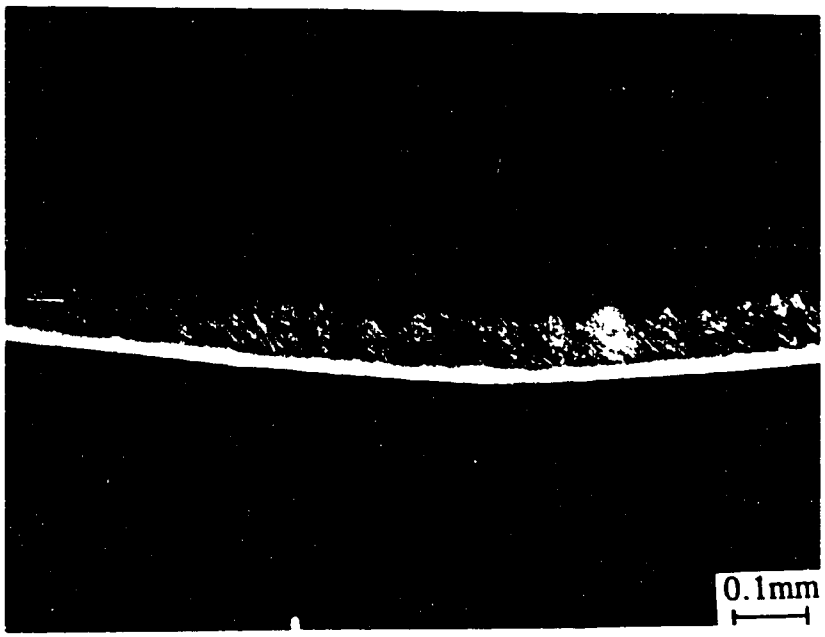

Fig. 4.59(a): Optical micrograph of a continuous or flow chip obtained at a feed of 0.055 mm/rev and a cutting speed of 350 m/min in Fe-18.9%Ni-0.10%C.

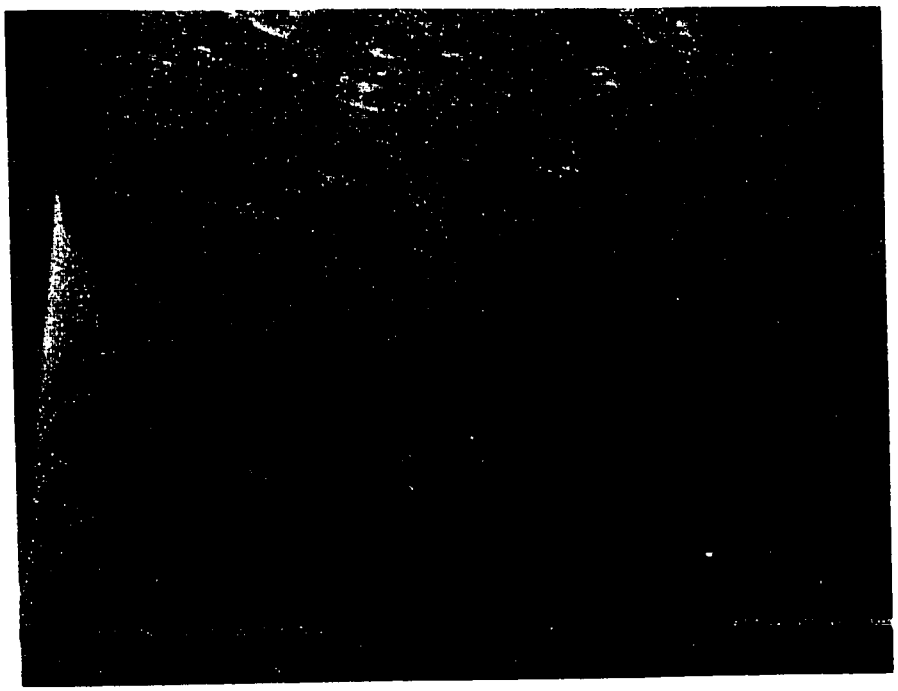

Fig. 4.59(b): SEM picture of tool crater wear, obtained at a feed of 0.055 mm/rev and a cutting speed of 350 m/min in Fe-18.9%Ni-0.10%C.

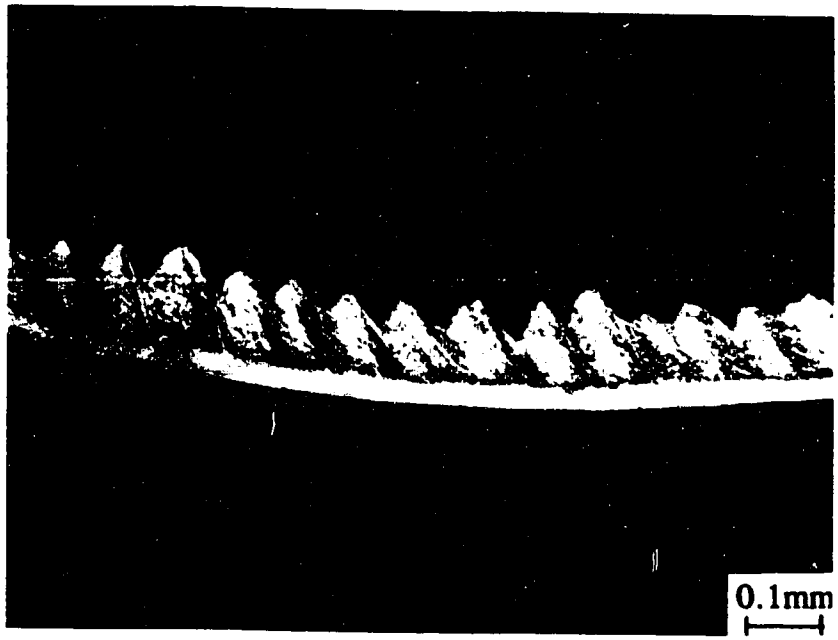

Fig. 4.60(a): Optical micrograph of a partially segmented chip obtained at a feed of 0.103 mm/rev and a cutting speed of 350 m/min in Fe-18.9%Ni-0.10%C.

Fig. 4.60(b): SEM picture of tool crater wear, obtained at a feed of 0.103 mm/rev and a cutting speed of 350 m/min in Fe-18.9%Ni-0.10%C.

Fig. 4.61(a): Optical micrograph of a fully segmented chip obtained at a feed of 0.206 mm/rev and a cutting speed of 350 m/min in Fe-18.9%Ni-0.10%C.

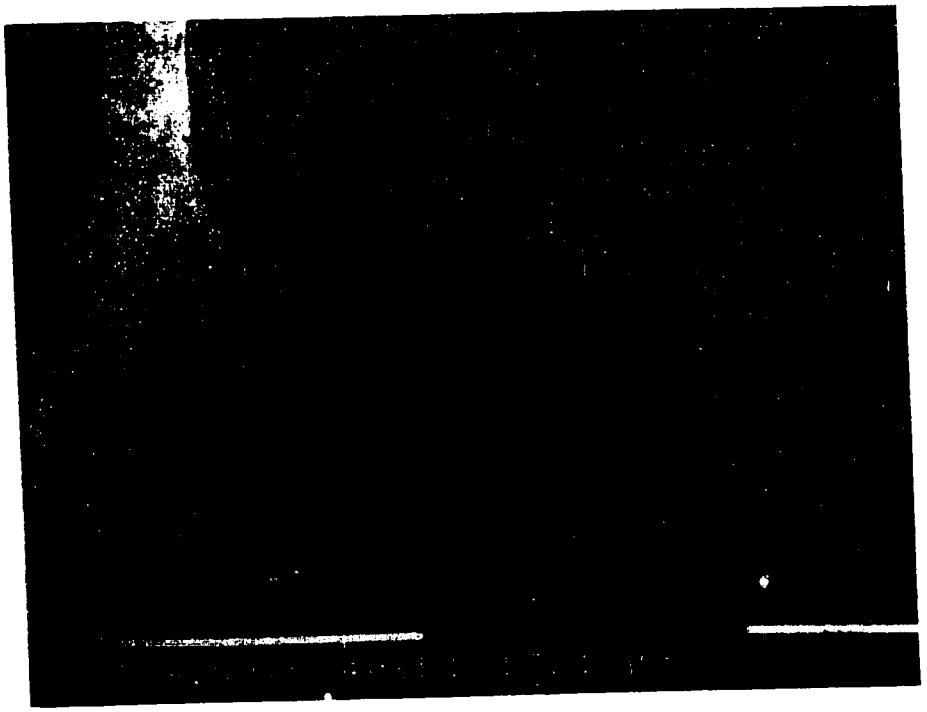

Fig. 4.61(b): SEM picture of tool crater wear, obtained at a feed of 0.206 mm/rev and a cutting speed of 350 m/min in Fe-18.9%Ni-0.10%C. Note the damage of the cutting edge of the tool.

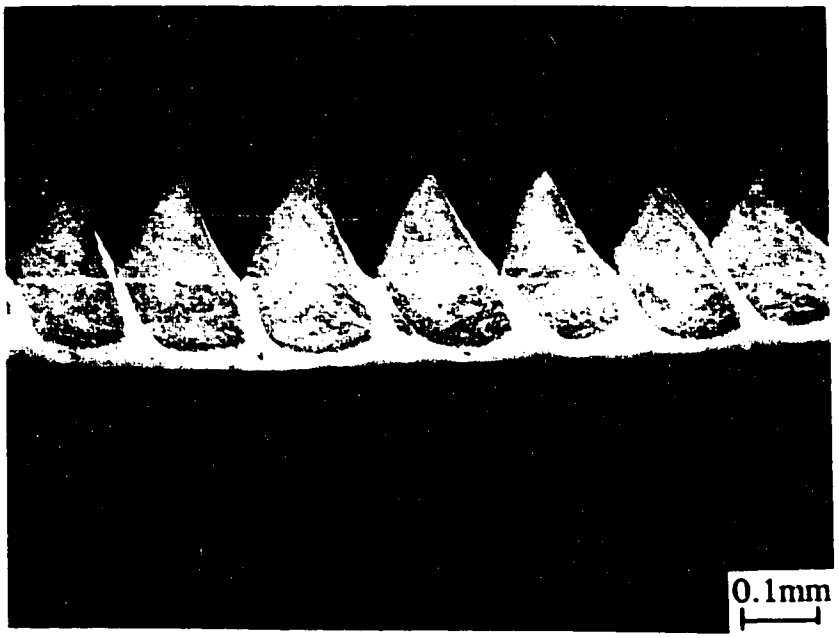

Fig. 4.62(a): Optical micrograph of a fully segmented chip obtained at a feed of 0.305 mm/rev and a cutting speed of 350 m/min in Fe-18.9%Ni-0.10%C.

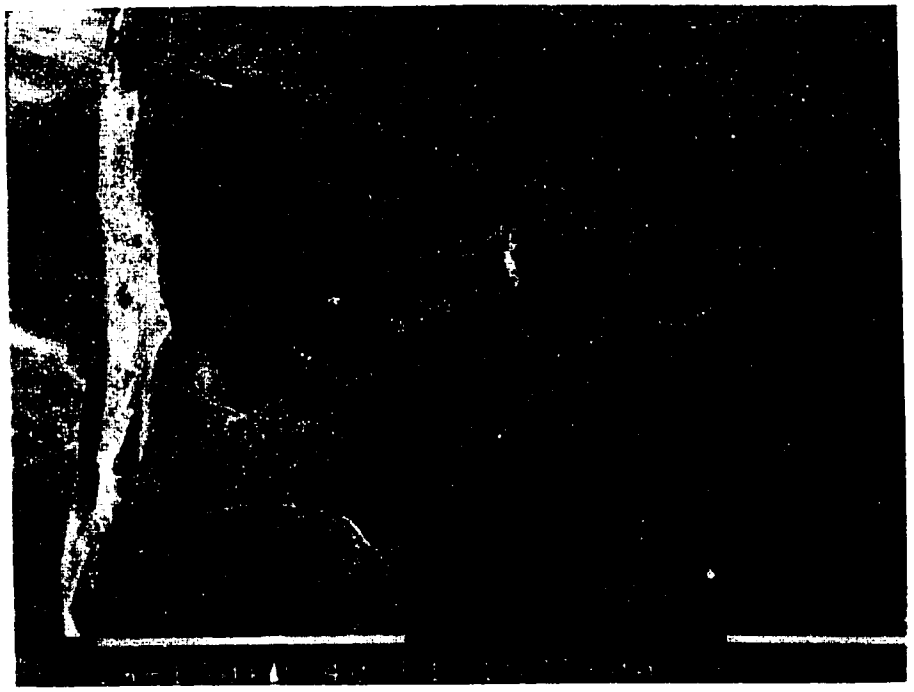

Fig. 4.62(b): SEM picture of tool crater wear, obtained at a feed of 0.305 mm/rev and a cutting speed of 350 m/min in Fe-18.9%Ni-0.10%C. Note the extensive cutting edge damage to the tool.

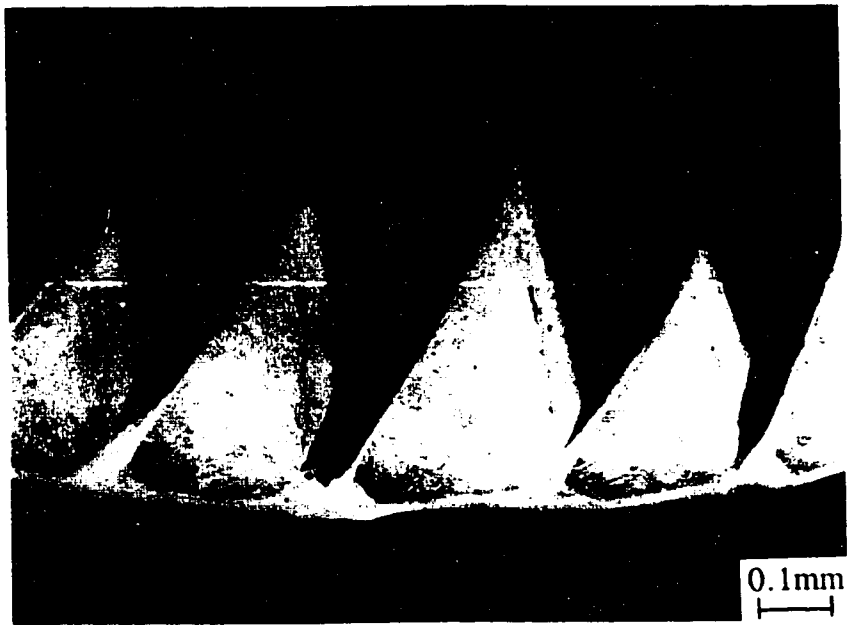

Fig. 4.63(a): Optical micrograph of a fully segmented chip obtained at a feed of 0.397 mm/rev and a cutting speed of 350 m/min in Fe-18.9%Ni-0.10%C.

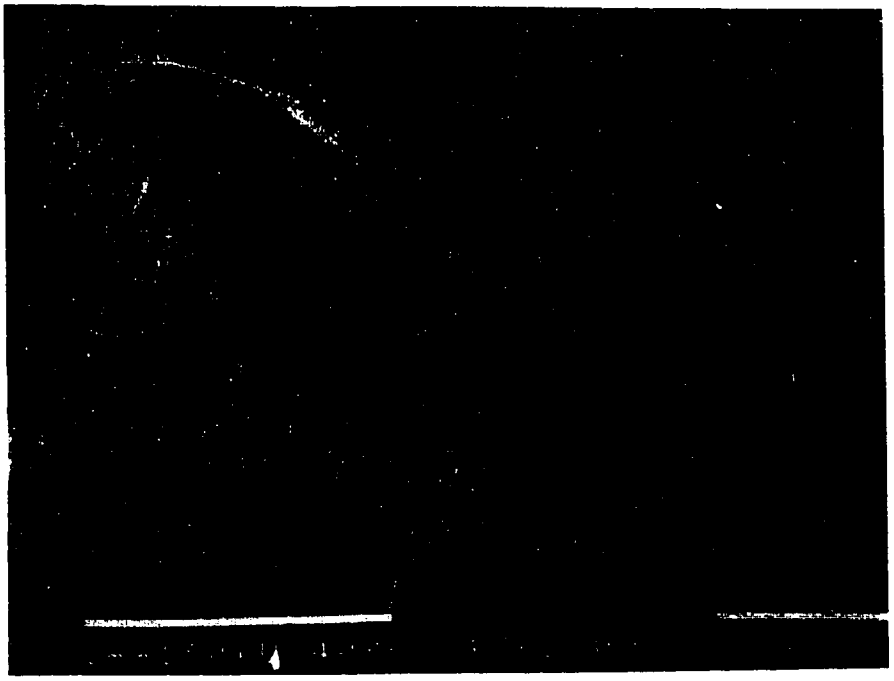

Fig. 4.63(b): SEM picture of tool crater wear, obtained at a feed of 0.397 mm/rev and a cutting speed of 350 m/min in Fe-18.9%Ni-0.10%C. Note the extensive cutting edge damage to the tool.

4.4.8 Effect of External Lubricant on Thermoplastic Shear:

Figs. 4.71-4.74 show the change in chip morphology and the corresponding crater wear of the tool during machining of martensitic Fe-28.9%Ni-0.10%C alloy at 25, 75 , 150 and 300 m/min respectively, while applying an oil based coolant. The corresponding wear of the tool is shown in the adjacent pictures of the craters. The chip morphology is exactly the same as in the case of dry machining, however, there appears to be a reduction in tool wear caused by the use of a coolant. (compare the chip morphologies and tool wear shown in Figs. 4.71 - 4.74 with those shown in Figs. 4.26-4.31). The critical speed for chip segmentation (75 m/min) remains the same as in dry machining. The results are found to be comparable over the range of higher cutting speeds investigated. Since the heat generated is adiabatic, external coolants are not effective at high cutting speeds.

Table 4.19: Measured cutting forces, calculated hydrostatic pressure and primary shear zone temperature as a function of feed in machining of hardened Fe-18.9Ni-0.1C alloy.

Feed (mm/rev)	Feed force (N)	Radial force (N)	Cutting force (N)	Hydrostatic pressure (MPa)	Temperature in the chip body (^{0}C)	Primary shear band Temperature (^{0}C)
0.055	171	56	306	2778	422	---
0.107	301	99	485	2356	337	---
0.206	629	212	744	1805	122	534

Table 4.20: Values of measured cutting forces and calculated energy, shear stress, strain rate and temperature at the primary shear zone as function of depth of cut.

Depth of cut (mm)	Feed force (N)	Radial force (N)	Cutting force (N)	Shear energy (Nm/s)	Shear stress (MPa)	Strain rate (/s)	Primary shear band temperature (^{0}C)
0.1	39	107	151	148	621	144789	716
0.5	117	153	289	440	370	124630	721
1.0	414	244	580	534	224	117178	759
1.5	495	258	739	1119	305	108051	762
2.0	619	244	1011	2069	424	101373	771

Fig. 4.64(a): Optical micrograph of a continuous or flow chip obtained at a feed of 0.055 mm/rev and a cutting speed of 400 m/min in Fe-9.7%Ni-0.10%C.

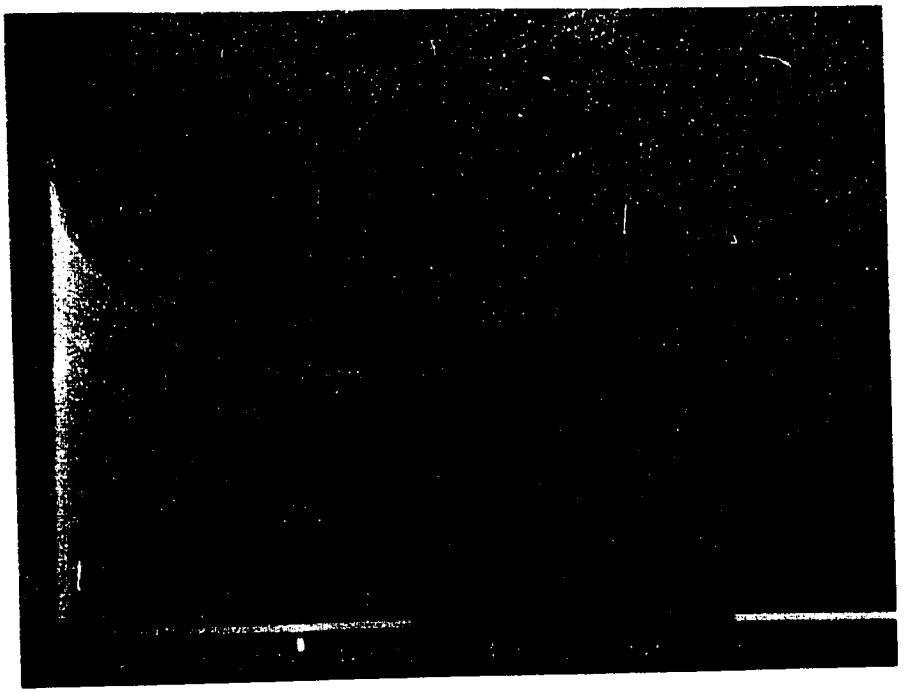

Fig. 4.64(b): SEM picture of tool crater wear, obtained at a feed of 0.055 mm/rev and a cutting speed of 400 m/min in Fe-9.7%Ni-0.10%C.

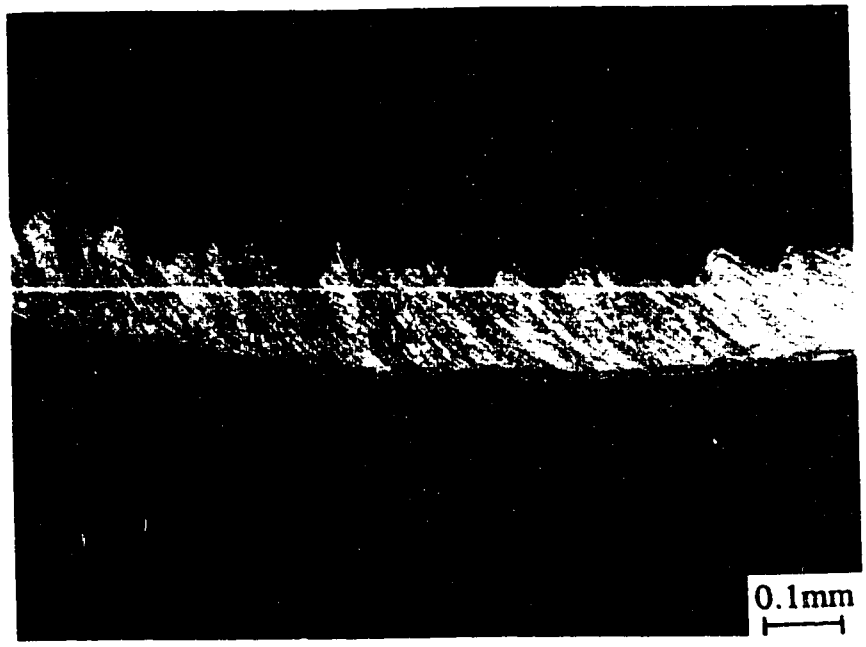

Fig. 4.65(a): Optical micrograph of a continuous chip obtained at a feed of 0.103 mm/rev and a cutting speed of 400 m/min in Fe-9.7%Ni-0.10%C.

Fig. 4.65(b): SEM picture of tool crater wear, obtained at a feed of 0.103 mm/rev and a cutting speed of 400 m/min in Fe-9.7%Ni-0.10%C.

Fig. 4.66(a): Optical micrograph of a fully segmented chip obtained at a feed of 0.259 mm/rev and a cutting speed of 400 m/min in Fe-9.7%Ni-0.10%C.

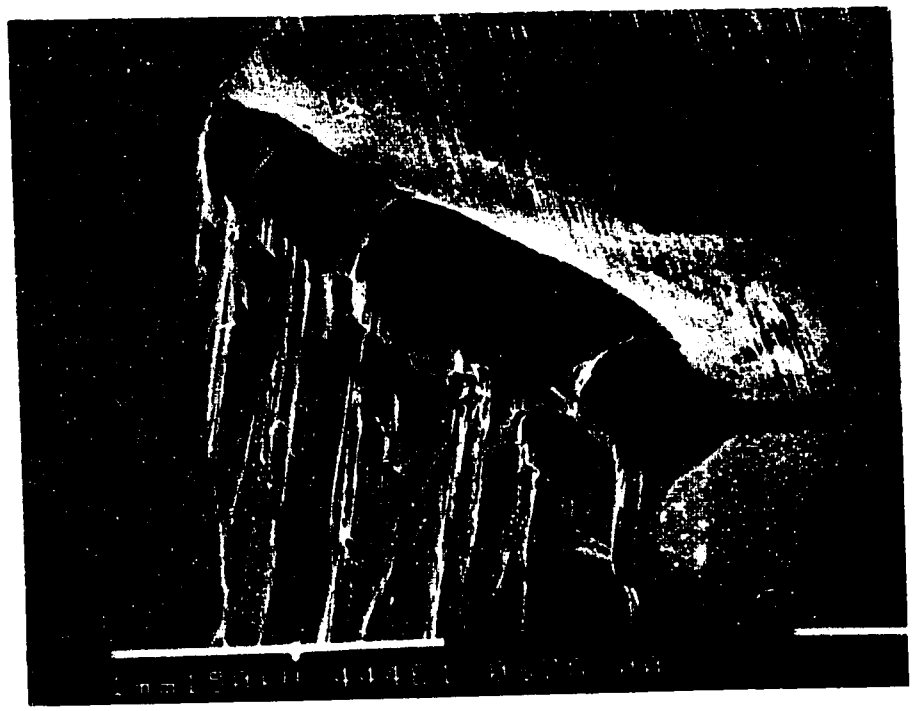

Fig. 4.66(b): SEM picture of tool crater wear, obtained at a feed of 0.259 mm/rev and a cutting speed of 400 m/min in Fe-9.7%Ni-0.10%C. Note the damage of the cutting edge of the tool.

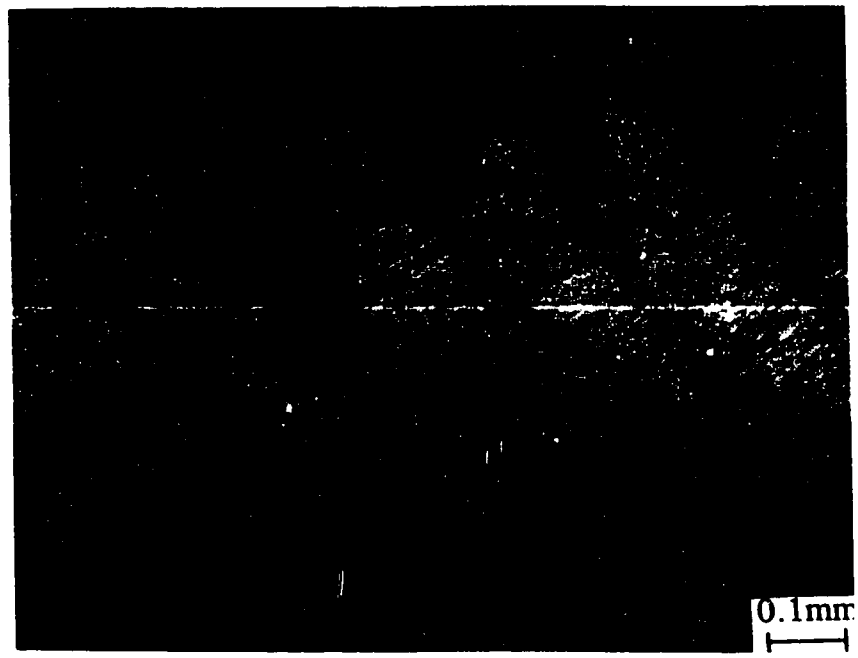

Fig. 4.67(a): Optical micrograph of a fully segmented chip obtained at a feed of 0.397 mm/rev and a cutting speed of 400 m/min in Fe-9.7%Ni-0.10%C.

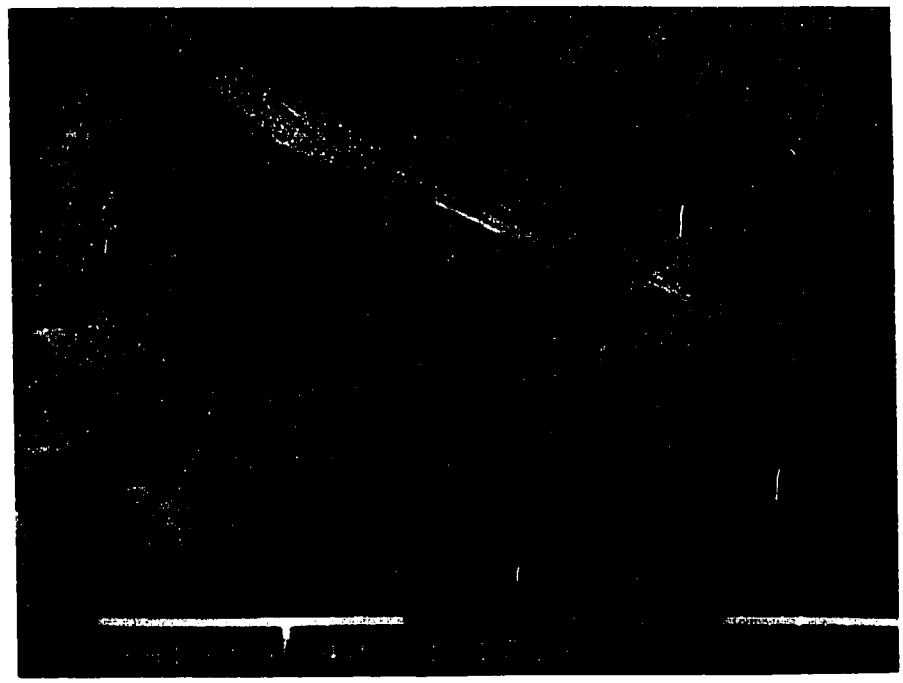

Fig. 4.67(b): SEM picture of tool crater wear, obtained at a feed of 0.397 mm/rev and a cutting speed of 400 m/min in Fe-9.7%Ni-0.10%C. Note the damage of the tool.

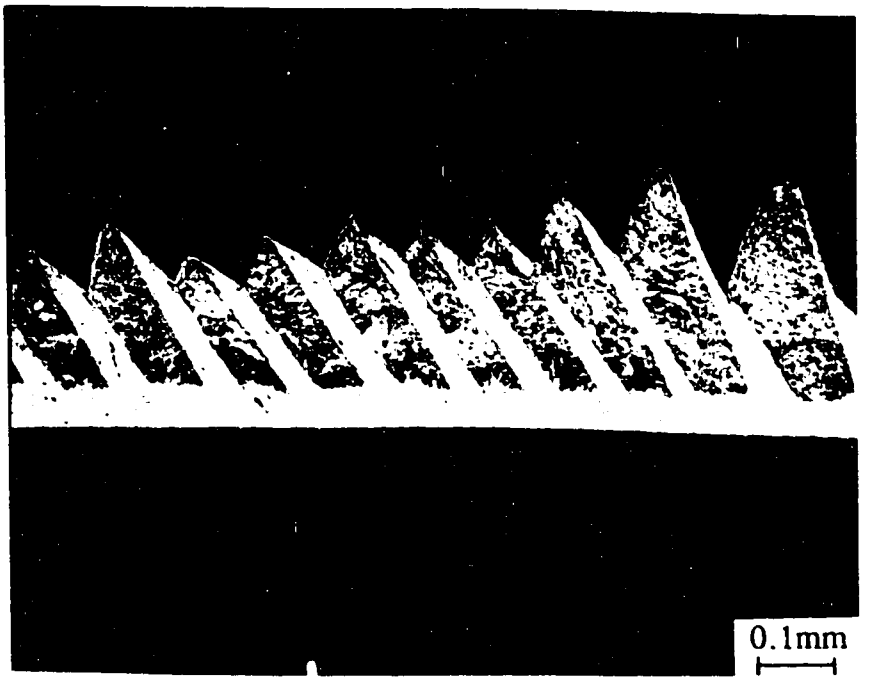

Fig. 4.68(a): Optical micrograph of a fully segmented chip obtained at a cutting speed of 300 m/min. and a depth of cut of 0.1 mm, showing transformation shear band enveloping the segmented chip obtained from an Fe-28.9wt%Ni-0.1wt%C alloy. The white region that has undergone phase transformation from martensite to austenite at 400°C.

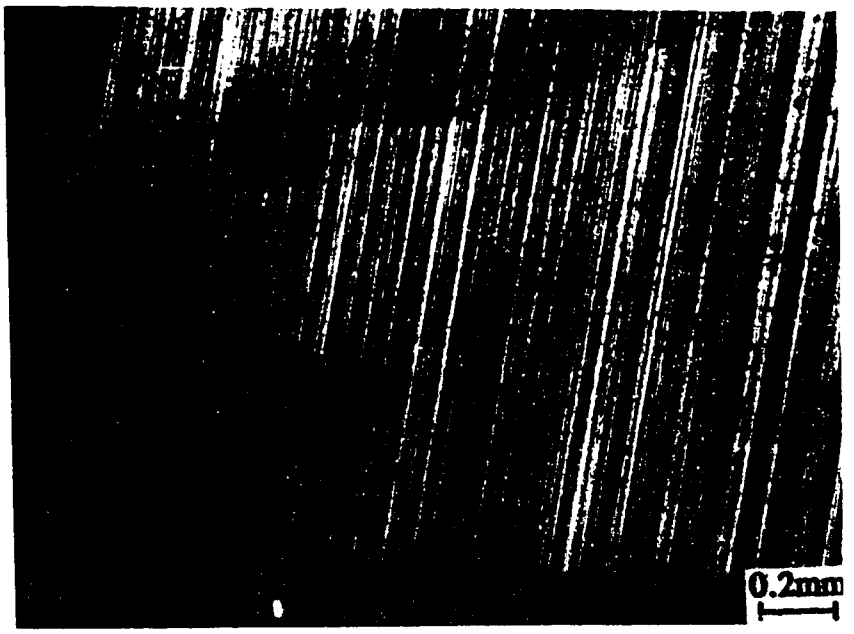

Fig. 4.68(b): Optical photograph of tool crater wear obtained at the end of 1 second machining of an Fe-28.9wt%Ni-0.1wt%C alloy at a cutting speed of 300 m/min. and depth of cut of 0.1 mm. Note the location of the crater at the tip of the tool.

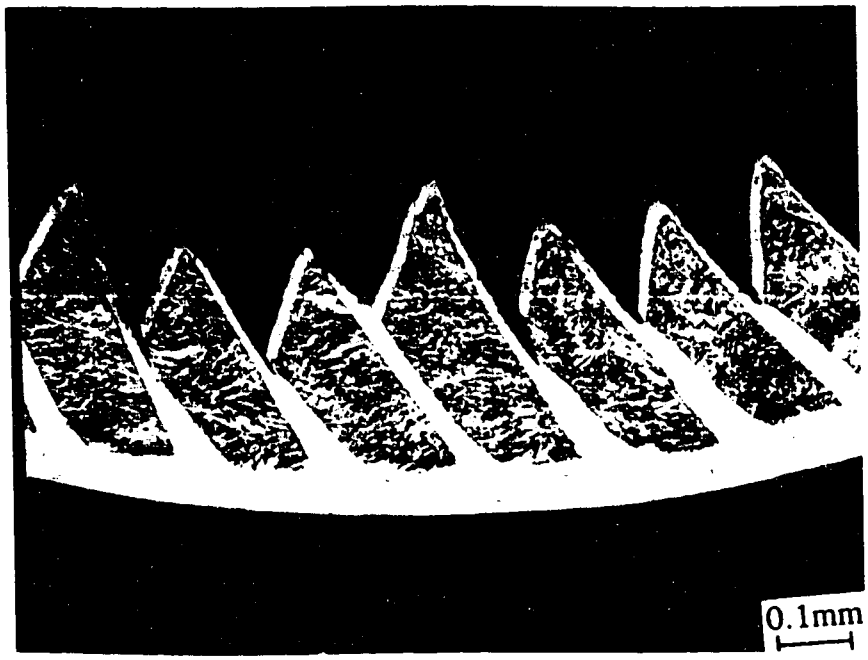

Fig. 4.69(a): Optical micrograph of a fully segmented chip obtained at a cutting speed of 300 m/min. and depth of cut of 1.0 mm, showing transformation shear band enveloping the segmented chip obtained from an Fe-28.9wt%Ni-0.1wt%C alloy. The white region that has undergone phase transformation from martensite to austenite at 400°C.

Fig. 4.69(b): Optical photograph of tool crater wear obtained at the end of 1 second machining of an Fe-28.9wt%Ni-0.1wt%C alloy at a cutting speed of 300 m/min. And depth of cut of 1.0 mm The crater is located at a small distance (0.14 mm) from the cutting edge.

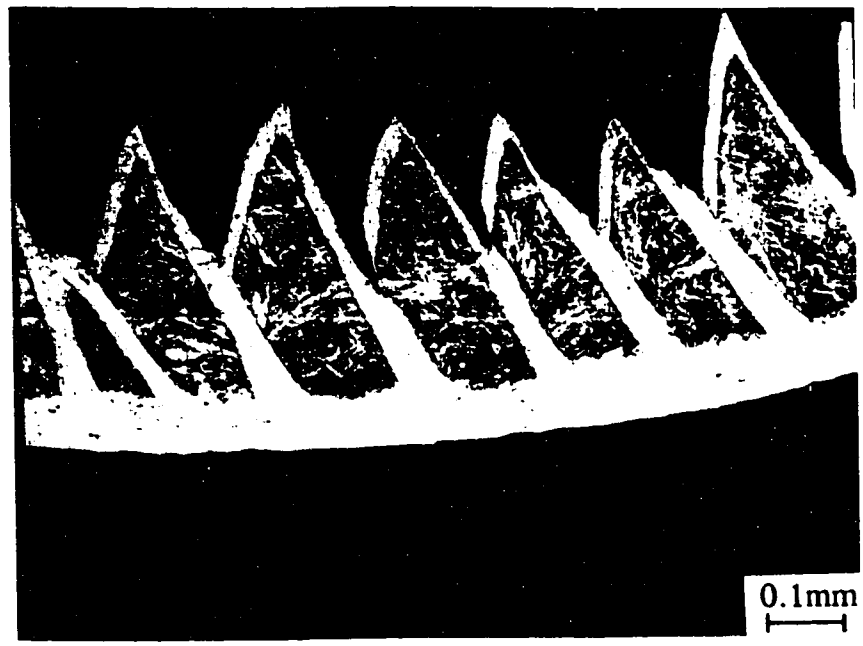

Fig. 4.70(a): Optical micrograph of a fully segmented chip obtained at a cutting speed of 300 m/min. and a depth of cut of 2.0 mm, showing transformation shear band enveloping the segmented chip obtained from an Fe-28.9wt%Ni-0.1wt%C alloy. The white band is the region that has undergone phase transformation from martensite to austenite at 400°C.

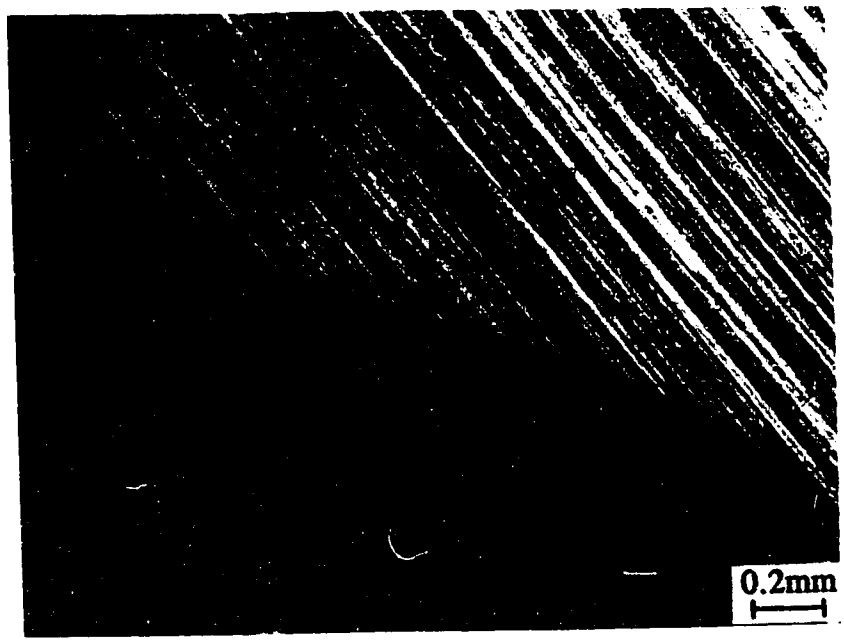

Fig. 4.70(b): Optical photograph picture of tool crater wear obtained at the end of 1 second machining of an Fe-28.9wt%Ni-0.1wt%C alloy at a cutting speed of 300 m/min. And depth of cut of 2.0 mm. Note the location of the crater at some distance (0.14) from to the cutting edge of the tool.

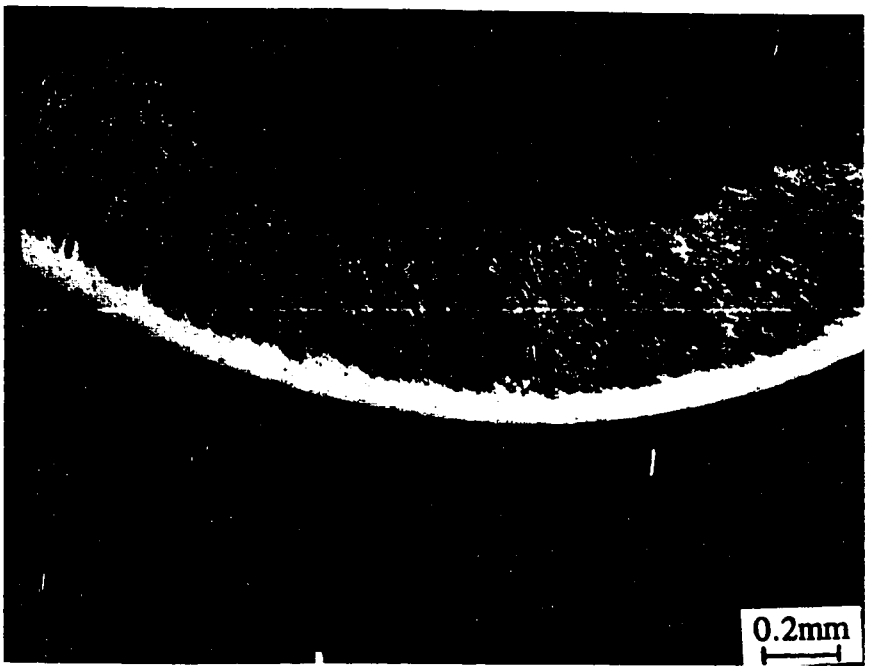

Fig. 4.71(a): Optical micrograph of a continuous or flow chip obtained at a cutting speed of 25 m/min., showing a transformation shear band located at and parallel to the tool-chip interface at a low cutting speed in machining of Fe-28.9wt%Ni-0.1wt%C alloy using a coolant. The morphology of the chip is the same as in dry machining.

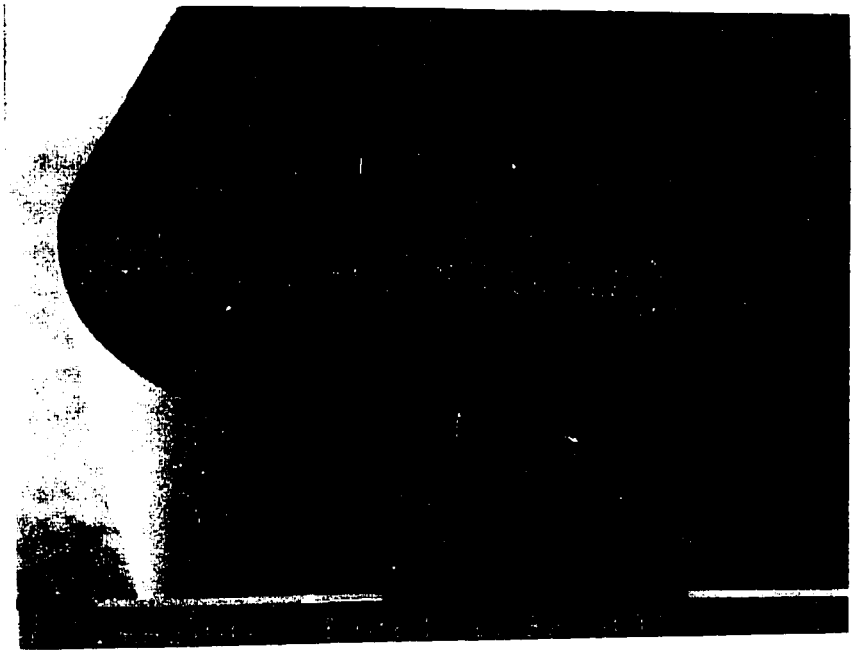

Fig. 4.71(b): SEM picture of tool crater wear obtained at the end of 10 seconds machining of an Fe-28.9wt%Ni-0.1wt%C alloy at a cutting speed of 25 m/min. and with use of a coolant.

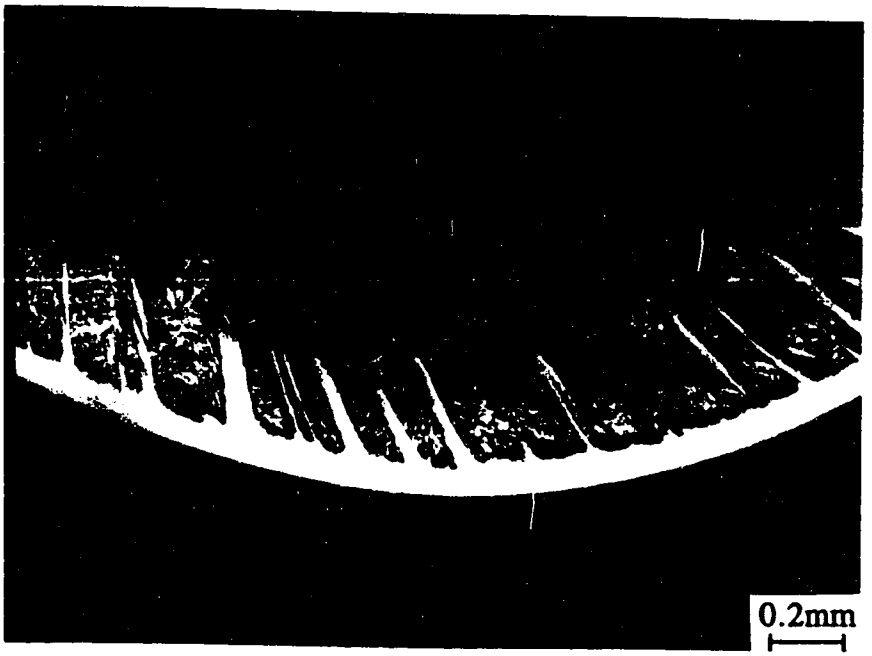

Fig. 4.72(a): Optical micrograph of a partially segmented chip obtained at a cutting speed of 75 m/min., showing transformation shear band located parallel and at an angle to the tool-chip interface at cutting speed of 75 m/min in machining of Fe-28.9wt%Ni-0.1wt%C alloy with the use of a coolant. The chip morphology is same as in dry machining.

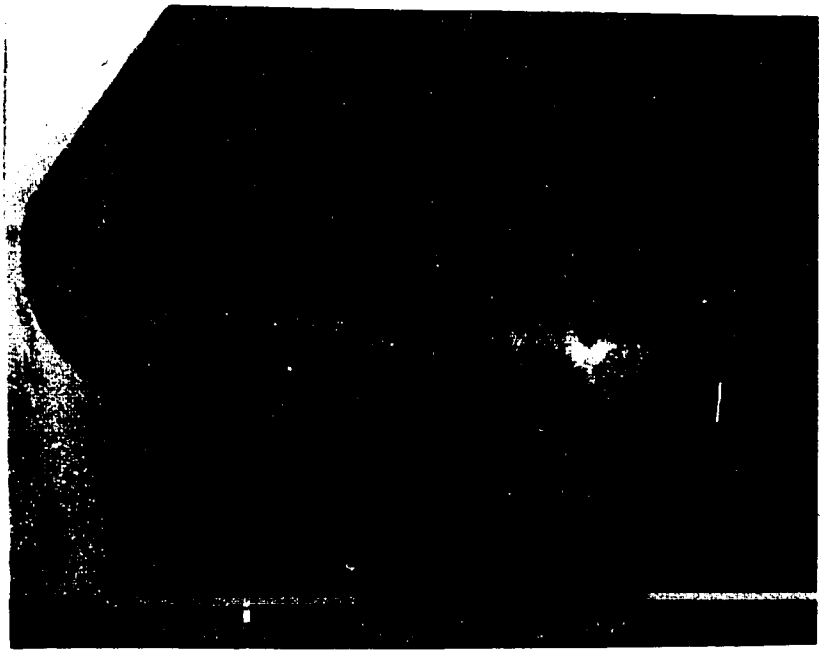

Fig. 4.72(b): SEM picture of tool crater wear obtained at the end of 10 seconds machining an Fe-28.86wt%Ni-0.1wt%C alloy at a cutting speed of 75 m/min. using a coolant. Note the location of the crater at some distance (0.33 mm) from the cutting edge is the same as in dry machining.

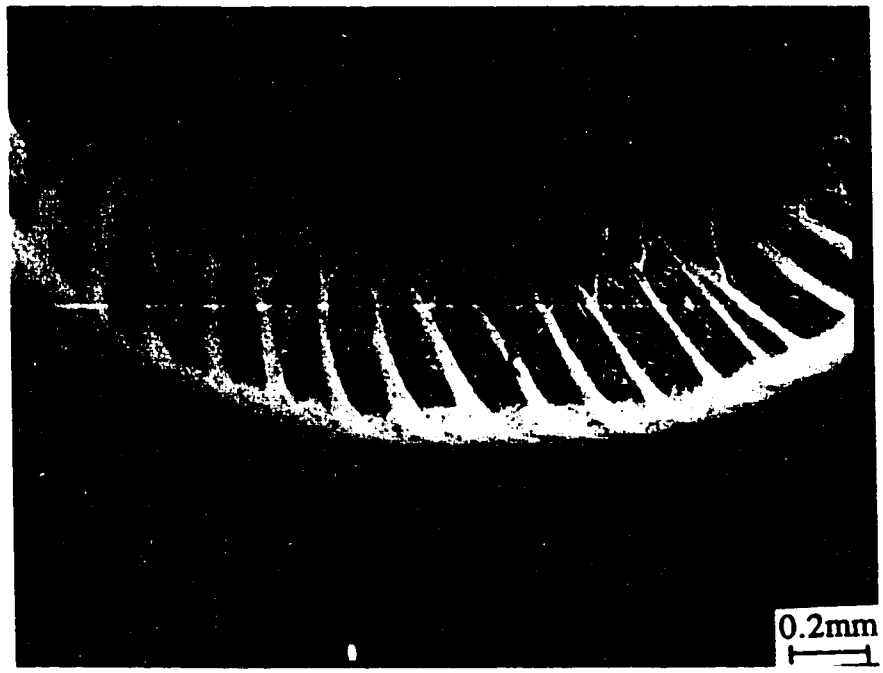

Fig. 4.73(a): Optical micrograph of a fully segmented chip obtained at a cutting speed of 150 m/min. And with use of a coolant, showing transformation shear band enveloping the segmented chip at cutting speed of 150 m/min in Fe-28.9wt%Ni-0.1wt%C alloy. The white region that has undergone phase transformation from martensite to austenite at 400°C.

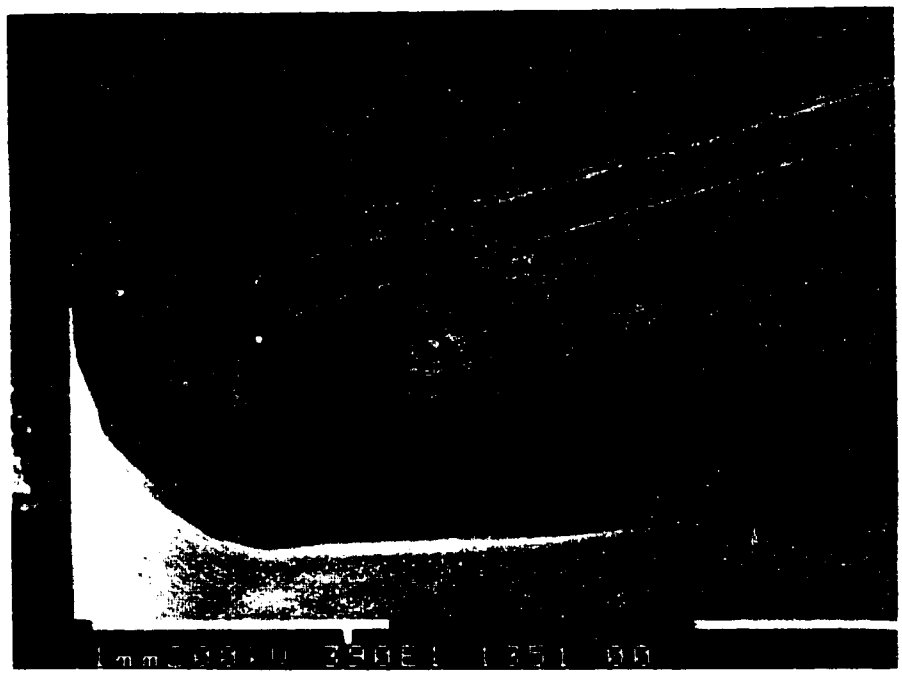

Fig. 4.73(b): SEM picture of tool crater wear obtained at the end of 10 seconds machining of an Fe-28.9wt%Ni-0.1wt%C alloy at a cutting speed of 150 m/min. using a coolant.

Fig. 4.74(a): Optical micrograph of a fully segmented chip obtained at a cutting speed of 300 m/min. With use of coolant, showing transformation shear band enveloping the segmented chip at cutting speed of 300 m/min in Fe-28.9wt%Ni-0.1wt%C alloy. The white region that has undergone phase transformation from martensite to austenite at 400^{0}C.

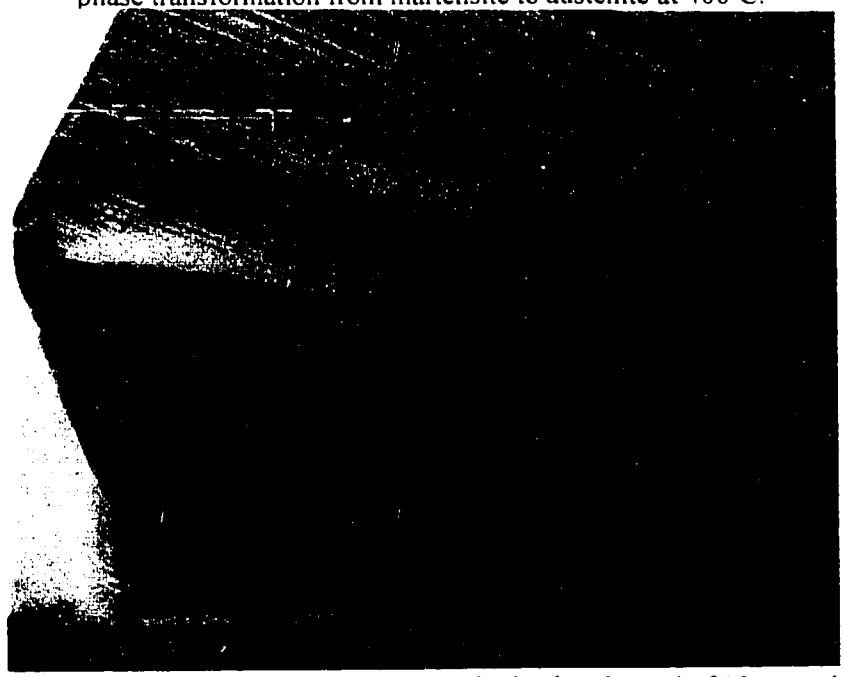

Fig. 4.74(b): SEM picture of tool crater wear obtained at the end of 10 seconds machining of an Fe-28.9wt%Ni-0.1wt%C alloy at a cutting speed of 300 m/min. using a coolant. Note the location of the crater closer to the cutting edge of the tool (0.18 mm away).

CHAPTER 5

DISCUSSION

5.1 Material Behaviour in Machining

Even though a large amount of literature has been reported on machining, material behaviour has not been given adequate attention. An attempt has been made in the present study to focus on the behaviour of workpiece material during high speed machining and its influence on tool wear, chip formation and surface finish. The important variables considered are matrix hardening and second phase particles. The microstructural properties of the workpiece material influence shear localisation and hence the critical speed for chip segmentation. The ductile behaviour of the chip can be analysed using damage concepts. Thus the critical accumulated damage before fracture (CAD), which is a measure of ductile fracture of workpiece material, is used to classify the workpiece materials according to their critical speed for chip segmentation. Table 5.1 gives a broad overview of the material behaviour during machining for the iron alloys investigated in the present work. The classification is based on the heat treatment condition of the matrix and the microstructural constituents of the matrix. The presence of inclusions in the matrix lowers the (CAD) and the critical speed for chip segmentation by increasing the contribution of geometrical softening to shear localisation in the primary shear zone. Hardening of the matrix lowers the CAD and the critical speed for chip segmentation by increasing the material's susceptibility to thermoplastic shear localisation in the primary shear zone. In the absence of geometrical and thermal softening, strain rate hardening of the matrix increases the damage rate to promote chip segmentation at high cutting speeds.

Ferritic ductile iron with a large volume fraction of graphite nodules was chosen in the present studies to elucidate the effect of geometrical softening on shear localisation and chip segmentation. A comparative study with AISI 1020 steel was carried out to demonstrate the ferritic matrix behaviour devoid of graphite inclusions. The effect of increasing the volume fraction of pearlite content in the iron matrix was investigated by comparing the machinability behaviour of AISI 1020 steel with AISI 1045 and AISI 1080 steel, i.e., by increasing the carbon content from 0.20, 0.45 to 0.80 wt%. In order to clarify the role of thermal softening, Fe-xNi-0.1wt%C alloy was chosen where x was varied from 1.5 wt% to 30wt%. This series of alloys allowed clarification of the role of thermal softening due to phase transformation as distinct from tempering of the hardened matrix. The effect of metal cutting variables, i.e., speed, feed, depth of cut and external lubrication on microstructural response to machining was analysed in terms of strain, strain rate, temperature and pressure effects to rationalise experimental observations on chip segmentation and tool wear in iron-nickel-carbon alloys.

Table 5.1: Material behaviour in machining

Microstructure	Hardened matrix with inclusions	Hardened matrix without inclusions	Unhardened matrix with inclusions	Unhardened matrix without inclusions
Examples investigated in present work	None	Fe-Ni-C alloy with 28.9 to 9.7 wt% Ni and 0.1wt%C	Ferritic ductile iron with ~10% graphite volume fraction	AISI 1020 steel, AISI 1045 steel, AISI 1080 steel, and annealed Fe-28.9Ni-0.1C alloy
CAD (measure of resistance to ductile fracture)	Lowest	Moderate	Moderate	Highest
Dominant mechanism of shear localisation in the primary shear zone	Thermal and geometrical softening	Thermal softening	Geometrical softening	Strain rate hardening followed by thermal softening
Critical speed for chip segmentation at a feed of 0.259 mm/rev.	Lowest	Moderate (75 m/min for 28.9Ni, 150 m/min for 18.9Ni 400 m/min for 9.7Ni alloy)	Moderate (350 m/min)	Highest (> 400 m/min)

5.2 The Tribological Condition at the Tool-Chip Interface

An attempt has been made to provide a comprehensive data base from which the conditions at the tool-chip interface can be defined as a function of metal cutting variables. On-line measurement of most cutting parameters is difficult and has not been possible to a larger extent. However, on-line measurement of the cutting forces was possible. Determination of the contact length and shear zone thickness was accomplished after the cutting process through optical and electron microscopy. Measurement of the chip thickness enabled estimation of the shear plane angle. Subsequently, the stresses, strain rates, strains and temperature were calculated using theoretical models and the measured parameters. It was shown in chapter 2 that the tribological condition at the tool-chip interface can be described using the adhesion and asperity deformation theories. These theories are combined in this section to develop a physical model for defining seizure in metal cutting based on experimental measurement of metal cutting parameters. Before this is done the tool-chip interfacial conditions which prevail before seizure occurs are examined as a function of cutting speed.

The tribological condition of the tool-chip interface is assumed to be controlled by junction growth, which gives rise to adhesion and friction as described by McFarlane and Tabor [175] and Tabor [47]. Adhesion is defined as a measure of the yield strength of the junctions i.e. the stress required to squeeze the asperities and bring them to a plastic state. Friction is a measure of the shear strength of the junctions i.e. the stress required to shear the asperities causing relative motion at the interface. According to McFarlane and Tabor [175] and Tabor [47], junction growth proceeds until practically the whole of the geometric area is in contact and gross seizure occurs in clean interfaces. If the interface is contaminated, junction growth occurs in clean metal regions until the shear stress reaches the critical shear strength of the interface beyond which further junction growth is impossible and gross sliding occurs within the interfacial layer. If the interface is lubricated the amount of metallic adhesion is so small that it is unable to withstand the released elastic stress when the load is removed.

In this case change over from elastic to plastic contact does not occur. The friction is determined by the shear strength of the lubricant film itself. Consequently the conditions at the interface are essentially sliding. The foregoing simplified picture suggests that three distinct kinds of interfaces can be encountered in metal cutting. These are clean, contaminated and lubricated interfaces. It is therefore worthwhile to examine the influence of the cutting conditions, the microstructure of the tool and workpiece and the state of stress of the workpiece on the type of interface formed in metal cutting.

At low cutting speeds < 100 m/min, the compressive stress at the tool chip interface is lower than the yield strength of the workpiece material, Fig. 4.5. Based on Tabor's [47] model only a few asperities are in contact under these conditions. The weak adhesive junctions formed are immediately broken by the elastic recovery of the chip. Even though the chip material may be clean during dry machining of pure metals, the tool surface is not clean at the beginning of the cutting process. The interface remains contaminated throughout the cutting process, leaving no chance for any perfect adhesion to occur. The result is the existence of essentially sliding conditions at the tool-chip interface. The contact lengths measured after machining AISI 1045 steel in air and with a jet of helium gas directed at the cutting point are equal at high cutting speeds, Fig. 4.9. This suggests that the tool stays unexposed for as long as the cutting continues. At high cutting speeds the compressive stress and the temperature at the tool-chip interface are high, Table 4.1. Thermal softening of the chip material can occur under these conditions. It is possible for contaminants and oxides to be worn away from the surface of the tool. Then gradual generation of clean surfaces as the cutting proceeds allows strong adhesive junctions to form. This action requires a finite time. The time taken by the chip to clean the surface of the tool of the oxides, adsorbed organic layers and other substances before seizure occurs is in the order of 2 seconds at moderate cutting speeds. This time would decrease with increase in strength of workpiece and the cutting speed. Such tool cleaning first arises further back along the contact length where the temperature is high. Near the cutting edge, the compressive stress is high but

due to the low temperature, the chip material at this point is highly strain hardened and does not experience sufficient thermal softening, hence little or no junction growth occurs in this region. Any oxides present on the tool in this region may stay and maintain sliding conditions throughout the cutting process.

Even though the tool surface is cleaned by the flowing chip material, the tool itself and the workpiece material may not be 100% metallic. The workpiece may contain inclusions which serve to contaminate or lubricate the interface. Thus it would be expected that workpiece materials with soft second phase particles or inclusions like cast iron and inclusion engineered steels would be less seized to the tool than pure metals. Ramanujachar and Subramanian [176] found a drastic reduction in the cutting forces, temperature and tool dissolution wear in inclusion engineered steels. The glassy phase inclusions could change the tribological phenomenon of seizure at the tool-chip interface thereby suppressing dissolution wear. In the present work it is suggested that the inclusions could reduce junction growth at the tool-chip interface by lubricating or contaminating the interface thereby reducing the actual area of contact which in turn suppresses the occurrence of seizure. Aside from the contaminated interface in metal cutting, a lubricated interface may be expected under conditions where an externally applied lubricant is used. However, at high cutting speeds where the compressive stresses are high, the access of the lubricant to the tool-chip interface is prevented by the atomic contact at the tool-chip interface. Thus the tribological phenomenon of sliding progressively gives way to the tribological phenomenon of seizure. During the transition, it is expected that both sliding and seizure operate in the region of sticking friction at the contact zone. Thus a physical model for defining the conditions under which seizure controls the tribological condition at the tool-chip interface is proposed in the next section.

5.2.1 Definition of Seizure in Metal Cutting

This section is aimed at developing an experimentally based physical model for seizure in metal cutting. Wright, Horne and Tabor [50] defined seizure between two surfaces in relative motion as a solid phase weld between the primary atomic bonds of the absolutely clean metallic surfaces. According to these authors the layer of atoms bonded at the interface is stationary and relative motion takes place in adjacent layers with the shear velocity increasing until the full speed is obtained.

Depending on the level of strain hardening and thermal softening achieved concurrently, the chip material adjacent to the tool-chip interface may be harder than the material in the chip body leading to formation of a built-up edge. In this case, shear occurs at the interface between chip material and the built-up material. The formation of a built-up edge lowers the cutting forces and contact length due to an apparent increase in rake angle. At moderate and high cutting speeds (>100 m/min for steel) where the compressive stress at the tool-chip interface is equal to or higher than the yield strength of the chip material at the interface, the asperities are deformed to increase the real area of contact and junction growth increases until the real area of contact approaches the apparent area of contact. Relative movement between the tool and the chip can occur only by shearing. This condition is referred to as seizure between the tool and the chip. If the total area of the chip material in apparent contact with the tool is plastic (atomic contact is established at the tool-chip interface by seizure), then it should be possible to correlate the compressive stress, calculated from the measured cutting forces as a function of cutting speed and temperature rise, with the strength-temperature relationship of the workpiece material. The onset of seizure should coincide with the point where the material first becomes fully plastic i.e. when the compressive stress equals or exceeds the yield strength of the material (asperities). In Fig. 4.5 the onset of seizure is predicted to lie between 100 and 150 m/min. Based on this experimental observation it is proposed that seizure in metal cutting occurs when the compressive stress at the tool-chip interface exceeds the yield strength of the chip material i.e., when the compressive pressure is sufficient to cause junction growth and plastic flow of the

asperities to the extent that the true area of contact, which occurs at the atomic level, approaches the apparent area of contact. Under these conditions a substantial portion of the plastic work (85-95%) is converted to heat in the local volume, which raises the local temperature in the flow zone. Thermally activated processes set in, which causes atomic transfer by diffusion at the interface forming a concentration profile which is measurable by SIMS analysis. It should be possible to correlate the onset of seizure predicted by the compressive stress with the onset of seizure predicted by the measured diffusion profile for tungsten and cobalt into the chips. From the diffusion profiles for tungsten and cobalt shown in Fig. 4.6 the onset of diffusion wear occurs at a cutting speed between 100 and 150 m/min which is in accordance with the physical model based on atomic contact. Thus the concept of seizure which is based on atomic contact at the tool-chip interface, when the compressive stress at the tool-chip interface exceeds the yield stress of the workpiece and the true area of contact approaches the apparent area of contact, is confirmed by experimental results in AISI 1045 steel in Figs 4.5 and 4.6. The model provides only the physical basis for seizure, though not for the nature of the chemical bonding at the interface, which is also important particularly when chemical reactions are involved at the interface.

5.2.2 Material Behaviour in the Secondary Shear Zone Following Seizure

The calculated and measured temperatures in both ductile iron and steel, given in Table 4.4, show that in high speed cutting, the maximum temperatures in the secondary shear zone approach typical hot-working temperatures (500 - 1000^{0}C) for the material being cut. The increased ductility at elevated temperatures and the high hydrostatic pressures (~ 700 MPa) at the secondary shear zone permit large strains to be achieved without fracture. The strain rate increases from 10^4 to 10^5 /s in the speed range of 100 to 350 m/min during machining of AISI 1045 steel. At shear strains of this order, it has been [47,48] suggested that the rate of dislocation movement is influenced by electron and

phonon damping effects generated in the deforming lattice. This dislocation dynamics lead to shear instability and localisation and formation of adiabatic shear bands in the secondary shear zone. If the adiabatic heat raises the temperature beyond the phase transformation temperature transformed shear bands are formed. It will be shown that in the process diffusion is enhanced. It is appropriate to view the tool-chip interface as a network of micro-regions each of which exhibits dynamic variations as proposed by Wright, Horne and Tabor [50]. At any instant some of these regions experience full seizure whereas others experience interfacial sliding. The proportion of seized areas A_s to real area of contact A_r is given by $A_s = kA_r$ where the constant k is controlled by both metal cutting and material parameters. In metal cutting the atomic layer of the chip material at the tool-chip interface is stationary at least for some time in one particular micro-region in which seizure operates while relative movement occurs within adjacent layers. When the intermittent separation of the micro-region occurs, it can either occur in the chip material if the binding forces in the tool and at the junction between the tool and chip are higher than those in the chip material, or at the interface if the junctions formed are weaker than the binding in the chip and tool material or in the tool material (especially at the coating/substrate interface) if the binding in the tool is weaker than both the strength of the junction formed between the chip and tool and the binding in the chip material. It has been demonstrated by Buckley [14] that the binding is stronger when similar metal surfaces come into contact. This raises the possibility for the junctions to break at the tool-chip interface or coating-substrate interface. The concept of dividing the interface into numerous micro-regions in which dynamic variations occur helps to explain why finite strains occur at the tool-chip interface and why seizure and rapid diffusion wear are suppressed by coating of the tool or by inclusion engineering of the work piece. Seizure operates in one micro-region for a time and then breaks down while elsewhere it is being established. Second phases such as free-machining additions intermittently arrive at the interface and temporarily destroy the metallic solid phase weld. The foregoing analysis underscores the importance of the

concept of in-situ lubrication rather than external lubricants in controlling the tribological phenomenon at the tool-chip interface at high cutting speeds.

5.3 Prediction of Temperature Profile along the Tool-Chip Interface

An attempt to measure the temperature at the tool-chip interface using an ultrasonic technique yielded only average temperatures at the tool-chip interface. An analytical heat transfer model has been developed to predict tool-chip interface temperature distribution in the secondary shear zone. The model is based on finite element analysis to solve Fourier's heat transfer equation for the tool-chip interface assuming seizure conditions. The first part of the analysis of the problem involves the partition of the energy generated by plastic deformation in the primary shear zone between the chip and the workpiece and determination of the average or distribution of the shear plane temperature. The second part involves the partition of the tool-face plastic deformation energy between the chip and tool and determination of the average or distribution of temperature along the tool-chip interface.

A number of assumptions are made in the analytical prediction of temperatures in metal cutting. Loewan and Shaw [75] made the following assumptions in their analytical evaluation of temperatures:

(a) That 99% of the strain energy goes into thermal energy and 1% is associated with permanent lattice deformation.

(b) An uniform distribution of shear and friction energy exists at the primary and secondary shear zones respectively.

(c) There is no redistribution of the thermal energy going into the chip during the short contact time the chip is in contact with the tool (i.e. adiabatic deformation).

In the present analysis the above assumptions except for (b) were adopted together with the following:

(a) A non-uniform energy distribution was assumed.

(b) The temperature dependence of the properties of the tool and the workpiece was taken into account by introducing an iteration procedure in the finite element analysis.

The primary shear zone temperature was calculated using Lowen and Shaw's model. The primary shear plane temperature is used as the boundary condition for the two nodes of the first element close to the tool-tip in the finite element analysis. The experimental input to the program comprises of: (1) contact length, (2) cutting force, (3) feed force, (4) chip thickness, (5) shear plane angle, (6) depth of cut and (7) cutting speed. The material parameters input to the program are: (1) density, (2) specific heat, (3) thermal conductivity and (4) flow stress of the material at the secondary shear zone. The first calculation is accomplished using a constant stress along the contact length which fixes the energy generated by shear at every point. Since the elements are continuously strained as they traverse the contact length, the heat energy increases with strain. However the heat energy also decreases due to the drop in flow stress brought about by thermal softening. A variable heat source strength (obtained by the use of the most current flow stress distribution) and variable material properties were assumed at the tool-chip interface for calculation of the temperature distribution. The interface temperature distribution obtained in the first calculation is used to evaluate the variable material properties at the points along the contact length where the temperature is evaluated. The second temperature distribution is again numerically evaluated by the finite element method. The iteration is continued until a self-consistent solution of stress and temperature distribution is obtained. Material parameters evaluated are the flow stress, thermal conductivity, and the specific heat. The details of the finite element development are outlined in appendix C. This approach yields temperature profile which starts from the primary shear zone temperature (chip body temperature) at the tool-tip increasing non-linearly to a maximum temperature at the end of the seized contact length, Fig. 4.16(b), 4.17(b) and 4.18(b). The average tool-chip interface temperature calculated from the model compares

closely with the experimental values obtained for AISI 1020 steel and ductile iron, Table 4.4.

The temperature distribution along the tool-chip interface shows that the maximum temperature is obtained at the end of the seized contact length. The maximum temperature increases with the cutting speed, because of the increased strain rate. Further, the seized contact length decreases with increasing cutting speed and therefore the maximum temperature draws closer to the cutting edge at higher cutting speed. The maximum temperature predicted by the model for each case of ductile iron, AISI 1020 steel and AISI 1080 steel is in excess of the phase transformation temperature for the matrix, as shown in Figs. 4.16(b), 4.17(b) , 4.18(b) and Table 4.10. The maximum temperature does not coincide with the position where the maximum depth of the crater occurs. Instead the position of the maximum depth of the crater corresponds to the phase transformation temperature of the materials. The analytical predictions of the temperature distribution fall within the range of the experimental values reported by Dearnley [150] for ductile iron. However, the limitations of the model developed in the present work for temperature calculation is that the material properties (flow stress, thermal conductivity, specific heat) at the tool-chip interface are not well established.

5.3.1 Effect of Coating on Temperature Rise at Tool-Chip Interface

It is shown in Table 4.3 that coating with TiN/TiC reduces the maximum temperature by about 70 ^{0}C. The thermal conductivity of TiN/TiC coating is ~20 W/m K which is lower than that of uncoated cemented carbide tool (92 W/m K). Thus the tool-chip interface temperature would be expected to be higher when machining with TiN/TiC coated tool than the uncoated tool. The results from the calculations shown that the coating lowers the tool-chip interface temperature because of reduction in contact length and cutting forces, see Table 4.2. This could be caused by the change in the tribological condition at the tool-chip interface effected by coating.

5.4 Micromechanisms of Tool Wear

Under conditions where seizure occurs at the tool-chip interface it has been demonstrated in section 5.2 that contact between the tool and the chip is intimate in the atomic level and the temperatures are high. This condition is favourable for transfer of tungsten and cobalt from the tool into the chip by a diffusion mechanism. Quantitative measurement of dissolution wear by inductively coupled plasma mass spectrometry has found dissolution wear to be the dominant wear mechanism in both steel and ductile iron. The effect of cutting speed is to increase the total wear as well as the percentage of dissolution wear whereas the mechanical wear remains constant. This increase of the percentage of dissolution wear correlates with increase in the tool-chip interface temperature as the cutting speed is increased. Based on the strong influence of temperature on dissolution wear rates and a positive correlation between the crater wear rate and the solubility of the tool material in the workpiece a diffusional hypothesis for crater wear of cutting tools was proposed by Trent [48]. Consequently the observed increase in the percentage of dissolution wear with cutting speed is attributed to the increase in the equilibrium solubility and the diffusion coefficient (i.e the term $c_o\sqrt{D}$) with increase of temperature.

5.4.1 Quantitative Modelling of Diffusion Wear

A diffusion model for crater wear has been developed by Bhattacharyya [152]. The model is based on diffusion and the solution of Fick's second law of diffusion for the boundary conditions at the tool-chip interface taking into account the non-static nature of the contact between the tool and the chip. The assumptions made in this model are:

1) Seizure occurs at the tool-chip interface i.e contact is intimate and the true area of contact equals the apparent area of contact.

2) Local equilibrium is reached at the tool-chip interface and determines the concentration of tungsten

at the interface.

3) Diffusion is one dimensional and takes place in the direction normal to the tool-chip contact area.

4) The variation of the tool-chip contact length, chip velocity and interface temperature with cutting time is negligible.

The effect of austenitisation in the secondary shear zone on the equilibrium concentration has been considered to be the major influence of plastic deformation [3]. Ingle [3] obtained about two orders of magnitude difference between the predicted and experimental dissolution wear during the machining of AISI 1045 steel with cemented carbide tool (K11) after considering the contributions from grain boundary diffusion and diffusion induced grain boundary migration. In the present work it is confirmed that the difference in the predicted and experimentally measured dissolution wear is such that the diffusion coefficient has to be increased by more than two orders of magnitude to get reconciliation. From the tool-chip interface temperature distribution predicted by Ramanujachar and Subramanian [176] and in the present work, it is obvious that the maximum depth of the crater measured does not coincide with the maximum temperature predicted. The present work has considered the possible role of dislocations generated by plastic deformation during phase transformation of the matrix to austenite in providing enhanced diffusion.

Using the temperature profile obtained in section 5.3 and the solution of Fick's second law of diffusion for the boundary conditions at the tool-chip interface diffusion wear was computed numerically. The method employs evaluation of the instantaneous values of the interfacial concentration (C_o), the diffusion coefficient (D), the diffusion flux and rate of material transport by diffusion. This is followed with summation over the entire contact length to obtain the amount of tool material transported when the chip traverses the iength of contact. The total wear is obtained by multiplying the latter amount with the cutting time. Therefore the wear is evaluated as:

$$W = \sum 2/\sqrt{\pi} \quad c_i A_i \sqrt{D_i / \tau_i} \tag{5.1}$$

where C_i, A_i, D_i, and τ are the interfacial concentration, area, diffusion coefficient and time for diffusion in the i^{th} element at the tool-chip interface.

Tables 5.2 and 5.3 show the comparison of the predicted dissolution wear rates and experimental values for ductile iron and steel when using K1 tool. The predicted dissolution wear is less than the experimentally measured value. The lattice diffusion coefficient should be increased by more than 3 orders of magnitude in order for the estimated dissolution wear to be equal to the measured amounts, see Table 5.4. The enhancement of the lattice diffusion coefficient is attributed to the deformation shear bands in the chip material adjacent to the tool-chip interface. Before discussing this in detail, it is pertinent to establish the mechanism of diffusional transport in dissolution tool wear.

Table 5.2: Experimentally measured and predicted dissolution wear during machining of ductile iron with K1 tool.

Cutting speed (mm/min)	Measured dissolution wear rate (ug/sec.)	Calculated dissolution wear rate (ug/sec.)
100	6.7	0.10
200	24.5	0.56
300	107.2	1.85

Table 5.3: Experimentally measured and predicted dissolution wear during machining low carbon steel with K1 tool.

Cutting speed (mm/min)	Measured dissolution wear rate (ug/sec.)	Calculated dissolution wear rate (ug/sec.)
100	15.8	0.12
200	56.4	0.83
300	171.8	1.62

Table 5.4: Average lattice diffusion coefficient enhancement factors required to match theoretical prediction with results from ICP-MS during the machining of ductile iron with K1 tool.

Cutting speed (m/min)	Enhancement factor for ductile iron	Enhancement factor for low carbon steel
100	4489	5155
200	1918	4624
300	3341	11236

5.4.2 Mechanism of Diffusional Transport in Dissolution Tool Wear

The definition of seizure given in the preceding sections has emphasized contact between the workpiece material and tool material at the atomic level forming a solid weld at the interface. At high cutting speeds, thermoplastic shear of the workpiece material as it flows over the tool leads to high temperatures at the interface. The atomic model for seizure and flow at the tool-chip interface proposed in this work suggests that the first atomic layers of each micro-region in the chip material are stationary at least for some time before the junction formed gets destroyed by arrival of a second phase particle or inclusion. Even though the time when the atomic layers are stationary is not known, the conditions are favourable for thermally activated processes to take place and for interdiffusion to occur. Local equilibrium concentration of interdiffusing solutes at the tool-chip interface is assumed. The gradient of solute concentration in the chip provides the driving force for diffusion

Assume that the amount of dissolution wear is the result of a two-stage process. The first stage involves diffusional transport of tungsten and cobalt from the tool into the chip during the time of contact between the tool and the chip. This time is typically in the order of milliseconds. For a contact length of 1.25 mm at a cutting speed of 200 m/min, the contact time is 0.75 millisecond. The second stage involves the redistribution of the original diffusional profile during the cooling of the chip.

From the solubility product of WC in austenite (~4.3) [142] the equilibrium concentration of W at the tool-chip interface is ~10 % for AISI 1045 steel. Transfer of W atoms at the tool-chip

interface could occur at the time of contact by diffusion in the dislocations generated by plastic deformation and phase transformation. The redistribution of the original diffusional profile into the bulk of the chip is assumed to occur by volume diffusion.

In this case the concentration variation can be approximated by the steady-state solution of Fick's second law

$$\nabla^2 C = 0 \qquad (5.2)$$

The lattice diffusion coefficient of tungsten in AISI 1045 steel has been assumed to be approximately equal to that of a 0.56%C steel given in reference [177] as,

$$D_l = D_o \exp(-\frac{Q}{RT}) \qquad (5.3)$$

where D_o = 38 cm^2/s and Q = 77.5 kcal/mol.

At a cutting speed of 200 m/min the average tool-chip interface temperature is about 850 ^{0}C which is above the phase transformation temperature for AISI 1045 steel. At this temperature the lattice diffusion coefficient of W from equation (5.3) will be 2.8×10^{-14} cm^2/s. The dislocation pipe diffusion coefficient D_p is 5×10^6 times the lattice diffusion coefficient at a temperature of 850 ^{0}C which is ~$0.6T_m$ [154]. Therefore $D_p = 1.4 \times 10^{-7}$ cm^2/s. Thus during the time the chip is in contact with the tool (0.75 milliseconds) diffusion would take place into a thickness of 102 nm. The concentration profile set up in this thickness is obtained from the solution of Fick's second law given as [154],

$$C_{x,t} = C_o(1 - erf(\frac{x}{2\sqrt{D_l t}}) \qquad (5.4)$$

where C_o is the surface concentration of tungsten, D_l is the diffusion coefficient and t is the time of

contact. The results obtained from calculations based on an establishment of local equilibrium at the tool-chip interface have been compared with the experimental results obtained from SIMS analysis. Fig. 5.1 shows the two profiles i.e., the calculated profile during the first stage of diffusion which occurs by dislocation pipe diffusion and the measured profile showing the redistributed profile which occurs by volume diffusion. The areas under the two curves should be equal by mass conservation and indeed they were found to be equal. Thus it is proposed that the mechanism of transport of tungsten across the tool-chip interface is by dislocation pipe diffusion.

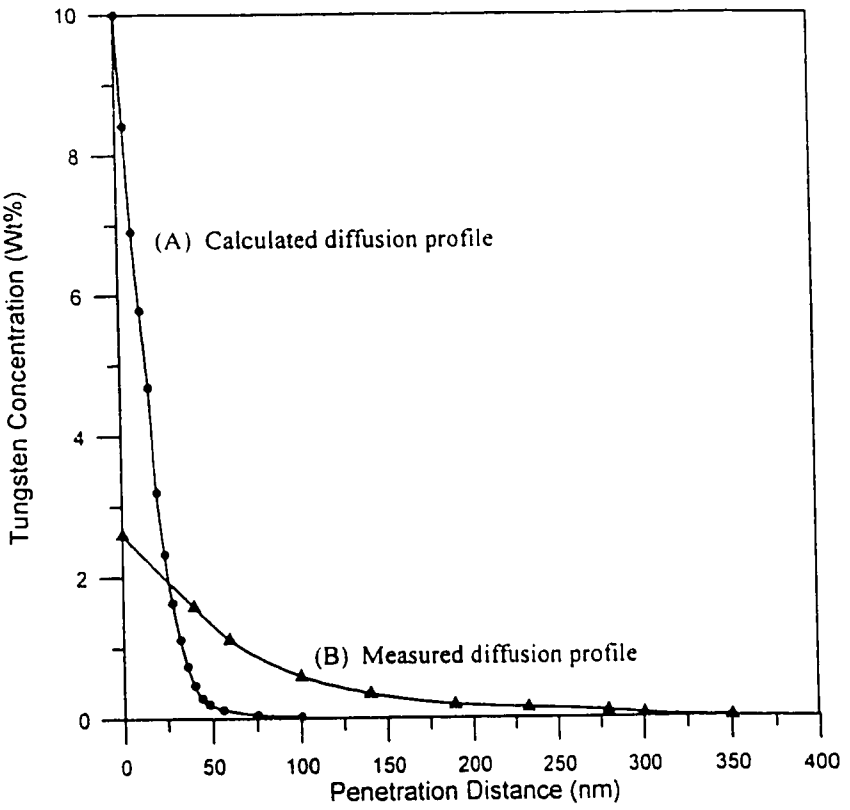

Fig. 5.1: (A) Calculated diffusion profile and (B) measured diffusion profile for tungsten in the chips after machining AISI 1045 steel at a cutting speed of 240 m/min using a cemented carbide tool.

5.4.3 The Effect of Phase Transformation on Crater Wear

It has been demonstrated in the preceding section that transfer of tool material into the chip occurs atomically by dislocation pipe diffusion. The dislocation pipe diffusion coefficient of tungsten is 1.4×10^{-7} cm^2/s which is more than six orders of magnitude higher than its lattice diffusion coefficient (2.8×10^{-14} cm^2/s) at the temperature of 850 ^{0}C. An important observation is that the maximum depth of crater does not coincide with the maximum predicted temperature but coincides with the phase transformation temperature. The role of phase transformation on crater wear is discussed.

An examination of the position of the maximum crater depth with respect to the tool-chip interface temperature shows that the maximum crater depth occurs close to 835^{0}C in ductile iron (Figs. 4.16(a) and 4.16(b)) at cutting speeds of 200 m/min and 300 m/min. In AISI 1020 steel the maximum crater depth occurs at approximately 840^{0}C at cutting speeds of 200 m/min and 300 m/min (Figs. 4.17(a) and 4.17(b)).The ferritic ductile iron and the AISI 1020 steel have an α-γ transformation temperature (A_{C3}) of about 840^{0}C. In AISI 1080 steel the maximum crater depth occurs at approximately 728^{0}C at cutting speeds of 100, 200 and 300 m/min (Figs. 4.18(a) and 4.18(b)). This steel has an α-γ transformation temperature (A_{C3}) of about 727^{0}C. It follows that maximum enhancement of the diffusion coefficient occurs at the point where the maximum depth of crater coincides with the phase transformation temperature. It is well known that dislocations provide high diffusivity paths. This enhancement of the diffusion coefficient is therefore attributed to the generation of dislocations as a result of the occurrence of phase transformation concurrent with plastic deformation. The manifestation of the interaction between phase transformation and plastic deformation, referred to as transformation plasticity has been reported to result in creation of the highest number of dislocations and a drop in flow stress as the material deforms to very large strains [130]. According to the authors when an iron undergoes the α-γ transformation it seems that it

acquires a transient plasticity associated with phase transformation, which greatly exceeds that of either ferrite or austenite. The transient plasticity is assumed to be exhibited by a transient crystal structure which is a source of dislocation generation. Dislocation pipe diffusion could enhance the diffusion coefficient by approximately seven orders of magnitude [153,154].

5.4.4 The Effect of Cutting Speed on the Location of Maximum Depth of Crater in AISI 1020 Steel and AISI 1080 Steel

It has been demonstrated in the previous sections that dissolution crater wear increases with increase in cutting speed under conditions of flow or continuous chip morphology in AISI 1020 steel. In this section the chip morphology is kept constant e.g., a continuous or flow chip morphology is maintained with all other cutting variables kept constant then the effect of cutting speed on the location of crater wear is investigated in AISI 1020 steel and AISI 1080 steel.

With increase in cutting speed the contact length decreases and the peak temperature increases. The net effect is that the phase transformation temperature is reached closer to the cutting edge of the tool. Thus, the maximum depth of crater as well as the crater move closer to the cutting edge of the tool even though the chip exhibits flow (continuous) chip morphology, Figs. 4.17 and 4.18.

5.4.5 The Effect of Chip Segmentation on the Location of Maximum Depth of Crater in ductile Iron

Ductile iron has essentially the same matrix as AISI 1020 steel with a dispersion of ~10% volume fraction of graphite in the matrix. Consequently it has a lower critical accumulated damage before fracture than AISI 1020 steel. For this reason ductile iron exhibits chip segmentation caused by geometrical shear instability at moderate cutting speeds whereas AISI 1020 steel does not. Ductile

iron also has a lower thermal diffusivity than AISI 1020 steel which makes it concentrate the heat from plastic deformation at the cutting edge of the tool. Temperature distributions measured [150] and predicted in the present work (Figs.4.16 and 4.17) show that the maximum temperature in ductile iron is closer to the cutting edge than in steel.

A comparison of SEM images of craters obtained in steel and ductile iron after 20 seconds of machining with K-1 tool at 300 m/min clearly shows that the crater is located closer to the cutting edge in the case of ductile iron, see Figs. 4.14 and 4.15. Analysis of the evolution of crater has shown that the crater is located closer to the cutting edge from the onset of cutting (early stages of crater development) in ductile iron. With increase in cutting speed the maximum depth of crater moves closer to the cutting edge. The cutting edge is severely damaged by dissolution wear at the end of 20 seconds at a cutting speed of 300 m/min, clearly suggesting that the temperature is maximised at the cutting edge during the machining of ductile iron at high cutting speeds corresponding to chip segmentation, see the crater depth profiles for ductile iron in Fig. 4.16(a). Thus in ductile iron shear localisation caused by geometrical softening causes chip segmentation at high cutting speeds which locates the crater close to the cutting edge of the tool. Damage of the cutting edge occurs at high cutting speeds corresponding to fully segmented chip morphology due to the interaction of the primary shear zone with the cutting edge of the tool. Even though the crater is larger and deeper in AISI 1020 steel compared to that in ductile iron the crater in steel is located far from the cutting edge of the tool, see the crater depth profiles for steel in Fig. 4.17(a). The cutting edge of the tool is retained for a longer cutting time at high cutting speeds thus maintaining good surface finish for long cutting times. Hence it is where the wear occurs that is important rather than the amount.

A more aggressive condition of crater wear is due to the interaction of primary shear with the cutting edge of the tool when shear localisation in the primary shear zone is caused by thermal softening rather than geometrical softening in the case of Fe-Ni-C alloys discussed in section 5.7.

5.5 Effect of Coating on Contact Mechanics and Micromechanisms of Tool Wear

5.5.1 Effect of Coating on Contact Mechanics

As a result of coating with TiN/TiC the contact length was decreased by more than 50% in the machining of AISI 1020 steel whereas it changed marginally in ductile iron, Table 4.2. When a cemented carbide tool is coated, the tool-chip interfacial bond may be stronger than the binder-carbide bond leading to plucking off of discrete tool particles from underneath the coating. If the matrix of the chip is weaker than the tool-chip interfacial bond strength fracture may occur in a plane above the tool-chip interface. This, in turn, determines where the chip leaves the tool rake face, effectively controlling the tool-chip contact length. The small differences in contact length between uncoated and coated tools during the machining of ductile iron suggest that the interface breaks in the chip body. The graphite nodules in ductile iron are responsible for the lower critical accumulated damage to fracture compared with steel. Graphite aids in geometrical shear localisation which leads to chip segmentation. When chip segmentation occurs the contact length is lowered. The exposure of the tool-chip interface to graphite which is non-metallic serves to contaminate the interface. This has the effect of weakening the interfacial bonding and thus lowering the contact length. However, when cutting a steel with large critical accumulated damage to fracture, shear strains up to 100 can be sustained without fracture for the uncoated carbide tools, resulting in a large contact length. Under these conditions, coating is observed to be very effective in decreasing the contact length. This is attributed to lowering of the interfacial tool-chip bond strength by coating. Coating with TiN/TiC was found to decrease the cutting forces during the machining of both ductile iron and steel, Table 4.2. This supports the argument that reduced junction growth due to coating leads to the formation of a weaker interfacial bond strength. Similarly a reduced chemical interaction between the coating and the chip material would cause a reduction in the interfacial bond strength.

5.5.2 Effect of Coating on Tool Dissolution Wear

Wear of the K1 tool was observed to be more in AISI 1020 steel than in ductile iron at the same cutting conditions. When the tool is coated with TiN/TiC, the observed decrease in wear in steel (64%) was more than the decrease in ductile iron (24%). The result is that ductile iron exhibited more dissolution wear for TiN/TiC coating than steel. The reason for this observation can be attributed to two factors. First the contact length in ductile iron is least changed by coating with TiN/TiC while that of steel is reduced by more than 50%. Secondly, even though the overall effect of coating is to decrease the solubility product, the solubility product of TiC in iron is carbon dependent as reported by Ohtani et al [178] and is higher in higher carbon irons. This arises because of the strong chemical interaction between carbon and titanium, increasing the equilibrium solubility of Ti in austenite with carbon content. Since the calculated results on the isothermal section of Fe-Ti-C system (Fig. 5.2) show an increase in the solubility of titanium with increasing carbon content, dissolution wear of the TiN/TiC coating would be expected to be more in ductile iron than in steel. However, the coating was observed to suffer from delamination wear as evidenced in the SEM image in Fig. 5.3, in which the grains of the coating are plastically deformed and uprooted from the surface of the tool. This made it difficult to confirm the effect of increased solubility of Ti in high carbon systems in increasing dissolution wear of Ti based tools. For this reason hafnium nitride was chosen to study the influence of coating on dissolution wear as the solubility of HfN in the iron matrix is seven orders of magnitude (10 million times) less than that of tungsten carbide (Table 5.5) and the coating did not suffer from delamination wear. Hafnium nitride was found to be very effective in suppressing diffusion wear in ductile iron, see Fig. 4.13. In the diffusional wear analysis, the local equilibrium concentration of the solute and the diffusion coefficient (i.e. the product $C_o\sqrt{D}$) are the key parameters that determine diffusional wear. Thus any method that reduces C_o or D at the interface will minimise dissolution wear.

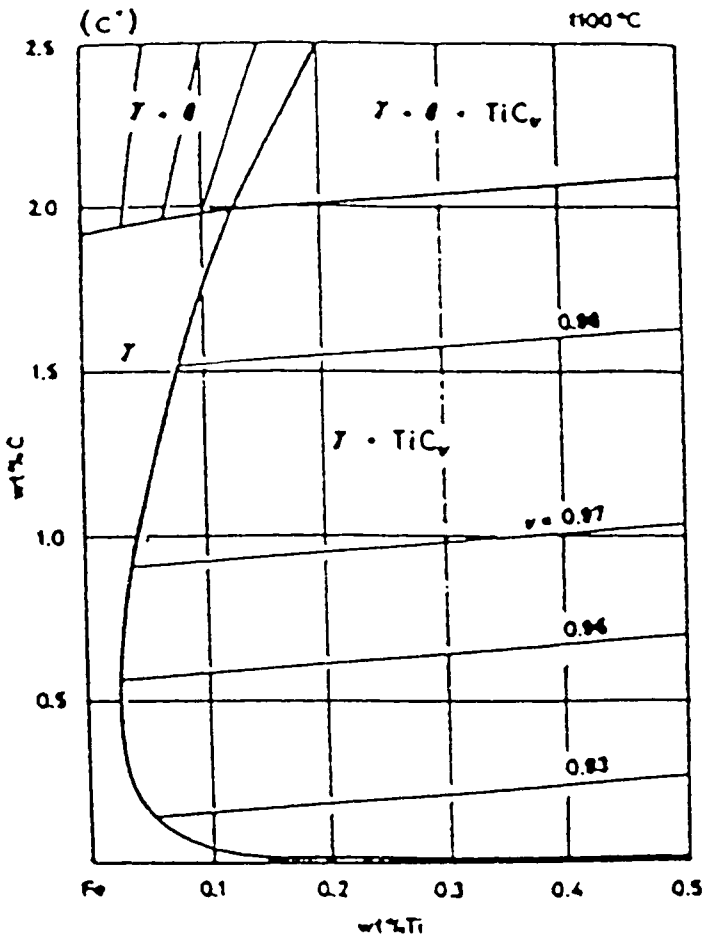

Fig.5.2: Calculated results on isothermal sections of Fe-Ti-C system. (After Ohtani et al [178])

One method is by coating the tool with a material that has the least solubility in the workpiece material to minimise C_o. Since C_o and D depend on temperature coating reduces these parameters by reduction in the tool-chip interface temperature. Reduction in the tool-chip interface temperature is brought about by the reduction in true area of contact and hence the reduction of seizure which results from the change in chemistry at the tool-chip interface due to coating. Since the temperature reduction as a result of coating is only about 70°C, the decrease in the local equilibrium concentration C_o resulting from coating has a dominating effect over the temperature effect on the $C_o\sqrt{D}$ term in reducing the overall diffusional wear. Thus crater wear can be suppressed by choosing a tool or a coating with the

least thermodynamic potential for dissolution in the workpiece. Even through hafnium nitride did not decrease the contact length in machining ductile iron by comparison with steel, the crater was located farther away from the tool tip (Fig. 4.19) with reduction in dissolution wear (Fig. 4.13).

Another method of reducing dissolution wear is by preventing seizure from occurring at the tool-chip interface. In the present definition of seizure in metal cutting, it has been emphasized that contact must occur at the atomic level and that any contamination in any micro-region will prevent local seizure from occurring. At high cutting speeds external lubrication is not effective in changing the tribological condition at the tool-chip interface. In-situ lubrication is recommended in this case. Thus introduction of glassy deformable inclusions which form a viscous layer of adequate thickness such that shearing takes place within the viscous layer rather than at the solid/solid interface will prevent seizure (atomic welding) and suppress diffusion wear [179].

Table 5.5: The solubility products of tool materials in ductile iron and low carbon steel at 1265 K expressed as $(Wt\%)^2$ [3,142].

Tool material	Solubility product in ferritic ductile iron	Solubility product in AISI 1020 steel
[W].[C]	1.27	1.27
[Ti].[C]	3.7×10^{-1}	2.5×10^{-3}
[Ti].[N]*	5.8×10^{-7}	5.8×10^{-7}
[Hf].[N]*	3.15×10^{-7}	3.15×10^{-7}

* Values in austenite at 1400 K

(a)

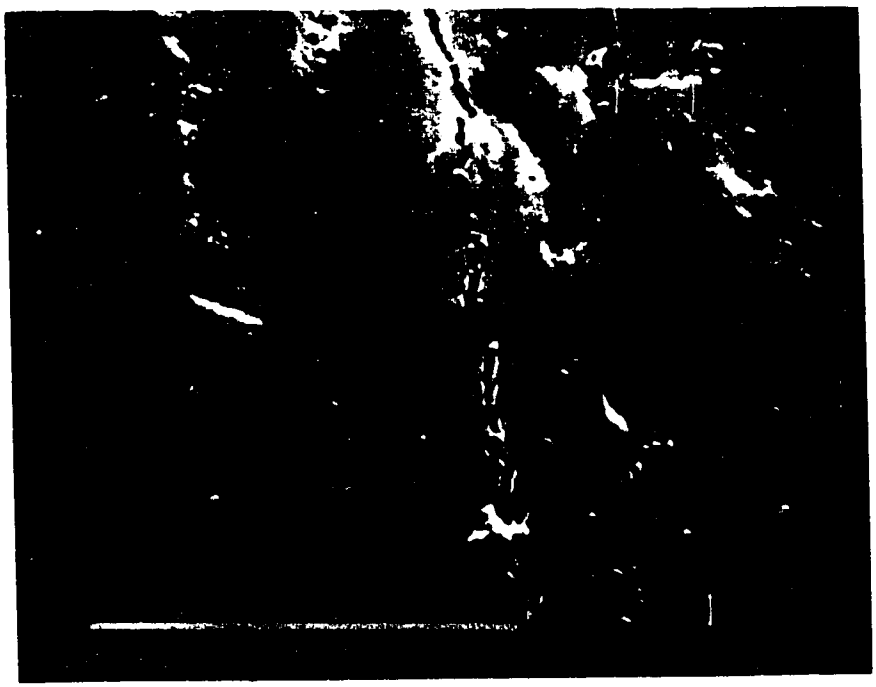

(b)

Fig. 5.3: SEM pictures showing the morphology of the rake face of a TiN/TiC coating (a) before and (b) after machining ferritic ductile iron at a cutting speed of 300 m/min.

5.6 The effect of Metal Cutting Variables on Chip Morphology, Tool Wear and Surface Finish

The metal cutting variables and material characteristics that influence the metal cutting process are reviewed in section 2.2. The important metal cutting variables are the cutting speed, feed, depth of cut, rake angle and cutting medium (i.e. use of a coolant/lubricant, dry machining in air or dry machining in an inert surrounding). A combination of these metal cutting variables imposes geometrical and material constraints on the tool and workpiece materials. The microstructural response resulting from the constraints in turn affect the chip morphology, tool wear and surface finish. The present work investigated the effect of metal cutting variables on the chip morphology, tool wear and surface finish through microstructural changes, influenced by temperature and pressure effects. The effects of the cutting speed, feed, depth of cut, and coolant/lubricant on the chip morphology, tool wear and surface finish are discussed in the right of the experimental results. Even though the rake angle was not investigated, the literature shows that an increase in the rake angle causes a decrease in the shear angle and the strain imparted on the chip. The overall effect of increasing the rake angle is to increase the tendency to form continuous or flow chip morphology.

5.6.1 The Effect of Cutting Speed on Chip Morphology, Tool Wear and Surface finish

The feed, depth of cut and rake angle were kept constant while the cutting speed was varied from 100 to 300 m/min in ductile iron and from 1 to 400 m/min in Fe-Ni-C alloys which were used to investigate the effect of cutting speed on the chip morphology, tool wear and surface finish. With increase in cutting speed the cutting forces and the stresses increase until there is a transition in the tribological phenomenon at the tool-chip interface from sliding to seizure as discussed in section 5.2. see Tables 4.1(a) and 4.1(b) and Figs. 4.1-4.6. The shear plane angle increases with increase in cutting speed, which implies a decrease in the strain required to fracture the chips. The chip morphology in

ferritic ductile iron changes from continuous at a cutting speed of 100 m/min through partially segmented to fully segmented at 350 m/min., Figs 4.10(a)-4.10(d). Details of the microstructure of the ductile iron chips produced at 350 m/min. show that chip segmentation in ferritic ductile iron is caused by shear localisation due to geometrical softening. In hardened Fe-28.9Ni-0.1C alloy, discontinuous chips are first formed at a cutting speed of 1 m/min (Fig.4.23(a)) with increased hardness in chip body from 374 to 675 VHN. With increase in cutting speed the chip morphology changes to continuous between 25 and 50 m/min., (Figs 2.26(a) and 4.27(a)), partially segmented at 75 m/min., (Fig. 4.28(a)) and fully segmented with formation of white etching (transformation) shear bands at cutting speeds of 150 m/min., and above (Figs 4.29(a) - 4.32(a)). Chip segmentation in the Fe-Ni-C alloys is caused by shear localisation due to thermal softening of the matrix.

There are several reasons attributed to the change in chip morphology with increase in cutting speed. The first reason is due to the change in the tribological condition at the tool-chip interface from sliding to seizure which causes partial chip segmentation as will be shown in section 5.7.1. Secondly, increase in cutting speed increases the strain rate, Tables 4.3, 4.12(b)-4.15(b). The effect of high strain rate is to lower the deformation time with respect to the heat dissipation time causing localised heat accumulation and rise in shear zone temperature, Tables 4.12(a)-4.15(a). The consequence of localised temperature rise is to promote shear localisation through thermal softening, which causes chip segmentation in the primary shear zone. Phase transformation promotes shear localisation, see section 5.8.3. Thirdly, in the presence of voids geometrical softening causes shear localisation and chip segmentation due to increased damage rates at high cutting speeds. Finally, if thermal and geometrical softening do not cause chip segmentation at low cutting speeds, strain rate hardening at high cutting speeds leads to thermal softening and chip segmentation.

As discussed in sections 5.2 and 5.4, the effect of cutting speed on tool wear is through the occurrence of seizure and increase in temperature at the tool-chip interface whereby thermally

activated (dissolution) wear increases with increase in cutting speed, Tables 4.3-4.9. At constant feed, depth of cut and rake angle, increasing the cutting speed draws the crater closer to the cutting edge of the tool due to the attendant decrease in contact length, see section 5.4.4 and Figs 4.16(a) - 4.18(a). The recent trend is to increase the cutting speed with advanced tools such as cubic boron nitride but decrease the feed to achieve good surface finish in finish machining. However, the present work shows that the interaction of the primary shear zone with the cutting edge of the tool can cause catastrophic damage to the cutting edge of the tool, leading to loss of surface finish, see Figs. 4.15, 4.32(b), 4.40(b) and 4.46(b).

In summary, increasing the cutting speed has the effect of (1) increasing the stresses in the primary and secondary shear zone leading up to seizure at the tool-chip interface, (2) increasing the tool-chip interface temperature, (3) increasing dissolution wear of the tool, (4) drawing the crater closer to the cutting edge of the tool, (5) causing shear localisation and chip segmentation due to strain rate hardening and (6) improving the surface finish through decreased feed if the cutting edge of the tool is retained.

5.6.2 The Effect of Feed on Chip Morphology, Tool Wear and Surface finish

The effect of feed on chip morphology was investigated using hardened Fe-Ni-C alloys while keeping the cutting speed, depth of cut and rake angle constant. The general observation is that the degree of chip segmentation increases with increase of feed at constant cutting speed and depth of cut, see Figs 4.54(a) to 4.58(a) for Fe-28.9Ni-0.1C alloy, Figs 4.59(a) to 4.63(a) for Fe-18.9Ni-0.1C alloy and Figs 4.64(a) to 4.67(a) for Fe-9.7Ni-0.1C alloy. As the feed is decreased the cutting forces decrease i.e., the mechanical load on the chip is decreased, Tables 4.18 and 4.19. Corresponding to decrease in feed is an increase in the normal compressive pressure at the primary shear zone and an increase in the chip body temperature, Tables 4.18 and 4.19. Similar observations of increase in

compressive pressure in the primary shear zone with decrease in feed have been made by Kopalinsky and Oxley in AISI 1048 steel [53]. A high compressive pressure suppresses the damage or void growth causing an increase in the strain required to fracture the chips which leads to continuous chip morphology. With decrease in feed the shear velocity decreases due to decrease in shear plane angle as reported by Cook, Finnie and Shaw [55] in beta-brass and Lemaire and Backofen [58] in Fe-18.5Ni-0.52C alloy. This could be attributed to lowering of the strain rate and suppressing of shear localisation which leads to continuous chip morphology. In Tables 4.18 and 4.19 the calculated temperature in the primary shear band increases whereas that of the chip body decreases with increase in feed. Thus even though the mechanical and thermal load increase with increase in feed the chip body temperature decreases whereas the shear band temperature increases, Tables 4.18 and 4.19. In Fe-28.9Ni-0.1C alloy, the whole of the chip body is predicted to attain a temperature of 418^{0}C, which is above the martensite to austenite phase transformation temperature of the alloy (duly corrected for the pressure effect 292^{0}C), at a feed of 0.055 mm/rev. The microstructure of the chips suggests that the whole of the chip body has undergone phase changes. Fig. 5.4 shows the x-ray diffraction intensities, taken from the chips obtained during machining of martensitic Fe-28.9Ni-0.1C alloy at a cutting speed of 400 m/min. and feed of 0.055 mm/rev., which confirm that the martensitic structure reverts to austenite in the whole of the chip body at a low feed.

A uniform distribution of the thermal load in the chip is suggested by uniform rise in the temperature of the chip body at low feeds. At high feeds the localisation of thermal load is suggested by the microstructural changes occurring only in the shear bands of the segmented chips. Thus the predicted temperature in the shear bands increases with increase in feed. The localisation of the thermal load causes thermal softening which in turn causes shear localisation leading to chip segmentation at high feeds, see Figs. 4.54 (a) to 4.58(a).

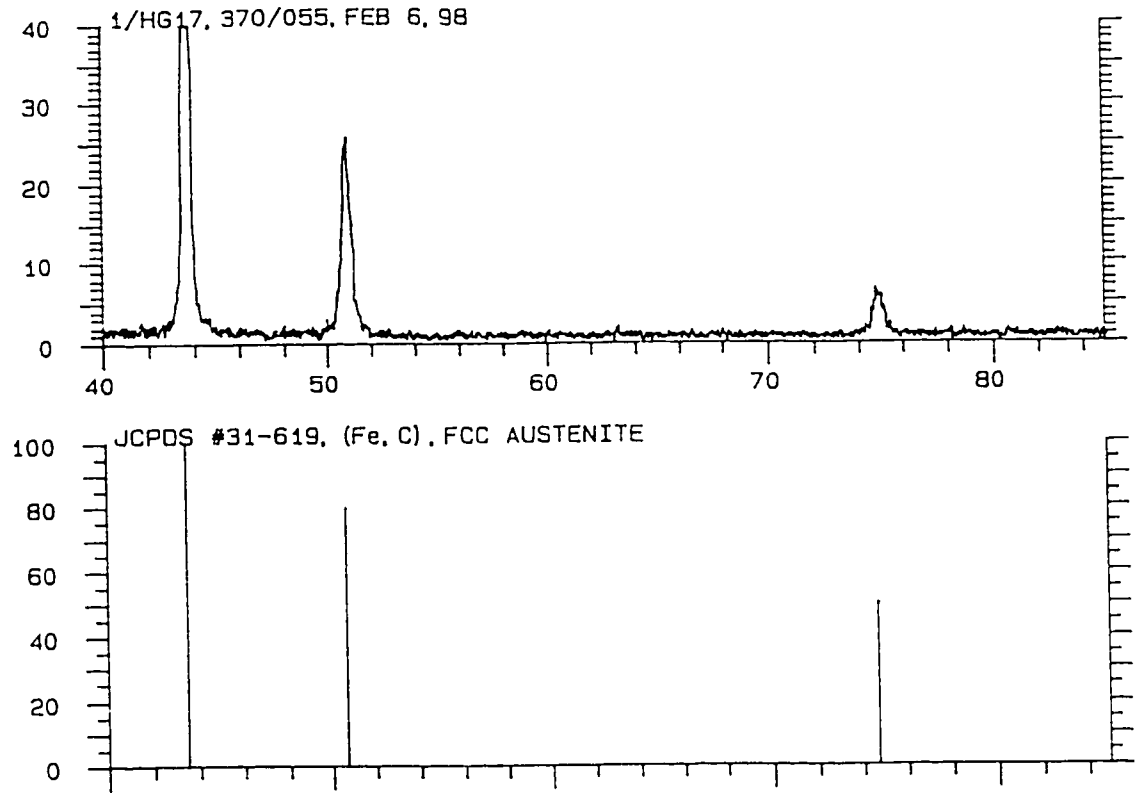

Fig. 5.4: X-ray diffraction intensities taken from the chips obtained during machining of martensitic Fe-28.9Ni-0.1C alloy at a cutting speed of 400 m/min. and feed of 0.055 mm/rev., showing that the martensitic structure reverts to austenite in the whole of the chip body at a feed of 0.055 mm/rev.

In the Fe-18.9Ni-0.1C alloy phase transformation occurs only in the secondary shear zone at feeds of 0.055 and 0.103 mm/rev., Figs 4.59(a) and 4.60(a). The chip is continuous and partially segmented at the feed of 0.055 and 0.103 mm/rev., respectively. The predicted chip body temperature at these feeds is lower than the martensite to austenite phase transformation temperature of the alloy (530 °C). The temperature of the chip body decreases with increase in feed, Table 4.19. When full chip segmentation commences at a feed of 0.206 mm/rev., the predicted temperature in the shear band is 534 °C which is above the martensite to austenite phase transformation temperature of the alloy (530 °C).

In the Fe-9.7Ni-0.1C alloy there is no phase transformation at the primary and secondary shear

zones at a feed of 0.055 mm/rev., Fig.4.64(a). The chip morphology remains continuous at a feed of 0.103 mm/rev and full segmentation commences at a feed of 0.259 mm/rev. in this alloy, see Figs. 4.65(a) and 4.66(a).

The effect of decreasing the feed is to locate the crater wear closer to the cutting edge of the tool (Figs 4.44(b)-4.58(b)). However, the cutting edge is not damaged due to the low cutting forces and the absence of interaction of the primary shear zone with the cutting edge of the tool in continuous chip morphology. Since the surface finish is governed by the feed marks, a low feed gives rise to a good surface finish.

In summary reducing the feed (1) decreases the contact length, (2) suppresses chip segmentation through increase in the compressive pressure which suppresses the damage or void growth and hence increases the strain required to fracture the chips in the primary shear zone, and (3) moves the crater close to the cutting edge of the tool.

5.6.3 The Effect of Depth of Cut Chip Morphology, Tool Wear and Surface finish

The variation of depth of cut did not show any significant effect on chip morphology. There is a significant increase in the feed force and cutting force and hence an increase in the deformation energy with increase in the depth of cut, Table 4.19. However, the strain rate and temperature rise do not show significant variation with depth of cut. Hence the chip morphology remains constantly segmented due to the high strain rates at the high cutting speed (300 m/min) used. The effect of reducing the depth of cut is to locate the crater closer to the cutting edge of the tool and also to reduce crater wear by reducing the contact area.

5.6.4 The Effect of Coolant on Chip Morphology, Tool Wear and Surface finish

The use of helium gas atmosphere instead of air did not show any effect on the contact length

and the intensity of crater wear (Fig. 4.9). The use of an oil based external coolant/lubricant was not effective in influencing the chip morphology in the Fe-Ni-C alloys as the heat is generated adiabatically and the contact at the tool-chip interface is essentially atomic, compare Figs 4.71(a) to 4.74(a) with Figs 4.26(a) to 4.31(a). The comparison of crater wear in the cutting tools used with and without coolant shows a slight reduction in tool crater wear caused by use of a coolant (compare Figs 4.71(b) to 4.74(b) with Figs 4.26(b) to 4.31(b)). The slight decrease in wear is attributed to an external cooling effect by the coolant on the tool. However use of an external coolant/lubricant does not suppress dissolution wear because there is no access of the coolant/lubricant to the tool-chip interface at high cutting speeds. The only feasible way to suppress dissolution wear is by suppressing seizure by in-situ lubrication of the tool-chip interface, through engineering lubricating inclusions into the workpiece or by coating of the tool.

5.7 Mechanism of Chip Segmentation

The deformation process in metal cutting is a heterogeneous one involving high strain rates (10^4 - 10^6 /s), large strains (>1), temperature rise and high compressive pressure in a highly localised flow zone. Heterogeneous deformation is brought about by shear localisation. Shear localisation in the secondary shear zone is caused by the tribological condition of seizure at the tool-chip interface. Chip segmentation in the primary shear zone is caused by shear localisation. At low cutting speeds shear localisation in the primary shear zone is caused by geometrical softening due to second phase particles. The sequence of events in this form of shear localisation which leads to fracture begins with formation of voids after a critical amount of strain followed by shear instability at the maximum shear stress; then at a critical volume fraction of voids or at a critical mean free path between the voids, strain concentrates in narrow shear bands connecting the voids culminating in separation along these bands. The temperature rise is low because the rate of dissipation of the plastic work converted into

heat exceeds the rate of heat generation. Shear localisation at high cutting speeds and in thermally sensitive materials is caused by thermal softening of the matrix. This form of shear localisation known as thermoplastic shear localisation occurs when the effects of thermal softening of the matrix offset the combined effects of strain hardening and strain-rate hardening of the matrix on the flow stress. The temperature rise is high because the rate of heat dissipation is lower than the rate of heat generation. In materials that are hardened and sensitive to microstructural changes either recrystallisation or phase transformation could cause shear localisation by thermal softening and lower the critical speed for chip segmentation. In the absence of geometrical and thermal softening chip segmentation is caused by strain rate hardening at high cutting speeds.

To support these arguments the following sections discuss the experimental results on chip segmentation in two materials in which geometrical and thermal softening dominate in causing shear localisation. Ductile iron was chosen as a material with a dispersion of second phase particles (graphite) in a ferritic matrix. The graphite acts as voids in the matrix influencing shear localisation through geometrical softening. In contrast a series of Fe-Ni-C alloys were designed with different nickel contents to vary the phase transformation temperature. The alloys were machined in their hardened condition. Thus they represent the class of materials that exhibit thermal sensitivity due to hardening and phase transformation which lower the critical speed for chip segmentation. In their unhardened (annealed) condition shear localisation is due to strain rate hardening and the critical speed for chip segmentation is expected to be high.

5.7.1 The Mechanism of Formation of Partially Segmented Chips in Ductile Iron

In ductile iron the chips changed from continuous at 100 m/min to partially segmented chips at 200 m/min, Figs. 4.10(a) and 4.10(b) respectively. At 300 m/min the chips formed by ductile iron exhibited partial separation, Fig. 4.10(c). In comparison the chips obtained from machining AISI 1020

steel using uncoated cemented carbide tool are still continuous at a cutting speed of 300 m/min as shown in Fig. 5.5. The secondary shear zone forms shear bands which is indicative of the occurrence of seizure throughout the speed range investigated in both AISI 1020 steel and ductile iron.

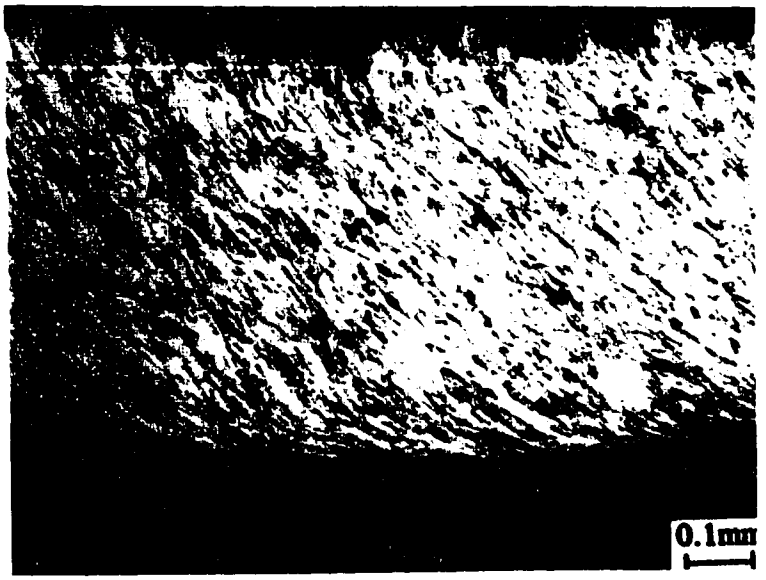

Fig. 5.5: An optical micrograph showing a section parallel to the chip flow direction of a continuous chip machined from AISI 1020 steel with a cemented carbide tool (K1) at a cutting speed of 300 m/min.

Since the atomic transfer of tungsten from the tool to the chips has been confirmed for these materials, seizure in the secondary shear zone is confirmed. Under the conditions of formation of continuous or partially segmented chips which involves seizure, a model for calculation of the temperature distribution based on finite element analysis has been developed in section 5.3.

In the literature different mechanisms have been proposed to describe the formation of partially segmented chips. Based on a detailed but qualitative examination of the longitudinal mid-sections of the chip roots at various stages on a scanning electron microscope, Komanduri and Brown [70] proposed that the primary shear zone is the source of instability. This instability is taken to be due to a mechanism similar to the negative stress-strain characteristics of the material involving void

formation around second phase particles, the propagation into micro-cracks and the coalescence of these cracks leading to partial fracture. Stick-slip friction at the tool-chip interface was proposed as a second source of instability. In contrast, Sullivan and co-workers [71] discount the primary shear zone as a source of large scale instability to cause partial chip segmentation. The model proposed is that the formation of partially segmented chips involves a dynamic variation of the flow stress of the material characterised by an increase due to strain hardening and a decrease over time due to thermal softening as it undergoes gross seizure at the secondary shear zone with an attendant variation of the shear plane angle. In the first part of the contact length the material is severely strain hardened and seizure occurs under the high compressive stress in this region. Owing to the heat generated after seizure a high temperature rise near the end of the zone causes thermal softening. The resulting lowering of the flow stress allows the material to flow over the secondary shear zone as selected shear occurs at the primary shear zone forming another chip segment. The experimental observations in the machining of ductile iron are consistent with the model for chip segmentation as proposed by Sullivan and co-workers [71]. Thus it is concluded that partial chip segmentation occurs as a result of seizure and strain hardening of the material in the secondary shear zone which leads to selected shear at the primary shear zone and a variation in the shear angle. The consequence of seizure under the formation of partially segmented chips is to cause thermoplastic shear in the secondary shear zone leading to high temperature rise at the tool-chip interface and diffusion wear of the tool.

5.7.2 The Mechanism of Formation of Fully Segmented Chips in Ductile Iron

As shown in Figs 4.10(a) through 4.10(d), the chip morphology changes from continuous or flow through partially segmented at 200-300 m/min to fully segmented morphology at 350 m/min. In consequence the crater moves close to the cutting edge and damage of the cutting edge occurs due to the interaction of the primary shear zone with the secondary shear zone causing chemical wear at

the cutting edge. Using the analysis by Recht [73] a critical speed for adiabatic shear localisation in the primary shear zone to occur leading to formation of fully segmented chips in ductile iron of 323 m/min has been predicted which is in conformity with the experimental value of 350 m/min, Fig. 4.10(d). The observations made from SEM analysis of the chips are documented in section 4.2.3. Heterogeneous deformation at the primary shear zone and the secondary shear zones, as shown in Fig.4.11(b) and Fig.4.11(c) respectively, depict the occurrence of shear localisation. The extensive growth of the voids and intensely localised deformation with cracking in the shear bands shown in Figs. 4.11(a) and 4.11 (b) suggest that flow localisation occurs under the combined effects of thermoplastic shear instability and geometrical softening. Intense deformation in the secondary shear zone, observed on the SEM image shown in Fig. 4.11(c), is attributed to the occurrence of seizure at the tool-chip interface during the formation of fully segmented chips in ductile iron. Dissolution wear measurements by ICP-MS and diffusion analysis by SIMS have confirmed the occurrence of seizure as it is defined in section 5.2, see Tables 4.5 to 4.9. These new observations can be summarised as follows:

In ductile iron chip segmentation is caused by shear localisation in the primary shear zone which is caused by geometrical softening due to the presence of a high volume fraction (>10%) of graphite particles in the matrix. Even though the shear localisation occurs in the primary shear zone by geometrical softening, dissolution wear of the tool into the chip as measured by increase in W concentration confirms the occurrence of seizure under conditions of fully segmented chip morphology. As a consequence of chip segmentation in the primary shear zone the interaction of the primary shear zone with the secondary hear zone leads to damage of the cutting edge of the tool due to chemical wear. This last point is examined in greater detail in the discussion of chip segmentation in Fe-Ni-C alloys. The next section is devoted to the development and discussion of a theoretical model which combines the effects of geometrical and thermal softening on shear localisation to

support the foregoing conclusions concerning shear localisation in ductile iron.

5.7.3 Model for Shear Localisation under Combined Thermal and Geometrical Softening

The criterion for thermoplastic shear instability to occur has been studied by a number of researchers, notably Culver [112], Dodd and Bai [106], Clifton et al [118] who assumed shear instability to occur at a maximum shear stress. In all these developments the effects of either geometrical softening or microstructural changes (recrystallisation and phase transformation) are neglected. In the analysis that follows the criterion for thermoplastic shear instability is combined with the criterion for geometrical softening to predict the onset of shear localisation under conditions of thermoplastic shear instability and geometrical softening in terms of a critical strain.

When a material contains voids or has potential for nucleation of voids during plastic deformation, the constitutive relation in equation 2.16 is modified to include the influence of damage accumulation A in the flow stress behaviour as:

$$\tau = f(\gamma,\dot{\gamma},T,\mathrm{A},\textit{deformation history}) \qquad (5.5)$$

For simplicity the deformation history, which refers to effects such as microstructural changes on the flow stress, is neglected. The general criterion for unstable plastic flow is that the next increment of strain-induced hardening at a location is balanced by an equal or greater amount of strain-induced softening. Since the increment of flow stress due to strain hardening is balanced by thermal softening, $d\tau = 0$. Then equation 5.5 becomes:

$$\left(\frac{\partial\tau}{\partial\gamma}\right)_{\dot{\gamma},T,\mathrm{A}} d\gamma + \left(\frac{\partial\tau}{\partial T}\right)_{\dot{\gamma},\gamma,\mathrm{A}} dT + \left(\frac{\partial\tau}{\partial\dot{\gamma}}\right)_{\gamma,T,\mathrm{A}} d\dot{\gamma} + \left(\frac{\partial\gamma}{\partial \mathrm{A}}\right)_{\dot{\gamma},\gamma,T} d\mathrm{A} = 0 \qquad (5.6)$$

where τ, γ,$\dot{\gamma}$,T are the stress, strain, strain rate and temperature of an element undergoing plane strain

deformation. The damage parameter A can be defined independently of other effects on flow stress behaviour as [180]:

$$\frac{d\bar{\sigma}}{d\bar{\epsilon}} = \frac{\partial\bar{\sigma}}{\partial\bar{\epsilon}}(1-A) - \bar{\sigma}(\bar{\epsilon})\frac{\partial A}{\partial\bar{\epsilon}} \qquad (5.7)$$

Assuming that failure corresponds to the vanishing of the global rate of work hardening, the criterion for failure is then:

$$\frac{1}{\bar{\sigma}}\frac{d\bar{\sigma}}{d\bar{\epsilon}} -(1-A) = \frac{\partial A}{\partial\bar{\epsilon}} = 0 \qquad (5.8)$$

As the hydrostatic pressure P is increased, the term $\partial A/\partial\epsilon(1-A)$ is decreased so that the criterion is not fulfilled unless a large enough deformation takes place to lower the hardening rate of the material between voids, $\partial\sigma/\partial\epsilon$.

It is depicted in equation 5.6 that instability and shear localisation will occur if any one of the variables attains a critical value. At extreme cases the effects of any one of the variables can dominate the critical event at which the onset of localisation or failure occurs making the contribution from all others insignificant. We consider the two extreme cases where flow localisation is caused by either thermal softening or geometrical softening and treat them separately. The intermediate case is obtained by a combining the two extreme effects. This approach was first used by Dodd and Atkins [181].

The Contribution from Thermoplastic Shear Instability to Flow Localisation

If the material does not contain any voids or has no potential for nucleation of voids during plastic deformation then the damage parameter can be eliminated from equation 5.6. Assuming a constant strain rate throughout the deformation equation 5.6 simplifies to:

$$\left(\frac{\partial \tau}{\partial \gamma}\right)_{\dot{\gamma},T} = -\left(\frac{\partial \tau}{\partial T}\right)_{\dot{\gamma},\gamma} \frac{dT}{d\gamma} = 0 \qquad (5.9)$$

The plastic work in the element undergoing shear can be balanced with the energy converted into heat as:

$$B\beta\tau \, d\gamma = \rho c \, dT \qquad (5.10)$$

where B is the fraction of plastic energy converted into heat (B~0.9) [182], β is the fraction of heat energy retained in the shear zone (β =1 for adiabatic conditions), ρ is the density and c is the specific heat of the material.

The isothermal stress strain relation at constant strain rate of the form given below is assumed as an approximate constitutive equation for the material:

$$\tau = \tau_o \gamma^n \qquad (5.11)$$

Then combining equations 5.9, 5.10, and 5.11 gives a criterion for the onset of shear instability as:

$$\gamma_i = \frac{n\rho c}{-B\beta\left(\frac{\partial \tau}{\partial T}\right)_{\gamma,\dot{\gamma}}} = nM \qquad (5.12)$$

where M may be regarded as a material constant which varies between 1 and 20 in most materials. The physical interpretation of equation 5.12 is as follows: when the plastic strain is less than the instability strain γ_i uniform deformation takes place. When the strain becomes larger than γ_i deformation localises to a small number of bands whose width and rate of development depend on the mechanical and thermo-physical properties of the material.

The Contribution from Geometrical Softening to Flow Localisation

In Fig. 4.11(a) it is shown that when chip segmentation occurs at the primary shear zone, ductile iron chips exhibits microstructural features characteristic of ductile fracture. Incompatibility of deformation between the second phase particles (graphite inclusions) and the metal matrix leads to decohesion between the particle and the matrix or particle breaking causing void nucleation. Increasing plastic strain promotes void growth or damage. With continuing deformation, damage accumulates to a critical value at which microstructural instability occurs, resulting in void coalescence and microcrack formation. Thus the fracture process during chip segmentation at the primary shear zone can be analysed in terms of damage accumulation in ductile fracture. The metal cutting conditions define the macroscopic strain distribution in the secondary shear zone. The geometry of metal cutting operation and the cutting velocity are the key variables of the metal cutting process. The microstructure and, in particular, the second phase particle dispersion and the matrix plasticity determine the strain localisation and the microscopic flow of the material. Thus both microscopic and macroscopic flow influence the damage process underlying ductile fracture. Micro cracking or fracture initiation occurs when the damage integrated along the fracture path exceeds a critical value, which is characteristic of a given material, and is referred to as critical accumulated damage, CAD. The dispersion of the particles determines the critical gauge length given by a material parameter, $\ln(\lambda_o/d_o)$ where λ_o is the initial void spacing and d_o the initial void dimension along the chosen orientation. The void growth under a triaxial system is complicated by the deformation behaviour that is a function of strain, strain rate and temperature. Sowerby and Chandrasekaran [134] have developed an upsetting test using a collar specimen to obtain a well defined strain path. The test allows the determination of critical accumulated damage by integrating damage along the strain path and at fracture according to McClintock's [132] model of void growth. By hardening the matrix (i.e. by decreasing the plasticity of the matrix), the CAD of the material can be decreased considerably. Once the CAD of the material

is decreased, the chip fracture occurs at low strain to fracture and the strain imparted in the primary shear zone may be adequate to promote chip segmentation, as in the case of grey cast iron. Ductile iron exhibits a low CAD by comparison with steel. Subramanian [183] has varied the CAD of ductile iron by varying independently the nodule count and the matrix structure. The CAD of ductile iron decreases with increased nodule density for a given matrix, or by hardening the matrix for a fixed nodule count.

In ferritic ductile iron, the chip can accommodate limited cumulative strain in the primary shear zone before fracture of the chip is caused by geometrical softening due to graphite nodules. By comparison, steel chips with characteristic high CAD can undergo considerable shear strain in the primary shear zone, which accounts for the higher critical speeds for chip segmentation observed in the case of steel. Since the fully segmented chips in ductile iron have been found to exhibit microstructural features of void coalescence characteristic of ductile fracture, the chip fracture in the primary shear zone at high cutting speeds is therefore analysed in terms of damage concepts.

The analysis used by Dodd and Atkins [181] is followed. In this analysis a specimen in which the deforming gauge length L contains an array of voids with the sum of diameters of all individual voids equal to D (Fig. 5.6), is considered.

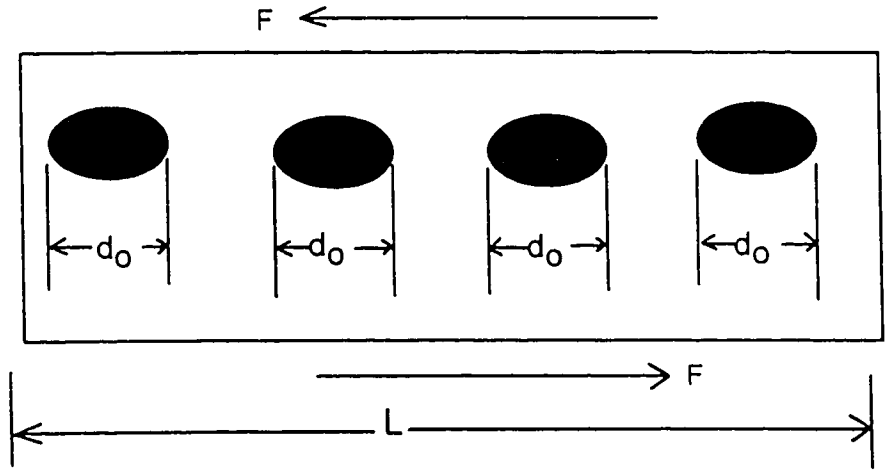

Fig. 5.6: A Shear band of length L containing voids with diameter d_o.

If a shear band having a width W is formed then the area is given as A = (L-D)W. Under the action of a shear stress τ the force acting on this area is given by $F=\tau A$. Since at instability $dF=0$,

$$\frac{d\tau}{\tau} = -\frac{dA}{A} \qquad (5.13)$$

Combining equation 5.9, 5.10, 5.11 and 5.13 gives:

$$\gamma_i = \frac{n}{\frac{1}{M} + \frac{dD/d\gamma}{L - D}} \qquad (5.14)$$

where γ_i is the critical strain for shear localisation. Assuming further that the interaction of the voids can be ignored and the void growth rate is pressure dependent then the growth rate of the voids is represented by Rice and Tracey [133] as:

$$\frac{\dot{D}}{D} = \dot{\gamma}(a + \frac{b\sigma_H}{\tau_y}) \qquad (5.15)$$

where a and b are material parameters.

Substituting equation 5.15 into equation 5.14 gives the critical strain for instability under combined thermoplastic shear and geometrical softening as

$$\gamma_i = \frac{n}{\frac{1}{M} + \frac{D_c(a+b\frac{\sigma_H}{\tau_y})}{L - D_c}} \qquad (5.16)$$

where D_c is the critical value of D when instability occurs.

In equation 5.16 the values of L, D_c, a, b, and σ_H/τ_y will influence the level of γ_t. In metal cutting where σ_H is compressive there is a threshold value of σ_H given by $\sigma_H/\tau_y = -a/b$ above which instability due to geometrical softening is suppressed. This is because the point of maximum shear stress is delayed to higher values of strain as the compressive pressure is increased. If the material contains no voids initially and further contains no void nucleation sites, the instability strain is given by equation 5.12 since $D_c = 0$. Obviously materials with large values of the characteristic constant M and work hardening index n will exhibit large instability strains and hence be more resistant to thermoplastic shear localisation. However there is a strong influence of strain rate on the instability strain that has been neglected in the analysis.

Whether the first occurrence of flow localisation is caused by thermoplastic or geometrical effects depends mainly on the comparative values of void nucleation strain γ_v and the thermoplastic shear instability strain $\gamma_t = nM$. If $\gamma_v > nM$ there are no voids to grow and produce geometrical instability before thermoplastic shear instability sets in. If $\gamma_v < nM$ voids will commence to grow, but it will still be a thermoplastic instability that first occurs if the geometrical γ_t is greater than nM. When the geometrical γ_t is less than nM flow localisation takes place by geometrical softening . This later condition demands a large number of inclusions or second phase particles in the material that may not be acceptable in clean steel technology. Equation 5 16 predicts that once a flow localisation commences (of whatever cause), and if fracture does not intervene, a second flow localisation produced by simultaneous geometric and thermal softening is possible.

Equation 5.16 can be written as

$$\frac{n}{\gamma_t} = \frac{1}{M} + \frac{(a+b\frac{P}{k})}{\frac{L}{D_c} - 1} \qquad (5.17)$$

where P represents the hydrostatic pressure σ_H and k is the flow stress τ.

In any material the value of M is constant. However, the values of P/k and L/D_c can be varied in the material. This enables the comparison of the contributions from thermal softening and geometrical softening to find out the condition under which each of these can dominate the instability criterion. Fig. 5.7 shows the predicted variation of the contribution from geometrical softening to n/γ_t as a function of L/D_c for P/k = -0.5 which is typical for moderate cutting speeds in metal cutting. L/D_c represents the reciprocal of the volume fraction of the voids present in the material at instability. As shown geometrical softening begins to dominate over thermal softening when L/D_c = 18.5 i.e. when the volume fraction of the voids is 5.4%. In ductile iron with more that 10% volume fraction of graphite dispersed in a ferritic matrix geometrical softening is predicted to dominate over thermal softening at the P/k ratio of -0.5. Geometrical softening exceeds thermal softening contribution by a factor of 2. At a volume fraction of voids of 0.005 in AISI 1020 steel with a similar ferritic matrix as in ductile iron, thermal softening is predicted to dominate over geometrical softening by a factor of 11. If M=4 as for Ti-6Al-4V, alloy thermal softening dominates over geometrical softening even when the volume fraction of voids is 20% for the P/k ratio of -0.5. Thus it is practically impossible for geometrical softening to dominate in such an alloy system. In clean steel with typical volume fractions of inclusions of the order of 0.1% thermal softening is predicted to dominate over geometrical softening. These theoretical results can be used to explain the experimental results obtained for the chip formation mechanism during the machining of ductile iron and AISI 1020 steel and the Fe-Ni-C alloys. The experimental results support the theoretical analysis as follows:

In ductile iron L/D_c =10 which gives a 10% voids volume fraction. Geometrical softening is effective in lowering the critical speed for chip segmentation. In contrast AISI 1020 steel with the same matrix but very small amount of voids is dominated with thermal softening. The value of M is 13.86 [181] giving a low value of 1/M = 0.072. A low value of 1/M is predicted to give a large critical

strain for instability and insufficient thermal softening for shear localisation to occur at low cutting speeds. However, in metal cutting the critical strain can be reached even at low cutting speeds without the occurrence of instability. Instability and localisation will however lead to chip segmentation at higher cutting speeds making strain rate an important factor. Thus when thermal softening dominates over geometrical softening or when both contribute competitively to shear instability, the criterion for instability and shear localisation is best expressed in terms of a critical strain rate.

The variation of n/γ_i with L/D_c for various values of P/k ratio is shown in Fig. 5.8. The critical strain at instability is predicted to decrease with increase in volume fraction of the voids. Higher compressive hydrostatic pressures (negative P/k ratio) are predicted to cause higher critical strains for the onset of instability. Higher tensile hydrostatic pressures are predicted to reduce the critical strain for instability. High tensile pressures are promoted at high cutting speeds or high strain rates [183]. The technological implication of this analysis is that shear localised chips can be promoted in clean steel at ultra-high cutting speeds.

In Fig. 5.9 the value of L/D_c at which the effects of geometrical and thermal softening on the critical strain for instability are equal is plotted against the P/k ratio for a range of materials having different values of M. A linear relationship is obtained between L/D_c and the P/k ratio. For AISI 1020 steel with M=13.86 the critical value of L/D_c at which geometrical softening begins to exceed thermal softening is 18.5 or a volume fraction of 5.4 % at a P/k ratio of -0.5. For Ti-6Al-4V alloy with M=4 geometrical effects are predicted to have significant contribution when $L/D_c = 5$ (i.e at a volume fraction of voids of 20%). The Fe-Ni-C alloys used in this study are expected to have an M value close to that of the titanium alloy. The analysis suggests that it is not feasible to influence the instability criterion in such alloys by addition of inclusions since the system demands a technologically unacceptable volume fraction of voids (>20 %). Thus in this case thermal softening will always control the process of shear localisation.

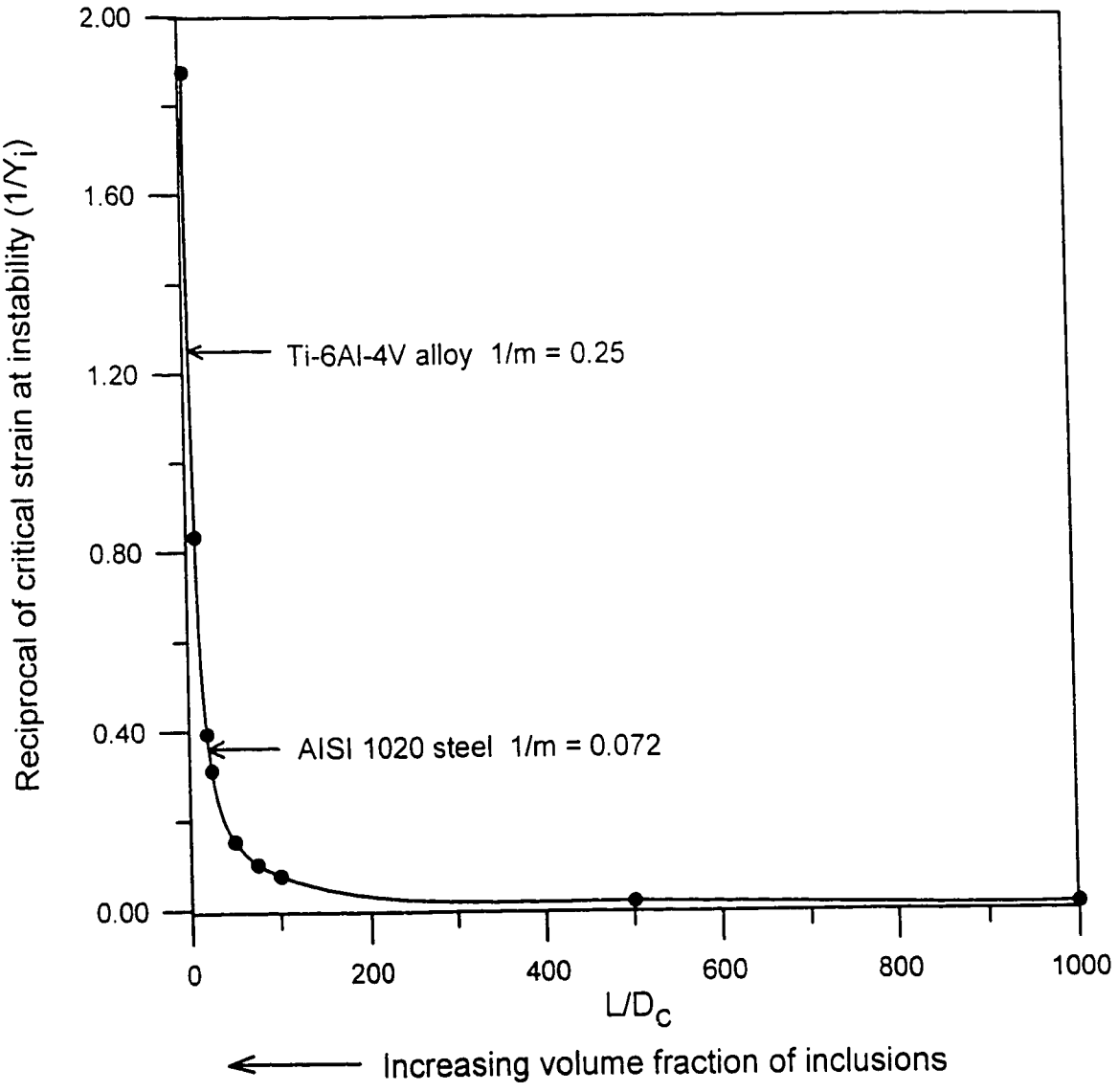

Fig. 5.7: Predicted contribution from geometrical softening to the critical strain at instability as a function of the reciprocal of volume fraction of voids for P/K = 0.

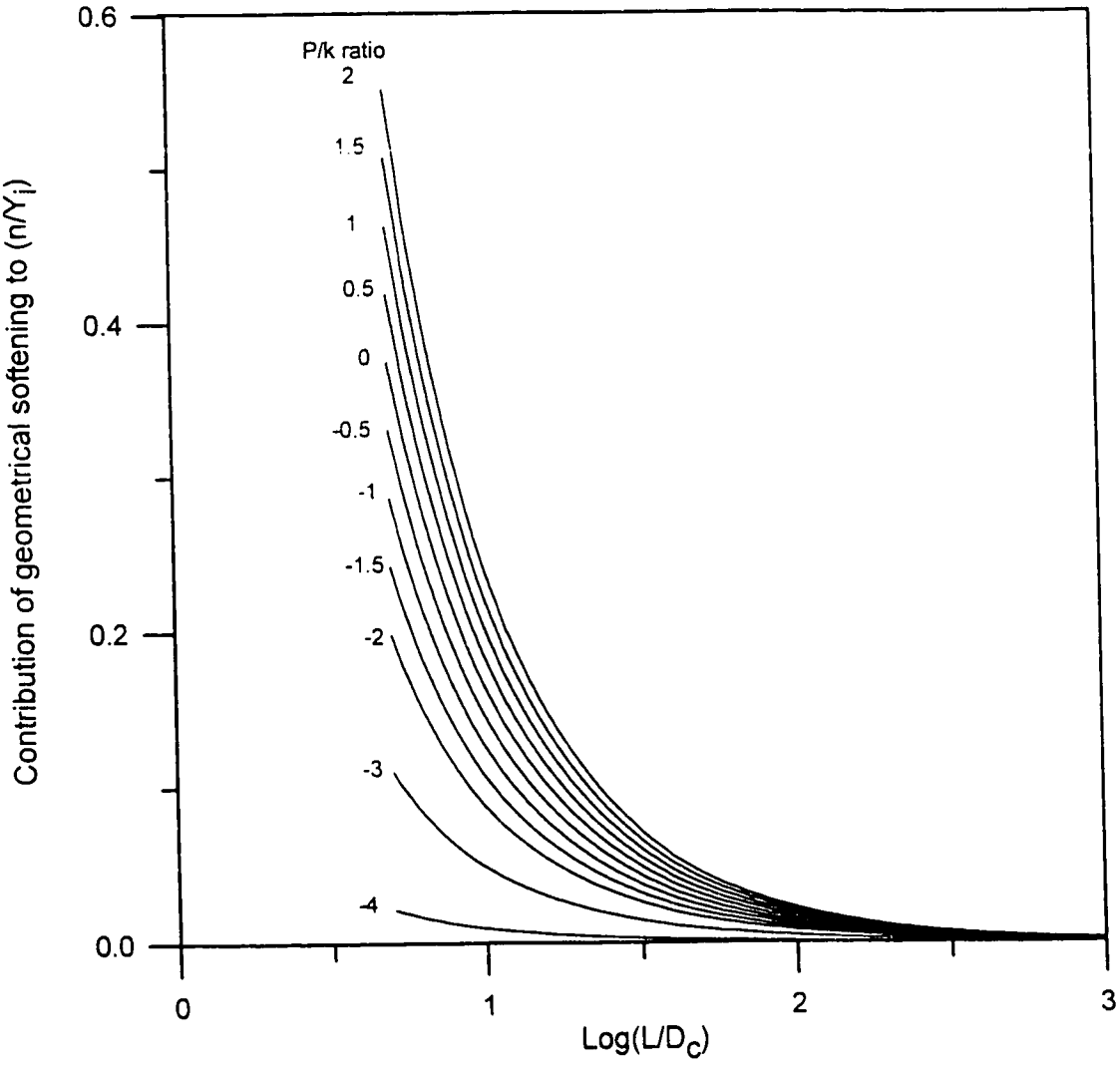

Figure 5.8: Contribution of geometrical softening to the reciprocal of the critical strain at instability (n/Y_i) plotted against the reciprocal of volume fraction of voids (L/D_c) for various P/k ratios.

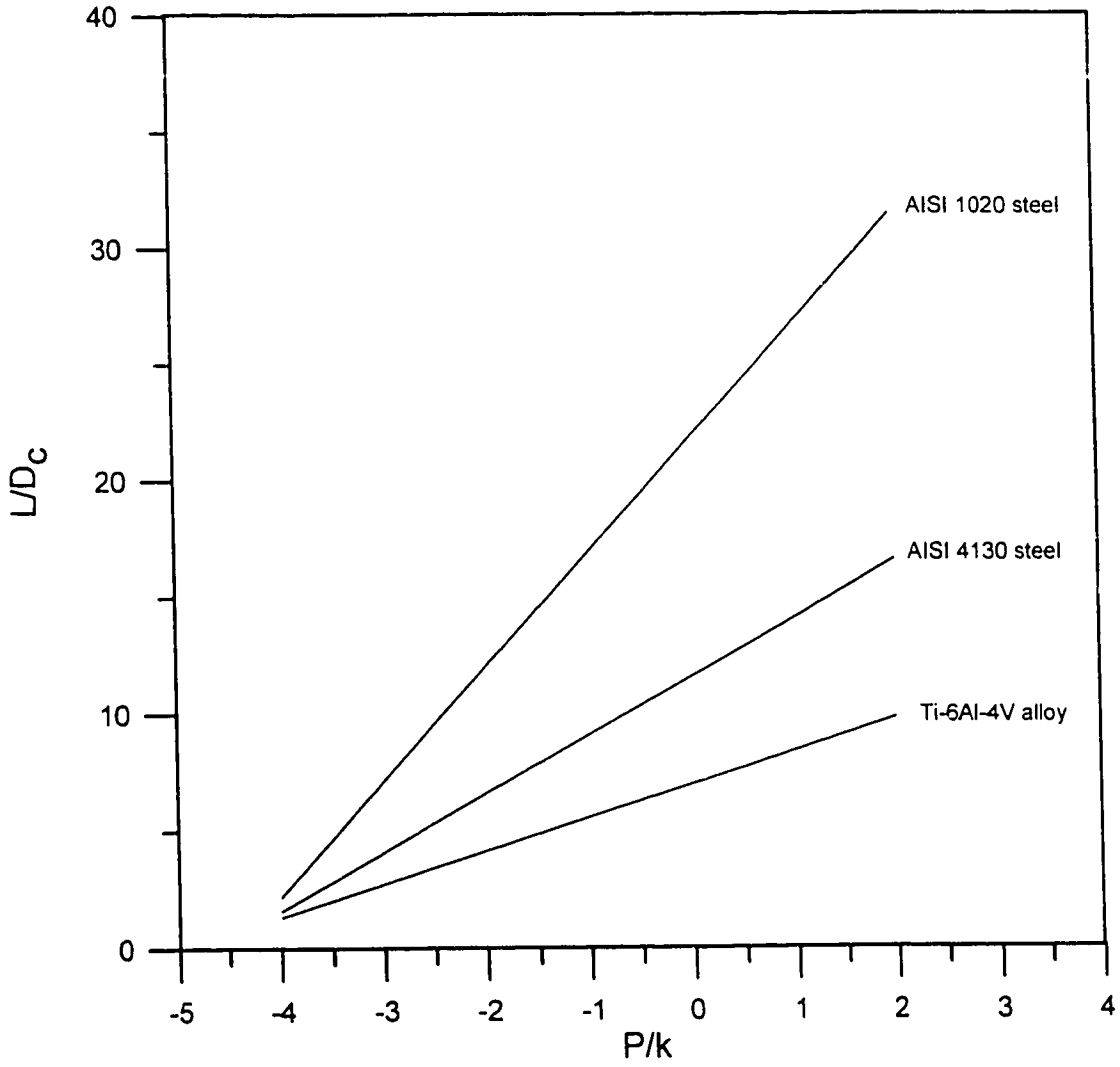

Fig.5.9: The ratio of hydrostatic pressure to yield stress (P/k ratio) versus the reciprocal of the volume fraction (L/D_c) at which contributions from geometrical and thermal softening to the onset of instability are equal for a range of materials.

In summary this study has revealed some new features of the competition between geometrical and thermal softening in shear localisation during chip segmentation. The first is that the onset of shear localisation is dominated by geometrical softening in materials such as ferritic ductile iron that are characterised with a low thermal softening and high content of void nucleation sites. In such materials flow localisation occurs as a result of void nucleation at a critical strain for void nucleation, void growth and void coalescence at a critical strain into shear bands leading to chip segmentation at lower cutting speeds (strain rates). Thus the criterion for flow localisation is best described with a critical strain for instability.

For a material such as AISI 1020 steel with a similar ferritic matrix and low thermal softening potential as ferritic ductile iron, but with a low amount of second phase particles (void nucleation sites), strain rate hardening of the matrix followed by thermal softening causes shear localisation at high cutting speeds and the critical condition is best described with a critical strain rate for shear instability and localisation as provided by Recht [73].

For materials such as the Fe-Ni-C alloys used in the hardened condition as in the present study, high thermal softening potential controls shear localisation process even at low and moderate cutting speeds.

In clean steel, the absence of inclusions and hardened matrix necessitates high cutting speeds for shear localisation. Machining of such materials demands utra-high cutting speeds.

A tensile stress tends to promote geometrical softening whereas a compressive stress tends to suppress geometrical softening. The effect of increasing the cutting speed is to decrease the ratio of hydrostatic stress to shear flow stress that promotes the tensile component required for void growth or geometrical softening.

5.8 Effect of Phase Transformation on Chip Segmentation, Tool Wear and Surface Finish

It the previous section, the role of second phase particles in promoting shear localisation in an unhardened matrix (graphite in ferritic matrix) was clarified. In the absence of a large volume fraction of second phase particles, the ferrite/pearlite matrix as in AISI 1020 steel exhibits flow chip morphology up to high cutting speeds, when strain rate hardening of the matrix can give rise to shear localisation. By hardening the matrix through heat treatment, thermal softening potential is induced in the matrix. The critical speed for chip segmentation is decreased with increasing hardness in quenched and tempered medium carbon steel as reported by a number of workers [69,129]. If thermal softening can be induced by phase transformation as in the martensite to austenite phase change, shear localisation should be aided by phase transformation. In order to clarify the role of phase transformation on shear localisation in the primary shear zone and its consequence on chip morphology, tool wear and surface finish, a series of Fe-Ni-C alloys was designed in which the martensite to austenite phase transformation temperature decreases with increase in nickel content.

5.8.1 Phenomenological Observations on Chip Morphology, Tool Wear and Surface Finish in Machining of Hardened Fe-Ni-C Alloys

The use of Fe-Ni-C alloys has made it possible to study the formation of a wide range of chip morphologies as a function of cutting speed and their effect on tool wear and surface finish within experimentally achievable cutting speeds. The white etching bands seen on optical micrographs of chips are confirmed to be austenite from X-ray and electron diffraction studies; the band is referred to as transformation shear band to imply that martensite to austenite phase transformation has occurred from temperature and pressure incident on this region. At low cutting speeds, the tribological condition of sliding operates at the tool-chip interface and the chips exhibit flow or continuous chip morphology. Tool

wear under this conditions is essentially physical. As the cutting speed is increased, the continuous chips formed in the machining of Fe-28.9Ni-0.1C and Fe-18.9Ni-0.1C alloys exhibit transformation shear bands in the secondary shear zone, i.e., in the region adjacent to the tool-chip interface, see Fig. 4.26(a). The transformation shear band at the tool-chip interface is caused by the tribological condition of seizure occurring at the tool-chip interface which causes thermoplastic shear. The local temperature rise causes chemical dissolution of the tool into the chip. Crater wear by diffusion commences at a cutting speed of 50 m/min and the crater is located far away from the cutting edge of the tool. The maximum depth of crater coincides with the phase transformation temperature. There is a critical speed (75 mm/min) at which Fe-28.9%Ni-0.10%C alloy exhibits shear bands corresponding to primary shear zone, and this coincides with the on-set of partial chip segmentation (see Figs. 4.26(a) - 4.32(a)). The degree of segmentation increases with increasing cutting speed, ultimately leading to full segmentation of the chip. As the degree of segmentation increases, the crater moves closer to the cutting edge of the tool, eventually damaging the cutting edge of the tool and extending into the flank face of the tool (Table 4.17). Damage of cutting edge of the tool impairs the surface finish. At higher cutting speed, there is metallographic evidence of microstructural change on the surface layers of the workpiece as well (see Fig. 4.34).

In conclusion the degree of chip segmentation increases with increase in cutting speed. The crater moves closer to the cutting edge of the tool with increase of cutting speed and the degree of chip segmentation. A high degree of chip segmentation caused by phase transformation in the primary shear zone localises the crater very close to the cutting edge of the tool. Eventually the crater extends to the flank face of the tool causing extensive damage to the cutting edge. The loss of cutting edge impairs the surface finish.

5.8.2 Origin of Transformation Shear Band in the Primary Shear Zone

The classical work of Zener and Hollmon has shown that shear localisation occurs dynamically when the rate of thermal softening exceeds the rate of strain hardening [1]. Bai and Dodd have used perturbation analysis to analyse the marginal instability problem in adiabatic shear and concluded that there is a gap between instability and localisation [77]. This gap may be attributed to the neglected contribution from microstructural changes in their analysis. Meyers has pointed out that instability is a necessary but not adequate condition for shear localisation [2]. He has proposed that a major microstructural change which causes a sudden drop in the flow stress is necessary for localisation to occur following instability. Andrade and Meyers have proposed dynamic recrystallisation as a possible cause for shear localisation but have proposed low temperature ($0.4T_m$) for shear localisation, which is more typical of static recrystallisation [82]. According to Derby, the temperature for dynamic recrystallisation is much higher, close to $0.8T_m$, where T_m is the melting point [185].

The microstructural observations of the chips machined from the Fe-Ni-C alloys suggest three microstructural events that can contribute to thermal softening. These are dynamic recrystallisation, phase transformation and tempering of martensite. The effect of thermal softening due to phase transformation in causing shear localisation in the primary shear zone is discussed.

5.8.3 The Effect of Phase Transformation on Shear Localisation

Mayers et al [186] and Andrade et al [82] have respectively attributed shear localisation in titanium and copper to an evolution of microstructure controlled by dynamic recrystallisation. In Fig. 5.10 the temperatures at which static and dynamic recrystallisation occur are plotted as a function of nickel content for the Fe-Ni-C alloys. The estimated phase transformation (As) temperatures for the alloys and the calculated temperatures at the primary shear zone corresponding to the critical speeds

for segmentation are plotted in the same figure. The martensite to austenite phase transformation temperature increases with decrease in nickel content. The critical cutting speed for chip segmentation increases with decrease in nickel content. Therefore the critical speed for chip segmentation increases with the martensite to austenite phase transformation temperature, see also Table 4.15. In Fe-Ni-C alloys the phase transformation temperature decreases with increasing nickel content but the recrystallisation temperatures remain constant with increasing nickel content (Fig. 5.10). If it is assumed that recrystallisation causes shear localisation leading to chip segmentation then segmentation should be observed at the same cutting speed for all alloys. The results show that the critical speed for chip segmentation increases with the phase transformation temperature but does not correlate with the recrystallisation temperature.

Assuming that the reverse martensite transformation occurs by a diffusionless mechanism, then the austenite formed is expected to inherit a high dislocation density rendering thermal softening ineffective in reducing the hardness. The reversal of martensite to austenite by a diffusionless (martensitic) mechanism is supported by a number of observations. Apple and Krauss [187] have shown that the reversal of martensite to austenite occurs by a martensitic mechanism when the heating rate is 28,000 ^{0}C/s. The resulting structure is shown to consist of plates of austenite with high dislocation densities and surface tilts characteristic of a shear-type transformation. From the present study the microstructure in the transformed shear bands has been characterised and found to consist of austenite and a small amount of untransformed martensite, see Fig. 4.22. At a cutting speed of 400 m/min. the time taken for deformation to be complete in the shear band is 3.6×10^{-6} second which gives a heating rate of 10^{6} ^{0}C/s. This heating rate is sufficient for the reversal of martensite to austenite in a quenched Fe-28.9Ni-0.1C alloy to occur by a diffusionless mechanism during rapid plastic deformation in high speed machining. A dramatic decrease in microhardness from that of highly deformed martensite (675 VHN at a cutting speed of 1 m/min.) to that of deformed austenite

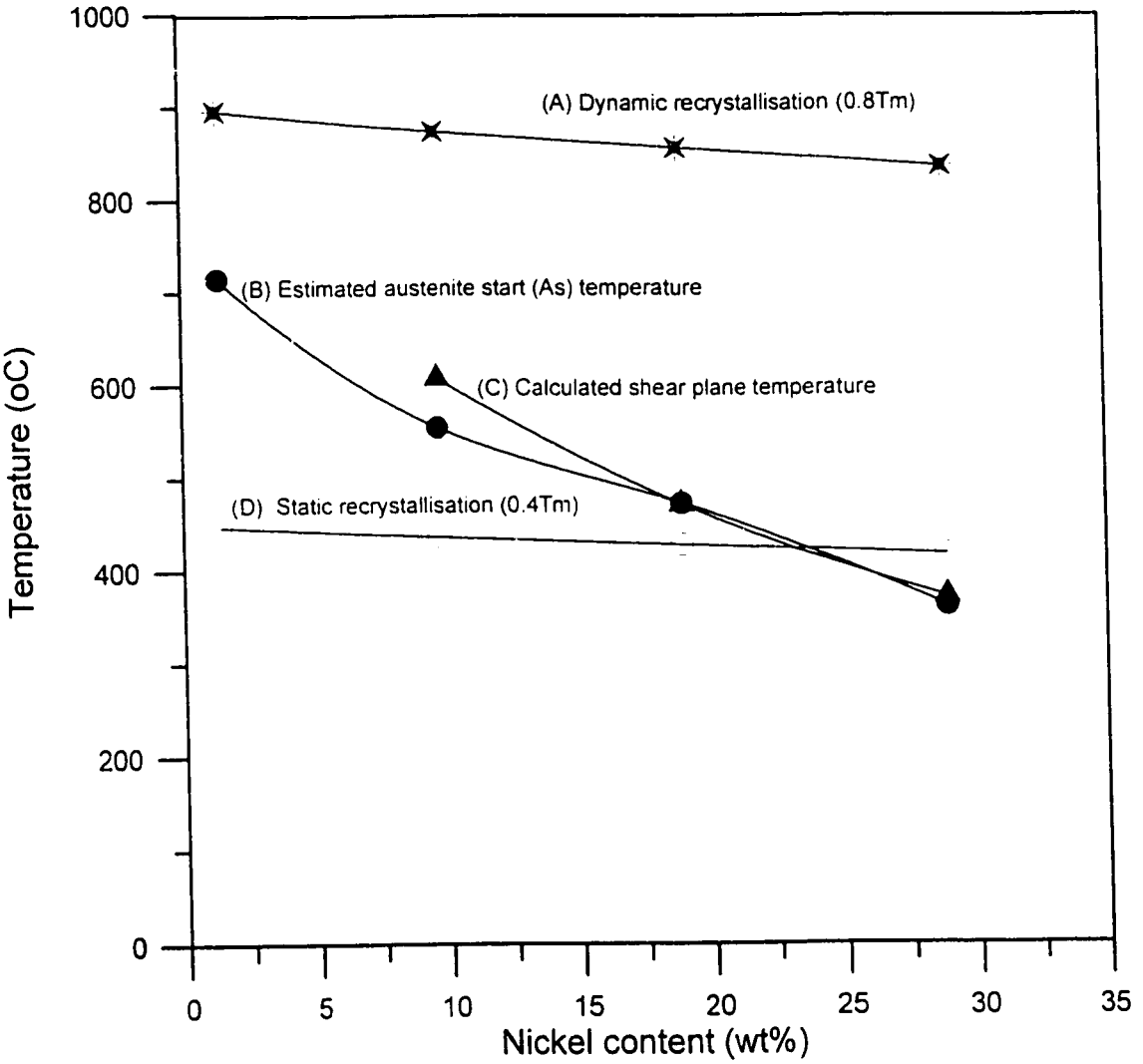

Fig. 5.10: (A) Dynamic recrystallisation temperature (0.8Tm), (B) estimated phase transformation temperature (As), (C) calculated primary shear zone temperature at the onset of full chip segmentation and (D) static recrystallisation temperature (0.4Tm) as functions of the nickel content in Fe-Ni-C alloys.

(402 VHN in the primary shear band and 369 VHN in the secondary shear band at a cutting speed of 400 m/min.) is shown in Table 4.11. The microhardness of reversed austenite (369 VHN) is higher than that of annealed austenite (151 VHN). This is indicative of the presence of a high dislocation density in reversed austenite, which is consistent with the doubling of the yield strength due to the reversal treatment reported by Krauss [188]. However an increase in hardness due to the refinement of the structure can not be ruled out. It is however, known that reversal of the martensite in Fe-Ni-C alloys can result in formation of very fine austenite which retains a high hardness hence phase transformation is a strong candidate in causing shear localisation.

Preliminary TEM studies of the transformation shear band occurring at the primary shear zone at high cutting speeds show ultra-fine austenite grains (10-20 nm), see Figs. 5.11 and 5.12. In addition, an amorphous region appears to be present at the centre of the transformation shear band in the primary shear zone, however this is not yet confirmed. Theoretical analysis, the results of which are shown in Fig. 5.13, has shown that the rate of heat generation by plastic work in the primary shear zone exceeds the rate of heat diffusion in all these alloys that exhibited transformation shear bands, and in all cases large strain rates and large strains are involved. For heat to localise the time for deformation must be smaller than the time for heat diffusion from the shear band. This condition is shown to be met in all cases where shear localisation occurred (Table 4.12(a)). In this case the heat diffusion time is more than one order of magnitude higher than the deformation time.

Summary

Since the critical speed for the onset of segmentation in the primary shear zone increases with increase in phase transformation temperature, it is proposed that the shear localisation is aided by phase transformation. Dynamic recrystallisation occurs subsequent to phase transformation but concomitant with plastic deformation during primary shear. Thus the occurrence of ultra-fine grains of austenite can be interpreted as arising from dynamic recrystallisation [82,185]. The occurrence of

(a)

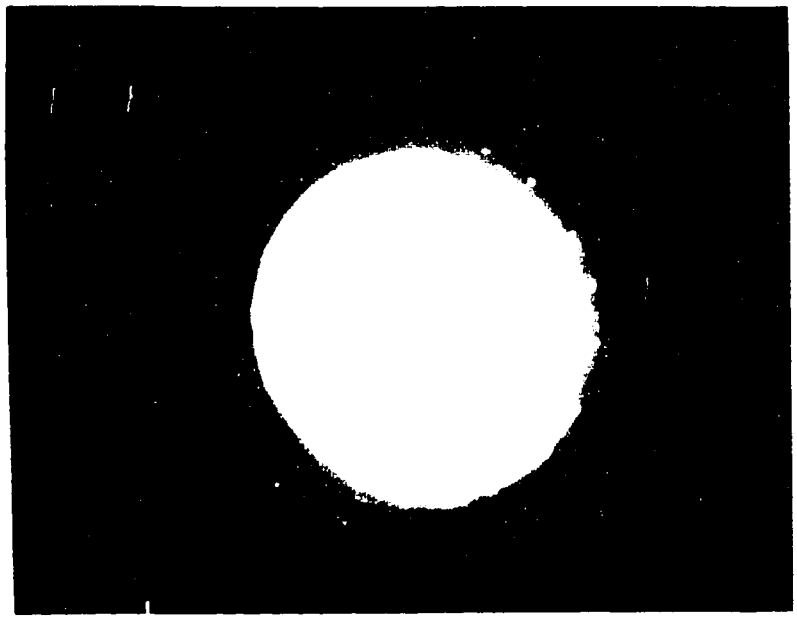

(b)

Fig. 5.11: (a) Transmission electron (bright field) micrograph of the shear band formed at the primary shear zone when martensitic Fe-28.9Ni-0.1C alloy is machined at a cutting speed of 400 m/min., showing ultra-fine grains (15-20 nm) of austenite in the region between the centre of the shear band and outer edge of the shear band, and (b) selected area diffraction pattern from the same region showing fcc structure of the austenite.

(a)

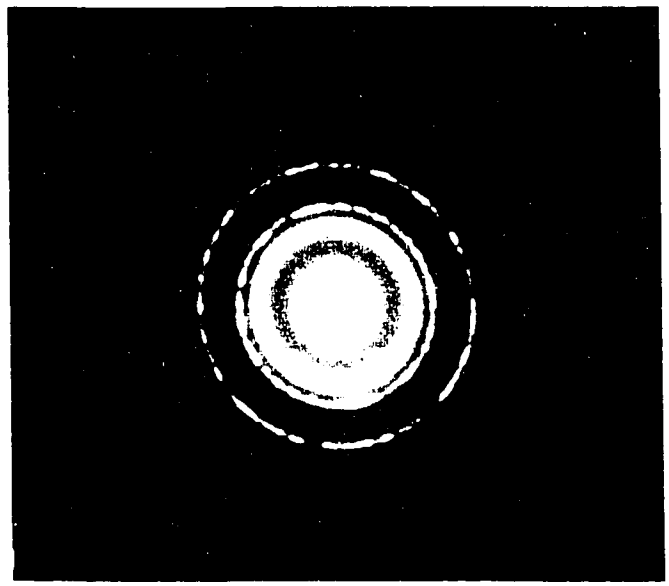

(b)

Fig. 5.12: (a) Transmission electron (dark field) micrograph of the shear band formed at the primary shear zone when martensitic Fe-28.9Ni-0.1C alloy is machined at a cutting speed of 400 m/min., showing ultra-fine grains (15-20 nm) of austenite in the region between the centre of the shear band and outer edge of the shear band, and (b) selected area diffraction pattern from the same region showing fcc structure of the austenite.

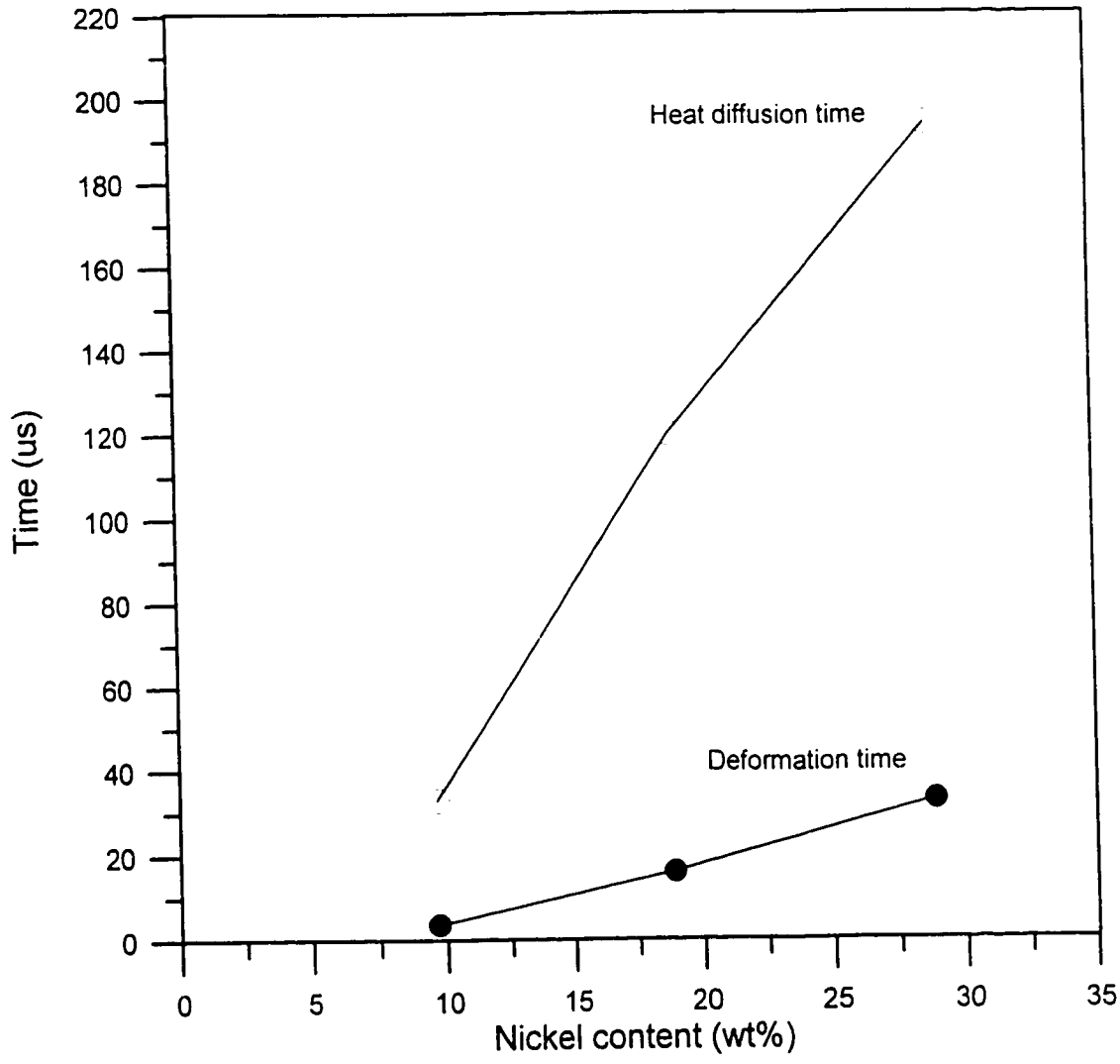

Fig. 5.13: Deformation and heat diffusion times as a function of nickel content during shear localisation in Fe-Ni-C alloys.

amorphous region is indicative of melting followed by rapid solidification, however, the present results are subject to experimental uncertainties which call for further investigation to be sure that they are not resulting from microstructural changes due to the specimen preparation technique used.

5.8.3.1 Thermal Softening due to Recrystallisation

For the Fe-28.9Ni-0.1C alloy transformation shear bands start appearing in the primary shear zone at a cutting speed of 75 m/min. The deformation time corresponding to this speed is 33 μs. This time is an order of magnitude less than the time required for dynamic recrystallisation to take place. At higher cutting speeds the deformation time is two orders of magnitude less that the time for dynamic recrystallisation to occur. This shows that recrystallisation is not the microstructural change that causes thermoplastic shear localisation. However, when machining Fe-28.9Ni-0.1C alloy at a cutting speed of 400 m/min. the calculated time for thermal diffusion to be complete is $t = 0.98 \times 10^{-4}$ s. This time is in the order of the time for dynamic recrystallisation to occur. Therefore the fine structure of the shear bands may be attributed to the occurrence of dynamic recrystallisation subsequent to phase transformation.

According to a preliminary TEM analysis of the shear bands obtained in the Fe-28.9Ni-0.1C alloy at a cutting speed of 400 m/min., there is a gradation of microstructure as the centre of the shear band is approached from the chip body. The microstructure has been confirmed by TEM analysis to consist of austenite in the outermost region of the shear band. Next to this region unconfirmed observations show a fine grained structure with a grain size in the order of 20 nm which is assumed to result from dynamic recrystallisation. Finally at the centre of the shear band is an amorphous structure (though not confirmed) which indicates melting followed by rapid solidification. From the foregoing it is proposed that thermoplastic shear localisation is caused by thermal softening due the martensite to austenite phase transformation. Once localisation has occurred the strain and strain rate

in the shear band are probably amplified resulting in a further increase in temperature beyond the phase transformation temperature to levels where dynamic recrystallisation probably takes place and possibly reaching the melting point. However, these observations are in their preliminary stage and it has not been confirmed whether the spotless pattern is an amorphous structure or not. Should melting occur, the cooling rate is adequately high ($>10^6$ ^{0}C/s) to give an amorphous structure. The uncertainities arise from the difficulties on specimen preparation due to the fact that the structure could have been altered by the ion milling process that was used. Further experimental work is recommended to eliminate these experimental problems and determine the exact structure in this region of the shear bands. Alternative techniques of this film preparation are being explored to confirm the structure of the "white" shear bands.

5.8.3.2 Effect of Eliminating Phase Transformation

By annealing the martensite into stable austenite, the shear localisation is suppressed, consistent with the hypothesis that thermal softening due to martensite to austenite phase transformation causes shear localisation. The chip morphology remains continuous without any shear localisation even at higher cutting speeds, Figs. 4.51-4.54. Annealing causes decrease in hardness from 374 VHN for martensite to 151 VHN for austenite, Table 4.11. The major point to be made here is that annealing has lowered the flow stress, and markedly decreased the thermal softening potential of the matrix and eliminated thermal softening due to phase transformation. The latter two parameters are considered to play a significant role in suppressing shear localisation in the primary shear zone. In quenched Fe-1.4Ni-0.1C alloy, the critical speed for chip segmentation is high. This is attributed to low hardenability of this alloy and the raised phase transformation temperature. Further work is required to resolve the relative contributions of thermal softening of the matrix to thermoplastic shear localisation from that of phase transformation.

5.8.3.3 Thermal Softening due to Tempering of Martensite

At a cutting speed of 5 m/min the chips formed from the machining of Fe-28.9Ni-0.1C alloy exhibit very thin white etching bands running from the bottom of the chip into the chip body. At 10 m/min the bands are thicker and span the whole thickness of the chip. The microstructure is clearly modified. At these low cutting speeds the strain rate is too low to permit thermoplastic shear localisation. However thermal softening by tempering can possibly occur and trigger shear localisation.

In the Fe-9.7Ni-0.1C alloy a deformation shear band is first formed at cutting speeds between 200 and 350 m/min. X-ray diffraction analysis has confirmed the presence of a bcc structure in the deformation shear band. The formation of a deformation shear band is in this case attributed to tempering of martensite. At a cutting speed of 400 m/min in the Fe-9.7Ni-0.1C alloy a transformation shear band forms at the centre of the deformation shear band. This serves to illustrate that once shear localisation occurs the strain rate and temperature in the shear band are further increased to the extent that phase transformation or dynamic recrystallisation may occur depending on which has a lower temperature. Even melting at the centre of the shear band could occur if the strain rate and temperature reached are extremely high .

5.8.4 Effect of Phase Transformation Temperature on the Critical Speed for Segmentation

Localisation of plastic flow is promoted by a sharp decrease in the flow stress with temperature caused by microstructural changes accompanying phase transformation or recrystallisation. The role of thermal softening due to phase transformation in bringing about shear localisation is to promote chip segmentation. By changing the phase transformation temperature through a change of alloy chemistry, the critical speed for chip segmentation is shown to increase with increase in the phase transformation temperature, see Table 4.16. However, still changing the

chemistry of the alloys through varying of nickel content must be accompanied with change in the thermo-physical and mechanical properties of the materials. Recht [73] developed a mathematical expression, equation 2.27, through which the critical strain rates hence the critical cutting speeds at the onset of chip segmentation can be compared between two materials. The expression incorporates the thermo-physical and mechanical properties of the two materials. However, the occurrence of phase transformation and its contribution to thermoplastic shear localisation is not considered in the analysis.

An evaluation of the various terms in Recht's expression using values from Table 5.6 shows that thermo-physical properties combined with the hardness contribute by a factor of 1.03 to the difference in the critical strain rates for chip segmentation in Fe-28.9Ni-0.1C and Fe-18.9Ni-0.1C alloys. But the critical speed for chip segmentation observed in the experiments for these alloys differs by a factor of two. The implication is that thermal softening and shear localisation ought to be the dominant contributing factor (2/1.03 = 1.94) to chip segmentation. The observed increase in the critical speed for chip segmentation correlates with the increase in phase transformation temperature. The removal of the thermal softening potential by annealing of the hardened Fe-28.9Ni-0.1C alloy results in the promotion of flow chip morphology even at a high cutting speed of 350 m/min, which is four times the critical speed for chip segmentation of the alloy in its hardened condition.

Table 5.6: Thermo-physical and mechanical properties of Fe-Ni-C alloys [173- 174].

Nickel content (wt%)	Specific heat J/kg K	Thermal conductivity W/mK	Density kg/m^3	Hardness of martensite VHN_{50}
28.9	499	11.6	8180	374±29
18.9	460	18.1	8175	454±26
9.7	488	29.0	8164	396±15
1.4	487	43.0	8149	223±29

5.8.5 The Role of Strain Rate in Shear Localisation due to Thermal Softening

At very low cutting speeds < 1 m/min the strain rate is low and hence the temperature rise in the chips is low. It is therefore possible for any voids initially present or nucleated during deformation to grow and link up at a critical strain leading to fracture before thermal softening occurs. In this case the formation of discontinuous chips is dominated by geometrical shear instability caused by inclusions and second phase particles in the material, see section 5.7.3. If the material is clean and contains very low amounts of inclusions or second phase particles, the formation of discontinuous chips at low cutting speeds can be explained by using the Zener-Hollomon parameter, given in equation 2.8, which shows that low-strain rate and low temperature combination effects on the flow stress of the material are equivalent to high strain rate and high temperature combination effects on flow stress of the material .

In the Fe-Ni-C alloys with low amount of inclusions and second phase particles and high thermal sensitivity compared to ductile iron thermoplastic shear localisation will precede geometrical softening and the segmentation process at high cutting speeds is dominated by thermoplastic shear localisation, caused by phase transformation. In this case the material is more sensitive to strain rate and the condition for shear localisation should be defined with a critical strain rate rather than a critical strain.

The condition for thermoplastic shear instability given in section 5.7.3 is based on a critical strain. In this section Recht's analysis which expresses shear instability in terms of a critical strain rate is re-examined to see how well it can be used to predict the critical strain rate at the onset of shear instability.

Following the analysis by Recht [73] the condition $d\tau = 0$ which yields equation 5.6 from equation 5.5 permits a constant value of shear strength to be used in calculating the rate of heat

generation in the shear zone, which is then given by

$$q = \frac{(\tau L)}{J}\dot{\gamma} \qquad (5.18)$$

where q is the heat generation rate per unit area, τ is the shear strength in the weak zone, L is the specimen length (deformation zone thickness in primary shear zone), $\dot{\gamma}$ is the strain rate and J is the work equivalent of heat.

Using Carslaw and Jaeger's [189] solution for temperature on a plane in an infinite medium upon which heat is being generated uniformly at a constant rate, the temperature in the shear zone is given as:

$$T_A = \frac{\tau L\dot{\gamma}}{J}\left(\frac{t}{\pi\lambda\rho c}\right)^{1/2} \qquad (5.19)$$

Assuming a constant strain rate in the shear zone, Recht expressed the rate of change of temperature in the shear zone as:

$$\frac{dT}{d\gamma} = \frac{1}{2}\frac{\tau_y L}{J}\left[\frac{\dot{\gamma}}{\pi\lambda\rho c(\gamma - \gamma_y)}\right]^{1/2} \qquad (5.20)$$

and the strain hardening rate as:

$$\frac{d\tau}{d\gamma} = -\frac{1}{2}\frac{\tau_y L}{J}\left[\frac{\dot{\gamma}_c}{\pi\lambda\rho c(\gamma - \gamma_y)}\right]^{1/2}\frac{\partial\tau}{\partial T} \qquad (5.21)$$

where $\rho, c, \lambda, \tau, T, \gamma, \dot{\gamma}$ are the density, specific heat, thermal conductivity, flow stress, temperature,

strain and strain rate of the material in the shear band respectively and $\dot{\gamma}_c$, γ_y, τ_y are the critical strain rate for catastrophic thermoplastic shear to occur, the strain at yield and the yield strength of the material respectively.

Equation (5.21) has frequently been used to compare the critical strain rates for catastrophic shear to occur in two materials and in the prediction of the critical speed for catastrophic shear to occur. However in order to make the comparison it is assumed that the critical strains and the deformation zone thicknesses are equal while they may not be equal in practice. The value of L in equation 5.21 is poorly defined. In metal cutting we can assume that L represents the zone in which deformation takes place before localisation occurs. The size of the deformation zone has been defined in terms of the feed by Stevenson and Oxley [190] as $\delta = t_1/C$ where C is a constant , which for a free cutting steel was found experimentally to be equal to 2.35. Assuming this value of C for AISI 1020 steel and using the critical strain at instability obtained by Culver [112] together with the thermo-physical properties provided by Recht [73] i.e., γ=1.6, ρ=7860 kg/m^3, c=500 J/kg K, λ=50 W/mK, $(\partial\tau/\partial\gamma)/(\partial\tau/\partial T)$ =4200, and τ=138 Mpa, the critical strain rate at instability is 3.6×10^8/s for a feed rate of 0.259 mm/rev. This strain rate is more than two orders of magnitude higher than that usually encountered in metal cutting.

A similar calculation for titanium using the critical strain obtained by Culver and the material properties provided by Recht yields a critical strain rate for instability of 3×10^4/s. Experimental work has shown that in orthogonal machining of titanium instability set in at a cutting speed of 1 sfm (0.3048 m/min). Assuming zero rake angle and a typical shear angle for segmented chips of 35^0 the shear velocity v_s = 0.0066 m/s. Assuming a shear band thickness of 50 μm the strain rate obtained in the primary shear zone at instability is ~130/s. Again the predicted strain rate is more than two orders of magnitude higher than the actual experimental value. It is therefore concluded that there must be a phenomenon not included in Recht's analysis that contributes to thermoplastic shear localisation.

As proposed by Meyers [2], this involves a major microstructural change which in the present study was found to be phase transformation in hardened Fe-Ni-C alloys. Recrystallisation represents the other softening mechanism encountered in a work hardened material.

5.8.5.1 The Contribution from Geometrical Softening by Damage Accumulation to Shear Localisation

We consider a shear band in which the critical strain for void nucleation has been attained to nucleate a row of voids with initial spacing or mean free path λ_o and size d_o. The shear band is subjected to a hydrostatic pressure σ_H and the flow stress in shear the band is τ_y. The growth rate of the voids is represented by Rice and Tracey [133] as given in equation 5.15.

It is assumed that at some critical strain γ_i or when the size of the voids have grown from an initial mean diameter d_o to the mean free path λ_o, plastic deformation is localised along shear bands between the voids. Then integration of equation (5.15) between initial and final stages of void growth in the shear band (i.e. from nucleation of voids to coalescence of the voids) and in the direction of maximum void growth (i.e., parallel to the length of the shear band) gives:

$$\ln\left(\frac{\lambda_o}{d_o}\right) = (\gamma_i - \gamma_y)\left(a + \frac{b\sigma_H}{\tau_y}\right) \qquad (5.22)$$

In performing this integration it has been assumed that the stress triaxiality remains constant throughout the history of void growth.

Next we combine the effect of thermoplastic shear instability and geometrical softening to determine the condition for flow localisation in terms of the critical strain rate. Assuming that the

critical strain for void nucleation and the yield strain are small compared to the critical strain at thermoplastic shear instability, and with further assumption that the thermal and geometrical instability strain are equal, equation 5.22 can be substituted into equation 5.21. The result gives the critical strain rate for thermoplastic flow localisation under the combined effect of thermoplastic shear and geometrical softening (represented by the micro-structurally controlled geometrical parameter, $\ln \lambda_o / d_o$) as:

$$\dot{\gamma}_i = \frac{\ln(\frac{\lambda_o}{d_o})}{(a + \frac{b\sigma_H}{\tau_y})}(\pi\lambda\rho c)\frac{[\partial\tau/\partial\gamma]^2}{[\partial\tau/\partial T]^2}\frac{4J^2}{\tau_y^2 L^2} \qquad (5.23)$$

Thus the critical strain which is directly proportional to the speed has been related to the micro-structurally controlled geometrical parameter ($\ln \lambda_o / d_o$), physical properties, the thermal softening parameter and flow stress of the material. The damage parameter is coupled with the thermal softening parameter in the above expression. As predicted by equation 5.23 a high compressive hydrostatic pressure tends to promote thermoplastic shear instability by increasing the stress triaxiality in shear. A high thermal softening rate of the material promotes thermoplastic shear instability. Materials with high shear strength will tend to be more susceptible to thermoplastic shear instability and segment at lower cutting speeds. Materials with low (kρc) value will be more susceptible to thermoplastic shear instability. A high capacity for damage accumulation in a material and high strain hardening rate retards thermoplastic shear instability until high strain rates are applied.

An essential result from the present analysis is realised by comparison of the theoretical predictions with experimental observations.

1) Materials with large volume fraction of second phase particles are predicted to segment due

to shear localisation by geometrical softening. The critical condition is best described by a critical strain for shear instability and localisation. Ferritic ductile iron was used as an example of these class of materials due to the presence of a large volume fraction (~10%) of graphite spherulites dispersed in the matrix. Chip segmentation in ductile iron was found to occur due to geometrical softening, Figs 4.10 and 4.11. Thus the theoretical predictions are validated by experimental observations.

2) In materials that exhibit high thermal sensitivity, chip segmentation occurs by shear localisation due to thermal softening. Geometrical softening contributes to fracture in the localised shear bands. The critical condition for flow localisation is best described by a critical strain rate. In the present analysis, the shear strain term is replaced by the $\ln \lambda_o / d_o$ term which can be measured independently. Hardened Fe-Ni-C alloys are used to represent this class of materials. Due to thermal sensitivity of the flow stress τ_y, they are predicted to have high σ_H/τ_y ratio which greatly reduces the critical strain rate for flow localisation in shear. There is three orders of magnitude difference in the predicted and experimental critical strain rate for thermoplastic shear localisation to occur. This is attributed to the microstructural changes caused by phase transformation in high nickel hardened Fe-Ni-C alloys, see section 5.8.3. In the absence of phase transformation tempering of martensite causes shear localisation in the low nickel hardened Fe-Ni-C alloys. Thus the necessity for microstructural changes in thermoplastic shear localisation, and the argument that phase transformation is a cause rather than an effect of shear localisation is validated, see sections 5.8.2 to 5.8.4.

3) In the absence of geometrical or thermal softening the critical speed for chip segmentation due to shear localisation is predicted to be high. Shear localisation is caused by strain rate hardening of the matrix followed by thermal softening. Experimental validation of this prediction lies in the observations made in unhardened carbon steels which represent the class of materials exhibiting this behaviour. The steels used in this study are AISI 1020 steel, AISI 1045 steel and AISI 1080 steel. The hardness in the unhardened condition increases with increasing carbon content. AISI 1020 steel

formed continuous chips at a cutting speed of 300 m/min, Fig. 5.5. AISI 1045 steel formed continuous chips at a cutting speed of 350 m/min., whereas AISI 1080 steel exhibited features of partial chip segmentation at the same speed due to its high carbon content, see Fig.4.7.

CHAPTER 6

TECHNOLOGICAL IMPLICATIONS

The present work focused on the behaviour of workpiece material and its influence on chip morphology, tool wear and surface finish in high speed machining of a range of iron alloys having different microstructures, see Table 5.1. The chip morphology is found to be influenced by the microstructure of the workpiece material. This chapter presents a summary of the findings and their technological implications.

6.1 The Role of Geometrical Softening in Chip Segmentation and Tool Wear

When the cutting speed is increased during machining of ductile iron the chips produced change from continuous at moderate cutting speeds in the range of 100-200 m/min to fully segmented chips at a cutting speed of 350 m/min. Chip segmentation in ductile iron occurs due to shear localisation in the primary shear zone caused by geometrical softening in the presence of a large volume fraction of second phase (graphite) particles in the ferritic matrix. Even though chip segmentation occurs in the primary shear zone the tribology of seizure controls the tool-chip interface causing chemical crater wear. The maximum depth of the crater coincides with the phase transformation temperature. Therefore chemical wear is phase transformation coupled. The implication of chemical wear is that a high temperature rise occurs at the tool-chip interface.

The crater is located close to the cutting edge of the tool from the start of the cutting process in machining of ductile iron. The effect of changing chip morphology from continuous to fully

segmented by increasing the cutting speed is to move the location of crater wear closer to the cutting edge of the tool. The interaction of the primary shear zone with the cutting edge of the tool causes damage to the cutting edge of the tool. Damage of the cutting edge of the tool impairs the surface finish. Thus in materials that are highly susceptible to chip segmentation, the problem of high speed machining is to protect the cutting edge of the tool at high cutting speeds. By comparison, in an AISI 1020 steel with a matrix similar to that of ductile iron but without inclusions, the chip morphology remains continuous over a wide range of high cutting speeds. The crater is located at a distance from the cutting edge of the tool. This helps to extend the life of the cutting edge. Thus it is not the amount of wear but the location of wear with respect to the cutting edge that is important in high speed machining.

It has been demonstrated in this work, using hafnium nitrite coating, that chemical wear in machining of ductile iron can be suppressed by selection of a tool material or coating with the least dissolution potential in the workpiece. In order to protect the cutting edge of the tool, it becomes imperative to prevent the tribology of seizure from occurring at the tool-chip interface. In-situ lubrication by inclusion engineering of the workpiece with glassy phase inclusions is a feasible method of preventing the tribology of seizure at the tool-chip interface, and hence suppressing chemical crater wear.

6.2 The Role of Thermal Softening in Chip Segmentation and Tool Wear

Hardened iron-nickel-carbon alloys have been found to exhibit chip segmentation due to shear localisation in the primary shear zone caused by thermal softening. Phase transformation of the alloys has been found to be the cause for shear localisation. In the absence of phase transformation (i.e., when the temperature rise does not reach the phase transformation temperature) shear localisation is caused by tempering of martensite. The effect of chip segmentation due to thermal softening is to

cause a high temperature rise in the primary shear zone which subjects the cutting edge to a high temperature causing chemical wear of the cutting edge. This direct interaction of the primary shear zone with the cutting edge causes damage to the cutting edge terminating tool life. However, as the feed is reduced, the chip morphology changes over to continuous type, as demonstrated in this research. High speed machining of martensitic structure at low feed is shown to have the potential to localise the crater nearest to the cutting edge of the tool and lead to loss of cutting edge. In-situ lubrication through inclusion engineering of the workpiece with glassy phase inclusions is a feasible method for preventing the tribology of seizure at the tool-chip interface, and hence suppressing chemical crater wear.

6.3 The Role of Strain Rate Hardening in Chip Segmentation and Tool Wear

In the absence of geometrical or thermal softening chip segmentation is delayed to high cutting speeds where it is caused by strain rate hardening followed with thermal softening. The steels used in this study are AISI 1020 steel, AISI 1045 steel and AISI 1080 steel. Due to increase in the pearlite content, the hardness of the unhardened steels increases with increasing carbon content. AISI 1020 steel formed continuous chips at a cutting speed of 300 m/min. AISI 1045 steel formed continuous chips at a cutting speed of 350 m/min., whereas AISI 1080 steel exhibited features of partial chip segmentation at the same speed due to its high pearlite content. The chip morphology remains continuous over a wide range of cutting speeds which renders coating of the tool effective in suppressing crater wear. Low feed is used to obtain good surface finish. High strain rate characteristic of high speed machining increases the temperature rise in the chip. Since the contact length at the tool-chip interface is proportional to feed, a low feed coupled with high strain rate characteristic of high speed machining localises the crater closest to the cutting edge of the tool. Protection of the cutting edge of the tool requires prevention of the tribology of seizure from occurring at the tool-chip

interface. In-situ lubrication at the tool-chip interface by glassy inclusions engineered in the steel is a feasible method for preventing tribology of seizure and hence crater wear.

6.4 Methods of Improving Tool Life

Tool life at high cutting speeds can be extended by controlling chemical wear. Chemical wear can be suppressed by selection of a tool material or coating with the least dissolution potential in the workpiece and by controlling the tribology of the tool-chip interface to reduce seizure. The protection of the cutting edge of the tool is a requirement when chip segmentation occurs.

6.4.1 Reduction of Dissolution Wear by Coating of the Tool

The local equilibrium concentration of solute, C_0 at the typical tool-chip interface temperature and the square root of diffusion coefficient of solute in the matrix are identified as critical parameters for diffusion wear control. Enhanced diffusion coefficient, caused by dislocations generated from phase transformation, operates at the tool-chip interface under conditions of thermoplastic shear triggered by seizure and high strain rate deformation of the chip material. The choice of a tool material with the least dissolution potential in the workpiece and the selection of a coating that acts as a diffusion barrier are identified as key parameters for the successful design of a tool to minimise crater wear in the high speed machining of steel and cast irons. The coating has been shown to act in a number of ways to reduce dissolution wear. The major effect is by direct reduction of the dissolution potential. Thus a tool with the least solubility product is selected (Table 5.5). Coating could also influence the tribology of the tool-chip interface to suppress seizure and hence reduce chemical wear by preventing the occurrence of seizure at the tool-chip interface. However, at higher cutting speeds coatings are susceptible to failure by delamination and become ineffective in protecting the tool from wear. This leaves us with the option of influencing the tribology through lubrication of the tool-chip

interface.

6.4.2 Change of the Tribology of the Tool-Chip Interface by Lubrication

At moderate and high cutting speeds the tribology of seizure at the tool-chip interface controls the tool life leading to dissolution of the tool into the workpiece involving a diffusion mechanism. An effective strategy to minimise the chemical crater wear is to engineer glassy inclusions in the workpiece that form a viscous layer of adequate thickness such that friction is minimised by accommodating the shear within the viscous layer. This concept has been demonstrated in free cutting steels to eliminate toxic lead addition [176]. The design of the glassy inclusions for in-situ lubrication is based on the temperature and pressure occurring at the tool-chip interface [179, 191].

6.4.3 Protection of the Cutting Edge

When chip segmentation takes place at the primary shear zone with a high temperature rise, the tool-tip is subjected to a high temperature which causes chemical wear of the cutting edge. The loss of the cutting edge of the tool leads to loss of surface finish. Further, the wear extends from the cutting edge to the flank face. The flank wear is chemical in origin and often times mistaken for physical wear. The development of high temperature in the primary shear zone can be decreased by inclusion engineering. In this case manganese sulphide (MnS) inclusions can be used to lower the critical accumulated damage and glassy oxide inclusions for in-situ lubrication of the tool-chip interface.

CHAPTER 7

CONCLUSIONS

Concept of Seizure at the Tool-Chip Interface

1) The concept of seizure in metal cutting is based on atomic contact at the tool-chip interface. A physical model for seizure is proposed that predicts the critical cutting speed for the onset of seizure from force measurement at which the normal stress exceeds the yield strength of asperities such that the true area of contact approaches the apparent area of contact.

The Consequences of Seizure at the Tool-Chip Interface

2) The tribology of seizure causes thermoplastic shear localisation and consequent temperature rise at the tool-chip interface. Dissolution wear of the tool into the chip takes place by a diffusion mechanism causing chemical crater wear of the tool.

3) The chemical crater wear dominates at high cutting speeds. Tool crater wear is shown to be phase transformation coupled. The maximum depth of the crater coincides with the phase transformation temperature of the workpiece material. Dislocations generated by deformation concomitant with phase transformation provide high diffusivity paths that contribute to enhanced diffusion wear.

4) Chemical crater wear can be suppressed by preventing the tribology of seizure from occurring by in-situ lubrication of the tool-chip interface which can be achieved by inclusion engineering of the workpiece. Alternatively, the diffusion wear can be minimised by coating the tool with a compound which has the least solubility in the work piece.

The Influence of Shear Localisation on Chip Morphology, Tool Wear and Surface Finish.

5) Chip segmentation is caused by shear localisation in the primary shear zone. The shear localisation is caused by (i) geometrical softening due to second phase particles, (ii) thermal softening of the workpiece due to phase transformation or recrystallisation, at moderate and low cutting speeds.

6) Thermal softening due to phase transformation is shown to cause shear localisation in the primary shear zone.

7) The effect of temperature rise in the primary shear band is to cause dissolution wear at the cutting edge of the tool. The loss of cutting edge in turn impairs surface finish.

8) The influence of metal cutting variables on shear localisation is analysed in terms of temperature and pressure effects on dynamic behaviour of workpiece material.

CHAPTER 8

RECOMMENDATIONS FOR FUTURE WORK

The following are recommendations for further work arising from the present research:

1) It is recommended that a study be conducted to investigate the behaviour of hardened alloys containing inclusions which were not included in the present study.

2) The sequence of events involved in shear localisation was not fully clarified. It is therefore recommended that further TEM work be conducted in order to obtain results free from uncertainties so as to clarify the structures of the shear bands and the mechanism of shear localisation.

3) It is recommended that inclusion engineering be carried out to test the proposed role of inclusions in minimising tool wear by suppressing seizure at the tool-chip interface.

4) It is recommended that CBN tools, currently used in hard turning, be tested with the Fe-Ni-C alloys to find the effect of microstructural changes of the workpiece on the wear of these tools.

REFERENCES

1. C. Zener and J.H. Hollomon, J. Appl. Phys. 15, 1944, p.22.
2. M.A.Meyers, Dynamic Behaviour of Materials, John Wiley & Sons, New York, 1995.
3. S.S.Ingle, Ph.D. Thesis, McMaster University, Hamilton, Ontario,1993
4. D.Dawson, History of Tribology, Longman , 1979.
5. F.P Bowden and D.Tabor, Friction and Lubrication of Solids, Clarendon Press, Oxford, 1964, Part 1 pp.90-121, 1950; Part 2, pp.52-86.
6. Nam. P. Suh, Tribophysics, Prentice - Hall inc., New Jersey, 1986.
7. M. C Shaw & E.F Macks, Analysis and Lubrication of Bearings, McGraw-Hill, New York, 1949, pp.457-461.
8. Rabinowicz, E., Friction and Wear of Materials, Wiley, New York, 1965, pp.51-108.
9. B. Bhushan, J.N. Israelachvili and U. Landman, Nature vol. 374, 1995, pp.607-616.
10. J.Krim, Scientific American, Oct., 1996 , pp.74-80.
11. U. Landman, W.D. Luedtke, N. Burnham and R.J. Colton, Science, vol. 248, 1990, p454.
12. Q. Guo, J.D.J. Ross, and H.M. Pollock, New Materials Approaches to Tribology: Theory and Application, L.E.Pope, L.L. Fehrenbacher, and W.O. Winer, Ed, Materials ResearchSociety, 1989, pp.51-66.
13. D.H Buckley, Tribology in the 80's vol 1, NASA Conf. Publ. 2300, National Aeronautics and Space Administration, 1983, pp.19-44.
14. D.H Buckley, Surface Effects in Adhesion, Friction, Wear and Lubrication, Elsevier, 1981.

15. C.S Yust, C.J McHargue and L.A Harris, Mater. Sci. Eng. vol. A105/106, 1988, p489.

16. E.Rabinowicz, ASLE Trans., vol 14, 1971, pp.198-205.

17. D.A Rigney, Ann Rev. Mater. Sci. Vol.18, 1988, p.141-163.

18. J.A Greenwood and J.B.P Willianson, Proc. R.Soc (London) A. Vol. 195, 1966, p.300.

19. K.L. Johnson, Contact Mechanics, Cambridge University Press, 1985.

20. D.A Rigney and J.P Hirth,Wear, vol. 53, 1979, pp.345-370.

21. S.T. Oktay and N.P. Suh, J. Tribology (Trans ASME), vol. 114, 1992, pp.379-393.

22. F.F. Ling and M.B. Peterson, Simple Model of Metal Working Friction Under Extreme Pressure, Approaches to Modelling of Friction and Wear, F.F.Ling and C.T.H. Pan, Ed., Springer-Verlag, 1987, pp.83-88.

23. E.M. Kopalinsky, X. Li, and P.L.B Oxely, Tribological Aspects in Manufacturing, M.H. Attia and R. Komanduri, Ed., ASME, 1991, pp.217-235.

24. E.G Thomsen, CIRP Ann.,17, 1969, p.187.

25. I. Ham, K.Hitomi and G.L Thuering, Trans.ASME, J.Eng.Ind., B83, 1961, p.142.

26. K.Hitomi and G.L Thuering, Trans.ASME, J.Eng.Ind., B84, 1962, p.282.

27. K.J.Trigger, L.B.Zylstra and B.T.Chao,Trans.ASME.74, 1952, p.1017.

28. J.A.Bailey, Wear, 31, 1975, pp.243-275.

29. N.N.Zorev, Proc. Conf. on Technology of Engineering Manufacture, Instn. Mech. Engrs. 1958, p.255.

30. M.C. Shaw, Proc. Conf. Machinability, ed. Iron and Steel Inst., Inst. Metals, Inst. Mech. Eng., and Inst. Prod. Eng., 1965, pp.1-9.

31. E.M. Trent, Conf. Machinability, ed. Iron and Steel Inst., Inst. Metals, Inst. Mech. Eng., and Inst. Prod. Eng., 1965, pp.11-18.

32. K. Nakajima, K.Ohgo, and T. Awano, Wear, 11, 1968, p.369.

33. P.W. Wallace and G.Boothroyd, J.Mech. Eng. Sci., 6, 1964, p.74.

34 H. Takayama and E. Usui, Trans. ASME, 80, 1958, p.1089.

35. B.T. Chao and K.J. Trigger, Trans. ASME, 81, 1959, p.139.

36. S. Kato, K. Yamaguchi and M. Yamada, Trans.ASME, J.Eng.Ind., 94, 1972, p.683.

37. N.N. Zorev, International Research in Production Engineering, Inst. Prod. Eng. Conf. ASME, Pittsburgh, U.S.A., 1963, p.42.

38. T.H.C.Childs, D.Richings and A.B. Wilcox, Int.J.Mech. Sci., 14, 1972, p.359

39. B.K. Mullick and A.J. Bhattacharya, J. Inst. Eng. (India), 46, 1966, p.183.

40. K. Iwata, J.Aihara and K.Okushima, Ann. CIRP, 24, 1971, p.323.

41. N.N. Zorev, Metal Cutting Mechanics, Pergamon Press, Oxford, 1966.

42. D.M. Eggleston, R.Herzog and E.G. Thomsen, Trans.ASME, J.Eng.Ind., B81, 1959 p.263.

43. J.E. Williams, E. Smart and D.Milner, Metallurgia, 81, 1970, p.3.

44. T.H.C.Childs, Proc. Inst. Mech. Engrs., 186, 1972, p.717.

45. E.D.Doyle and D.Tabor, Proc.R.Soc.London, Ser.A,173, 1973, p.336.

46. E.M.Trent, Metal Cutting, 3rd edition, Butterworth-Heinmann, London, 1984.

47. D.Tabor, Proc. Royal Soc. London Series A vol. 257, 1957, pp.378-93.

48. E.M.Trent, J.Iron and Steel Institute, 1963, pp.847-855.

49. P.K.Wright and E.M.Trent, J.Iron and Steel Inst., 1973, p.364.

50. P.K.Wright, J.G.Horne and D.Tabor, Wear, 54, 1979, pp. 371-90.

51. A.Nadai, Plasticity, McGraw-Hill, New York, 1931.

52. E.M Trent, Wear, 128, 1988, pp.29-81.

53. E.M.Kopalinsky and P.L.B.Oxley,Proc. 3rd Conf. Mech. Prop. High strain rates, Oxford, 1984, pp.389-396.

54. W.N. Findley, J.Eng. Ind., 1963, pp.49-67.

55. N.H.Cook,Iain Finnie andM.C.Shaw, Trans.ASME,76, 1954, pp.153-162.

56. A.Moufki, A.Morinari and D.Dudzinski, 1st French and German Conference on High Speed Machining, 1997, pp.8-28.

57. R.Komanduri and B.F.Von Turkovich, Wear vol. 69, 1981, pp.179-188.

58. J.C.Lemaire and W.A.Backofen, Metall.Trans.3, 1972, pp.477-482.

59. H.Ernst, "Physics of Metal Cutting",Machining of Metals, ASM, 1938, p.24.

60. Merchant, M.E., J.Applied Physics, Vol.16, No.5 part I p.267, part II p.318, 1945.

61. Lee,E.H.,Shaffer,B.W.,J. Applied Mechanics, Vol.18, 1951, p.405.

62. G.W.Rowe, P.T.Spick, Trans. ASME J.Eng.Industry, 1967, p.530.

63. W.F.Hastings, P.Matthew and P.L.B.Oxley, Proc.R.Soc.Lond.A 371, 1980, p.569.

64. P.L.B. Oxley, Mechanics of Machining, Ellis Horwood, Chichester, U.K., 1980.

65. J.S.Strenkowski and J.T.Caroll, J.Eng.Ind., 107, 1985, pp.349-354.

66. J.S.Strenkowski and J.K.Moon, J.Eng.Ind., 112, 1990, pp.313-318.

67. G.S. Sekhon and J.L. Chenot, Engng. Comput., 10, 1993, pp.31-48.

68. T. Marusich and M. Ortiz, Int. J. Numer. Meth. Engng., 38, 1995, pp.3675-3694.

69. R.Komanduri,T.Schroeder,J.Hazra,B.F.Von Turkovich and D.G.Flom, Trans. ASME J.Eng.Ind. vol.104, 1982, pp.121-131.

70. R.Komanduri and R.H.Brown, Trans ASME J.Eng.Ind. vol. 103, 1982, pp. 33-51.

71. K.F.Sullivan, P.K.Wright and P.D.Smith, Metals Technol., 1978, pp.181-189.

72. M.C.Shaw, Annals of the CIRP vol.42/1, 1993, pp.29-33.

73. R.F.Recht, Trans. ASME, J.Applied Mechanics, 1964, p.189.

74. R.Komanduri and T.Schroeder, Trans. ASME J.Eng.Ind. vol.108, 1986, pp.93-100.

75. E.G. Leowen and M.C.Shaw, Trans of the ASME, 1954, pp.217-231.

76. C.W.McGregor andJ.C.Fisher,Trans ASME J.Appl.Mech.13, 1946, A-11.

77. Y. Bai and B. Dodd, Adiabatic Shear Localization: Occurrence, Theories and Applications, Pergamon Press, 1992.

78. J.D. Campell and W.G. Ferguson. Phil. Mag. 21, 1970, p63.

79. R.W. Klopp, R.J. Cliflon, and T.G. Shawki, Mech. Mat, 4, 1985, p375.

80. G.R. Johnson and W.H. Cook, in Proc 7th Int. Sym. Ballistics, Am. Def. Prep. Org. (ADPA). Netherlands, 1983, p541.

81. G.R. Johnson, J.M. Hoegfeldt, U.S. Lindholm, and A. Nagy. ASME J. Eng. Mater. Tech. Vol.105, 1983), p.42.

82. U.R. Andrade, M.A.Meyers and A.H.Chokshi, Scripta Metall. et Mater., Vol.30, 1994, p.933.

83. J.D. Campell, Dynamic plasticity, Oxford University, Press, New York

84 U.S. Lindholon and L.M. Yeaklay, Exp. Mech. 7 1967, p.1.

85 J.D. Campell and J. Harding, in Response of Metals to High Velocity Deformation, P.G. Shewmon and V.F. Zachary (eds) Interscience, New York, 1961, p.51.

86. U.F. Kocks, A.S. Argon and M.F. Ashby, Progr. Metals Sci, 19, 1975, p.1.

87. K.G. Hoge and A.K. Mukherjee, J. Mater. Sci, 12, 1977, p.1666.

88. P.S. Follansbee and F.U.Kocks, Acta Met.,36, 1988, p.81.

89. F.J.Zerilli and R.W.Armstrong, J.Appl. Phys.,61, 1987, p.1816.

90. J.R.Klepaczko, J.de Physique,9, 1988, p.49.

91. P.S.Follansbee, in Metallurgical Applications of Shock-wave and High-strain Rate Phenomena, eds. L.E.Murr, K.P.Staudhammer, and M.A. Mayers, New York, 1986, p.451.

92. M.A.Meyers and K.K.Chawla, Mechanical Metallurgy, Principles and Applications, Prentice-Hall, Englewood Cliffs, NJ., 1984, p.304.

93. J.J.Gilman, Micromechanics of Flow in Solids, McGraw-Hill, New York, 1969, p.195.

94. P.P.Gillis, J.J.Gilman, and J.W.Taylor, Phil. Mag.,20, 1969, p.279.

95. V.R.Parameswaran and J.Weertman, Met. Trans.,2, 1971, p.1233.

96. J.D.Eshelby, Phys.Rev., 90, 1953, p.248.

97. J.Weertman and R.Weertman, Elementary Dislocation Theory, McMillan, New York, 1964.

98. J.D.Eshelby, Proc.Phys. Soc. (London) B69, 1956, p.1013.

99. M.R.Staker, Acta Metallurgica Vol.29, 1981, p.683.

100. Rosenfeld, A.R. and Hann, G. T. Trans. ASM 59, 1966, pp.962-980.

101. M.E. Backman and S.A. Finnegan, in Metallurgical Effects of High Strain Rates, (ed. R.W. Ronda et at) plenum press, New York, 1973, p.531.

102. S.P.Timothy, Acta Metall. vol.35,No.2, 1987, pp.301-306.

103. J.M.Yellup and R.L.Woodward, Res Mechanica, 1, 1980, pp.41-57.

104. S.P. Timothy and I.M. Hutchings, in Proc. 3rd Int. Conf. in Mechanical properties of materials at High strain rates (ed. J. Harding) Inst. of Physics, Bristol, 1984, p. 397.

105. P.W. Leech, Metall. Trans. 16A, 1985, p.1900.

106. Dodd & Bai, Mat. Sci. Tech. 1, 1985, pp.38-40.

107. Bai, Y. cheng, C. and Yu S., Acta Mechanica Sinica, 2, 1986, pp.1-7.

108. H.C. Rogers and C.B. Shastry, in Shock Waves and High Strain Rate Phenomena in Metals, ed. M.A. Meyers and L.E. Murr Plenum Press, New York., 1981, p.285.

109. R. E. Winter and J.E. Field, Proc. Roy. Soc.A.343 London, 1975, pp.399-413.

110. W.G. Johnston and J.J. Gilman, J. Appl. phys 30, 1954, p.129.

111. J.O.Williams,J.M.Thomas,Y.P.Savintser and V.V.Boldyrev, J.Chem.Soc.A,11, 1971, p.1757.

112. R.S.Culver, In Metallurgical Effects at High Strain Rates, ed. R.W. Rohde, B.M.Butcher,J.R.Holland & C.H.Karnes,Plenum Press New York, 1973, pp.519-530.

113. Y.L.Bai, In Shock Waves and High-Strain Rate Phenomena in Metals, Ed. Meyers,M.A. and Murr L.A., Plenum Press, London, 1981, pp.277-283.

114. Lindhom S.and Johnson, G.R., in Material Behaviour Under High Stress and Ultra-high Loading Rates, (ed Mescal, J. and Weiss, V.) Plenum Press, New York, 1983, pp 61-79.

115. T.W. Wright and J.W. Walter, J.Mech. Phys.Solids, Vol.35, 1987, p.701.

116. J.W.Rudnicki and J.R.Rice, J.Mech.Phys.Solids,Vol.23, 1975, p.371.

117. J.R.Rice, Theoretical and Applied Mechanics, Proc. Of the 14th IUTAM Congress, Delft , (ed. W.T.Koiter), North Holland, New York, 30 Aug - 4 Sept, 1976, p.207.

118. Clifton,R.J.,Duffy,J.,Hartley K.A.,Shawki,T.G. Scripta Metall.18, 1984, pp.443-448.

119. Bai, Y. J. Mech. Phys. solids, 30, 1982, pp.195-207.

120. L.Anand, K.H.Kim, and T.G.Shawki, J. Mech. Phys. Solids 35, 1987, pp.407-429.

121. C.S. Coffey, in Mechanical Properties of Materials at High Strain Rates, (Hardening,J.) Inst. of Phys. conf. series 42, Bristol, 1984, pp.519-574.

122. Drew, D.A. and Flaherty, J.E. in Phase Transformation and Material Instabilities in Solids, (e.d. Gartin, M.E.) Academic Press, Orlando, USA , 1984, pp.37-60.

123. J.H.Andrews,H.Lee, L.Bourne and D.V.Wilson, J.I.S.I. Vol.165, 1950, p.369.

124. H.O.McIntire and G.K. Manning, Met. Prog., 1970, p.94.

125. S.A.Manion and T.A.C.Stock, Int.J.Fract.Mech. Vol.6, 1969, p.106.

126. R.C.Glenn and W.C.Leslie, Met.Trans.Vol.2, 1971, p.2945.

127. P.A.Thornton and F.A.Heiser, Met.Trans.Vol.2, 1971, p.1496.

128. R.L.Woodward and R.L.Aghan, Met. Forum Vol.1, 1978, p.180,.

129. Y.Matsumoto, M.M.Barash and C.R.Liu, Trans ASME J.Eng. & Ind. Vol.108, 1986, p.169.

130. G.W.Greenwood and R.H.Johnson, Proc. Royal Soc. London A Vol.183, 1965, pp.403-422.

131. R.W.Rohde and R.A.Graham, Trans. Metall.Soc. AIME, Vol. 245, 1969,pp.2441-2445.

132. F.A.McClintock, J.Applied Mechanics, 1968, p.363.

133. J.R.Rice and D.M.Tracey, J.Mech.Phys.Solids, Vol.17, 1969, pp.201-217.

134. R.Sowerby and N.Chandrasekaran, Mat.Sci.and Engg.,79, 1986, pp.27-36.

135. F.A.McClintock,S.M.Kaplan and C.A.Berg,Int.J.Fract.Mech.,Vol.4, 1966, p.614.

136. G.R.Johnson,J.M.Hoegfeldt,U.S.Lindholm,A.Nagy, J.Eng.Mat.Tech.105, 1983, p.42.

137. J.H.Giovanola, Mechanics of Materials, Vol.7, 1988, pp.59-71, and pp.73-87.

138. B.Dodd and A.G.Atkins, Acta Metall.Vol.31, 1983, pp.9-15.

139. Y.B.Xu,Z.G.Wang,X.L.Hung,D.Xing and Y.L.Bai, Mat.Sci.Engg. A114 , 1989, p.81.

140. J.J Manson, A.J.Rosakis, and G.Ravichandran, Mech. of Matls.,17, 1994, p.135.

141. Y.Naerheim and E.M.Trent, Metals Technol., 4(12), 1977, p.548.

142. Kramer,B.M. and Suh,N.P., J.Eng.Ind., vol.102, 1980, p.303.

143. K.J.Trigger, Trans. ASME, Vol.70, 1948, p.91.

144. K.J.Kusters, Dissertation, T.H.Aachen, 1956.

145. G. Boothroyd, Proc. Inst Mech Engrs Vol. 177, 1963, p.789.

146. P.K.Wright and E.M.Trent, J.Iron and Steel Inst., 1973, p.364.

147 P.A.Dearnley, Met. Technol.,10 (6), pp.205-214, (1983).

148. B.T.Chao, J.Trigger, Trans of the ASME, 1955, pp.1107-1121.

149. A.O.Tay, M.G.Stevenson, G.D.Vahl, and P.L.B.Oxley, Int. J. Mech. Tool Des Res vol.16, 1976, pp.335-349.

150. P.A. Dearnley, Wear, Vol. 101, 1985, pp.33-68.

151. S.V.Subramanian, S.S.Ingle and D.A.R.Kay, Surf. and Coatings Technol. 61, 1993, p.293.

152. A.Bhattacharyya, Metal Cutting: Theory and Practice, Central Book Publishers, Culcutta, 1984.

153. D.Turnbull and R.E.Hoffman,Acta Met.Vol.2, 1954, pp.419-426.

154. P.G. Shewmon, Diffusion in Solids, 2nd Edition, TMS Publication, 1989.

155. Properties and Uses of Kenaametal Tools: Kennametal Catalogue, 1987.

156. L.Kaufman and M.Cohen, Trans. AIME, J. of Metals, 1953, pp.1393-1401.

157. R.J.Russell and P.G.Winchell, Metall. Trans. Vol.3, 1972, pp.2403-2409 .

158. M.M.Rao, R.J.Russell, and P.G Winchell, Trans. Metall. Soc. AIME, Vol.239, 1967, p .634.

159. L.Kaufman, A. Leyenaar and J.S. Harvey, Progress in High Pressure Research: Proc. Int. Conf.; Bolton Landing, Lake George, New York, Ed. F.P.Bundy, W.R. Hibbard,Jr and H.M. Strong, John Wiley & Sons. N.Y., 1960 , pp.90-108.

160. R.W.Rohde and R.A.Graham, Trans. Metall.Soc. AIME, Vol. 245, 1969, pp.2441-2445.

161. C.T.Lai, M.Eng. Thesis, McMaster University, Hamilton, Ontario, 1986.

162. N.D.Patel and M.A.Elbestawi, Patent pending.

163. D.J.Douglas,R.S.Houk, Prog. Anal. At.Spectrosco., vol. 8, 1985, p.1-18.

164. R.S.Houk and J.J.Thompson, Mass Spectroscopy Reviews, Vol.7, 1988, pp.425-461 .

165. Alan L. Gray, Spectrochemica Acta, Vol.40B Nos 10-12, 1985, pp.1525-1537 .

166. A.R.Date and A.L.Gray, Applications of Inductively Coupled Plasma Mass Spectrometry, Blackie Glasgrow and London, 1989.

167. K.E.Javis, A.L.Gray, and J.G. Williams, Plasma Source Mass Spectrometry: The Proc. of the Third Surrey Conf.on Plasma Source Mass Spectrometry, University of Surrey, 16th-19th July, 1989

168. P.A.W. van der Heide, S.Ramamuthy and N.S. McIntyre, Surf. Interf. Anal., vol. 23, 1995, pp.163-170.

169. B.D.Cullity, Elements of X-ray Diffraction, Reading Mass, Addison Wesley Pub. Co., 1956.

170. W.F.Simmons and H.C.Cross, Elevated Temperature Properties of Carbon Steels, ASTM Special Technical Publication No.180, ASTM, Philadelphia,Pa., 1955.

171. A.H Cottrell, Phil. Mag. 44, 1953, p.829-832.

172. B.J.Brindley and J.T. Barnby, Acta Metall., Vol.14, 1966, pp.1765-1779 .

173. Thermophysical Properties of High Temperature Solid Materials Volume 3: Ferrous Alloys, Purdue University, Thermophysaical properties Research center,ed.Y.S. Touloukian, McMillan Co., New York, 1967.

174. L.R. Ingersoll and others, Physical Rev. Vol. 16(2), 1920, pp.126-132 .

175. J.S.McFarlane and D.Tabor, Proc. Royal Soc. London Series A Vol.202, 1950, pp.224-253.

176. K.Ramanujachar and S.V.Subramanian, Wear 197, 1996, pp.45-56.

177. J. Askill, Tracer Diffusion Data for Metals, Alloys, and Simple Oxides, Plenum, New York, 1970.

178. H.Ohtani,T.Tanaka,M.Hasebe and T.Nishizawa, Calphad Vo.12, 1988, pp.225-246.

179. S.V.Subramanian and D.A.R.Kay, Proc. 38th MWSP Conf., ISS, Vol.XXXIV, 1997, p.125.

180. Didier Teirlinck, Influence of the Stress State on Various Fracture Modes, Ph.D. Thesis, McMaster University, 1983.

181. B.Dodd and A.G.Atkins Acta Metall. Vol.31, 1983, pp.9-15.

182. G.I.Taylor and H.Quinney, Proc. Royal Soc. 143, 1934, p.307.

183. S.V.Subramanian, Unpublished work.

184. S.V.subramanian, D.A.R.Kay and Jiang Junpu, Inclusions and their Influence on Material Behaviour,Proc. Of a Symposium, World Mater. Cong., Chicago, Illinois, Sep. 1988, p.73.

185. B. Derby, Acta Metall.,Vol.39, No.5, 1991, pp.955-962.

186. M.A.Meyers, G.Subhash, K.B.Kad and L.Prasad, Mechanics of Materials Vol.17, 1994, pp.175-193.

187. C.A. Apple and G.Krauss, Acta Metall., Vol. 20, 1972, pp.849-856.

188. G.Krauss,Jr., Acta Metall. Vol.11, 1963, pp.499-509.

189. H.S.Carslaw and J.C. Jaeger, Conduction of Heat in Solids, Oxford, Clarendon Press, 1959.

190. M.G.Stevenson and P.L.B.Oxley, Proc. Instn. Mech.Engrs., 1970-71, pp.741-754.

191. H.O.Gekonde and S.V.Subramanian, Tool Wear and Surface Finish in High Speed Machining of Steel, 39th M.W.S.P. conf. Proceedings, Proc. Of Mechanical Working and Steel Proceeding Conf., Indianapolis, October 9-12, 1997.

192. J.J Jonas, Thermec'97, Int. Conf. Thermomechanical Processing of Steel and Other Materials, Wollongong, Australia, TMS Publication, USA, 1997, pp.31-45.

193. C.M. Sellars, Hot Working and Forming Processes, ed., C.M. Sellars and J.G. Davies, Metals Soc., London, 1980, pp.3-15.

194. P.D. Hodgson, Thermec'97, Int. Conf. Thermomechanical Processing of Steel and Other Materials, Wollongong, Australia, TMS Publication, USA, 1997, pp.121-131.

APPENDIX A

ESTIMATION OF (A_S) TEMPERATURE FOR Fe-Ni-C ALLOYS

Following the development of Kaufman and Cohen [156] a temperature T_o has been defined at which the free energy change during the reversal reaction of martensite to austenite is zero, i.e. when

$$F^{\acute{\alpha}}_{Fe\text{-}Ni\text{-}C} = F^{\gamma}_{Fe\text{-}Ni\text{-}C} \text{ or } \Delta F^{\acute{\alpha}\rightarrow\gamma}_{Fe\text{-}Ni\text{-}C} = 0 \qquad (A1)$$

In the Fe-Ni system $\acute{\alpha}$ and α are both b.c.c. [159] therefore,

$F^{\acute{\alpha}}_{Fe\text{-}Ni} = F^{\alpha}_{Fe\text{-}Ni}$ hence T_o occurs at $\Delta F^{\acute{\alpha}\rightarrow\gamma}_{Fe\text{-}Ni\text{-}C} = 0$

In the Fe-Ni-C system a correction must be made to $F^{\acute{\alpha}}_{Fe\text{-}Ni\text{-}C}$ to account for tetragonality of the martensite.

The molar free energy for b.c.c. and f.c.c. Fe-Ni-C systems have been written [158] as:

$$F^{\alpha}_{Fe\text{-}Ni\text{-}C} = F^{\alpha}_{Fe\text{-}Ni} - RT\,x_c + x_c(F^{s}_{c} + RT \ln x_c + 15{,}000 - 3.75RT) \qquad (A2)$$

$$F^{\gamma}_{Fe\text{-}Ni\text{-}C} = F^{\gamma}_{Fe\text{-}Ni} - RTx_c(1+3.74x_c) + x_c(F^{s}_{c}+RT\ln x_c+7.48RTx_c+3530RTx_{Ni}+1.26RTx_{Ni}) \qquad (A3)$$

Where $F^{\alpha}_{Fe\text{-}Ni}$ and $F^{\gamma}_{Fe\text{-}Ni}$ are the free energy of mixing of Fe and Ni atoms in the α and γ phases at zero carbon content, i.e $x_c = 0$ and (F^{s}_{c} is the partial molar free energy of carbon in the standard state selected that $a_c/x_c \rightarrow 1$ as $x_c \rightarrow 0$ in f.c.c. alloys. For tetragonal martensite this equation is modified by addition of x_c RT ln 3 to the right hand side.

The change in free energy accompanying the phase change for tetragonal martensite to austenite at fixed composition can be calculated from the difference in equation A3 and A2 (modified by addition of x_c RT ln 3).

In order to calculate T_o, $F^{\acute{\alpha}}_{Fe\text{-}Ni}$ and $F^{\gamma}_{Fe\text{-}Ni}$ and $\Delta F^{\acute{\alpha}\rightarrow\gamma}_{Fe\text{-}Ni}$ must be expressed as a function of temperature and x_{Ni}.

From the work of Kaufman, Leyenaar and Harvey [159] and Kaufman and Cohen [156],

$$\Delta F^{\alpha\rightarrow\gamma}_{(x_{Ni},T)} = (1-x_{Ni})(1202 - 2.63\times10^{-3}T^2 + 1.54\times10^{-6}T^3)$$
$$+ x_{Ni}(-3700 + 7.09\times10^{-4}T^2 + 3.91\times10^{-7}T^3)$$
$$+ x_{Ni}(1-x_{Ni})(3600 + 0.58T(1 - \ln T) \qquad (A4)$$

At T_o, $F^{\alpha}_{Fe\text{-}Ni\text{-}C} = F^{\gamma}_{Fe\text{-}Ni\text{-}C}$ or $\Delta F^{\alpha\rightarrow\gamma}_{Fe\text{-}Ni\text{-}C} = 0$, therefore from equation A2 and A3,

$$\Delta F^{\alpha\rightarrow\gamma}_{Fe\text{-}Ni} = x_c[3.74RTx_c + 3530Rx_{Ni} + 1.26RTx_{Ni} + 3.65RT - 15{,}000] \qquad (A5)$$

When equations A4 and A5 are equated the values for T_o can be computed by iteration for known pairs of x_c and x_{Ni}.

The ternally formulation assumes that the iron-nickel atom ratio remains unchanged during transformation i.e. negligible nickel partitioning in the Fe-Ni-C system. A numerical iteration was used to calculate values of T_o for the alloys used in this work. It was assumed that the carbon does not affect the A_s-T_o and T_o-M_s range and that T_o lies between the A_s and M_s for each alloy. The A_s and M_s temperatures for the Fe-Ni-C alloys were estimated using the computed T_o values and data for the A_s-T_o and T_o-M_s ranges for Fe-Ni alloys measured by Kaufman and Cohen [156].

APPENDIX B

CALCULATION OF STRESSES BY MERCHANT'S MODEL

In the mechanistic approaches to the analysis of the shearing action during machining Merchant assumed continuous chip formation without a build-up edge with shear occurring in a very narrow lamina which in the idealised limit becomes a plane. From these assumptions Merchant proposed the famous shear angle and force circle through which he developed the following expressions which have been useful for the analytical evaluation of the metal cutting process to-date.

Shear plane angle is given as:

$$\tan\phi = r\cos\alpha/(1 - r\sin\alpha) \qquad (B1)$$

where $r = t_1/t_2$ is the chip thickness ratio; t_1 is the undeformed chip thickness (depth of cut); t_2 is the deformed chip thickness and α is the rake angle.

The shear strain at the primary shear zone is given by:

$$\gamma = \cos\alpha/(\sin\phi\cos(\phi - \alpha)) \qquad (B2)$$

Shear force along primary shear plane is given by:

$$F_s = F_z\cos\phi - F_f\sin\phi \qquad (B3)$$

where F_z = cutting force and F_f = feed force. Consequently, the mean shear stress at the primary shear zone is given by:

$$\tau_s = F_s/A_s = (F_z\cos\phi - F_f\sin\phi)\sin\phi/A_o \qquad (B4)$$

where $A_o = wt_1$ and w is the depth of cut.

The normal force on primary shear plane is given by:

$$F_N = F_z \sin\phi + F_f \cos\phi \qquad (B5)$$

Consequently, the mean normal stress on the primary shear zone is given by:

$$\sigma_N = F_N/A_s = (F_z \sin\phi + F_f \cos\phi)\sin\phi/A_s \qquad (B6)$$

The shear force along tool-chip interface is given by

$$F = F_z \sin\alpha + F_f \cos\alpha \qquad (B7)$$

Consequently, the mean shear stress at the tool-chip interface is given by:

$$\tau_{ssz} = F/A_{ssz} = (F_z \sin\alpha + F_f \cos\alpha)/A_{ssz} \qquad (B8)$$

The normal force at the tool-chip interface is given by:

$$N = F_z \cos\alpha - F_f \sin\alpha \qquad (B9)$$

Consequently, the mean normal stress at the tool-chip interface is given by:

$$\sigma_{ssz} = N/A_{ssz} = (F_z \cos\alpha - F_f \sin\alpha)/A_{ssz} \qquad (B10)$$

The shear velocity in the primary shear zone is given as:

$$V_s = V_c\cos\alpha/\cos(\phi-\alpha) \qquad (B11a)$$

The chip velocity in the secondary shear zone is given as:

$$V_f = V_c\sin\phi/\cos(\phi-\alpha) \qquad (B11b)$$

APPENDIX C

TEMPERATURE RISE DURING MACHINING

This model is based on use of the finite element method to solve the field equation describing the heat transfer processes at the tool-chip interface with the assumption of seizure at the tool-chip interface. The first part of the analysis of the problem involves the partition of the energy generated by plastic deformation at the shear plane between the chip and the workpiece and determination of the average or distribution of the shear plane temperature. The second part involves the partition of the tool-face plastic deformation energy between the chip and tool and determination of the average or distribution of interface temperature along the tool-face or in the chip. The following assumptions are made in the present analytical evaluation of metal temperatures:

(a) That 99% of the strain energy goes into thermal energy and 1% is associated with permanent lattice deformation.

(b) A uniform distribution of shear energy and non-uniform distribution friction energy exists at the primary and secondary shear zones respectively.

(c) There is no redistribution of the thermal energy going into the chip during the short contact time the chip is in contact with the tool (i.e. adiabatic deformation).

The temperature dependence of the properties of the tool and the workpiece was taken into account by introducing an iteration procedure in the finite element analysis. Variable heat source strength and material properties are assumed, and the temperature distribution is computed by solving the steady state two dimensional energy equation. The interface temperature distribution obtained is used to evaluate the variable material properties at the points along the contact length where the temperature is evaluated. The second temperature distribution is again numerically evaluated by the finite element method. The iteration is continued until a self-consistent solution of stress and

temperature distribution are obtained. The model utilises as inputs:

(i) the work-piece material properties which include specific heat, density, thermal conductivity,

(ii) tool material properties which include specific heat, thermal conductivity and density, and

(iii) cutting conditions and measured variables which include rake angle, shear plane angle, cutting speed, feed, depth of cut, forces, contact length, and thickness of the secondary shear zone.

The output from the model is the temperature distribution at the tool-chip interface. The primary shear plane temperature is evaluated from Loewen and Shaw's model [75].

Assuming that there is no accumulation of heat in the secondary shear zone the equation describing the heat transfer processes occurring during orthogonal machining is the steady state two dimensional energy equation:

$$\rho C(u\frac{dT}{dx} + v\frac{dT}{dy}) - (\frac{dq_x}{dx} + \frac{dq_y}{dy}) - Q = 0 \qquad (C1)$$

where $q^T = [q_x, q_y]$ = rate of heat transfer per unit area; Q = rate of heat generation per unit area

u,v = velocity components in the x and y directions; T = variable temperature

In orthogonal cutting the velocity component in the y-direction and the temperature gradient in the x-direction can be neglected so that the field equation reduces to:

$$d/dx(k_x.dT/dx + k_y.dT/dy) + Q = 0 \qquad (C2)$$

The above field equation is also subject to the following boundary conditions for orthogonal cutting.

$$T = T_A \qquad \text{on } S_A \qquad (C3)$$

$$k_x(dT/dx).n_x + k_y(dT/dy).n_y + q + h(T-T_B) = 0 \quad \text{on } S_B \qquad (C4)$$

where T(x,y) = temperature; Q(x,y) = heat generation per unit area; $k_x(x,y)$ = thermal conductivity in x-direction; $k_y(x,y)$ = thermal conductivity in y-direction; C = heat capacity of work-piece: ρ

= density of work-piece; T_A = specified temperature on boundary A; n_x,n_y = direction cosines of the outward normal to the boundary surface; h = coefficient of the surface heat transfer; S = running coordinate along the boundary.

The variational principle for equations C2, C3, C4 for linear problems is well established and given by:

$$I(T) = [1/2\{k_x(dt/dx)2 + k_y(dt/dy)2\} - QT]\, dA + [q+h(T/2-T_B)]T\, dS \qquad (C5)$$

The solution of equation C5 is obtained by minimizing the functional I(T).

A two dimensional triangular element is employed to model the heat flow. A triangular secondary shear zone reported in the literature is used to define the domain for calculation of the temperature distribution. Using equation C5 the following discretized form is obtained:

$$\tfrac{1}{2}\{[N_{i,x}k_xN_{j,x} + n_{i,y}k_yN_{j,y}]\, T_iT_j - N_iQT_i + [q\, N_i + h(1/2N_iN_jT_j - T_BN_i)]\, T_i\}\, dS \qquad (C6)$$

where $N_{i,x}$ represents the derivative of N_i with respect to x and I denotes the nodal number.

Equation C6 can be written in the following matrix form:

$$[A]\{T\} = \{f(t)\}$$

where [A] = heat conductance matrix and $A_{ij} = (N_{i,x}k_xN_{j,x} + n_{i,y}k_yN_{j,y})dA + h\, N_iN_j\, dS$

{f} = heat output vector and $f_i = N_i\, Q\, dA - N_i(q - h\, T_B)\, dS$

The matrices [A] and {T} are evaluated using the Gaussian technique. The computation was accomplished using a computer algorithm. The analytical results show an increase of temperature from the cutting edge of the tool to the point where the chip loses intimate contact with the tool, see Figs. 4.16(b), 4.17(b) and 4.18(b). The maximum tool-chip interface temperatures increase with increase of cutting speed. The analytical predictions fall within the range of the experimental values obtained by the ultrasonic technique in the present work and those reported by Dearnley [150]. However, the limitations of the model for temperature calculation developed in the present work is that the material properties at the tool-chip interface are not well established.

APPENDIX D

DYNAMIC RECRYSTALLISATION IN PRIMARY SHEAR BAND

Dynamic recrystallisation is favoured under large strain, high strain rate deformation conditions [192-194]. Hodgson has reported an empirical relationship, relating dynamic recrystallisation with the Zener Hollomon parameter, which is shown below:

$$d_{dyn} = 3.9x10^{4}Z^{-0.27} \qquad (D1)$$

where, $Z = \dot{\epsilon} \exp(Q_{def}/RT)$, ($Q_{def}$ = 312kJ/mole and R is the universal gas constant.

In the present work on Fe-28.9Ni-0.1C alloys, the transformation shear band occurring in the primary shear zone exhibits recrystallised grain size of 40-100 nm corresponding to a cutting speed of 400 m/min. It is instructive to calculate the temperature for the observed grain size and strain rate ($2x10^5$ /s). For recrystallised austenite grain size of 100 nm, the calculated average temperature of primary shear band is 1058 K (785^0C) which is $\approx 0.6T_m$. The important inference is that dynamic recrystallisation could occur at low temperature, lower than the reported $0.8T_m$ [185], under conditions of large strain, high strain rate deformation characteristic of metal forming.